TECHNISCHE UNIVERSITÄT MÜNCHEN

Lehrstuhl für Numerische Mechanik

Computational Modelling of Thermo-Structure Interaction with Application to Rocket Nozzles

Caroline Danowski

Vollständiger Abdruck der von der Fakultät für Maschinenwesen der Technischen Universität München zur Erlangung des akademischen Grades eines

Doktor-Ingenieurs (Dr.-Ing.)

genehmigten Dissertation.

Vorsitzender:	Univ.-Prof. Dr.-Ing. Wolfram Volk
Prüfer der Dissertation:	
	1. Univ.-Prof. Dr.-Ing. Wolfgang A. Wall
	2. Prof. Laurent Stainier, Ph.D. École Centrale Nantes, Frankreich

Die Dissertation wurde am 7. Mai 2014 bei der Technischen Universität München eingereicht und durch die Fakultät für Maschinenwesen am 7. Juli 2014 angenommen.

Der höchste Lohn für unsere Bemühungen ist nicht das,
was wir dafür bekommen, sondern das, was wir dadurch werden.

The highest reward for man’s toil is not what he gets for it,
but what he becomes by it.

John Ruskin (1819-1900)

Abstract

Thermodynamics is a fundamental discipline of science and engineering, where the relation and interaction between the deformation of a body and the corresponding temperature state are investigated. The target application to rocket nozzles describes a complex thermo-fluid-structure interaction (TFSI) problem. Challenging features of this particular problem type concern extreme temperatures and temperature gradients which are introduced into the very thin structure of the rocket nozzle due to combustion and cooling. Furthermore, high Mach and Reynolds numbers as well as complex shock-boundary-layer interactions have to be considered. As a consequence of cyclic loading, creep and chemical damage, the so-called dog-house effect can occur. The dog-house effect is a complex cracking phenomenon which is deemed responsible for control loss and therefore failure of an Ariane 5 ECA launcher in the year 2002.

For advanced design of future rocket nozzles, improved understanding of the TFSI problem is essential. Since it is extremely complicated to reproduce the actual environment of a rocket in an experimental setup, computer simulations play an important role.

To enable a realistic description of the deformation behaviour in the flexible rocket nozzle structure under large deformations and the aforementioned thermomechanical loadings, in this thesis, a comprehensive numerical model for the analysis of the challenging volume-coupled problem of thermo-structure interaction (TSI) is developed. Since the simulation approach can only be verified with experiments of model scenarios and since it is a priori not clear what property is relevant, the present TSI computational approach is aimed at avoiding all simplifications and assumptions which are not mandatory and whose influence is not completely clear with respect to the target application. Thus, full coupling is taken into account, i.e. the solution of the displacement field depends on the temperature field and vice versa. Additionally, all coupling terms arising in the target system are considered.

The proposed volume-coupled TSI model is based on the finite element method for structural and thermal field, yielding separate discretisations. Various temperature-dependent, isotropic, elastic as well as elastoplastic material models for small and finite strains can be applied, which are capable of incorporating the effect of the highly elevated temperatures predominating in rocket nozzles. Furthermore, first steps towards including ductile damage into the computational model are accomplished using Lemaitre's material model.

To solve fully coupled thermomechanical systems, both partitioned and monolithic coupling algorithms are conceivable. In the literature, usually partitioned algorithms are considered, hence in this thesis different loosely and strongly coupled partitioned schemes, possibly including acceleration techniques, as e.g. the Aitken Δ^2 method, are established. Moreover, motivated by the excellent performance of monolithic schemes for fluid-structure interaction problems in Gee et al. [47], a novel monolithic Newton-Krylov scheme with problem-specific block Gauss-Seidel preconditioner and algebraic multigrid methods is developed for the TSI problem. It is shown that both partitioned and monolithic algorithms provide a solution for TSI problems. However, for several problem configurations, monolithic schemes exhibit improved robustness compared to partitioned schemes and enable the handling of a broader spectrum of physical parameters.

The proposed model is tested for various meaningful numerical examples. They demonstrate that the computational method is robust and provides accurate results. Among others, realistic configurations with complex three-dimensional geometries and large numbers of degrees of freedom are presented.

In summary, the developed computational model enables an efficient and robust solution of a wide range of TSI applications and establishes an important, reliable and well-validated building block for complex multiphysics simulations, such as the overall TFSI model.

Deutsche Zusammenfassung

Thermomechanische Systeme findet man in einer Vielfalt von alltäglichen und technischen Anwendungen. Hierbei liegt der Fokus auf den Wechselwirkungen zwischen der Deformation und der Temperatur, wie z.B. bei dem hier betrachtete Problem der komplexen Thermo-Fluid-Struktur-Interaktionen (TFSI) in Raketendüsen. Dieses anspruchsvolle gekoppelte TFSI-Problem kann beispielsweise anhand der Schubkammer des Vulcain-Triebwerks demonstriert werden. Aufgrund der Verbrennung wird die sehr dünne Düsenstruktur mit extremen Temperaturen und Temperaturgradienten belastet (d.h. Verbrennungstemperaturen von ca. $3600\ \mathrm{K}$ und Kühlmitteltemperaturen von ca. $73\ \mathrm{K}$), die besonders an der Wand zwischen Heißgas und Kühlmittel zu sehr großen Wärmeflüssen und thermischen Spannungen führen. Durch die extremen Belastungen treten plastische Deformationen in der Düse auf, die die Lebenszeit des Triebwerks und somit der ganzen Trägerrakete stark begrenzen können. Zusätzlich tritt infolge Kriechen, zyklischer Belastungen und chemischer Schädigung, der sogenannte "dog-house effect" auf, der ein komplexes Versagensphänomen beschreibt. So ist der Verlust der Ariane 5 ECA Trägerrakete der ESA im Jahr 2002 vermutlich auf den "dog-house effect" zurückzuführen. Abgesehen von den komplexen Phänomen in der Düsenstruktur wird das TFSI-Problem durch ein anspruchsvolles Strömungsproblem vervollständigt, bei dem hohe Mach- und Reynoldszahlen sowie komplexe Schock-Grenzschicht-Wechselwirkungen auftreten.

Für die Entwicklung von zukünftigen Raketensystemen ist es wichtig, das gegebene komplexe TFSI-Problem vollständig abzubilden. Da es schwierig oder gar unmöglich ist, die TFSI und somit die Funktionsweisen einer Rakete, auf der Erde und im Weltall, in einem Experiment realistisch nachzubilden, kommen immer mehr mathematische Modelle und numerische Simulationen zum Einsatz.

Um das Verhalten der flexiblen Düsenstruktur unter Berücksichtigung großer Deformationen und den genannten thermomechanischen Belastungen realistisch darzustellen, wird in der vorliegenden Arbeit ein umfassendes numerisches Modell entwickelt, welches das volumengekoppelte Problem der Thermo-Struktur-Interaktion (TSI) vollständig beschreiben kann. Dieses Modell trägt zur Verbesserung des Verständnisses der physikalischen Vorgänge in der Struktur der Raketendüse bei und ermöglicht somit die Entwicklung von verbesserten Triebwerkskomponenten.

Für die Simulation in der Strukturmechanik hat sich die Finite-Element-Methode (FEM) als eine hervorragend geeignete numerische Approximationsmethode bewährt. Daher wird die FEM ausschließlich für das vorliegende TSI-Problem verwendet. Ansätze in der Literatur basieren oft auf kleinen Verzerrungen oder vereinfachten Kopplungstermen oder vernachlässigen diese sogar. Im Gegensatz dazu berücksichtigt das vorliegende Modell alle Kopplungsterme und enthält sowohl einfachere als auch komplexere Modellierungsansätze, wie z.B. kleine und große Verzerrungen oder thermoelastische und thermoplastische Materialmodelle. Dies ist für die Abbildung des realen Düsenverhaltens wichtig, da der benötigte Komplexitätsgrad sowie die relevanten Eigenschaften und Lastzustände, die zur Abbildung des realen Düsenverhaltens nötig sind, nicht a priori bekannt sind.

Zur Lösung eines thermomechanischen Problems werden in der Literatur üblicherweise partitionierte Ansätze verwendet. Aus diesem Grund werden in dieser Arbeit verschiedene schwach

und stark koppelnde partitionierte Ansätze implementiert, die auch Konvergenzbeschleunigungsmethoden wie z.B. die Aitken Δ^2 Methode beinhalten. Darüber hinaus wird ein neues, sehr effizientes, monolithisches Newton-Krylov-Verfahren etabliert, das auf problemspezifischen Block-Gauss-Seidel-Vorkonditionierern mit Algebraischen Mehrgitter-Verfahren basiert. Während partitionierte und monolithische Ansätze für die Lösung von TSI-Problemen verwendet werden können, ermöglicht das hier entwickelte monolithische Verfahren oft eine robustere und effizientere Lösung und ist nicht begrenzt auf bestimmte Materialparameter. Weiter wird gezeigt, dass Lösungen oft einzig mit diesem monolithischen Ansatz erzielt werden können.

Langfristiges Ziel ist es, das in der vorliegenden Arbeit entwickelte TSI-Modell mit einem kompressiblen, turbulenten Strömungslöser zu einem vollständigen TFSI-Modell zu verbinden. Somit wird es erstmals möglich sein, das gegebene TFSI-Problem in der Raketendüse räumlich und zeitlich vollständig aufzulösen. Erste Schritte wurden bereits in Hammerl et al. [53] and Grilli et al. [52] umgesetzt. Darüber hinaus, kann das entwickelte TSI-Modell auf weitere Mehrfeldprobleme angewendet werden, wie z.B. nichtlineare thermomechanische Kontaktprobleme, siehe Gitterle [49].

Die vorliegende Arbeit gliedert sich wie folgt. In **Kapitel 2** werden die Grundlagen der nichtlinearen Kontinuumsthermodynamik präsentiert und die kinematischen Beziehungen sowie die Bilanzgleichungen diskutiert. Im Anschluß wird auf die Konstitutivtheorie im Allgemeinen eingegangen, die als Grundlage für die Ableitung der Spannungen und der Kopplungsterme des TSI-Problems dient. In **Kapitel 3** und **Kapitel 4** werden die notwendigen Gleichungen für das Strukturfeld bzw. das Temperaturfeld zusammengefasst. Hierbei wird auf die schwache Formulierung der jeweiligen Bilanzgleichungen eingegangen, sowie deren räumliche und zeitliche Diskretisierung mit der FEM bzw. finiten Differenzen präsentiert. Um das Einzelfeldproblem zu vervollständigen, werden verschiedene Konstitutivgesetze herausgestellt. Für ein nichtlineares rein strukturmechanisches Problem werden verschiedene Konstitutivgesetze unterschieden, während für das thermische Problem ausschließlich das Fourier Gesetz der Wärmeleitung gewählt wird. **Kapitel 5** verbindet die zuvor einzeln betrachteten Felder Struktur und Temperatur zu einem volumengekoppelten TSI-Problem. Hierbei werden besonders die durch die Kopplung sich verändernden Terme sowie zusätzlich auftretenden Terme herausgestellt. Die Wärmekonvektionsrandbedingungen benötigen im Rahmen der TSI mit großen Deformationen spezielle Ansätze, welche hier präsentiert werden. Außerdem wird das zu lösende voll diskrete TSI-Gleichungssystem angegeben, das aus den kontinuierlichen Gleichungen der Einzelfelder erhalten wird. Das darauf folgende **Kapitel 6** stellt zu Beginn die verschiedenen Lösungsverfahren für ein TSI-Problem vor. Besonderes Augenmerk liegt dabei auf den partitionierten und monolithischen Verfahren, die im Rahmen dieser Arbeit untersucht werden. In **Kapitel 7** werden anschließend aussagekräftige numerische Beispiele vorgestellt. Unter anderem werden realistische Probleme mit komplexen dreidimensionalen Geometrien betrachten. Die Beispiele demonstrieren, dass das vorgestellte TSI-Berechnungsverfahren robust ist und korrekte Ergebnisse liefert. Abweichende Ergebnisse von anderen numerischen Ergebnissen aus der Literatur werden an den entsprechenden Stellen diskutiert und können dabei auf abweichende Modellierungsannahmen zurückgeführt werden. Abschließende Bemerkungen und eine kurze Diskussion der Ergebnisse sowie mögliche zukünftige Forschungsschwerpunkte werden in **Kapitel 8** erörtert. Zusätzliche nützliche Beziehungen werden im **Anhang** zusammengefasst.

Danksagung

An dieser Stelle möchte ich einen ganz herzlichen Dank an all jene aussprechen, die mich in den intensiven Jahren meiner Promotion auf so vielfältige Weise unterstützt haben.

Mein besonderer Dank gilt meinem Doktorvater, Prof. Wolfgang A. Wall, für das in mich gesetzte Vertrauen, die fachliche und persönliche Unterstützung und Förderung sowie die exzellenten Rahmenbedingungen, die man hier am Lehrstuhl vorfindet. Seine Leidenschaft für die Forschung haben mich stark geprägt und stets motiviert.

Bei den weiteren Mitgliedern der Prüfungskommission, Herrn Prof. Laurent Stainier und Herrn Prof. Wolfram Volk, bedanke ich mich für die aufgebrachte Zeit und Mühe im Zusammenhang mit meinem Promotionsverfahren.

Der Deutsche Forschungsgemeinschaft danke ich für die Finanzierung meiner Promotion im Rahmen des Sonderforschungsbereichs SFB/TRR 40 “Technologische Grundlagen für den Entwurf thermisch und mechanisch hoch belasteter Komponenten zukünftiger Raumtransportsysteme”.

Ein ganz besonderes Dankeschön geht auch an meine Kollegen, von denen ich so viel gelernt habe. Die großartige Arbeitsatmosphäre und die vielen fachlichen (und nicht-fachlichen) Diskussionen haben für mich die Promotionszeit zu einem unvergesslichen Lebensabschnitt gemacht, an den ich mich auch in Zukunft gerne erinnern werde. Besonders die uneingeschränkte Hilfsbereitschaft, die ich stets erfahren habe, wenn es galt Probleme gemeinsam zu verstehen und zu lösen waren so wichtig für mich. Vor allem Dr. Sophie Rausch, Dr. Lena Yoshihara, Dr. Volker Gravemeier, Andreas Ehrl, Georg Hammerl, Keijo Nissen, Dr. Shadan Shahmiri, Jonas Biehler und Susanna Tinkl möchte ich für die tolle Zusammenarbeit und auch Freundschaft danken. Außerdem möchte ich mich bei Dr. Georg Bauer, Burkhard Bornemann, Ph.D., Alexander Seitz und Tobias Wiesner für Ihre Unterstützung bedanken. Nicht zu vergessen ist das Herzstück des Lehrstuhls Frau Renata Nagl, die mir in so vielen Situationen stets kompetent geholfen hat. Den fleißigen Korrekturlesern des Manuskripts möchte ich ebenfalls ein großes Dankeschön aussprechen. Sie haben beigetragen die schriftlichen Arbeit grundlegend zu verbessern.

Schließlich danke ich von ganzem Herzen meiner Familie, insbesondere meinen Eltern, meiner Schwester Katrin und vor allem meinem Freund Hannes für das in mich gesetzte Vertrauen, die unerschöpfliche Unterstützung und für so manchen Rat und Zuspruch in schwierigen Situationen. Ohne ihren Rückhalt wäre diese Arbeit undenkbar. Darüber hinaus danke ich all meinen Freunden, die trotz räumlicher Ferne immer Anteil an mir und meiner Arbeit genommen haben und mir somit das Weitermachen erleichtert haben.

München, Juli 2014 Caroline Danowski

Contents

Nomenclature

Representation of scalars, tensors and other quantities

q, Q	Scalar quantity
$\boldsymbol{q}$	Vector
$\boldsymbol{Q}$	Second-order tensor
$\boldsymbol{\mathscr{Q}}$	Higher-order tensor
$\mathbf{q}$	Discrete vector
$\mathbf{Q}$	Discrete matrix, Voigt notation of second-order tensor

Operators and Symbols

$(\cdot)^{\mathsf{T}}$	Transpose of a tensor
$(\cdot)^{-1}$	Inverse of a tensor or mapping
$(\cdot)^{-\mathsf{T}}$	Transpose of the inverse of a tensor
$\hat{(\cdot)}$	Prescribed quantity
$\dot{(\cdot)}$, $\ddot{(\cdot)}$	First and second time derivative at a fixed reference position
$\tilde{(\cdot)}$	Modified or transformed quantity
$\boldsymbol{I}$	Identity tensor
$\mathbf{0}$	Zero tensor or matrix
$\det$	Determinant
tr	Trace operator
$\ln$	Natural logarithm
Grad	Material gradient operator
Div	Material divergence operator
grad	Spatial gradient operator
div	Spatial divergence operator
Lin	Linearisation operator
sym	Symmetric part of $(\cdot)$
dev	Deviator
sign	Signum function
$\Delta(\cdot)$	Increment, change of $(\cdot)$ within a time step
$\exp$	Exponential function
$\times$	Cross product
$\otimes$	Dyadic product
$\odot$	Specific tensor product
$\mathcal{E}$	Levi-Civita symbol
δ_{jk}	Kronecker delta
$\|\| \cdot \|\|$	Vector norm

Superscripts and Subscripts

$(\cdot)^{(e)}$	Element
$(\cdot)^{h}$	Discretised in space with the FEM
$(\cdot)^{\mathsf{trial}}$	Trial
$(\cdot)_{\mathsf{gp}}$	Gauss point
$(\cdot)_{\mathsf{int}}$	Internal
$(\cdot)_{\mathsf{ext}}$	External
$(\cdot)_{\mathsf{kin}}$	Kinetic
$(\cdot)_{\mathsf{cond}}$	Conductivity
$(\cdot)_{\mathsf{S}}$	Structural field
$(\cdot)_{\mathsf{T}}$	Thermo field

Mappings

φ	Mapping between reference and current configuration
ζ	Mapping between reference configuration and parameter space
$\check{\boldsymbol{J}}$	Jacobian of mapping $\varphi \circ \zeta$

Domains and boundaries

Ω_0	Reference (material) configuration
Ω	Current (spatial) configuration
$\partial\Omega_0$	Boundary in reference configuration
$\partial\Omega$	Boundary in current configuration
$\Gamma_{0;\mathsf{D}}$	Dirichlet partition of boundary in reference configuration
Γ_{D}	Dirichlet partition of boundary in current configuration
$\Gamma_{0;\mathsf{N}}$	Neumann partition of boundary in reference configuration
Γ_{N}	Neumann partition of boundary in current configuration
$\Gamma_{0;\mathsf{C}}$	Heat convection boundary belonging to $\Gamma_{0;\mathsf{N}}$
Γ_{C}	Heat convection boundary belonging to Γ_{N}

Kinematics

$\boldsymbol{X}$, $\boldsymbol{x}$	Position in reference and current configuration
$\boldsymbol{u}$	Displacement
$\dot{\boldsymbol{u}}$	Velocity
$\ddot{\boldsymbol{u}}$	Acceleration
$\boldsymbol{F}$	Deformation gradient
$\tilde{\boldsymbol{F}}$, $\boldsymbol{F}_v$	Isochoric and volumetric part of $\boldsymbol{F}$
$\boldsymbol{F}^e$, $\boldsymbol{F}^p$, $\boldsymbol{F}^t$	Elastic, plastic, and thermal part of $\boldsymbol{F}$
J	(Jacobi) determinant of $\boldsymbol{F}$
J^e, J^p, J^t	Elastic, plastic, and thermal part of J
V_0, V	Reference and current volume
A_0, A	Reference and current surface area
$\boldsymbol{g}_0$, $\boldsymbol{g}$	Basis vectors in reference and current configuration

$\boldsymbol{n}_0, \boldsymbol{n}$	Unit normal vector in reference and current configuration
$\boldsymbol{R}, \boldsymbol{U}, \boldsymbol{V}$	Rotation tensor, material and spatial stretch tensors
$\boldsymbol{C}$	Right Cauchy-Green deformation tensor
$\tilde{\boldsymbol{C}}$	Isochoric part of $\boldsymbol{C}$
$\boldsymbol{B}$	Left Cauchy-Green deformation tensor
$\tilde{\boldsymbol{B}}$	Isochoric part of $\boldsymbol{B}$
$\boldsymbol{E}_{\mathsf{GL}}$	Green-Lagrange strain tensor
$\boldsymbol{E}_{\mathsf{EA}}$	Euler-Almansi strain tensor
$\boldsymbol{\varepsilon}$	Linearised strain tensor
$\boldsymbol{\varepsilon}^e$, $\boldsymbol{\varepsilon}^p$, $\boldsymbol{\varepsilon}^t$	Elastic, plastic, and thermal part of $\boldsymbol{\varepsilon}$
$\dot{\boldsymbol{E}}_{\mathsf{GL}}$	Material strain rate tensor
$\boldsymbol{L}, \boldsymbol{D}$	Spatial velocity gradient and its symmetric equivalent
$\mathcal{L}_t$	Lie-derivative
$\dot{\boldsymbol{\varepsilon}}$	Linearised strain rate tensor

Stresses

$\boldsymbol{\sigma}$	Cauchy stress tensor
$\boldsymbol{\tau}$	Kirchhoff stress tensor
$\boldsymbol{P}$	First Piola-Kirchhoff stress tensor
$\boldsymbol{S}$	Second Piola-Kirchhoff stress tensor
p	Pressure
$\boldsymbol{s}$	Deviatoric stress component
$\boldsymbol{\sigma}_{\mathsf{lin}}$	Linearised stress tensor

Constitutive laws

$\mathcal{P}_{\mathsf{int}}$	Internal power
Ψ	Strain energy density function
$\mathscr{C}_{\mathsf{mat}}$	Constitutive tensor and matrix
$\boldsymbol{C}_{\mathsf{T}}$	Thermal constitutive tensor and matrix
λ, μ	Lamé parameters
E	Young's modulus
ν	Poisson's ratio
K	Bulk modulus
e	Internal energy
ζ	Gibbs free energy
ψ	Helmholtz free energy
η	Entropy
k_0, k	Reference and current heat conductivity
C_{V}	Specific heat capacity at constant volume
α_{T}	Coefficient of thermal expansion
$\mathcal{H}^e$, $\mathcal{H}^{ep}$	Thermoelastic and thermo-elasto-plastic heating term

Plastic constitutive laws

$\boldsymbol{\alpha}_{\mathsf{k}}$	Generic set of internal (state) variables
$\boldsymbol{A}_{\mathsf{k}}$	Generic set of thermodynamical forces
Φ	Yield function
$\dot{\gamma}$, $\Delta\gamma$	Time continuous and incremental plastic multiplier
J_2	Second invariant of stress deviator
q	Von Mises effective stress
$\bar{\varepsilon}^p$	Accumulated plastic strain
$\hat{H}$	Heaviside function
$\boldsymbol{N}_0$, $\boldsymbol{N}$	Reference and current plastic flow vector
$\boldsymbol{H}$	Hardening modulus
$\mathcal{D}_{\mathsf{mech}}$	Mechanical internal dissipation
$\boldsymbol{\beta}$	Back stress tensor
$\boldsymbol{\eta}$	Relative stress tensor (in context of kinematic hardening)
$\boldsymbol{Z}$	Internal variable associated to $\boldsymbol{\beta}$
σ_{f}	Failure stress
σ_{m}	Maximal stress
σ_{y}	Yield stress
$\sigma_{\mathsf{y},0}$	Initial yield stress
$\sigma_{\mathsf{y},\infty}$	Saturation hardening stress
κ	Thermodynamical force associate to isotropic hardening
H^{iso}	Isotropic hardening modulus
H^{kin}	Kinematic hardening modulus
δ	Hardening exponent
ω_0	Thermal softening parameter for $\sigma_{\mathsf{y},0}$
ω_{H}	Thermal softening parameter for $\sigma_{\mathsf{y},\infty}$ and H^{iso}
$(\cdot)_{\mathsf{eff}}$	Effective quantity
Y	Energy-release rate
D	Isotropic scalar-valued damage variable
R	Scalar-valued isotropic hardening variable
ω_{D}	Integrity

Governing equations

m	Mass
ρ_0, ρ	Mass density in reference and current configuration
$\hat{\boldsymbol{b}}_0$, $\hat{\boldsymbol{b}}$	Body force in reference and current configuration
$\boldsymbol{t}$	Traction vector in current configuration
$\boldsymbol{t}_0$	Pseudo-traction vector in reference configuration
$\hat{\boldsymbol{t}}$, $\hat{\boldsymbol{t}}_0$	Prescribed equivalent to $\boldsymbol{t}$ and $\boldsymbol{t}_0$
$\boldsymbol{r}$	Residual vector
$\hat{\boldsymbol{u}}_0$, $\hat{\dot{\boldsymbol{u}}}_0$	Initial displacement and velocity at time $t = 0$
$\hat{T}_0$	Initial temperature at time $t = 0$

$\boldsymbol{Q}$, $\boldsymbol{q}$	Heat flux in reference and current configuration
$\hat{Q}$, $\hat{q}$	Prescribed material and spatial thermal Neumann boundary condition
$\hat{Q}_{\mathsf{C}}$, $\hat{q}_{\mathsf{C}}$	Material and spatial heat convection boundary condition
h	Heat transfer coefficient
r	Heat source
$\boldsymbol{w}$	Weighting function vector
$\delta(\cdot)$	Virtual quantity
$\mathcal{W}$	Work
$\mathcal{P}$	Power

FE space discretisation

nele	Number of elements
nnod	Number of element nodes
ndim	Number of spatial dimensions
ndof	Number of degrees of freedom
ngp	Number of Gauss points per element
$\tilde{N}_I$	FE shape function of node I in reference configuration
N_I	FE shape function of node I in parameter space
$\boldsymbol{\xi}$	Position in FE parameter space
$\mathbf{X}$, $\mathbf{x}$	Discrete nodal positions in reference and current configuration
$\mathbf{d}$, $\dot{\mathbf{d}}$, $\ddot{\mathbf{d}}$	Discrete nodal displacements, velocities, and accelerations
$\mathbf{T}$, $\mathbf{t}$	Discrete nodal temperatures and temperature rates
h	Characteristic element size
$\mathbf{N}_{\mathsf{d}}$, $\mathbf{N}_{\mathsf{T}}$	Matrix containing shape function entries for displacements and temperatures
w_{GP}	Gaussian weight
$\mathbf{K}_{\mathsf{SS}}$	Dynamic effective tangential stiffness matrix
$\mathbf{K}_0$	Initial tangential stiffness matrix
$\mathbf{D}$	Damping matrix
$\mathbf{M}$	Mass matrix
c_{M}, c_{K}	Parameters for Rayleigh damping
$\mathbf{f}$	Discrete force vector
$\mathbf{K}_{\mathsf{TT}}$	Thermal dynamic effective tangential matrix
$\mathbf{C}$	Capacity matrix

Time discretisation

Δt	Time step size
n	Time step index
$\mathbf{d}_n$, $\mathbf{v}_n$, $\mathbf{a}_n$	Discrete nodal displacements, velocities and accelerations at t_n
$\mathbf{T}_n$, $\mathbf{t}_n$	Discrete nodal temperatures and temperature rates at t_n
$\beta, \gamma, \gamma_{\mathsf{T}}$	Parameters of Newmark's method for structure and thermo
$\alpha_{\mathsf{f(;S/T)}}$, $\alpha_{\mathsf{m(;S/T)}}$	Parameters of generalised-α method for structure and thermo

$\rho_{\infty(;\mathsf{S}/\mathsf{T})}$	Spectral radius of time integration scheme in high-frequency limit for structure and thermo
$\theta, \theta_{(\mathsf{S}/\mathsf{T})}$	Parameter of one-step-θ method for structure and thermo

Solution techniques

i	Nonlinear iteration index
$\mathbf{r}$	Discrete residual vector
$\mathbf{K}$	Tangential matrix
$\mathbf{K}_{\mathsf{SS}}$, $\mathbf{K}_{\mathsf{TT}}$	Structural and thermal tangential matrix
$\mathbf{K}_{\mathsf{ST}}$, $\mathbf{K}_{\mathsf{TS}}$	Structural and thermal coupling tangential matrix
$\epsilon_{r^{\mathsf{TSI}}}$, $\epsilon_{x^{\mathsf{TSI}}}$	Convergence criterion for residual and increment of nonlinear solver
ϵ_{out}	Convergence criterion of outer loop in partitioned TSI
l	Iteration index of outer loop in partitioned TSI
$\check{\mathbf{y}}$	Iterative solution vector in partitioned TSI
ω	Relaxation parameter in partitioned TSI

Iterative solvers for linear systems

j	Linear iteration index
$\mathbf{A}, \mathbf{x}, \mathbf{f}$	System matrix, solution and right-hand side vector of original linear inverse system
$\mathcal{K}$	Krylov space
k	Dimension of Krylov space
$\mathbf{M}_{\mathsf{L}}$, $\mathbf{M}_{\mathsf{R}}$	Left and right preconditioning matrix of the original linear system
$\mathbf{M}_{\mathsf{L}}^{-1}$, $\mathbf{M}_{\mathsf{R}}^{-1}$	Inverse of $\mathbf{M}_{\mathsf{L}}$ and $\mathbf{M}_{\mathsf{R}}$
$\check{\mathbf{x}}$	Intermediate solution vector of original linear system
ϵ_{lin}	Convergence criterion for linear iteration
$\Delta\check{\mathbf{x}}$	Krylov increment
$\mathbf{z}$	"Solution" vector of linear system in preconditioning process
$\mathbf{y}$	Right-hand side vector of linear system in preconditioning process
$\mathbf{z}^d$, $\mathbf{z}^T$	Structural and thermal part of $\mathbf{z}$
$\mathbf{y}^d$, $\mathbf{y}^T$	Structural and thermal part of $\mathbf{y}$
ω_{BGS}	Relaxation parameter within stationary Richardson iteration

Return-mapping

Φ^{trial}	Trial value of yield function
$\Delta\gamma$	Increment of plastic multiplier
m	Iteration index for local Newton to calculate $\Delta\gamma$

Abbreviations

AMG	Algebraic multigrid
BEM	Boundary element method
BGS	Block Gauss-Seidel
CDM	Continuum damage mechanics
CTE	Coefficient of thermal expansion
CPP	Closest point projection
DOF	Degree of freedom
EAS	Enhanced assumed strain
ECA	Evolution Cryotechnique Type A
ESA	European Space Agency
FE	Finite element
FDM	Finite difference method
FEM	Finite element method
FSI	Fluid-structure interaction
FVM	Finite volume method
GMRES	Generalised minimal residual
GP	Gauss point
HPC	High performance computing
IBVP	Initial boundary value problem
ILU	Incomplete lower upper triangular matrix
LU	Lower and upper triangular matrix
LES	Large-eddy simulation
ODE	Ordinary differential equation
PDE	Partial differential equation
PMTPE	Principle of minimum of total potential energy
PVW	Principle of virtual work
RMS	Root mean square
SEF	Strain energy density function
SI	International system of units (from French: Système international)
SVK	Saint Venant-Kirchhoff
TFSI	Thermo-fluid-structure interaction
TSI	Thermo-structure interaction
TSVK	Thermoelastic Saint Venant-Kirchhoff
TPM	Theory of porous media
UMFPACK	Unsymmetrical multifrontal sparse LU factorisation package
ψTC	Pseudo-transient continuation

1 Introduction

This chapter motivates the scientific interest of thermo-structure interaction (TSI) in general and for the target application in rocket nozzles in particular, and addresses the need for a comprehensive and complete numerical TSI model. The first section 1.1 will be dedicated to the relevance of thermomechanics for real application and will motivate the necessity for a numerical approach. In the second section 1.2, the research objectives of the present work will be summarized and the individual components for an efficient and robust numerical approach for TSI are highlighted. Finally, to conclude the chapter, the outline of this thesis will be stated in section 1.3.

1.1 Motivation

In various engineering applications, the temperature can be assumed to be constant and only negligible temperature changes occur, so that an isothermal, purely mechanical analysis fully capture the behaviour which is aimed to be modelled. Exemplarily, biomechanical applications, as e.g. fluid-structure interaction (FSI) in lung mechanics or in abdominal aortic aneurysm can be mentioned in this context (see e.g. Wiechert [143], Yoshihara et al. [148] or Maier et al. [83]). For instance during breathing, the lung tissue deforms mechanically and interactions between the air and the lung tissue takes place, while the temperature remains nearly constant, namely at human body temperature of about $37\ ^{\circ}\mathrm{C} = 310\ \mathrm{K}$. Hence, for this problem temperature changes are small and the isothermal analysis is a valid assumption.

However, the target of this thesis is on problems where an isothermal, purely mechanical analysis is not able to reproduce the real behaviour satisfactory. Hence, the focus of this study is on the volume-coupled problem of TSI in solid bodies. Here, the relation and interaction between the deformation of a body (i.e. the mechanics) and the corresponding temperature state is investigated which equivalently can be summarized in the common, more general term thermomechanics. This coupled thermomechanical problem can be found in everyday life as well as in engineering applications. A very common and simple example, where thermomechanics can be observed in everyday life, is the cyclic bending of a paper clip until it breaks. It can be observed that the clip is heated up in the failure zone until it breaks due to dissipated plastic work in the material. Hence, the paper clip describes a coupled thermomechanical problem, where the deformation interacts with the temperature and vice versa. To correctly describe this problem, not only the deformation but also its temperature evolution need to be considered. In engineering applications as life prediction, fatigue induced by cyclic loading, rubber friction, crash tests, forming processes, combustion processes, etc., the coupled thermomechanical analysis is inevitable. Furthermore, various engineering applications exist, in which especially the interaction between deformation and temperature is consciously exploited. One very famous example is a crash test in automotive engineering: when a car hits a stationary, immovable object (e.g. a tree or a wall), the crunching chassis converts the kinetic energy of the car moving into

thermal energy due to bending of the chassis material, thereby protecting the passenger inside the car. Another example concerns a forming process: herein, the metal workpiece is heated to facilitate the forming process.

Apart from the aforementioned examples, the present thesis aims at optimizing the design of future rockets by improving the understanding of the complex problem of thermo-fluid-structure interaction (TFSI) in rocket nozzles. Challenging features of this particular problem type can be demonstrated when considering the thrust chamber of the Ariane 5 main engine "Vulcain" (depicted in Figure 1.1). Elevated temperatures (combustion temperature up to $3,600\ \mathrm{K}$) with

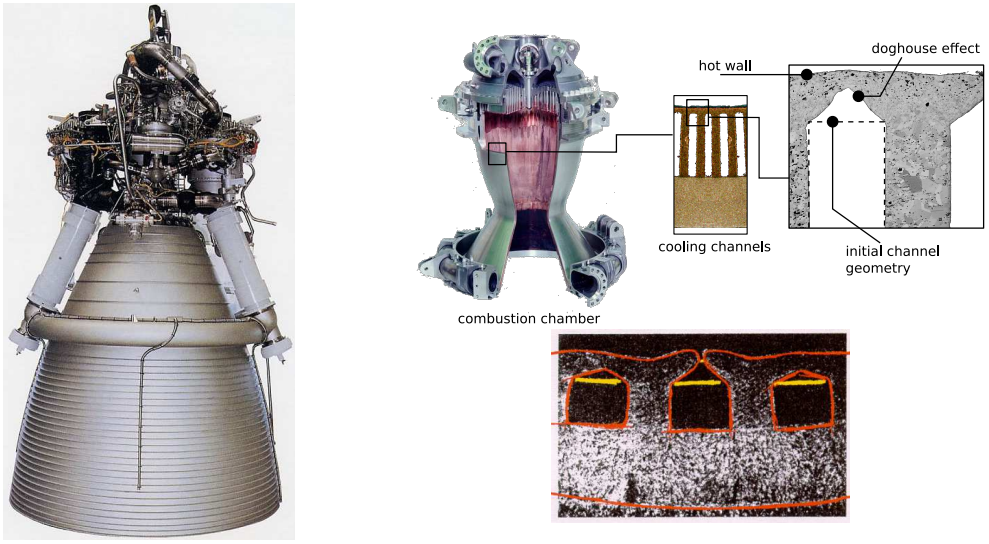

Figure 1.1: Regeneratively cooled thrust chamber of the main engine "Vulcain 2" utilised in the Ariane 5 launcher of the European Space Agency (ESA) (from http://www.capcomespace.net/dossiers/espace_europeen/ariane/ariane5/) (left) and cooling channel structure in a cryogenic rocket combustion chamber and the dog-house-like deformation of the hot wall (from Schwarz et al. [114]) (right top) and the dog-house effect and typical failure of a combustion chamber wall (from Riccius and Zametaev [109]) (right bottom).

high temperature gradients (coolant fluid inlet temperature approximately $73\ \mathrm{K}$), high wall heat fluxes (of about $120\ \frac{\mathrm{MW}}{\mathrm{m}^2}$), very thin structures, high Mach and Reynolds numbers, and complex shock-boundary-layer interactions have to be considered in the target system of such a rocket nozzle (see e.g. Kuhl et al. [69] and Riccius and Zametaev [109]). Due to the combustion of the propellant, high thermal and mechanical loads evolve which decisively influence the behaviour of the rocket structure. To reduce the applied loadings, on the one hand the structure is cooled by introducing a cooling medium into the cooling channels, which on the other hand introduces enormous temperature gradients, yielding large heat fluxes and large thermal stresses. Further challenges are the consequences of unsteady flow separation or reattachment of the supersonic flow within the nozzle, which can result in often dangerous side loads. These unsymmetrical side loads, which occur mainly during the transient start-up phase, can negatively influence the behaviour or damage the nozzle itself, as shown e.g. in Baars et al. [12], Frey and Hagemann [43], Grilli et al. [52] and Östlund et al. [102]. In Brown et al. [20], the side loads are specified

for the Apollo Saturn V rocket to reach extreme magnitudes of about 10^3 kN. Moreover, the material modelling of the rocket structure is challenging. As a consequence of cyclic loading, creep, and chemical damage, the so-called dog-house effect can occur (see Figure 1.1 (right) and, e.g. Schwarz et al. [114] for a material model considering these effects). The dog-house effect is a complex cracking phenomenon which is deemed responsible for control loss and therefore failure of an Ariane 5 ECA launcher of the European Space Agency in the year 2002.

The focus of this study is set on a realistic description of the deformation behaviour in the flexible rocket nozzle structure under the aforementioned thermomechanical loadings, i.e. on the challenging volume-coupled problem of thermo-structure interaction (TSI). For correctly representing deformations in rocket nozzles due to hot gases, both the displacement field and the temperature field need to be considered in the target TSI model. The resulting thermomechanical system is a fully coupled problem, that is, the solution of the temperature field depends on the displacement field and vice versa. Additional strong nonlinearities can further be introduced into the thermomechanical system via inclusion of large deformations, dynamics, plasticity or damage. Altogether, the challenges and difficulties of mathematically describing and solving these thermomechanical problems become obvious, even if the given problem setup is quite simple. Due to this complexity, only very few thermomechanical problems exist, where analytical solution techniques are actually applicable. Analytical solutions exist, for instance for the solution of free cooling of a specimen from a prescribed temperature difference to surrounding temperature assuming a linear analysis and constant material parameters or for uniaxial tensile tests with constant temperatures, see e.g. Hartmann [54]. Nowadays, analytical solution techniques are still utilised for validation purposes of numerical models, such as e.g. in Hartmann [54] and Erbts and Düster [38].

The thesis aims at general nonlinear thermomechanical solid problems, thus for mathematical analyses experimental procedure and numerical modelling attract increasing interest. Physical experiments are commonly utilised to gain information about certain aspects, however, for the whole range of applications, experimental procedures are limited or practically impossible. For instance, experiments investigating crucial phenomena of a rocket nozzle are expensive and extremely complicated among others because of the difficulty to get measurements at the important interfaces of this multi-coupled problem and since the actual environment is impossible to be realised in a lab on earth. Hence, combining the aforementioned arguments, it becomes obvious that there is a high and ever-growing demand for powerful numerical modelling and simulation techniques which enable accurate, efficient, and robust computer simulations for thermomechanical applications, even for problems where no analytical solutions exist or which are at least difficult to solve.

1.2 Research objective

The work described in this thesis is part of a Collaborative Research Centre SFB/TRR 40 “Fundamental Technologies for the Development of Future Space-Transport-System Components under High Thermal and Mechanical Loads” of the German Research Foundation (Deutsche Forschungsgemeinschaft - DFG). The long-term perspective of this project is to couple the developed TSI model to a large-eddy simulation (LES) approach to turbulent flow, including shock-boundary-layer interactions. First steps in direction of TFSI can be found in Hammerl et al. [53]

and Grilli et al. [52]. The complete TFSI model is intended to account for all working stages of a rocket nozzle while resolving effects on all spatial and temporal scales. Consequently, the model is intended to improve the design and prediction of future rocket nozzles by showing its functionality not only on earth but also in space. Since no detailed experimental data will be available for rocket nozzles in flight conditions, an accurate and reliable computational approach is essential which is composed of well-validated, reliable, efficient and robust building blocks such as the TSI model developed in this work.

Since the present TSI approach can only be verified with experiments of model scenarios, the simulation approach is aimed at avoiding all simplifications and assumptions which are not mandatory and whose influence is not completely clear with respect to the target application. A flexible approach is realized which enables to switch between simpler and more complex modelling approaches such as geometrically linear and nonlinear analysis, monolithic or partitioned solution strategy, and elastic or plastic material modelling.

All governing equations of TSI are exclusively expressed with respect to the finite element method (FEM). The variety of textbooks about general FEM is enormous, exemplarily the reader is referred to Bathe [15], Zienkiewicz and Taylor [149], and Zienkiewicz et al. [150]. Over the last decades, the FEM has been successfully established as a flexible, robust and accurate discretisation approach for the solution of partial differential equations (PDEs) within various classes of problems. Particularly within solid mechanics, contact mechanics, computational fluid dynamics, or in coupled problems as electrochemistry, FSI, or TSI, the FEM has performed excellently. For the sake of completeness alternative approaches to the FEM exist, as e.g. the boundary element method (BEM), the finite difference method (FDM), or the finite volume method (FVM). Since possibly nonlinear kinematics, nonlinear material behaviour, thin structures, etc. may be included, the FEM is the method of choice for this thesis. The FEM is applied to both structural and thermal field, yielding separate discretisations such that a conforming finite element (FE) approach is constructed. Furthermore, there is an increasing interest of combining TSI with other physical phenomena, such as contact mechanics, theory of porous media (TPM) or FSI which are commonly also based on finite elements (FEs). First steps in coupling the present TSI model with contact mechanics are realised, e.g. in Gitterle [49]. For the purpose of universality, the model includes different first- and second-order FE interpolations for full three dimensions.

To solve fully coupled thermomechanical systems, both partitioned and monolithic coupling algorithms are basically conceivable (for a detailed overview on existing coupling algorithms for TSI, the reader is referred to the introduction of chapter 6). In current literature, usually partitioned algorithms are chosen, where loosely and strongly coupled partitioned algorithms can be distinguished. Partitioned algorithms are very flexible with respect to the formulation and the solution methods of the individual fields, but a significant problem of them is either their conditional stability (for loosely coupled schemes) or their potentially very slow convergence or even divergence (for strongly coupled schemes). To circumvent these drawbacks, various stabilisation techniques have been proposed to retain unconditional stability properties and acceleration techniques to improve convergence behaviour, respectively. However, in the context of the surface-coupled problem of FSI, it was recently pointed out, e.g. in Gee et al. [47] and Klöppel et al. [67] that well-designed monolithic algorithms are superior to strongly coupled partitioned schemes, even if acceleration procedures are utilised in the latter. Based on the excellent performance of monolithic algorithms in FSI, in this work a novel monolithic Newton-Krylov approach to TSI

is established using block Gauss-Seidel (BGS) preconditioners and algebraic multigrid (AMG) methods for the approximation of the field inverses. For the sake of completeness, different loosely and strongly coupled partitioned schemes are further established since they represent the default coupling strategy in literature for TSI problems. All presented TSI approaches feature bi-directional coupling, i.e. the influence of temperature on the mechanical side as well as the influence of deformation on the thermal side is considered, including all coupling terms.

An efficient and robust solution even for large problem sizes is enabled by integrating all proposed methods into a high performance computing (HPC) framework which allows fully parallel multiprocessor computations utilising direct solvers as well as iterative solvers with corresponding preconditioning techniques. Consequently, the target of the present thesis is on a universal fully coupled nonlinear thermomechanical solid model which can be used like a black box including different materials, different time integrators, different coupling strategies, different solvers, etc., and which furthermore enables efficient and robust solutions even if expensive physical effects as plasticity in nonlinear dynamics are considered.

All numerical methods and models are implemented in our in-house FE software package BACI (see Wall and Gee [142]) jointly developed at the Institute of Computational Mechanics and the Mechanics & High Performance Computing Group at Technische Universität München. BACI represents a multiphysics multi-purpose parallel research code which is written in C++ and utilises powerful open-source libraries developed by Sandia National Laboratories, as e.g. the Trilinos Project (Heroux et al. [56]). Consequently, the present model is based on existing features in BACI such as different FE formulations and time integration schemes for the structure or direct and iterative solver techniques, which are reused for this thesis and moreover are supplemented with various new algorithmic extensions and code modules.

1.3 Outline

The present thesis is divided into eight chapters. **Chapter 2** will cover the fundamentals of nonlinear continuum thermodynamics. In this chapter, the basic kinematical relations, the mechanical as well as the thermodynamical balance relations, as well as the basics of the constitutive theory will be reviewed. **Chapter 3** will outline the relevant governing equations of nonlinear solid mechanics, the basic concepts of weak formulations, FE discretisation, time discretisation, and different constitutive laws for purely mechanical analyses. Current rocket nozzles are mainly made of metals, hence the constitutive will be based on isotropic ductile material behaviour. With regard to irreversible deformations, for instance von Mises plasticity will be chosen. In addition, nonlinear and linear solution techniques will be summarized in a general way. While **Chapter 3** will be devoted to the structural field, i.e. isothermal solid mechanics, **Chapter 4** will present the corresponding equations for the thermal field. Herein, the instationary heat conduction equation will be establish in a strong and a weak form. The fully discrete thermo equations will be derived and Fourier's law will be used as the constitutive law for the heat flux. **Chapter 5** will combine the aforementioned relations of the single fields structure and thermo to the volume-coupled problem of TSI to enable the description of fully nonlinear non-isothermal solid mechanics. Herein, the coupled balance relations and the corresponding coupled constitutive laws will be reviewed as an extension of the equations of the single fields. Moreover, additional dependencies arising due to the coupling will be outlined and the special treatment of so-called nonlinear

heat convection boundary conditions within large deformation TSI will be specified. In **Chapter 6**, first a detailed overview on different existing solution strategies for TSI in literature will be given. Subsequently, partitioned and monolithic solution algorithms utilised in this work for TSI problems will be presented. While different loosely and strongly coupled partitioned algorithms will be distinguished, the monolithic TSI algorithm will be based on BGS preconditioners with AMG methods.

Chapter 7 will present six meaningful numerical examples, where the first examples will be considered for validating the different (thermo-)elastoplastic material models for small and finite strains, followed by the so-called second Danilovskaya problem, which will be used for validation of the TSI algorithms. In the last example of a fully three-dimensional rocket nozzle, various aspects such as solution strategy, material modelling, time integration, high performance computing with large numbers of degrees of freedom will be tested in one complex simulation.

Finally, in **Chapter 8** the most important results will be briefly summarized and discussed, and a short outlook to possible and necessary enhancements of the present model will be provided. Herein, several improvements and extensions will be suggested, so that TSI problems can be computed even more efficiently and hence a larger area of TSI applications can be covered.

Further useful relations in the context of tensor notation, linearisation and physical measures in conjunction with the used units are summarized in **Appendix A-C**. Moreover, additional details with respect to material modelling, such as the full Lemaitre material model and the finite strain thermo-hyperelasto-plastic material model are established in **Appendix D**.

2 Nonlinear continuum thermodynamics

In this chapter, the basic concepts of nonlinear continuum thermodynamics are reviewed for the later application to the three different problems, namely the single field problem of solid dynamics, the single field problem of thermal dynamics, and finally the coupled field problem of thermo-structure interaction (TSI). The term continuum thermodynamics combines the theory of continuum mechanics and thermodynamics. While continuum mechanics considers the kinematics and the mechanical behaviour of continuously distributed media, thermodynamics originates from the words "therm" and "dynamics" which mean heat and power, respectively. Thermodynamics comprises the theory of energy and heat which is used to describe processes that involve changes in temperature, transformation of energy, and the relation between heat and work. It considers energy conversion between mechanical work and heat, and the macroscopic variables such as temperature, volume, and pressure. More extensive reviews on nonlinear continuum thermodynamics can be found in the literature, as e.g. in the basic textbooks Bonet and Wood [17], Holzapfel [58], Lemaitre and Chaboche [78], Maugin et al. [85], and Truesdell and Noll [136], or especially for plasticity in de Souza Neto et al. [33] and Simo and Hughes [120].

This chapter will first review relevant continuum mechanical equations and the balance relations, before the relevant theory of thermodynamics will be discussed which is utilised to describe a problem in a thermodynamically consistent way.

2.1 Kinematics

2.1.1 Kinematics of a three-dimensional continuum body

The following sections offer a brief overview of the required kinematical relations to describe nonlinear deformation processes of a homogeneous, continuous body for the target application of TSI. In the present context, the term kinematics is defined as the mathematical description of the motion and deformation of a body. The present work exclusively uses the total Lagrangian formulation which is convenient for solids since the initial state of the solid is fully known. Furthermore, a common Cartesian coordinate system is assumed for all configurations. In this case, as shown in Figure 2.1, the initial, material, or reference configuration Ω_0 describes the undeformed and stress-free body at time $t_0 = 0$ which is occupied by material points P whose position is described by $\boldsymbol{X}$. In contrast, the current configuration Ω describes the current deformed position $\boldsymbol{x}$ at an arbitrary time t. The nonlinear map

$$\varphi : \begin{cases} \Omega_0 \mapsto \Omega \\ \boldsymbol{X} \mapsto \boldsymbol{x}(\boldsymbol{X}, t) \end{cases} \tag{2.1}$$

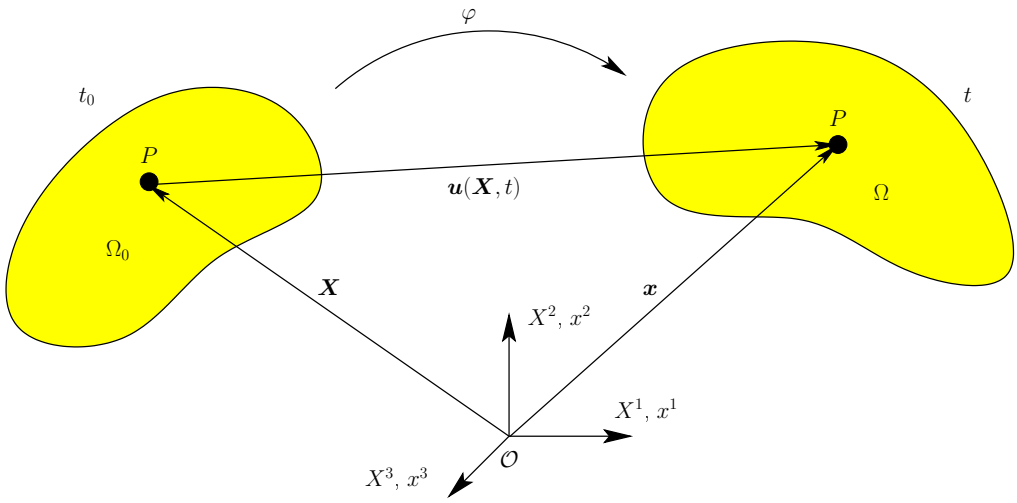

Figure 2.1: Motion of a continuum body in Lagrangian description.

describes the motion from the reference to the current configuration, which also allows to write the unique motions as $\boldsymbol{x} = \varphi(\boldsymbol{X},t)$ and $\boldsymbol{X} = \varphi^{-1}(\boldsymbol{x},t)$, respectively. The absolute displacement (as depicted in Figure 2.1) of a material point reads

$$\boldsymbol{u}(\boldsymbol{X},t) = \boldsymbol{x}(\boldsymbol{X},t) - \boldsymbol{X}\,. \tag{2.2}$$

As mentioned previously, the total Lagrangian description is employed in this work. Consequently, all kinematic quantities are expressed with respect to material points in the reference configuration, i.e. the initial position $\boldsymbol{X}$ represents an independent variable, whereas the deformation $\varphi(\boldsymbol{X},t)$ or $\boldsymbol{u}(\boldsymbol{X},t)$ describes the unknown field which needs to be solved. However, to describe the volume or shape changes of the body, the deformation $\varphi(\boldsymbol{X},t)$ or $\boldsymbol{u}(\boldsymbol{X},t)$ are not appropriate. For this reason, the deformation gradient $\boldsymbol{F}$ is introduced. The deformation gradient $\boldsymbol{F}$ is defined as

$$\boldsymbol{F} = \frac{\partial \boldsymbol{x}(\boldsymbol{X},t)}{\partial \boldsymbol{X}} = \frac{\partial \boldsymbol{u}(\boldsymbol{X},t)}{\partial \boldsymbol{X}} + \boldsymbol{I}\,, \tag{2.3}$$

with the second-order identity tensor $\boldsymbol{I}$. Note that $\boldsymbol{F}$ represents a so-called two-point tensor, i.e. one basis lies in the reference and one in the current configuration, which can be emphasized using the index notation of $\boldsymbol{F}$, so that

$$F_{iI} = \frac{\partial x_i}{\partial X_I} = \frac{\partial u_i}{\partial X_I} + I_{iI}\,, \tag{2.4}$$

where I and i correspond to the reference and the current configuration, respectively. Furthermore, $\boldsymbol{F}$ can be interpreted as the mapping of a material line element $\mathrm{d}\boldsymbol{X}$ in the undeformed reference domain Ω_0 to its current position $\mathrm{d}\boldsymbol{x}$ in the current domain Ω, i.e.

$$\mathrm{d}\boldsymbol{x} = \boldsymbol{F}\cdot\mathrm{d}\boldsymbol{X}\,, \tag{2.5}$$

often denoted as push-forward operation. Assuming unique motions φ and φ^{-1}, the inverse mapping or pull-back operation

$$\boldsymbol{F}^{-1} = \frac{\partial \boldsymbol{X}}{\partial \boldsymbol{x}} \tag{2.6}$$

only exists if the determinant of $\boldsymbol{F}$ (or Jacobi-determinant of the deformation) is non-singular and positive, i.e.

$$J := \det \boldsymbol{F} > 0\,. \tag{2.7}$$

Furthermore, the Jacobi-determinant links infinitesimal volume elements of both configurations:

$$\mathrm{d}V = J\,\mathrm{d}V_0 \tag{2.8}$$

with the reference and the current volume element, $\mathrm{d}V_0$ and $\mathrm{d}V$, respectively. In contrast, an oriented material surface element $\mathrm{d}\boldsymbol{A}_0$ can be mapped to the current configuration, yielding

$$\mathrm{d}\boldsymbol{A} = \mathrm{d}\boldsymbol{x}_1 \times \mathrm{d}\boldsymbol{x}_2 = J\,\boldsymbol{F}^{-\mathsf{T}}\,\mathrm{d}\boldsymbol{A}_0\,, \tag{2.9}$$

which is known as Nanson's formula and alternatively can be expressed as

$$\boldsymbol{n}\,\mathrm{d}A = J\,\boldsymbol{F}^{-\mathsf{T}}\,\boldsymbol{n}_0\,\mathrm{d}A_0\,, \tag{2.10}$$

where $\boldsymbol{n}_0$ and $\boldsymbol{n}$ denote the outward unit normal vectors in the reference and the current configuration, and $\mathrm{d}A_0$ and $\mathrm{d}A$ are the scalar physical area of the infinitesimal area element in the reference and the current configuration, respectively. Mapping the square of material line elements $\mathrm{d}\boldsymbol{X}$ to the current configuration including (2.5) yields

$$\mathrm{d}\boldsymbol{x}\cdot\mathrm{d}\boldsymbol{x} = (\boldsymbol{F}\,\mathrm{d}\boldsymbol{X})\cdot(\boldsymbol{F}\,\mathrm{d}\boldsymbol{X}) = \mathrm{d}\boldsymbol{X}\cdot(\boldsymbol{F}^{\mathsf{T}}\cdot\boldsymbol{F})\,\mathrm{d}\boldsymbol{X} =: \mathrm{d}\boldsymbol{X}\cdot\boldsymbol{C}\,\mathrm{d}\boldsymbol{X} \tag{2.11}$$

with the right Cauchy-Green deformation tensor

$$\boldsymbol{C} = \boldsymbol{F}^{\mathsf{T}}\cdot\boldsymbol{F}\,, \tag{2.12}$$

describing a material single field tensor. In addition, via pull-back of the square of current line elements $\mathrm{d}\boldsymbol{x}$, it follows

$$\mathrm{d}\boldsymbol{X}\cdot\mathrm{d}\boldsymbol{X} = (\boldsymbol{F}^{-1}\,\mathrm{d}\boldsymbol{x})\cdot(\boldsymbol{F}^{-1}\,\mathrm{d}\boldsymbol{x}) = \mathrm{d}\boldsymbol{x}\cdot(\boldsymbol{F}^{-\mathsf{T}}\cdot\boldsymbol{F}^{-1})\,\mathrm{d}\boldsymbol{x} =: \mathrm{d}\boldsymbol{x}\cdot\boldsymbol{B}^{-1}\,\mathrm{d}\boldsymbol{x}\,, \tag{2.13}$$

where the left Cauchy-Green deformation tensor $\boldsymbol{B}$ can be defined as

$$\boldsymbol{B} = \boldsymbol{F}\cdot\boldsymbol{F}^{\mathsf{T}}\,, \tag{2.14}$$

describing a spatial single field tensor. The deformation gradient $\boldsymbol{F}$ can be split into a rotational part $\boldsymbol{R}$ and a material or spatial stretch tensor, $\boldsymbol{U}$ or $\boldsymbol{V}$, as

$$\boldsymbol{F} = \boldsymbol{R}\cdot\boldsymbol{U} = \boldsymbol{V}\cdot\boldsymbol{R}\,. \tag{2.15}$$

Herein, $\boldsymbol{R}$ represents an (proper) orthogonal tensor obeying the following relations $\boldsymbol{R}^{-1} = \boldsymbol{R}^{\mathsf{T}}$ and $\det\boldsymbol{R} = 1$, whereas $\boldsymbol{U}$ and $\boldsymbol{V}$ are symmetric tensors (i.e. $\boldsymbol{U} = \boldsymbol{U}^{\mathsf{T}}$ and $\boldsymbol{V} = \boldsymbol{V}^{\mathsf{T}}$). Consequently, the deformation gradient $\boldsymbol{F}$ is not invariant with respect to rigid body rotations. However, equations (2.12) and (2.14) can be reformulated, yielding

$$\boldsymbol{C} = \boldsymbol{U}\cdot\boldsymbol{U}\,, \quad \boldsymbol{B} = \boldsymbol{V}\cdot\boldsymbol{V}\,, \tag{2.16}$$

i.e. $\boldsymbol{C}$ and $\boldsymbol{B}$ are invariant with respect to rigid body rotations and motions, so that they can be called objective deformation measures: at any rigid body motion the current deformation state remains constant.

In contrast to the deformation tensors, a strain measure describes the relative change of the deformation with respect to a chosen initial state. Consequently, different strain measures exist. For instance, computing the difference of the squared length of line elements (2.11) and expressing them with respect to the reference configuration, the well-known Green-Lagrange strain tensor $\boldsymbol{E}_{\mathsf{GL}}$, defined as

$$\boldsymbol{E}_{\mathsf{GL}} = \frac{1}{2}\left(\boldsymbol{C} - \boldsymbol{I}\right), \tag{2.17}$$

is introduced. The Green-Lagrange strain tensor is invariant with respect to rigid body motions and vanishes for undeformed bodies ($\boldsymbol{F} \equiv \boldsymbol{I}$). Using (2.13), a strain measure with respect to the current configuration can be introduced, denoting the Euler-Almansi strain tensor

$$\boldsymbol{E}_{\mathsf{EA}} = \frac{1}{2}\left(\boldsymbol{I} - \boldsymbol{B}^{-1}\right). \tag{2.18}$$

Via push-forward and pull-back operation these two measures correlate:

$$\mathrm{d}\boldsymbol{X}\cdot\boldsymbol{C}\,\mathrm{d}\boldsymbol{X} - \mathrm{d}\boldsymbol{X}\cdot\mathrm{d}\boldsymbol{X} =: \mathrm{d}\boldsymbol{X}\cdot 2\,\boldsymbol{E}_{\mathsf{GL}}\,\mathrm{d}\boldsymbol{X} = \mathrm{d}\boldsymbol{x}\cdot\mathrm{d}\boldsymbol{x} - \mathrm{d}\boldsymbol{x}\cdot\boldsymbol{B}^{-1}\,\mathrm{d}\boldsymbol{x} =: \mathrm{d}\boldsymbol{x}\cdot 2\,\boldsymbol{E}_{\mathsf{EA}}\,\mathrm{d}\boldsymbol{x}\,. \tag{2.19}$$

The Green-Lagrange and the Euler-Almansi strain tensors, $\boldsymbol{E}_{\mathsf{GL}}$ and $\boldsymbol{E}_{\mathsf{EA}}$, respectively, are suitable for large deformations but only for moderate strains during compression or extensions. In case of finite strain application, as e.g. finite strain plasticity, the logarithmic strain tensor is a further suitable measure.

For solid dynamical problems, material time differentiation of the deformation and the strain measures need to be introduced. The first and second derivative of the displacement field $\boldsymbol{u}(\boldsymbol{X},t)$, i.e. the material velocity and acceleration, $\dot{\boldsymbol{u}}$ and $\ddot{\boldsymbol{u}}$, respectively, result in

$$\dot{\boldsymbol{u}}(\boldsymbol{X},t) = \frac{\mathrm{d}\boldsymbol{u}(\boldsymbol{X},t)}{\mathrm{d}t} = \left.\frac{\partial\boldsymbol{u}(\boldsymbol{X},t)}{\partial t}\right|_{\boldsymbol{X}}, \tag{2.20}$$

$$\ddot{\boldsymbol{u}}(\boldsymbol{X},t) = \frac{\mathrm{d}\dot{\boldsymbol{u}}(\boldsymbol{X},t)}{\mathrm{d}t} = \frac{\mathrm{d}^2\boldsymbol{u}(\boldsymbol{X},t)}{\mathrm{d}t^2} = \left.\frac{\partial^2\boldsymbol{u}(\boldsymbol{X},t)}{\partial t^2}\right|_{\boldsymbol{X}}, \tag{2.21}$$

where (2.2) can be used to show that due to the constant initial position $\boldsymbol{X}$

$$\dot{\boldsymbol{x}}(\boldsymbol{X},t) \equiv \dot{\boldsymbol{u}}(\boldsymbol{X},t)\,. \tag{2.22}$$

According to (2.3), the material velocity gradient results in

$$\dot{\boldsymbol{F}} = \frac{\mathrm{d}\dot{\boldsymbol{F}}}{\mathrm{d}t} = \frac{\partial\dot{\boldsymbol{x}}}{\partial t} = \frac{\partial\dot{\boldsymbol{u}}}{\partial t} =: \mathrm{Grad}\,\dot{\boldsymbol{x}} = \mathrm{Grad}\,\dot{\boldsymbol{u}}\,, \tag{2.23}$$

with the material gradient operator $\mathrm{Grad}\,(\cdot)$. Equation (2.23) can be reformulated, yielding the spatial velocity gradient

$$\boldsymbol{L} = \dot{\boldsymbol{F}}\cdot\boldsymbol{F}^{-1}\,, \tag{2.24}$$

and its symmetric part

$$\boldsymbol{D} = \frac{1}{2}\left(\boldsymbol{L} + \boldsymbol{L}^{\mathsf{T}}\right). \tag{2.25}$$

The rate of the Green-Lagrange strain tensor results in the material strain rate tensor

$$\dot{\boldsymbol{E}}_{\mathsf{GL}} \;=\; \frac{1}{2}\,\dot{\boldsymbol{C}} \;=\; \boldsymbol{F}^{\mathsf{T}} \cdot \boldsymbol{D} \cdot \boldsymbol{F}\,, \tag{2.26}$$

which can be expressed as pull-back of the symmetric spatial strain rate tensor $\boldsymbol{D}$. Via the Lie-derivative or Oldroyd-Lie derivative of the Euler-Almansi strain tensor $\mathcal{L}_t[\boldsymbol{E}_{\mathsf{EA}}]$, which represents an objective material time derivative, a relation to the rate of the Euler-Almansi strain tensor is achieved as

$$\mathcal{L}_t[\boldsymbol{E}_{\mathsf{EA}}] \;=\; \varphi\left[\frac{\mathrm{d}}{\mathrm{d}t}\Big(\varphi^{-1}[\boldsymbol{E}_{\mathsf{EA}}]\Big)\right] \;=\; \boldsymbol{D} \;=\; \boldsymbol{F}^{-\mathsf{T}} \cdot \dot{\boldsymbol{E}}_{\mathsf{GL}} \cdot \boldsymbol{F}^{-1}\,. \tag{2.27}$$

Moreover, the rate of volume changes is described by $\dot{J}$ and can be expressed through

$$\dot{J} \;=\; J\,\mathrm{tr}\,\boldsymbol{D}\,. \tag{2.28}$$

2.1.2 Kinematics of curved surfaces

For the computation of convective thermal heat boundary conditions in large deformation TSI problems (see chapter 5), the characterization of the surface will be essential. The derivations are based on Wiechert [143]. In the following, surface areas, their corresponding normal vectors, and the corresponding mapping will be derived.

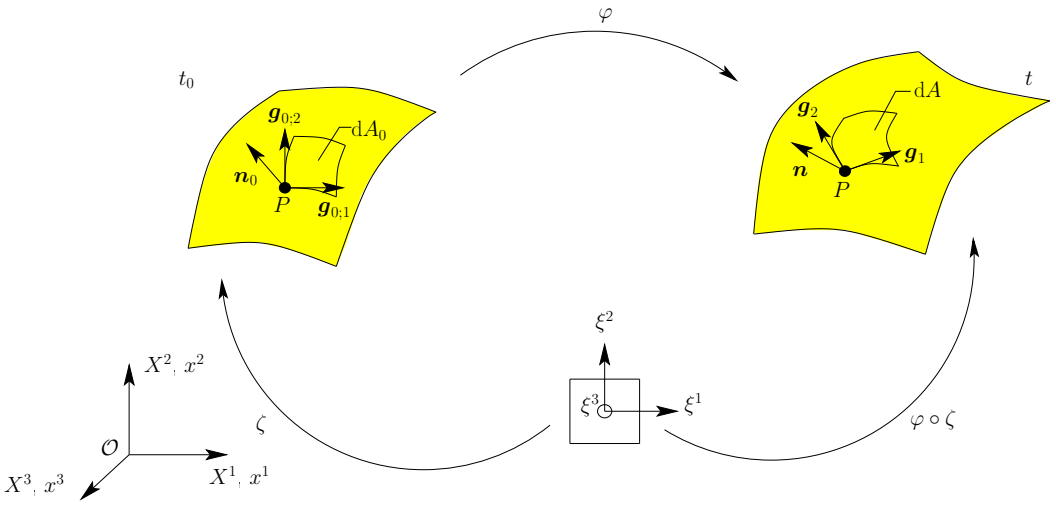

Figure 2.2: Mapping of a curvilinear surface.

As depicted in Figure 2.2, a material point P on a surface can be expressed by the tangent space with its covariant basis vectors

$$\boldsymbol{g}_{0;a} \;=\; \frac{\partial \boldsymbol{X}}{\partial \xi^a}\,, \tag{2.29}$$

$$\boldsymbol{g}_{a} \;=\; \frac{\partial \boldsymbol{x}}{\partial \xi^a} \tag{2.30}$$

in the reference and the current configuration, respectively. Here, ξ^a represents the curvilinear coordinates with $a \in 1,2,3$ for a general three-dimensional problem. The infinitesimal oriented surface area in the current configuration $\mathrm{d}\boldsymbol{A}$ is spanned by two in-plane basis vector $\boldsymbol{g}_1$ and $\boldsymbol{g}_2$. It follows

$$\mathrm{d}\boldsymbol{A} \;=\; \boldsymbol{g}_1\,\mathrm{d}\xi^1 \times \boldsymbol{g}_2\,\mathrm{d}\xi^2 \;=\; \check{\boldsymbol{n}}\,\mathrm{d}\xi^1\,\mathrm{d}\xi^2 \tag{2.31}$$

with the surface normal $\check{\boldsymbol{n}}$ defined as

$$\check{\boldsymbol{n}} \;=\; \begin{bmatrix} \dfrac{\partial x^2}{\partial \xi^1}\dfrac{\partial x^3}{\partial \xi^2} - \dfrac{\partial x^2}{\partial \xi^2}\dfrac{\partial x^3}{\partial \xi^1} \\ \dfrac{\partial x^3}{\partial \xi^1}\dfrac{\partial x^1}{\partial \xi^2} - \dfrac{\partial x^3}{\partial \xi^2}\dfrac{\partial x^1}{\partial \xi^1} \\ \dfrac{\partial x^1}{\partial \xi^1}\dfrac{\partial x^2}{\partial \xi^2} - \dfrac{\partial x^1}{\partial \xi^2}\dfrac{\partial x^2}{\partial \xi^1} \end{bmatrix} \;=\; \frac{1}{\det \tilde{\boldsymbol{J}}}\,\boldsymbol{g}^3\,, \tag{2.32}$$

including the contravariant basis vector $\boldsymbol{g}^3$ pointing in the direction of the surface normal $\check{\boldsymbol{n}}$. Furthermore, as shown in Figure 2.2, the Jacobian of the mapping $\varphi \circ \zeta$ is defined as

$$\check{\boldsymbol{J}} \;=\; \begin{pmatrix} \dfrac{\partial x^1}{\partial \xi^1} & \dfrac{\partial x^2}{\partial \xi^1} & \dfrac{\partial x^3}{\partial \xi^1} \\ \dfrac{\partial x^1}{\partial \xi^2} & \dfrac{\partial x^2}{\partial \xi^2} & \dfrac{\partial x^3}{\partial \xi^2} \\ \dfrac{\partial x^1}{\partial \xi^3} & \dfrac{\partial x^2}{\partial \xi^3} & \dfrac{\partial x^3}{\partial \xi^3} \end{pmatrix} \;=\; \begin{pmatrix} \boldsymbol{g}_1 \\ \boldsymbol{g}_2 \\ \boldsymbol{g}_3 \end{pmatrix}\,, \tag{2.33}$$

with the tangential (covariant) basis vector $\boldsymbol{g}_a$. Subsequently, the scalar-valued physical area of the infinitesimal surface is obtained as absolute value of (2.31), yielding

$$\mathrm{d}A \;=\; |\check{\boldsymbol{n}}|\,\mathrm{d}\xi^1\,\mathrm{d}\xi^2\,. \tag{2.34}$$

The present concept of curvilinear coordinates is generally valid. For instance, by interpreting the curvilinear coordinates as a parameter space with linear coordinates, the present concept can be applied in the context of spatial discretisation within the finite element method (FEM).

2.1.3 Split of the deformation

Since various materials behave differently in bulk and shear, it is common in material modelling to split the deformation into a volumetric (volume-changing) and an isochoric (volume-preserving) contribution, see e.g. Holzapfel [58] and Ogden [100] for finite strain elasticity and, e.g. Simo et al. [124] and Stainier and Ortiz [128] for finite strain (visco-)elastoplasticity which is based on the work of Lee [73]. Consequently, in the finite strain regime the deformation gradient is multiplicatively split into

$$\boldsymbol{F} \;=\; \boldsymbol{F}_v \cdot \tilde{\boldsymbol{F}} \;=\; \tilde{\boldsymbol{F}} \cdot \boldsymbol{F}_v\,, \tag{2.35}$$

where $\tilde{\boldsymbol{F}}$ and $\boldsymbol{F}_v$ denote the isochoric and the volumetric part of $\boldsymbol{F}$ defined as

$$\tilde{\boldsymbol{F}} \;=\; J^{-\frac{1}{3}} \cdot \boldsymbol{F}\,, \quad \boldsymbol{F}_v \;=\; J^{\frac{1}{3}}\,\boldsymbol{I}\,, \tag{2.36}$$

respectively. Furthermore, for the isochoric contribution

$$\tilde{J} \;=\; \det(\tilde{\boldsymbol{F}}) \;=\; 1\,. \tag{2.37}$$

Correspondingly, for the right Cauchy-Green deformation tensor follows

$$\boldsymbol{C} = \boldsymbol{C}_v \cdot \tilde{\boldsymbol{C}} \tag{2.38}$$

with the isochoric and the volumetric counterparts defined as

$$\tilde{\boldsymbol{C}} = J^{-\frac{2}{3}} \cdot \boldsymbol{C}\,, \quad \boldsymbol{C}_v \;=\; J^{\frac{2}{3}}\,\boldsymbol{I}\,, \tag{2.39}$$

respectively. Accordingly, $\tilde{J} \;=\; (\det \tilde{\boldsymbol{C}})^{\frac{1}{2}} \;=\; 1$.

2.2 Stress measures

The deformation of a body is always linked with a resistance. A possibility to measure this resistance is by introducing the stress, which is defined as force per unit area. Hence, different stress measures can be introduced according to the configuration in which force and area are defined. For instance, the traction vector $\boldsymbol{t}$ in the current configuration is introduced as

$$\boldsymbol{t}(\boldsymbol{x}, \boldsymbol{n}, t) \;=\; \lim_{\Delta A \to 0} \frac{\Delta \boldsymbol{f}}{\Delta A}\,, \tag{2.40}$$

which describes the limit value of a force $\boldsymbol{f}$ at a material point P on an element surface ΔA, where the latter is characterized by the spatial unit normal vector $\boldsymbol{n}$. Via Cauchy's theorem a relation between the stresses and the traction vector $\boldsymbol{t}$ in the current configuration can be stated as

$$\boldsymbol{\sigma}(\boldsymbol{x}, t) \cdot \boldsymbol{n} \;=\; \boldsymbol{t}(\boldsymbol{x}, \boldsymbol{n}, t)\,. \tag{2.41}$$

Herein, the symmetric Cauchy stress tensor $\boldsymbol{\sigma}$ describes the true stress state of a body with respect to an a priori unknown configuration. Instead of relating the current force $\boldsymbol{f}$ to the current surface A, $\boldsymbol{f}$ can be expressed with respect to the undeformed material area A_0, i.e.

$$\boldsymbol{t}_0 \;=\; \frac{\mathrm{d}A}{\mathrm{d}A_0}\,\boldsymbol{t}\,, \tag{2.42}$$

including $\mathrm{d}\boldsymbol{A}_0 \;=\; \mathrm{d}A_0\,\boldsymbol{n}_0$. This defines the so-called pseudo traction vector $\boldsymbol{t}_0$ which can be described as

$$\boldsymbol{t}_0 \;=\; \boldsymbol{P} \cdot \boldsymbol{n}_0\,, \tag{2.43}$$

where $\boldsymbol{n}_0$ and $\boldsymbol{P}$ denote the material unit normal vector and the first Piola-Kirchhoff stress tensor, respectively. Furthermore, $\boldsymbol{P}$ can be stated as

$$\boldsymbol{P} \;=\; J\,\boldsymbol{\sigma} \cdot \boldsymbol{F}^{-\mathsf{T}}\,, \tag{2.44}$$

using Cauchy stresses (2.41) and Nanson's formula (2.10). As $\boldsymbol{P}$ has been introduced as the map of the current traction with respect to the material area, the first Piola-Kirchhoff stress tensor

represents a two-point tensor. Moreover, the Kirchhoff stress and the second Piola-Kirchhoff stress tensor, $\boldsymbol{\tau}$ and $\boldsymbol{S}$, respectively, are introduced as

$$\boldsymbol{\tau} \;=\; J\,\boldsymbol{\sigma}\,, \tag{2.45}$$

$$\boldsymbol{S} \;=\; \boldsymbol{F}^{-1}\cdot\boldsymbol{P} \;=\; J\,\boldsymbol{F}^{-1}\cdot\boldsymbol{\sigma}\cdot\boldsymbol{F}^{-\mathsf{T}}\,, \tag{2.46}$$

where $\boldsymbol{\tau}$ is a symmetric two-point tensor also known as weighted Cauchy stresses, and $\boldsymbol{S}$ is a symmetric, purely material, one-field tensor obtained from $\boldsymbol{P}$ by transforming also the resultant force to the material configuration.

Finally, it can be concluded that any of the mentioned stress and strain measures can be used. However, if a certain stress measure is chosen, the corresponding strain measure cannot be selected arbitrarily. The scalar-valued internal stress power $\mathcal{P}_{\mathsf{int}}$ is frame-invariant, i.e. objective. Hence, $\mathcal{P}_{\mathsf{int}}$ can be used to correlate certain stress-strain pairs in an objective manner, viz.

$$\mathcal{P}_{\mathsf{int}} \;=\; \int_{\Omega_0} \boldsymbol{S} : \dot{\boldsymbol{E}}_{\mathsf{GL}}\,\mathrm{d}A_0 \;=\; \int_{\Omega_0} \boldsymbol{P} : \dot{\boldsymbol{F}}\,\mathrm{d}A_0 \;=\; \int_{\Omega} \boldsymbol{\sigma} : \boldsymbol{D}\,\mathrm{d}A\,, \tag{2.47}$$

defining so-called energy-conjugated pairs $\{\boldsymbol{S}, \boldsymbol{E}_{\mathsf{GL}}\}$, $\{\boldsymbol{P}, \boldsymbol{F}\}$, and $\{\boldsymbol{\sigma}, \boldsymbol{E}_{\mathsf{EA}}\}$, where (2.27) has been used for the latter pair.

In the purpose of constitutive modelling, it is common to split the stress tensor, e.g. the Cauchy stress tensor, into a deviatoric and a volumetric part (see Appendix B.3)

$$\boldsymbol{\sigma} \;=\; \boldsymbol{s} \;+\; p\,\boldsymbol{I}\,, \tag{2.48}$$

where the stress deviator and the scalar-valued hydrostatic pressure are introduced as

$$\boldsymbol{s} := \operatorname{dev}\boldsymbol{\sigma} \;=\; \boldsymbol{\sigma} \;-\; \frac{1}{3}\operatorname{tr}\boldsymbol{\sigma}\,\boldsymbol{I}\,, \tag{2.49}$$

$$p := \frac{1}{3}\operatorname{tr}\boldsymbol{\sigma}\,, \tag{2.50}$$

respectively. This split will be used for constitutive modelling of solid materials, e.g. in section 3.4.

2.3 Balance relations

In this section the fundamental laws of thermodynamics are summarized via stating the balance relations which are valid for any continuum body regardless of its material. Apart from kinematics and stresses, mechanical systems are characterized by balance relations or balance equations for mass, linear and angular momentum, respectively, energy, and entropy.

2.3.1 Master balance relations

As a basis of the balance relations, the so-called master balance relations can be stated for arbitrary volume-specific physical quantities. Hereby, scalar-valued and vector-valued (volumetric)

mechanical quantities, χ and $\boldsymbol{\chi}$, respectively, are differentiated which are balanced over the current volume V and time t. As examples for a scalar-valued quantity of a volume element $\mathrm{d}V$, the density ρ, the internal energy $\rho\, e$, and the entropy $\rho\, \eta$ can be stated. As vector-valued quantities the momentum or the moment of momentum, $\rho\, \dot{\boldsymbol{x}}$ or $\boldsymbol{x} \times (\rho\, \dot{\boldsymbol{x}})$ can be mentioned, where $\times$ describes the cross product between two vectors. The master balance can be written for both χ and $\boldsymbol{\chi}$ as

$$\begin{aligned} \frac{\mathrm{d}}{\mathrm{d}t} \int\limits_{\Omega} \chi \, \mathrm{d}V &= \int\limits_{\partial\Omega} \boldsymbol{\Phi} \cdot \boldsymbol{n} \, \mathrm{d}A + \int\limits_{\Omega} \sigma \, \mathrm{d}V + \int\limits_{\Omega} \hat{\chi} \, \mathrm{d}V \,, \\ \frac{\mathrm{d}}{\mathrm{d}t} \int\limits_{\Omega} \boldsymbol{\chi} \, \mathrm{d}V &= \int\limits_{\partial\Omega} \boldsymbol{\Phi} \cdot \boldsymbol{n} \, \mathrm{d}A + \int\limits_{\Omega} \boldsymbol{\sigma} \, \mathrm{d}V + \int\limits_{\Omega} \hat{\boldsymbol{\chi}} \, \mathrm{d}V \,. \end{aligned} \tag{2.51}$$

The first term on the right hand side, i.e. $\boldsymbol{\Phi} : \boldsymbol{n}$ or $\boldsymbol{\Phi} \cdot \boldsymbol{n}$ using the outward pointing unit surface normal vector $\boldsymbol{n}$, is identified as the outflow over the surface $\partial\Omega$ or the so-called close-up effect. The second term σ or $\boldsymbol{\sigma}$ describes the supply or the long-distance effect, and the third term a possible production of the chosen mechanical quantity. In case of open or multiphase systems, the production term, $\hat{\chi}$ or $\hat{\boldsymbol{\chi}}$, is unequal to zero due to loss or source in open systems or phase changes in multiphase systems. In contrast, for closed systems and especially for single-phase quantities such as considered in the present work, the production term is equal to zero, i.e. $\hat{\chi} \equiv 0$ and $\hat{\boldsymbol{\chi}} \equiv \boldsymbol{0}$, respectively. To balance a chosen quantity, each term of the master balance has to be specified according to classical continuum mechanics. Equation (2.51) balances the mechanical quantity for the whole body. In contrast, the integral form can be transformed into a local form which balances the quantity locally, i.e. at a specific material point P. The local form is achieved by assuming steady and steady differentiable integrands, by applying a material time derivative to the left hand side, and by rewriting the surface integrals of the right-hand side using Gauss divergence theorem. The corresponding local form of the master balance equations (2.51) then results in:

$$\begin{aligned} \dot{\chi} + \chi \, \mathrm{div}\, \dot{\boldsymbol{x}} &= \mathrm{div}\, \boldsymbol{\Phi} + \sigma + \hat{\chi} \,, \\ \dot{\boldsymbol{\chi}} + \boldsymbol{\chi} \, \mathrm{div}\, \dot{\boldsymbol{x}} &= \mathrm{div}\, \boldsymbol{\Phi} + \boldsymbol{\sigma} + \hat{\boldsymbol{\chi}} \,. \end{aligned} \tag{2.52}$$

Herein, the spatial divergence operator $\mathrm{div}\,(\cdot)$ is used. In the following sections, the master balance relations (2.51) and (2.52) are specified for different mechanical quantities.

2.3.2 Conservation laws

The master balance equations (2.51) and (2.52) are defined in the current configuration. In addition, material versions are obtained by transformation and mapping of the integrals from current to reference configuration and by introduction of material quantities. For the application to structural dynamics, the material version is the common way so that this approach is adopted here exclusively. It is worth noting, that the material versions still describe equilibrium in the deformed configuration. However, for the sake of a complete overview, the balance equations are expressed in both, material and spatial description.

Conservation of mass

The conservation of mass states, that in a closed system the mass m of a body is constant, i.e.

$$\dot{m} \;=\; \frac{\mathrm{d}}{\mathrm{d}t}\int\limits_{\Omega} \rho \,\mathrm{d}V \;=\; \int\limits_{\Omega} (\dot{\rho} \;+\; \rho \,\mathrm{div}\, \dot{\boldsymbol{u}})\,\mathrm{d}V \;=\; 0\,. \tag{2.53}$$

Herein, Reynold's transport theorem (see e.g. Belytschko et al. [16]) and the velocity $\dot{\boldsymbol{u}}$ (2.22) are used. Introducing the reference mass density

$$\rho_0 \;=\; J\,\rho \tag{2.54}$$

and the reference domain Ω_0, the balance equation in material description reads

$$\frac{\mathrm{d}}{\mathrm{d}t}\int\limits_{\Omega_0} \rho_0 \,\mathrm{d}V_0 \;=\; 0\,. \tag{2.55}$$

Since the reference domain Ω_0 is independent of time, the global form of the conservation of mass in material description simplifies to

$$\int\limits_{\Omega_0} \frac{\mathrm{d}\rho_0}{\mathrm{d}t}\,\mathrm{d}V_0 \;=\; \int\limits_{\Omega_0} \dot{\rho}_0 \,\mathrm{d}V_0 \;=\; 0\,. \tag{2.56}$$

According to section 2.3.1, the local form, which has to be fulfilled at any material point P, can be established for spatial and material description as

$$\dot{\rho} \;+\; \rho \,\mathrm{div}\, \dot{\boldsymbol{u}} \;=\; 0\,, \tag{2.57}$$

$$\dot{\rho}_0 \;=\; 0\,. \tag{2.58}$$

Conservation of linear momentum

The conservation of linear momentum states, that the temporal change of the body momentum equals the sum of forces acting on the body at the vicinity and from a distance, i.e.

$$\frac{\mathrm{d}}{\mathrm{d}t}\int\limits_{\Omega} \rho\, \dot{\boldsymbol{u}}\,\mathrm{d}V \;=\; \int\limits_{\partial\Omega} \boldsymbol{\sigma}\cdot\boldsymbol{n}\,\mathrm{d}A \;+\; \int\limits_{\Omega} \hat{\boldsymbol{b}}\,\mathrm{d}V\,. \tag{2.59}$$

The outflow over the surface described by $\boldsymbol{\sigma}\cdot\boldsymbol{n}$ can be summarized to the external traction vector $\boldsymbol{t}$, see (2.40). The vector field $\hat{\boldsymbol{b}}$ is introduced as the spatial body force where the superimposed hat identifies a prescribed quantity. After application of Reynold's theorem and integrating the conservation of mass (2.53) to the left-hand side, and using (2.41), an alternative version of the balance of linear momentum in spatial description can be achieved as

$$\int\limits_{\Omega} \rho\, \ddot{\boldsymbol{u}}\,\mathrm{d}V \;=\; \int\limits_{\partial\Omega} \boldsymbol{t}\,\mathrm{d}A \;+\; \int\limits_{\Omega} \hat{\boldsymbol{b}}\,\mathrm{d}V\,. \tag{2.60}$$

Similarly, the material version of (2.60) is determined by

$$\int_{\Omega_0} \rho_0 \, \ddot{\boldsymbol{u}} \, \mathrm{d}V_0 \;=\; \int_{\partial\Omega_0} \boldsymbol{t}_0 \, \mathrm{d}A_0 \;+\; \int_{\Omega_0} \hat{\boldsymbol{b}}_0 \, \mathrm{d}V_0 \,, \tag{2.61}$$

where the pseudo traction vector $\boldsymbol{t}_0$ (2.43) and the external body force vector on the reference domain $\hat{\boldsymbol{b}}_0 \;=\; J \, \hat{\boldsymbol{b}}$ are used. Furthermore, (2.61) can be reformulated by applying Gauss divergence theorem (see e.g. Holzapfel [58]) and inserting the first Piola-Kirchhoff stress tensor according to (2.43), yielding

$$\int_{\Omega_0} \rho_0 \, \ddot{\boldsymbol{u}} \, \mathrm{d}V_0 \;=\; \int_{\Omega_0} \mathrm{Div}\, \boldsymbol{P} \, \mathrm{d}V_0 \;+\; \int_{\Omega_0} \hat{\boldsymbol{b}}_0 \, \mathrm{d}V_0 \,, \tag{2.62}$$

where the material divergence operator $\mathrm{Div}\,(\cdot)$ is used. The corresponding local form of (2.62) and the corresponding spatial form are given by

$$\rho_0 \, \ddot{\boldsymbol{u}} = \; \mathrm{Div}\, \boldsymbol{P} \;+\; \hat{\boldsymbol{b}}_0 \,, \tag{2.63}$$

$$\rho \, \ddot{\boldsymbol{u}} = \; \mathrm{div}\, \boldsymbol{\sigma} \;+\; \hat{\boldsymbol{b}} \,. \tag{2.64}$$

Conservation of angular momentum

The conservation of angular momentum states, that the temporal change of an angular momentum with respect to an arbitrary fixed point equals the sum of all external moments acting on the body. It reads

$$\frac{\mathrm{d}}{\mathrm{d}t} \int_{\Omega} (\boldsymbol{x} \times \rho \, \dot{\boldsymbol{u}}) \, \mathrm{d}V \;=\; \int_{\partial\Omega} (\boldsymbol{x} \times \boldsymbol{t}) \, \mathrm{d}A \;+\; \int_{\Omega} (\boldsymbol{x} \times \hat{\boldsymbol{b}}) \, \mathrm{d}V \,. \tag{2.65}$$

Transforming (2.65) to the reference domain yields the material version of the balance of angular momentum

$$\frac{\mathrm{d}}{\mathrm{d}t} \int_{\Omega_0} (\boldsymbol{x} \times \rho_0 \, \dot{\boldsymbol{u}}) \, \mathrm{d}V_0 \;=\; \int_{\partial\Omega_0} (\boldsymbol{x} \times \boldsymbol{t}_0) \, \mathrm{d}A_0 \;+\; \int_{\Omega_0} (\boldsymbol{x} \times \hat{\boldsymbol{b}}_0) \, \mathrm{d}V_0 \,. \tag{2.66}$$

According to the previous balance equations, the balance of angular momentum can also be reformulated by applying Gauss divergence theorem to the boundary terms in (2.65) and (2.66), and by transforming the resulting equations to their local forms. In contrast to the previous balance equations, this balance equation does not enter the initial boundary value problem (IBVP) as independent equation, but reduces the number of unknowns by demanding a symmetric stress tensor in spatial and material description. The Cauchy and the second Piola-Kirchhoff stresses, respectively, are symmetric, i.e.

$$\boldsymbol{\sigma} \;=\; \boldsymbol{\sigma}^{\mathsf{T}} \,, \quad \boldsymbol{S} \;=\; \boldsymbol{S}^{\mathsf{T}} \,, \tag{2.67}$$

hence these two stress measures are applicable for the given IBVP.

Conservation of energy

The conservation of energy also known as balance of energy or the first law of thermodynamics states, that the sum of temporal changes of internal and kinetic energy of a body equals the sum of external mechanical and non-mechanical, thermal powers as

$$\frac{\mathrm{d}}{\mathrm{d}t}\int_{\Omega}(\rho\, e\,+\,\rho\,\dot{\boldsymbol{u}}\cdot\dot{\boldsymbol{u}})\,\mathrm{d}V\,=\int_{\partial\Omega}(\dot{\boldsymbol{u}}\cdot\boldsymbol{t}\,-\,\boldsymbol{q}\cdot\boldsymbol{n})\,\mathrm{d}A\,+\int_{\Omega}(\rho\,\dot{\boldsymbol{u}}\cdot\hat{\boldsymbol{b}}\,+\,\rho\, r)\,\mathrm{d}V \tag{2.68}$$

with the vector field $\boldsymbol{q}$ introduced as the spatial heat flux and the scalar field r introduced as the external heat source. Equation (2.68) can be reformulated, assuming mass conservation (2.57), equilibrium of forces and momentum, (2.65) and (2.66), respectively, introducing the symmetric rate of the deformation tensor $\boldsymbol{D}$ (2.25), and applying Gauss divergence theorem. Consequently, the local form is achieved as

$$\rho\,\dot{e}\,=\,\boldsymbol{\sigma}:\boldsymbol{D}\,-\,\operatorname{div}\boldsymbol{q}\,+\,\rho\, r\,. \tag{2.69}$$

The material version of (2.69) is achieved as

$$\rho_0\,\dot{e}\,=\,\boldsymbol{S}:\dot{\boldsymbol{E}}_{\mathsf{GL}}\,-\,\operatorname{Div}\boldsymbol{Q}\,+\,\rho_0\, r\,, \tag{2.70}$$

where the temporal rate of Green-Lagrange strain tensor $\dot{\boldsymbol{E}}_{\mathsf{GL}}$ defined in (2.26) and the material heat flux $\boldsymbol{Q}$ are used.

2.3.3 Second law of thermodynamics

The second law of thermodynamics also known as the balance of entropy states, that the temporal change of the entropy of a body equals the sum of external entropy changes at the vicinity and from a distance, and the internal entropy production. Thus, it follows

$$\dot{H}\,=\,\frac{\mathrm{d}}{\mathrm{d}t}\int_{\Omega}\rho\,\eta\,\mathrm{d}V\,=\int_{\partial\Omega}\frac{\boldsymbol{q}\cdot\boldsymbol{n}}{T}\,\mathrm{d}A\,+\int_{\Omega}\frac{\rho\, r}{T}\,\mathrm{d}V\,+\int_{\Omega}\hat{\eta}\,\mathrm{d}V \tag{2.71}$$

with the absolute temperature T, the specific entropy η of a mass element $\mathrm{d}m=\rho\,\mathrm{d}V$ resulting in the entropy H of the body, and the entropy production $\hat{\eta}$. In this respect, the entropy production is never negative. Furthermore, the balance of entropy states that heat always flows from the warmer to the colder region of a body.

In contrast to the balance equations in section 2.3.2, which represent conservation laws, the second law of thermodynamics does not describe a balance principle and the entropy is not conserved either (see e.g. Holzapfel [58]). The entropy is a not-measurable physical quantity and represents a measure of the disorder and the distribution of energy of a system. Hence, only changes of entropy can be captured. The entropy is used to describe heat transfer and irreversible processes. Besides the temperature, the entropy represents the most important measure of the theory of heat.

As for the balance relations, (2.71) can be reformulated using the balance principles of section 2.3.2, defining the local form of the entropy balance as

$$\rho\,\dot{\eta} \;=\; -\mathrm{div}\left(\frac{\boldsymbol{q}}{T}\right) \;+\; \left(\frac{\rho\,r}{T}\right) \;+\; \hat{\eta}\,. \tag{2.72}$$

Considering the axiom that for a physically admissible process the entropy production can never adopt a negative value, i.e.

$$\hat{\eta} \;\geq\; 0\,, \tag{2.73}$$

equations (2.72) and (2.73) are used to derive an inequality

$$\rho\,\dot{\eta} \;\geq\; -\mathrm{div}\left(\frac{\boldsymbol{q}}{T}\right) \;+\; \left(\frac{\rho\,r}{T}\right), \tag{2.74}$$

which always has to be satisfied for all possible processes. According to the previous subsections, a material version of the local form (2.74) can be achieved as

$$\rho_0\,\dot{\eta} \;\geq\; -\mathrm{Div}\left(\frac{\boldsymbol{Q}}{T}\right) \;+\; \left(\frac{\rho_0\,r}{T}\right). \tag{2.75}$$

In the following, only the spatial form of the entropy balance equation, e.g. (2.74), is used for further investigations. As a next step, the divergence term of the right-hand side can be reformulated, yielding

$$\mathrm{div}\left(\frac{\boldsymbol{q}}{T}\right) \;=\; \frac{1}{T}\,\mathrm{div}\,\boldsymbol{q} \;-\; \frac{1}{T^2}\,\boldsymbol{q}\cdot\mathrm{grad}\,T\,, \tag{2.76}$$

where the spatial gradient operator $\mathrm{grad}\,(\cdot)$ is used. Inserting (2.76) and (2.69) into (2.74) results in

$$\rho\,\dot{\eta} \;\geq\; -\frac{1}{T}\left(\boldsymbol{\sigma} : \boldsymbol{D} \;+\; \rho\,r \;-\; \rho\,\dot{e}\right) \;+\; \frac{1}{T^2}\,\boldsymbol{q}\cdot\mathrm{grad}\,T \;+\; \left(\frac{\rho\,r}{T}\right), \tag{2.77}$$

which can be summarized to

$$\rho\,(T\,\dot{\eta} \;-\; \dot{e}) \;\geq\; -\boldsymbol{\sigma} : \boldsymbol{D} \;+\; \frac{\boldsymbol{q}}{T}\cdot\mathrm{grad}\,T\,, \tag{2.78}$$

or expressed in the Helmholtz free energy ψ as

$$-\rho\,(\dot{\psi} \;+\; \dot{T}\,\eta) \;\geq\; -\boldsymbol{\sigma} : \boldsymbol{D} \;+\; \frac{\boldsymbol{q}}{T}\cdot\mathrm{grad}\,T\,, \tag{2.79}$$

which is known as the Clausius-Duhem dissipation inequality. In equation (2.79), the Helmholtz free energy and its time derivative, ψ and $\dot{\psi}$, respectively, are used. This energy ψ can be defined using the so-called Legendre transformation as

$$\psi \;:=\; e \;-\; T\,\eta \tag{2.80}$$

and its time derivative follows as

$$\dot{\psi} \;=\; \dot{e} \;-\; \dot{T}\,\eta \;-\; T\,\dot{\eta}\,. \tag{2.81}$$

The Clausius-Duhem inequality (2.79) is alternatively called reduced dissipation inequality, as e.g. in André [5], Glaser [50], Ibrahimbegovic and Chorfi [61], and Montáns and Bathe [95]. Furthermore, two special forms of the second law of thermodynamics are commonly differentiated in literature, namely the Clausius-Duhem and the Clausius-Planck inequality. In the following, these two forms are compared with each other.

Clausius-Duhem inequality vs. Clausius-Planck inequality

As a starting point, (2.79) can be reformulated and split into two terms yielding

$$\underbrace{\boldsymbol{\sigma} : \boldsymbol{D} - \rho\,(\dot{\psi} + \dot{T}\,\eta)}_{\mathcal{D}_{\mathsf{mech}}} \underbrace{- \frac{\boldsymbol{q}}{T} \cdot \operatorname{grad} T}_{\mathcal{D}_{\mathsf{cond}}} \geq 0 \tag{2.82}$$

with the mechanical internal dissipation $\mathcal{D}_{\mathsf{mech}}$ and the dissipation due to heat conduction $\mathcal{D}_{\mathsf{cond}}$. The so-called Clausius-Planck inequality is achieved by neglecting $\mathcal{D}_{\mathsf{cond}}$, leading to

$$\mathcal{D}_{\mathsf{mech}} = \boldsymbol{\sigma} : \boldsymbol{D} - \rho\,(\dot{\psi} + \dot{T}\,\eta) \geq 0\,. \tag{2.83}$$

For the isothermal, purely structural case, i.e. $T = const.$, the Clausius-Duhem and the Clausius-Planck inequality are identical and are described by

$$\mathcal{D}_{\mathsf{mech}} = \boldsymbol{\sigma} : \boldsymbol{D} - \rho\,\dot{\psi} \geq 0\,. \tag{2.84}$$

In case the entropy balance is equal to zero (i.e. $\mathcal{D}_{\mathsf{mech}} \equiv 0$), a perfect elastic material is described, where all processes are fully reversible. In case of irreversible processes, e.g. plasticity, the entropy balance is larger than zero (i.e. $\mathcal{D}_{\mathsf{mech}} > 0$). Consequently, within continuum mechanics, the second law of thermodynamics can be used to derive restrictions with respect to the constitutive relations and the dissipation behaviour, i.e. will be later used to specify the material behaviour.

2.4 Constitutive theory

For a complete physical description of a body, the kinematical relations and the balance relations, presented in section 2.1 and 2.3, respectively, do not provide sufficient information to fully describe the system. Consequently, to close the problem, additional constitutive equations are required.

Balance equations are generally valid, i.e. independent of the material behaviour. In contrast, constitutive equations are not unique, but can be chosen arbitrarily, while they must fulfil the second law of thermodynamics. Several choices of constitutive equations are conceivable, concerning the independent and dependent variables also known as state variables which can either be mechanical or non-mechanical quantities. Thus, constitutive equations introduce the material behaviour into the problem at hand.

A continuum mechanical theory is assumed, i.e. the complete movement is known. Hence, all unknown quantities adjust in the way that the balance equations together with the constitutive equations are fulfilled.

2.4.1 Thermodynamical principles

The basic physical principles of thermodynamics for constitutive modelling have to be considered, which were proposed by Coleman and Noll [26], Noll [98, 99], Truesdell [135], and Truesdell and Noll [136]. Thus, determinism, equipresence, local action, material frame indifference

or objectivity, material symmetry, and universal dissipation are specified. To achieve a thermodynamically consistent formulation, all these basic principles have to be fulfilled.

In the following, a short overview of the basic principles is given. For further details, the interested reader is referred to the literature mentioned above, or to de Souza Neto et al. [33] and Karajan [65]. The principle of determinism states that all constitutive quantities of a body at time t, summarized in a response functions $\mathcal{R}$, are uniquely determined by the history of the motion and the temperature state up to the current time t. For a thermodynamical system, $\mathcal{R}$ yields

$$\mathcal{R} = \{\psi, \boldsymbol{\sigma}, \eta, \boldsymbol{q}\}\,, \tag{2.85}$$

while assuming that $\hat{\boldsymbol{b}}$ and r are determined by the balance of linear momentum and the balance of energy, respectively. The principle of equipresence (see Truesdell [135]) implies, that in general each component of $\mathcal{R}$ may depend on each thermodynamic state variable. Subsequently, the principle of material frame indifference or material objectivity introduced by Noll [98] states, that a material response is independent of the observer, which can mathematically be expressed by a constitutive equation which is invariant to rigid body rotations of the current configuration. Based on rotated current line elements, a rotated current configuration is given by

$$\boldsymbol{x}^* \;=\; \boldsymbol{Q} \cdot \boldsymbol{x}\,, \tag{2.86}$$

where the $(\cdot)^*$ indicates rotated quantities and $\boldsymbol{Q}$ denotes a (proper) orthogonal rotation tensor. Thus, a rotated deformation gradient follows as

$$\boldsymbol{F}^* = \boldsymbol{Q} \cdot \boldsymbol{F}\,. \tag{2.87}$$

Since material quantities satisfy a priori the principle of frame indifference, the initial position $\boldsymbol{X}$ and the Green-Lagrange strain tensor $\boldsymbol{E}_{\mathsf{GL}}$ fulfil this principle. In contrast, considering (2.87), the deformation gradient $\boldsymbol{F}$ is not invariant under rigid body rotations, i.e. $\boldsymbol{F}$ is not an appropriate measure. It can be shown that the velocity tensor $\boldsymbol{D}$ also fulfils the principle. The principle of universal dissipation, see Coleman and Noll [26] or Truesdell and Noll [136] says, that an admissible thermodynamic process has to fulfil the Clausius-Duhem inequality (2.79). Hence, according to section 2.3.3, (2.79) can be used to reduce the number of unknowns due to the fact that each term of (2.79) has to be equal to or greater than zero. Next, the principle of material symmetry (see Coleman and Noll [26]) comprises, that different reference configurations at the same time lead to the same physical response, e.g. the same microscopic structure may be observed at different referential positions so that a deformation leads to the same results.

In the present thesis, isotropic materials are exclusively considered, i.e. there is no favoured direction in which the body deforms. Thus, the validity of the principle of material symmetry is guaranteed. Finally, the principle of local action, invented in Noll [99], establishes that the behaviour of a material point P is determined by the values of chosen variables at this point or its direct neighbourhood, whereas the values are insensitive to what happens in the distance.

2.4.2 State variables

In the context of the principle of local action, a material point P is influenced by so-called external and internal variables. On the one hand, these state variables or thermodynamic, independent

variables are observable, external variables which can be observed from outside, as e.g. the displacement $\boldsymbol{u}$ or the temperature T. On the other hand, the state variables are the internal variables which are not prescribed from outside, nor can explicitly be observed during the process. They do not appear in the balance relations, but are developed within the process using so-called evolution equations. The internal variables, summarized in $\boldsymbol{\alpha}_{\mathrm{k}}$, describe the internal change of a load state.

The success of a constitutive model which shall describe a particular realistic material behaviour depends critically on the choice of the state variables. The choice of the state variables is very important (see e.g. Lemaitre and Chaboche [78] or de Souza Neto et al. [33]) and according to Lemaitre and Chaboche [78] further defines the weakness and the richness of the so-called phenomenological thermodynamics: weakness because the choice is subjective and influences decisively the results of the model, richness because different physical effects can be treated separately or can be coupled easily with another effect.

The importance of the correct choice of state variables to account for the requirements of a considered material can be emphasized by a simple example of a steel bar: when the bar is subjected to a small axial strain at room temperature, the bar can be modelled with the linear elasticity theory. If strain becomes larger, the assumption of linear elasticity is no longer a good approximation. Instead, finite strain elasticity or plasticity may be a better choice. By further increasing the load, it may be necessary to also include damage into the model. Hence, the number of internal variables may be steadily increasing. Apart from very large loads and large axial strains, i.e. a nonlinear deformation state, the temperature can vary from a constant room temperature. Even at small strains, linear elasticity may not capture correctly the behaviour of the steel bar. In this case thermoelasticity may be more appropriate. For instance, in thermoelasticity, the temperatures T and the total strains $\boldsymbol{\varepsilon}$ can be used to fully describe a process at time t. For plasticity, these observable variables T and $\boldsymbol{\varepsilon}$ are not sufficient to describe the complete process, because the current state of the body also depends on the deformation history. To include the history, internal variables are introduced, e.g. for small strain plasticity in form of plastic strains (i.e $\boldsymbol{\alpha}_{\mathrm{k}} \equiv \boldsymbol{\varepsilon}^{p}$). In case of finite strain plasticity, the multiplicative split of $\boldsymbol{F}$ into an elastic and a plastic contribution has to be considered, which was first introduced by Lee [73]. Consequently, it is very important to choose an appropriate constitutive theory for a given problem with the appropriate set of variables.

After having defined a set of state variables, a thermodynamic potential has to be defined which is used to determine all associated state variables describing each a certain thermodynamic state. As shown in (2.82), two thermodynamic potentials are required for a general solid: firstly, a potential which characterizes all thermodynamical properties, secondly, a potential which characterizes the heat flux. In the present work, only associative thermodynamic potentials are used. Thus, the Helmholtz free energy ψ which is defined per unit reference volume is assumed. Homogeneous materials are exclusively investigated, so that the associative function is independent of the position in the medium. Based on a chosen Helmholtz free energy for a given process, the physical quantities associated to the state variables (as e.g. the stress tensor $\boldsymbol{\sigma}$ associated to the strain tensor $\boldsymbol{\varepsilon}$) can directly be identified as a consequence of the restrictions derived from the second law of thermodynamics. In the following section, the choice of a potential with the state variables and their associated counterparts are discussed based on a general thermomechanical problem.

2.4.3 General nonlinear thermomechanical problem

A general thermomechanical problem for arbitrary time t is expressed by the following general set of state variables:

$$\{\boldsymbol{F},\, T,\, \operatorname{grad} T,\, \boldsymbol{\alpha}_{\mathsf{k}},\, \boldsymbol{X}\}\,, \tag{2.88}$$

where $\boldsymbol{\alpha}_{\mathsf{k}}$ denotes a set of internal variables, which can describe tensor-valued, vector-valued, and scalar-valued quantities. Exemplarily, $\boldsymbol{\alpha}_{\mathsf{k}}$ can represent the tensor-valued plastic deformation gradient $\boldsymbol{F}^p$, the strain-like tensor $\boldsymbol{Z}$ associated with kinematic hardening, or the scalar-valued accumulated plastic strain $\bar{\varepsilon}^p$ associated to isotropic hardening. Further details on internal variables will be drawn in section 3.4.2. Defining the thermodynamic potential ψ in the variables (2.88) yields

$$\psi(\boldsymbol{F}, T, \operatorname{grad} T, \boldsymbol{\alpha}_{\mathsf{k}}, \boldsymbol{X}) \tag{2.89}$$

and its time derivative gives

$$\dot{\psi} \;=\; \frac{\partial \psi}{\partial \boldsymbol{F}} : \dot{\boldsymbol{F}} \;+\; \frac{\partial \psi}{\partial T}\,\dot{T} \;+\; \frac{\partial \psi}{\partial \operatorname{grad} T} \cdot (\operatorname{grad} T)^{\cdot} \;+\; \frac{\partial \psi}{\partial \boldsymbol{\alpha}_{\mathsf{k}}} \star \dot{\boldsymbol{\alpha}}_{\mathsf{k}} \;+\; \frac{\partial \psi}{\partial \boldsymbol{X}} \cdot \dot{\boldsymbol{X}}\,, \tag{2.90}$$

where the '$\star$' is used as appropriate scalar product operation dependent on the order of $\boldsymbol{\alpha}_{\mathsf{k}}$. As the initial position $\boldsymbol{X}$ is constant, the time derivative $\dot{\boldsymbol{X}}$ vanishes. Hence, this term is dropped in the following. Inserting (2.90) into (2.82) yields

$$\boldsymbol{\sigma} : \boldsymbol{D} \;-\; \rho \left(\frac{\partial \psi}{\partial \boldsymbol{F}} : \dot{\boldsymbol{F}} \;+\; \frac{\partial \psi}{\partial T}\,\dot{T} \;+\; \frac{\partial \psi}{\partial \operatorname{grad} T} \cdot (\operatorname{grad} T)^{\cdot} \;+\; \frac{\partial \psi}{\partial \boldsymbol{\alpha}_{\mathsf{k}}} \star \dot{\boldsymbol{\alpha}}_{\mathsf{k}} + \dot{T}\,\eta \right) \;-\; \frac{\boldsymbol{q}}{T} \cdot \operatorname{grad} T \;\geq\; 0\,, \tag{2.91}$$

which can be reordered to

$$\begin{aligned} \left(\boldsymbol{\sigma} \cdot \boldsymbol{F}^{-\mathsf{T}} \;-\; \rho\, \frac{\partial \psi}{\partial \boldsymbol{F}} \right) : \dot{\boldsymbol{F}} \;-\; \rho \left(\frac{\partial \psi}{\partial T} \;+\; \eta \right) \dot{T} \;-\; \rho\, \frac{\partial \psi}{\partial \operatorname{grad} T} \cdot (\operatorname{grad} T)^{\cdot} \;- \\ - \rho\, \frac{\partial \psi}{\partial \boldsymbol{\alpha}_{\mathsf{k}}} \star \dot{\boldsymbol{\alpha}}_{\mathsf{k}} \;-\; \frac{\boldsymbol{q}}{T} \cdot \operatorname{grad} T \;\;\geq\; 0 \end{aligned} \tag{2.92}$$

using the corresponding relation for the stress power

$$\boldsymbol{\sigma} : \boldsymbol{D} \;=\; \boldsymbol{\sigma} \cdot \boldsymbol{F}^{-\mathsf{T}} : \dot{\boldsymbol{F}}\,. \tag{2.93}$$

A material version of (2.92) follows as

$$\begin{aligned} \left(\boldsymbol{P} \;-\; \rho_0\, \frac{\partial \psi}{\partial \boldsymbol{F}} \right) : \dot{\boldsymbol{F}} \;-\; \rho_0 \left(\frac{\partial \psi}{\partial T} \;+\; \eta \right) \dot{T} \;-\; \rho_0\, \frac{\partial \psi}{\partial \operatorname{Grad} T} \cdot (\operatorname{Grad} T)^{\cdot} \;- \\ - \rho_0\, \frac{\partial \psi}{\partial \boldsymbol{\alpha}_{\mathsf{k}}} \star \dot{\boldsymbol{\alpha}}_{\mathsf{k}} \;-\; \frac{\boldsymbol{Q}}{T} \cdot \operatorname{Grad} T \;\;\geq\; 0\,. \end{aligned} \tag{2.94}$$

The Clausius-Duhem inequality (2.92) or (2.94) has to be fulfilled for an admissible thermodynamical process, that is, each component has to fulfil the equation. Hence, e.g. (2.94) can be used to define constraints for the problem. It is assumed that (2.94) must be valid for any pair of functions $\dot{\boldsymbol{F}}(t)$ and $\dot{T}(t)$. Thus, the term in parenthesis in front of the deformation rate (here

described via $\dot{\boldsymbol{F}}$) must vanish. Subsequently, this term in parenthesis is used to determine the stress via

$$\boldsymbol{P} \,=\, \rho_0 \, \frac{\partial \psi}{\partial \boldsymbol{F}} \,. \tag{2.95}$$

Furthermore, (2.95) can be used to derive equations for other stress measures introduced in section 2.2. Subsequently, the different stresses can be determined via

$$\boldsymbol{S} = \, \rho_0 \, \boldsymbol{F}^{-1} \cdot \frac{\partial \psi}{\partial \boldsymbol{F}} \,=\, \rho_0 \, \frac{\partial \psi}{\partial \boldsymbol{E}_{\mathsf{GL}}} \,=\, 2 \, \rho_0 \, \frac{\partial \psi}{\partial \boldsymbol{C}} \,, \tag{2.96}$$

$$\boldsymbol{\sigma} = \, \rho_0 \, J \, \frac{\partial \psi}{\partial \boldsymbol{F}} \cdot \boldsymbol{F}^{\mathsf{T}} = \rho \, \frac{\partial \psi}{\partial \boldsymbol{F}} \cdot \boldsymbol{F}^{\mathsf{T}} = \rho \, \boldsymbol{F} \cdot \frac{\partial \psi}{\partial \boldsymbol{E}_{\mathsf{GL}}} \cdot \boldsymbol{F}^{\mathsf{T}} = 2 \, \rho \, \boldsymbol{F} \cdot \frac{\partial \psi}{\partial \boldsymbol{C}} \cdot \boldsymbol{F}^{\mathsf{T}} = \, \rho \, \frac{\partial \psi}{\partial \boldsymbol{E}_{\mathsf{EA}}} \,, \tag{2.97}$$

$$\boldsymbol{\tau} = \, \rho_0 \, \frac{\partial \psi}{\partial \boldsymbol{F}} \cdot \boldsymbol{F}^{\mathsf{T}} \,=\, \rho_0 \, \boldsymbol{F} \cdot \frac{\partial \psi}{\partial \boldsymbol{E}_{\mathsf{GL}}} \cdot \boldsymbol{F}^{\mathsf{T}} \,=\, 2 \, \rho_0 \, \frac{\partial \psi}{\partial \boldsymbol{B}} \cdot \boldsymbol{B} \,=\, \rho_0 \, \frac{\partial \psi}{\partial \boldsymbol{E}_{\mathsf{EA}}} \,, \tag{2.98}$$

where appropriate push-forward and pull-back operations, as well as (2.54) have been used. With arbitrary temperature rate $\dot{T}$, the well-known relation between entropy η and temperature T is achieved as

$$\eta \,=\, -\frac{\partial \psi}{\partial T} \,, \tag{2.99}$$

hence $\{T, \eta\}$ defines a so-called thermal energy-conjugated pair analogously to the mechanical pairs introduced in section 2.47, as for instance $\{\boldsymbol{S}, \boldsymbol{E}_{\mathsf{GL}}\}$. Furthermore, as a result of the equipresence (see section 2.4.1), the rates of the temperature gradient $\mathrm{Grad}\, \dot{T}$ are arbitrary, so that

$$\rho_0 \, \frac{\partial \psi}{\partial \mathrm{Grad}\, T} \,=\, \boldsymbol{0} \,. \tag{2.100}$$

According to the energy-conjugated stress-strain pairs in (2.47), a thermodynamic force $\boldsymbol{A}_{\mathsf{k}}$ is defined as

$$\boldsymbol{A}_{\mathsf{k}} \,:=\, \rho_0 \, \frac{\partial \psi}{\partial \boldsymbol{\alpha}_{\mathsf{k}}} \,, \tag{2.101}$$

which is conjugated to the internal variable $\boldsymbol{\alpha}_{\mathsf{k}}$. Finally, by inserting all aforementioned relations (2.95) to (2.101), the Clausius-Duhem inequality reduces to the dissipation inequality

$$-\boldsymbol{A}_{\mathsf{k}} \star \dot{\boldsymbol{\alpha}}_{\mathsf{k}} \,-\, \frac{\boldsymbol{Q}}{T} \cdot \mathrm{Grad}\, T \,\geq\, 0 \,. \tag{2.102}$$

2.4.4 Dissipation, complementary laws

The thermodynamic potential introduced in the previous section allows to write relations between the observable state variables (e.g. displacement, temperature) and their associated variables (e.g. stress, entropy). However, for the internal variables $\boldsymbol{\alpha}_{\mathsf{k}}$, the potential defines only the associated variables of $\boldsymbol{\alpha}_{\mathsf{k}}$, i.e. $\boldsymbol{A}_{\mathsf{k}}$ (see (2.101)).

To describe the dissipation process, i.e. the evolution of the internal variables $\dot{\boldsymbol{\alpha}}_{\mathsf{k}}$, a complementary formalism is needed. Dissipation potentials aim to be complementary to thermodynamic potentials. Subsequently, based on (2.102) a dissipation potential ϕ is assumed, which depends on the products of thermodynamical force variables or dual variables (e.g. $\boldsymbol{A}_{\mathsf{k}}$, $\mathrm{Grad}\, T$) with their

corresponding flux variables (e.g. $\dot{\boldsymbol{\alpha}}_{\mathsf{k}}$, $\frac{\boldsymbol{Q}}{T}$), as well as possibly on the state variables. According to (2.102), it can result in

$$\phi \;=\; \phi(\dot{\boldsymbol{\alpha}}_{\mathsf{k}}, \frac{\boldsymbol{Q}}{T}) \;:=\; -\boldsymbol{A}_{\mathsf{k}} \star \dot{\boldsymbol{\alpha}}_{\mathsf{k}} \;-\; \frac{\boldsymbol{Q}}{T} \cdot \operatorname{Grad} T \geq\; 0\,. \tag{2.103}$$

Equation (2.103) can be split into two sub-potentials

$$\phi_{\mathsf{mech}} \;=\; -\boldsymbol{A}_{\mathsf{k}} \star \dot{\boldsymbol{\alpha}}_{\mathsf{k}} \;\geq\; 0\,, \quad \phi_{\mathsf{cond}} \;=\; -\frac{\boldsymbol{Q}}{T} \cdot \operatorname{Grad} T \;\geq\; 0\,, \tag{2.104}$$

where ϕ_{mech} denotes the intrinsic or mechanical dissipation, which describes the plastic dissipation and the dissipation associated with the evolution of the internal variables, and ϕ_{cond} is the thermal dissipation, which describes the thermal dissipation due to the conduction of heat. Commonly, dissipated mechanical energy is converted into heat, which cannot be converted back into mechanical energy.

It can be shown, see Lemaitre and Chaboche [78], that a dual potential $\phi^* = \phi^*(\boldsymbol{A}_{\mathsf{k}}, \operatorname{Grad} T)$ exists, which is defined in the dual variables and which can be used to define the complementary evolution laws for the internal variables as

$$\dot{\boldsymbol{\alpha}}_{\mathsf{k}} \;=\; -\frac{\partial \phi^*}{\partial \boldsymbol{A}_{\mathsf{k}}}\,, \quad \frac{\boldsymbol{Q}}{T} \;=\; -\frac{\partial \phi^*}{\partial \operatorname{Grad} T}\,, \tag{2.105}$$

where the so-called normal dissipativity or normality property is assumed. Normal dissipativity means, that the thermodynamical forces ($\boldsymbol{A}_{\mathsf{k}}$, $\operatorname{Grad} T$) are interpreted as the components of the vector $\operatorname{grad} \phi^*$. This vector $\operatorname{grad} \phi^*$ is assumed to be normal to the surface ($\phi^* = const.$) in the space of the flux variables ($\dot{\boldsymbol{\alpha}}_{\mathsf{k}}$, $\frac{\boldsymbol{Q}}{T}$). To satisfy the second law of thermodynamics, ϕ and ϕ^* are assumed to be positive, continuous, convex with respect to the dual variables, scalar-valued and zero at the origin (i.e. $\{\boldsymbol{A}_{\mathsf{k}}, \operatorname{Grad} T\} = \{\boldsymbol{0}, \boldsymbol{0}\}$). If the normality rule is ensured, the second law of thermodynamics is a priori satisfied. Furthermore, the additive split of ϕ is transferred to ϕ^*, hence separate potentials for the mechanical and the thermal contributions, ϕ^*_{mech} and ϕ^*_{cond}, respectively, can be assumed. While the physics of the two sub-potentials are still coupled, ϕ^*_{mech} is assumed to depend solely on the mechanical variables, whereas ϕ^*_{cond} is assumed to depend on the thermal gradients only. Moreover, to be thermodynamically consistent each sub-potential has to fulfil its inequality given each in (2.104). For a detailed description on dissipation potentials, complementary laws and the derivations of them, the interested reader is referred to the literature, such as Armero and Simo [7], de Souza Neto et al. [33], Lemaitre and Chaboche [78], and Maugin [84].

2.5 Special case of small strains

Since some of the present applications can be described based on small strains, subsequently the resulting simplifications are briefly summarized. In case the body undergoes small deformations, i.e.

$$\begin{aligned} \boldsymbol{x} &\approx \boldsymbol{X}\,, \\ \boldsymbol{F} &\approx \boldsymbol{I}\,, \\ \operatorname{div} \boldsymbol{u} &\approx \operatorname{Div} \boldsymbol{u}\,, \\ \operatorname{grad} \boldsymbol{u} &\approx \operatorname{Grad} \boldsymbol{u}\,. \end{aligned} \tag{2.106}$$

Moreover, starting from small strains, linearised quantities have to be considered for the stress and the strain tensors, recovering the linearised strain tensor

$$\boldsymbol{\varepsilon} \;=\; \frac{1}{2}\,(\operatorname{grad}\boldsymbol{u} \;+\; \operatorname{grad}^{\mathsf{T}}\boldsymbol{u}) \tag{2.107}$$

and hence the linearised stress tensor $\boldsymbol{\sigma}_{\mathsf{lin}} = \boldsymbol{\sigma}(\varepsilon)$ is obtained. Furthermore, $\boldsymbol{F}$ can be replaced by the linearised strain tensor ε, as e.g. in (2.88) and the velocity gradient $\boldsymbol{D}$ by the linearised strain rate tensor $\dot{\varepsilon}$, as e.g. in (2.93).

The infinitesimal elastic strains are additively split into isochoric deviatoric and volumetric contributions, $\boldsymbol{\varepsilon}_d^e$ and $\boldsymbol{\varepsilon}_v^e$, respectively, yielding

$$\boldsymbol{\varepsilon}^e \;=\; \boldsymbol{\varepsilon}_d^e \;+\; \boldsymbol{\varepsilon}_v^e\,, \tag{2.108}$$

where the two contributions can be further specified to

$$\begin{aligned} \boldsymbol{\varepsilon}_v^e \;&=\; \frac{1}{3}\,\varepsilon_v^e\,\boldsymbol{I} \;=\; \frac{1}{3}\,(\boldsymbol{\varepsilon}^e : \boldsymbol{I})\,\boldsymbol{I} \;=\; \frac{1}{3}\operatorname{tr}\boldsymbol{\varepsilon}^e\,\boldsymbol{I}\,, \\ \boldsymbol{\varepsilon}_d^e \;&=\; \boldsymbol{\varepsilon}^e \;-\; \boldsymbol{\varepsilon}_v^e\,, \end{aligned} \tag{2.109}$$

with $\varepsilon_v^e \;=\; \operatorname{tr}\boldsymbol{\varepsilon}^e$ and $\operatorname{tr}\boldsymbol{\varepsilon}_d^e \;=\; 0$.

3 Structural field

In the present chapter, the necessary fundamentals for solid mechanics, i.e. the general thermodynamical problem introduced in section 2 will be specified to a purely mechanical analysis whilst thermal terms will be neglected. For a more comprehensive and extensive review on solid mechanics, the interested reader is referred to the corresponding literature, e.g. Belytschko et al. [16], Bonet and Wood [17], Holzapfel [58], Lemaitre and Chaboche [78], and Zienkiewicz and Taylor [149]. The chapter starts by presenting the balance equation for the structural field in strong and weak form. Then, the target initial boundary value problem (IBVP) will be presented, followed by the solution techniques, which will be applied for the solution of this IBVP. An overview of the discretisation techniques is given, which focuses on the finite element method (FEM) for spatial discretisation and the finite difference method for time discretisation. At this point all equations will be available so that, by specifying the constitutive laws, the structural problem can be closed. Herein, elastic and elastoplastic material models will be distinguished. Subsequently, the structural problem is fully determined, so that solution techniques for this nonlinear system of equations in form of a Newton-Raphson scheme will be presented. In this context, direct and iterative solvers will be established to enable a robust and efficient solution of the resulting linear system of equation.

3.1 Governing equations

The structural field is assumed to be governed by the local material form of the balance of linear momentum introduced in (2.63), i.e.

$$\rho_0 \, \ddot{\boldsymbol{u}} \;=\; \mathrm{Div}\, \boldsymbol{P} \;+\; \hat{\boldsymbol{b}}_0 \quad \text{in } \Omega_0 \,. \tag{3.1}$$

For the sake of convenience, the structural field is exclusively formulated with respect to the reference configuration Ω_0. Again, it is worth noting, that (3.1) still characterizes equilibrium in the current configuration, although all quantities are expressed with respect to the reference configuration. Moreover, to describe a purely mechanical, isothermal solid (with a constant temperature $T = const.$), the second law of thermodynamics in the form of the Clausius-Planck inequality (2.84) has to be fulfilled to obtain a consistent formulation. Since the first Piola-Kirchhoff stresses $\boldsymbol{P}$ in (3.1) are unknown, a thermodynamic potential in the form of the Helmholtz free energy ψ, need to be chosen. Based on ψ, (2.84) defines constraints for the problem which will be used to determine for instance the stresses.

3.2 Finite element formulation and solution schemes

The IBVP of nonlinear solid mechanics is described via a nonlinear coupled system of partial differential equations (PDEs) including (3.1), combined with the previously presented kinematic

relations (see section 2.1), a chosen constitutive model which will be specified later on in section 3.4, and a set of initial conditions and boundary conditions, respectively. The boundary $\partial\Omega_0$ is divided into a Dirichlet and a Neumann boundary, $\Gamma_{0;\mathsf{D};\mathsf{S}}$ and $\Gamma_{0;\mathsf{N};\mathsf{S}}$, respectively, where the index S represents the boundary of the structural problem. On the Dirichlet boundary $\Gamma_{0;\mathsf{D};\mathsf{S}}$, the displacements are prescribed, whereas on the Neumann boundary $\Gamma_{0;\mathsf{N};\mathsf{S}}$ the traction vector is prescribed. Thus, the following conditions

$$\boldsymbol{u} = \hat{\boldsymbol{u}} \quad \text{on } \Gamma_{0;\mathsf{D};\mathsf{S}}\,, \tag{3.2}$$

$$\boldsymbol{P}\cdot\boldsymbol{n}_0 = \hat{\boldsymbol{t}}_0 \quad \text{on } \Gamma_{0;\mathsf{N};\mathsf{S}} \tag{3.3}$$

need to be satisfied. The superimposed hat in (3.2) and (3.3) identifies prescribed quantities, as already used for the prescribed body force $\hat{\boldsymbol{b}}_0$ in (3.1). It is noted that the boundary $\partial\Omega_0$ is divided into pairwise disjoint partitions, i.e.

$$\partial\Omega_0 = \Gamma_{0;\mathsf{D};\mathsf{S}} \cup \Gamma_{0;\mathsf{N};\mathsf{S}}\,, \quad \Gamma_{0;\mathsf{D};\mathsf{S}} \cap \Gamma_{0;\mathsf{N};\mathsf{S}} = \emptyset\,. \tag{3.4}$$

As (3.1) describes a second-order PDE in time, initial conditions for both displacements $\boldsymbol{u}$ and velocities $\dot{\boldsymbol{u}}$ need to be specified at time $t = 0$ following

$$\boldsymbol{u}_0 = \boldsymbol{u}(\boldsymbol{X}, t=0) = \hat{\boldsymbol{u}}_0 \quad \text{on } \Omega_0\,, \tag{3.5}$$

$$\dot{\boldsymbol{u}}_0 = \dot{\boldsymbol{u}}(\boldsymbol{X}, t=0) = \hat{\dot{\boldsymbol{u}}}_0 \quad \text{on } \Omega_0\,. \tag{3.6}$$

The above system of PDEs defines the so-called strong form of nonlinear solid mechanics problems, i.e. the IBVP is satisfied in a strong, pointwise manner. As an analytical solution to this class of IBVP is possible only for very simple cases, e.g. small deformations, simple geometries, etc., an alternative solution approach is required. Hence, numerical (discretisation) techniques are used instead. The IBVP contains PDEs in space and time, thus a full discretisation, i.e. in space and time, is needed. For space discretisation the finite element method (FEM) and for temporal discretisation the finite difference method is used. Basis for the FEM is the conversion of the problem from the strong to the so-called weak form. In contrast to the strong form, which fulfils the equations at each point, the weak form fulfils the equations only in an integral sense. To derive a weak form, the principle of virtual work (PVW) is utilised, which is based on the method of weighted residuals. The method of weighted residuals is applied to the balance equation (3.1) and the traction boundary condition (3.3), yielding

$$\int_{\Omega_0} \underbrace{(\rho_0\,\ddot{\boldsymbol{u}} - \operatorname{Div}\boldsymbol{P} - \hat{\boldsymbol{b}}_0)}_{\boldsymbol{r}^{\mathsf{BE}}}\cdot\boldsymbol{w}\,\mathrm{d}V_0 + \int_{\Gamma_{0;\mathsf{N};\mathsf{S}}} \underbrace{(\boldsymbol{P}\cdot\boldsymbol{n}_0 - \hat{\boldsymbol{t}}_0)}_{\boldsymbol{r}^{\mathsf{TBC}}}\cdot\boldsymbol{w}\,\mathrm{d}A_0 = 0\,, \tag{3.7}$$

where $\boldsymbol{r}^{\mathsf{BE}}$ and $\boldsymbol{r}^{\mathsf{TBC}}$ denote the residual of (3.1) and (3.3), respectively, and $\boldsymbol{w}$ denotes a weighting function vector, which satisfies

$$\boldsymbol{w} = \boldsymbol{0} \quad \text{on } \Gamma_{0;\mathsf{D};\mathsf{S}} \tag{3.8}$$

and which can be interpreted as virtual displacements in solid mechanics, i.e.

$$\boldsymbol{w} = \delta\boldsymbol{u}\,. \tag{3.9}$$

Finally, the weak form of (3.7) is obtained by integration by parts of the divergence theorem and insertion of (2.46) and (3.9), that is

$$\int_{\Omega_0} \rho_0 \, \ddot{\boldsymbol{u}} \cdot \delta \boldsymbol{u} \, \mathrm{d}V_0 + \int_{\Omega_0} (\mathrm{Grad}\, \delta \boldsymbol{u})^{\mathsf{T}} : (\boldsymbol{F} \cdot \boldsymbol{S}) \, \mathrm{d}V_0 - \int_{\Omega_0} \hat{\boldsymbol{b}}_0 \cdot \delta \boldsymbol{u} \, \mathrm{d}V_0 - \int_{\Gamma_{0;\mathsf{N};\mathsf{S}}} \hat{\boldsymbol{t}}_0 \cdot \delta \boldsymbol{u} \, \mathrm{d}A_0 \; = \; 0 \,, \tag{3.10}$$

which can be further simplified to

$$\underbrace{\int_{\Omega_0} \rho_0 \, \ddot{\boldsymbol{u}} \cdot \delta \boldsymbol{u} \, \mathrm{d}V_0}_{-\delta \mathcal{W}_{\mathsf{kin}}} + \underbrace{\int_{\Omega_0} \delta \boldsymbol{E}_{\mathsf{GL}}^{\mathsf{T}} : \boldsymbol{S} \, \mathrm{d}V_0}_{-\delta \mathcal{W}_{\mathsf{int}}} \underbrace{- \int_{\Omega_0} \hat{\boldsymbol{b}}_0 \cdot \delta \boldsymbol{u} \, \mathrm{d}V_0 - \int_{\Gamma_{0;\mathsf{N};\mathsf{S}}} \hat{\boldsymbol{t}}_0 \cdot \delta \boldsymbol{u} \, \mathrm{d}A_0}_{-\delta \mathcal{W}_{\mathsf{ext}}} \; = \; 0 \,. \tag{3.11}$$

Herein, the kinetic, the internal and the external virtual works, $\delta \mathcal{W}_{\mathsf{kin}}$, $\delta \mathcal{W}_{\mathsf{int}}$, and $\delta \mathcal{W}_{\mathsf{ext}}$, are distinguished respectively. Furthermore, the symmetric second Piola-Kirchhoff stress $\boldsymbol{S}$ and the total variation of the Green-Lagrange strain tensor (2.17) given by

$$\delta \boldsymbol{E}_{\mathsf{GL}} \; = \; \frac{1}{2} \left((\boldsymbol{F}^{\mathsf{T}} \cdot \mathrm{Grad}\, \delta \boldsymbol{u})^{\mathsf{T}} \; + \; \boldsymbol{F}^{\mathsf{T}} \cdot \mathrm{Grad}\, \delta \boldsymbol{u} \right) \tag{3.12}$$

are used.

An alternative approach to the weak formulation is obtained by the variation of an assumed energy potential $\mathcal{W}$ which yields the so-called principle of minimum of total potential energy (PMTPE). As $\mathcal{W}$ does not generally exist, the PMTPE is not generally valid either. Consequently, the PVW is utilised here exclusively.

3.2.1 Space discretisation

3.2.1.1 Basics

As stated in the previous section, the FEM is used here for the numerical solution of the given IBVP. As a detailed introduction of the FEM is beyond the scope of the present explanations, the reader is referred to numerous textbooks, as e.g. Belytschko et al. [16], Hughes [60], Zienkiewicz et al. [150], and Zienkiewicz and Taylor [149]. Instead, the explanations are restricted to the basic notations.

The basic idea of the FEM is to replace the continuous solution of the problem on a continuous domain Ω_0 by the solution at discrete points, the so-called nodes, while the solution remains continuous in time. The nodes are further connected to form elements so that the domain Ω_0 is partitioned into a finite number of nele elements, viz.

$$\Omega_0 \; \approx \; \Omega_0^h \; = \; \bigcup_{e=1}^{\mathsf{nele}} \Omega_0^{(e)} \,. \tag{3.13}$$

The finite elements (FE) approximate the continuous domain Ω_0 via smaller, non-overlapping subdomains $\Omega_0^{(e)}$ which can be summarized in the discrete domain Ω_0^h. Introduction of the shape

functions $\check{N}$ and the nodal displacement vector $\mathbf{d}$ enables the approximation of the continuous displacements within an element by

$$\boldsymbol{u}^{(e)}(\boldsymbol{X},t) \approx \boldsymbol{u}^{(e);h}(\boldsymbol{X},t) = \sum_{I=1}^{\mathsf{nnod}} \check{N}_I(\boldsymbol{X})\,\mathbf{d}_I(t)\,, \tag{3.14}$$

where I and nnod denote the current node and the total number of nodes per element, respectively. As the shape function $\check{N}$ depends only on the position $\boldsymbol{X}$, the time dependency is decoupled from them and is found only in the nodal displacement vector $\mathbf{d}$. The accelerations $\ddot{\boldsymbol{u}}$, the virtual displacements $\delta\boldsymbol{u}$, and the element geometry in the reference and the current configuration, $\boldsymbol{X}$ and $\boldsymbol{x}$, respectively, are discretised equally. This leads to the well-known isoparametric concept. Moreover, as same shape functions are used for the primary variable $\boldsymbol{u}$ and its virtual counterpart $\delta\boldsymbol{u}$, the present approach is further known as Bubnov-Galerkin approach, in contrast to the Petrov-Galerkin approach, where different shape functions are used for $\boldsymbol{u}$ and $\delta\boldsymbol{u}$. Furthermore, it is common to use polynomials for the shape functions whose order is chosen according to the requirements of the weak form. Depending on the number of nodes and the order of the polynomial, different finite element shapes are obtained, as for instance for three-dimensions eight-noded hexahedral elements (named Hex8), four-noded tetrahedral elements (named Tet4), or 27-noded hexaeder elements (named Hex27). While Hex8 and Tet4 elements use linear polynomials in each direction, i.e. (tri-)linear shape functions, Hex27 elements use quadratic polynomials.

For evaluating the weak form (3.11), a numerical integration technique such as the Gauss quadrature is used. Following this, the element is expressed in local coordinates $\boldsymbol{\xi}$ which is achieved by mapping the global quantities to a reference geometry, known as parameter space. Hence, for instance the reference position follows as

$$\zeta : \boldsymbol{\xi} \mapsto \boldsymbol{X}^{(e);h}(\boldsymbol{\xi}) = \sum_{I=1}^{\mathsf{nnod}} N_I(\boldsymbol{\xi})\,\mathbf{X}_I\,, \tag{3.15}$$

where N defines the shape functions in the parameter space. Thereby, e.g. for Hex8 elements, the reference geometry is described by a normalized cube $[-1;1]\times[-1;1]\times[-1;1]$, which is used to determine the Jacobian matrix

$$\mathbf{J}^{(e)} = \frac{\partial \boldsymbol{X}^{(e)}}{\partial \boldsymbol{\xi}}\,. \tag{3.16}$$

An important advantage of the FEM is that any integral over the domain Ω_0 can be written as sum of elementwise integrals, i.e. assembled, which reads

$$\int_{\Omega_0} (\cdot)\,\mathrm{d}V_0 = \sum_{e=1}^{\mathsf{nele}} \int_{\Omega_0^{(e);h}} (\cdot)\,\mathrm{d}V_0\,, \tag{3.17}$$

indicating that the integration requires only the knowledge of the corresponding elementwise values. Finally, all elementwise contributions are assembled leading to the semi-discrete (i.e. discrete in space but still continuous in time) weak form of the balance of linear momentum by

$$\delta\mathbf{d}\left[\mathbf{M}\,\ddot{\mathbf{d}} + \mathbf{f}_{\mathsf{int;S}}(\mathbf{d}) - \mathbf{f}_{\mathsf{ext;S}}\right] = 0 \tag{3.18}$$

with the mass matrix $\mathbf{M}$, the internal force vector $\mathbf{f}_{\mathsf{int;S}}$, the external force vector $\mathbf{f}_{\mathsf{ext;S}}$, the globally virtual displacement vector $\delta\mathbf{d}$, and the global acceleration and displacement vector, $\ddot{\mathbf{d}}$ and $\mathbf{d}$, respectively. For simplicity, the external forces $\mathbf{f}_{\mathsf{ext;S}}$ are assumed to be independent of the unknown displacements $\mathbf{d}$. The index S represent the structural problem. By assuming arbitrary virtual displacements $\delta\mathbf{d}$, (3.18) can further be rewritten to

$$\mathbf{M}\,\ddot{\mathbf{d}} + \mathbf{f}_{\mathsf{int;S}}(\mathbf{d}) - \mathbf{f}_{\mathsf{ext;S}} = \mathbf{0}\,. \tag{3.19}$$

For completeness, viscous damping can be considered, so that (3.19) results in

$$\mathbf{M}\,\ddot{\mathbf{d}} + \mathbf{D}\,\dot{\mathbf{d}} + \mathbf{f}_{\mathsf{int;S}}(\mathbf{d}) - \mathbf{f}_{\mathsf{ext;S}} = \mathbf{0}\,, \tag{3.20}$$

where the damping matrix $\mathbf{D}$ and the global velocity vector $\dot{\mathbf{d}}$ are inserted. Exemplarily, $\mathbf{D}$ is given as

$$\mathbf{D} = c_{\mathsf{M}}\,\mathbf{M} + c_{\mathsf{K}}\,\mathbf{K}_{\mathsf{S}}^{0} \tag{3.21}$$

with free parameters c_{M} and c_{k}, and the initial tangential stiffness matrix $\mathbf{K}_{\mathsf{S}}^{0}$, which will be specified in section 3.3. This procedure is known as the Rayleigh ansatz.

3.2.1.2 F-bar element technology

It is common to use low-order displacement-based elements, as e.g. Hex8 elements which utilise linear polynomials in each direction for the shape functions in (3.14) to approximate the displacements. Since they are simple, cheap, and fast, they are the element of choice in most applications. Issues arise for problems near the incompressibility, for instance for plasticity or rubber elasticity where spurious volumetric locking occurs, resulting in too small deformations. For an overview on different locking effects, the reader is referred to Klöppel [66] and the references therein. In metal plasticity, which is one target application of the present thesis, the deformation is assumed to be isochoric at each point (e.g. in finite strain plasticity $\det \boldsymbol{F}^{p} = 1$, see section 3.4.2.5) while the compressible part of the deformation, resulting from elasticity, is rather small. In rubber elasticity, the ratio between bulk modulus K and Poisson's ratio ν is very large, i.e. alternatively isochoric deformations are characterizes by $K \to \infty$ and $\nu \to 0.5$. Since volume-preserving displacements fields cannot be correctly represented by standard linear displacement-based elements, these elements are not applicable for isochoric deformations. To overcome volumetric locking issues, either linear displacement-based finite elements in conjunction with element technology or higher-order elements are conceivable. While locking effects for higher-order elements are decisively smaller, they can be used with the expense of cheapness and velocity. For linear displacement-based elements several approaches have been established to overcome the volumetric locking issues, such as selective reduced integration (SRI), e.g. in Doll et al. [36], mixed finite elements based on mixed variational formulations, see e.g. Simo and Miehe [122], Simo et al. [124], and Zienkiewicz and Taylor [149], and assumed strain methods, such as the enhanced assumed strain (EAS) method (applied for instance in Simo and Armero [119] and Adam and Ponthot [1]) or F-bar methods (see e.g. de Souza Neto et al. [31, 32, 33]). For an overview on different element technologies, the reader is referred, e.g. to Doll et al. [36] and the references therein.

In the present work, quadratic Hex27 elements will be applied for the small strain plasticity models of sections 3.4.2.3 and 3.4.2.4 as well as sections 5.3.2.1 and 5.3.2.2. However, to circumvent volumetric locking in the range of finite strain plasticity applications, a F-bar method will be applied to the Hex8 elements.

The F-bar method postulates that in the context of an arbitrary potential (2.89) the deformation gradient $\boldsymbol{F}$ is replaced with a modified equivalent $\bar{\boldsymbol{F}}$. To get the modified deformation gradient $\bar{\boldsymbol{F}}$, the current deformation gradient $\boldsymbol{F}$ is first split into volumetric and isochoric parts, $\boldsymbol{F}_v$ and $\tilde{\boldsymbol{F}}$, respectively, according to (2.35). Volumetric locking is caused by parasitic stresses arising in the element, so that a too stiff response is obtained. These stresses are linear within the element, i.e. they are zero at the element centre. Hence, to circumvent volumetric locking, the incompressibility constraint is weakened by replacing $\boldsymbol{F}_v$ at each Gauss point of an element with the volumetric deformation gradient at the centre of the element $\boldsymbol{F}_0$, where these parasitic stresses vanish. Subsequently, employing $\boldsymbol{F}_0$ for all Gauss points of an element, $\bar{\boldsymbol{F}}$ follows as

$$\bar{\boldsymbol{F}} := \boldsymbol{F}_{0;v} \cdot \tilde{\boldsymbol{F}} = \left(\frac{\det \boldsymbol{F}_0}{\det \boldsymbol{F}}\right)^{\frac{1}{3}} \boldsymbol{F} \,, \tag{3.22}$$

so that, for instance according to (2.97), the Cauchy stresses result in

$$\bar{\boldsymbol{\sigma}} = \check{\boldsymbol{\sigma}}(\psi(\bar{\boldsymbol{F}})) \,. \tag{3.23}$$

Via pull-back of (3.23) using (2.46), the Cauchy and the second Piola-Kirchhoff stresses are related, so that

$$\bar{\boldsymbol{\sigma}} = \frac{1}{\det \bar{\boldsymbol{F}}} \bar{\boldsymbol{F}} \cdot \bar{\boldsymbol{S}} \cdot \bar{\boldsymbol{F}}^{\mathsf{T}} \,. \tag{3.24}$$

Subsequently, (3.24) is inserted into the weak form (3.11) which yields after reformulations a modified semi-discrete element internal force vector

$$\bar{\mathsf{f}}^{(e)}_{\mathsf{int;S}} = \int\limits_{\Omega_0^{(e)}} \left(\frac{\det \mathsf{F}_0}{\det \mathsf{F}}\right)^{-\frac{1}{3}} \delta\mathsf{E}^{\mathsf{T}} \, \bar{\mathsf{S}} \, \mathrm{d}V_0 \tag{3.25}$$

in combination with the standard virtual strain tensor $\delta\mathsf{E}^{\mathsf{T}}$. As volumetric locking arises only due to the incompressibility condition which is assumed for the plastic behaviour within the constitutive theory, $\bar{\mathsf{F}}$ is only applied for the stress function while the strain state remains unchanged, see de Souza Neto et al. [33]. Consequently, the weak form (3.11), including standard displacement-based elements only differs in the application of the modified stresses (3.24), while all other terms remain unaltered. Thus, the benefit of the F-bar method becomes obvious, namely only small changes in comparison with standard FE-formulations. In contrast, for instance EAS involves large changes, as e.g. static condensation of internal degrees of freedom (DOFs) at element level which need to be performed in every iteration. Moreover, the F-bar element technology can be extended to two-dimensional four-noded quadrilateral elements and, as shown in de Souza Neto et al. [32], to two-dimensional triangular or three-dimensional tetrahedral elements.

3.2.2 Time discretisation

Equation (3.20) is still continuous with respect to time t, thus time discretisation of the semi-discrete equations is performed in the following to reach the fully discrete structural equations. In literature, commonly finite difference methods are utilised for time differentiation by replacing continuous time derivatives with difference quotients. Defining the time step size Δt, the time interval $[t_0, t_{\mathsf{max}}]$ is partitioned into time intervals $[t_n, t_{n+1}]$ where n denotes the time step index and t_{n+1} denotes the unknown searched point in time. Implicit and explicit schemes are distinguished. While for explicit time integration schemes the new unknown displacements $\mathbf{d}_{n+1}$ are directly extrapolated, implicit schemes require the solution of a system of ndof nonlinear fully discrete equations for $\mathbf{d}_{n+1}$. Here, ndof defines the number of unknown DOFs.

For the final target application to thermo-fluid-structure interaction (TFSI), where the present thermo-structure interaction (TSI) model is coupled to a compressible high Mach turbulent flow solver, see e.g. Hammerl et al. [53], explicit schemes are applicable due to the very small time step required in the fluid field, for instance as a result of the utilised turbulence model. In contrast, for the simulation of solids with low frequency response, which are the focus of the present work, implicit schemes are the method of choice, since they are more stable and allow larger time steps. Unfortunately, it is more challenging to include them in the FE formulation, because the nonlinear solution method requires a full linearisation of the given problem. To conclude, as the present work aims at pure TSI, implicit schemes are only utilised, and in the following two different schemes will be presented.

3.2.2.1 Generalised-α time integration

A widely used implicit method is the so-called generalised-α method, proposed by Chung and Hulbert [25], which is based on Newmark's method (see Newmark [97]). Newmark's method looks for equilibrium at the end of the time step t_{n+1}. Hence, the endpoint solutions for velocity $\dot{\mathbf{d}}_{n+1}$ and acceleration $\ddot{\mathbf{d}}_{n+1}$ at t_{n+1} can be expressed using $\mathbf{d}_{n+1}$ as

$$\dot{\mathbf{d}}_{n+1}(\mathbf{d}_{n+1}) \approx \mathbf{v}_{n+1}(\mathbf{d}_{n+1}) = \frac{\gamma}{\beta \Delta t}\left(\mathbf{d}_{n+1} - \mathbf{d}_n\right) - \frac{\gamma - \beta}{\beta}\mathbf{v}_n - \frac{\gamma - 2\,\beta}{2\,\beta}\Delta t\,\mathbf{a}_n\,, \tag{3.26}$$

$$\ddot{\mathbf{d}}_{n+1}(\mathbf{d}_{n+1}) \approx \mathbf{a}_{n+1}(\mathbf{d}_{n+1}) = \frac{1}{\beta \Delta t^2}\left(\mathbf{d}_{n+1} - \mathbf{d}_n\right) - \frac{1}{\beta \Delta t}\mathbf{v}_n - \frac{1 - 2\,\beta}{2\,\beta}\mathbf{a}_n\,, \tag{3.27}$$

where the approximation of the velocity and the acceleration is based on known quantities at t_n with the exception of the unknown primary variable $\mathbf{d}_{n+1}$. As parameters $\beta \in [0,\, 0.5]$ and $\gamma \in [0,\, 1.0]$ are used. Inserting these quantities into (3.20) would yield a solution of the balance of linear momentum at the end of the discrete time step $n + 1$. Newmark's method shows unstable behaviour in nonlinear dynamics, thus an improved version, namely the generalised-α method established by Chung and Hulbert [25] is proposed, which is robust even in nonlinear dynamics and, for an appropriate choice of the parameters, in addition stable. The generalised-α method uses (3.26) and (3.27) for the new solution of the velocities and the accelerations, respectively, but shifts the evaluation point from t_{n+1} to general mid-points $t_{n+1-\alpha_\mathsf{m}}$ and $t_{n+1-\alpha_\mathsf{f}}$, respectively. Thus, corresponding approximations for displacements, velocities, accelerations,

and the external force vector follow as

$$\mathbf{d}_{n+1-\alpha_\mathsf{f}} = (1 - \alpha_\mathsf{f})\,\mathbf{d}_{n+1} + \alpha_\mathsf{f}\,\mathbf{d}_n\,, \tag{3.28}$$

$$\mathbf{v}_{n+1-\alpha_\mathsf{f}} = (1 - \alpha_\mathsf{f})\,\mathbf{v}_{n+1} + \alpha_\mathsf{f}\,\mathbf{v}_n\,, \tag{3.29}$$

$$\mathbf{a}_{n+1-\alpha_\mathsf{m}} = (1 - \alpha_\mathsf{m})\,\mathbf{a}_{n+1} + \alpha_\mathsf{m}\,\mathbf{a}_n\,, \tag{3.30}$$

$$\mathbf{f}_{\mathsf{ext};\mathsf{S};n+1-\alpha_\mathsf{f}} = (1 - \alpha_\mathsf{f})\,\mathbf{f}_{\mathsf{ext};\mathsf{S};n+1} + \alpha_\mathsf{f}\,\mathbf{f}_{\mathsf{ext};\mathsf{S};n} \tag{3.31}$$

with the two additional generalised-α parameters $\alpha_\mathsf{m} \in [0,\,1]$ and $\alpha_\mathsf{f} \in [0,\,1]$. For the approximation of the force vector $\mathbf{f}_{\mathsf{int};\mathsf{S};n+1-\alpha_\mathsf{f}}$ a so-called tr-like approach is chosen, i.e. the internal force vector is interpolated between solutions at t_n and t_{n+1}

$$\begin{aligned} \mathbf{f}_{\mathsf{int};\mathsf{S};n+1-\alpha_\mathsf{f}} &= (1 - \alpha_\mathsf{f})\,\mathbf{f}_{\mathsf{int};\mathsf{S};n+1} + \alpha_\mathsf{f}\,\mathbf{f}_{\mathsf{int};\mathsf{S};n} \\ &= (1 - \alpha_\mathsf{f})\,\mathbf{f}_{\mathsf{int};\mathsf{S}}(\mathbf{d}_{n+1}) + \alpha_\mathsf{f}\,\mathbf{f}_{\mathsf{int};\mathsf{S}}(\mathbf{d}_n) \end{aligned} \tag{3.32}$$

using a trapezoidal rule (tr). In contrast, the so-called imr-like (implicit midpoint rule) approximation exists, however, this approach is not pursued in the present work. The big advantage of the present generalised-α method is the inclusion of controllable numerical dissipation into the system of equations while second-order accuracy and stability remain valid. Hence, the spectral radius ρ is introduced which accommodates higher numerical dissipation or numerical damping with smaller values of ρ. In practice, damping is desirable in the spurious high frequency regime, whereas it should be as small as possible in the low frequency regime, see e.g. Mok [93] and the references therein for further explanations. Consequently, with increasing frequency the values of ρ should decrease. To summarize all the requirements, ρ_∞ is introduced as the maximal spectral radius for high frequencies. Subsequently, ρ_∞ represents the sole free parameter, which can be used to get optimal values of the four generalised-α parameters:

$$\alpha_\mathsf{f} = \frac{\rho_\infty}{\rho_\infty + 1}\,, \qquad \alpha_\mathsf{m} = \frac{2\,\rho_\infty - 1}{\rho_\infty + 1}\,, \tag{3.33}$$

$$\beta = \frac{1}{4}\,(1 - \alpha_\mathsf{m} + \alpha_\mathsf{f})^2\,, \quad \gamma = \frac{1}{2} - \alpha_\mathsf{m} + \alpha_\mathsf{f}\,. \tag{3.34}$$

Integration of all aforementioned results into (3.20) gives the fully discrete structural equation by

$$\mathbf{M}\,\mathbf{a}_{n+1-\alpha_\mathsf{m}} + \mathbf{D}\,\mathbf{v}_{n+1-\alpha_\mathsf{f}} + \mathbf{f}_{\mathsf{int};\mathsf{S}}(\mathbf{d}_{n+1-\alpha_\mathsf{f}}) - \mathbf{f}_{\mathsf{ext};\mathsf{S};n+1-\alpha_\mathsf{f}} = \mathbf{0}\,. \tag{3.35}$$

Finally, Newmark's method can be recovered as special case of the generalised-α method for the choice $\alpha_\mathsf{m} = \alpha_\mathsf{f} = 0$. Furthermore, by neglecting the inertia effect, $\mathbf{M}\,\mathbf{a} \approx \mathbf{0}$, a quasi-static formulation is obtained which is widely used in structural mechanics. In this case, t plays the role of a pseudo-time, i.e. a sequence of static equilibrium states is computed.

3.2.2.2 One-step-θ time integration

The generalised trapezoidal (or one-step-θ) scheme can be applied as an alternative time integration approach to the generalised-α method. It is a linear combination of forward and backward Euler time integration schemes. According to (3.26) and (3.27), the corresponding values are

approximated for the one-step-θ scheme by

$$\dot{\mathbf{d}}_{n+1}(\mathbf{d}_{n+1}) \approx \mathbf{v}_{n+1}(\mathbf{d}_{n+1}) = \frac{1}{\theta\,\Delta t}\,(\mathbf{d}_{n+1} - \mathbf{d}_n) - \frac{1-\theta}{\theta}\,\mathbf{v}_n\,, \tag{3.36}$$

$$\ddot{\mathbf{d}}_{n+1}(\mathbf{d}_{n+1}) \approx \mathbf{a}_{n+1}(\mathbf{d}_{n+1}) = \frac{1}{\theta^2\Delta t^2}\,(\mathbf{d}_{n+1} - \mathbf{d}_n) - \frac{1}{\theta^2\Delta t}\,\mathbf{v}_n - \frac{1-\theta}{\theta}\,\mathbf{a}_n\,, \tag{3.37}$$

where θ represents the sole parameter of this time integration method. Subsequently, the accelerations are approximated using a finite difference scheme, i.e.

$$\frac{\mathbf{v}_{n+1} - \mathbf{v}_n}{\Delta t} = \theta\,\mathbf{a}_{n+1} + (1-\theta)\,\mathbf{a}_{n+1}\,. \tag{3.38}$$

Including (3.38) into (3.20), the fully discrete equation reads

$$\begin{aligned} \mathbf{M}\,\frac{\mathbf{v}_{n+1} - \mathbf{v}_n}{\Delta t} &+ \theta\left[\mathbf{D}\,\mathbf{v}_{n+1} + \mathbf{f}_{\mathsf{int;S}}(\mathbf{d}_{n+1}) - \mathbf{f}_{\mathsf{ext;S};n+1}\right] \\ &+ (1-\theta)\left[\mathbf{D}\,\mathbf{v}_n + \mathbf{f}_{\mathsf{int;S}}(\mathbf{d}_n) - \mathbf{f}_{\mathsf{ext;S};n}\right] = \mathbf{0}\,, \end{aligned} \tag{3.39}$$

which can be transformed to a more common form expressed only in current displacements $\mathbf{d}_{n+1}$, leading to

$$\begin{aligned} &\left[\frac{1}{\theta\,\Delta t^2}\,\mathbf{M} + \frac{1}{\Delta t}\,\mathbf{D}\right]\mathbf{d}_{n+1} + \theta\,\mathbf{f}_{\mathsf{int;S}}(\mathbf{d}_{n+1}) - \left[\frac{1}{\theta\,\Delta t^2}\,\mathbf{M} + \frac{1}{\Delta t}\,\mathbf{D}\right]\mathbf{d}_n + \\ &\quad + (1-\theta)\,\mathbf{f}_{\mathsf{int;S}}(\mathbf{d}_n) + \theta\,\mathbf{f}_{\mathsf{ext;S};n+1} + (1-\theta)\,\mathbf{f}_{\mathsf{ext;S};n} + \mathbf{M}\,\frac{\mathbf{v}_n}{\theta\,\Delta t} = \mathbf{0}\,. \end{aligned} \tag{3.40}$$

For $\theta = 0.5$, the so-called Crank-Nicolson scheme is obtained and a quasi-static formulation is recovered by neglecting the first term in (3.39).

3.3 Linearisation and solution techniques for nonlinear equations

Equation (3.35) or (3.40) describe both a system of nonlinear algebraic equations which is solved iteratively by applying a Newton-Raphson method. Hence, the residual of the fully discrete balance of linear momentum, e.g. in form of (3.35) is defined for an iteration step i as

$$\mathbf{r}_{\mathsf{S}}(\mathbf{d}^i_{n+1}) = \mathbf{M}\,\mathbf{a}^i_{n+1-\alpha_{\mathsf{m}}} + \mathbf{D}\,\mathbf{v}^i_{n+1-\alpha_{\mathsf{f}}} + \mathbf{f}_{\mathsf{int;S}}(\mathbf{d}^i_{n+1-\alpha_{\mathsf{f}}}) - \mathbf{f}_{\mathsf{ext;S};n+1-\alpha_{\mathsf{f}}}\,. \tag{3.41}$$

A Taylor expansion around the current solution $\mathbf{d}^i_{n+1}$ is performed which is truncated after the linear term, yielding the linearised form of (3.41) by

$$\mathrm{Lin}\,\mathbf{r}_{\mathsf{S}}(\mathbf{d}^i_{n+1}) = \mathbf{r}_{\mathsf{S}}(\mathbf{d}^i_{n+1}) + \underbrace{\left.\frac{\partial \mathbf{r}_{\mathsf{S}}(\mathbf{d}_{n+1})}{\partial \mathbf{d}_{n+1}}\right|^i}_{\mathbf{K}_{\mathsf{SS}}(\mathbf{d}^i_{n+1})}\Delta\mathbf{d}^{i+1}_{n+1}\,, \tag{3.42}$$

with the dynamic effective tangential stiffness matrix $\mathbf{K}_{\mathsf{SS}}(\mathbf{d}^i_{n+1})$. The linearisation of the internal forces included in $\mathbf{K}_{\mathsf{SS}}$ is known as the tangential stiffness matrix $\mathbf{K}$, which is defined as

$$\mathbf{K}^i_{\mathsf{S}} \;=\; \left.\frac{\partial \mathbf{f}_{\mathsf{int;S}}(\mathbf{d}_{n+1-\alpha_{\mathsf{f}}})}{\partial \mathbf{d}_{n+1}}\right|^i . \tag{3.43}$$

Equilibrium is achieved if

$$\mathrm{Lin}\,\mathbf{r}_{\mathsf{S}}(\mathbf{d}^i_{n+1}) \;\overset{!}{=}\; \mathbf{0}\,, \tag{3.44}$$

so that a linear system of equation is given by

$$\mathbf{K}_{\mathsf{SS}}(\mathbf{d}^i_{n+1})\,\Delta\mathbf{d}^{i+1}_{n+1} \;=\; -\mathbf{r}_{\mathsf{S}}(\mathbf{d}^i_{n+1})\,. \tag{3.45}$$

Thus, a new solution of the displacement increment $\Delta\mathbf{d}^{i+1}_{n+1}$ for current iteration step $i+1$ is determined, and the final displacement solution of time step $n+1$ is obtained via updating

$$\mathbf{d}^{i+1}_{n+1} \;=\; \mathbf{d}^i_{n+1} \;+\; \Delta\mathbf{d}^{i+1}_{n+1}\,. \tag{3.46}$$

A solution of t_{n+1} is found, i.e. an equilibrium state is reached and $\mathbf{d}_{n+1} = \mathbf{d}^{i+1}_{n+1}$, if prescribed, user-defined convergence criteria are fulfilled. Hence, the calculation of (3.45) and (3.46) is repeated until the following conditions are fulfilled, i.e.

$$||\mathbf{r}_{\mathsf{S}}(\mathbf{d}^{i+1}_{n+1})|| \;<\; \epsilon_{\mathsf{tol;r}}\,, \quad ||\mathbf{d}^{i+1}_{n+1} \;-\; \mathbf{d}^i_{n+1}|| \;=\; ||\Delta\mathbf{d}^{i+1}_{n+1}|| \;<\; \epsilon_{\mathsf{tol;d}}\,, \tag{3.47}$$

where $\epsilon_{\mathsf{tol;r}}$ and $\epsilon_{\mathsf{tol;d}}$ are the user-defined convergence tolerances for the residual and the displacement increment, respectively. Commonly, a L^2-norm is chosen for convergence, but in general the criteria have to be chosen for each problem separately. For instance, it can be more appropriate to use a L^1 or a L^∞-norm, or to choose relative norms, as e.g. a relative norm for the residual with respect to the initial residual of step $i = 0$, i.e.

$$\frac{||\mathbf{r}_{\mathsf{S}}(\mathbf{d}^{i+1}_{n+1})||}{||\mathbf{r}_{\mathsf{S}}(\mathbf{d}^{i=0}_{n+1})||} \;<\; \epsilon_{\mathsf{tol;r}}\,. \tag{3.48}$$

It is worth noting, that the convergence criterion is an important task. Exemplarily, for a given problem, it can be sufficient to reduce relatively the residual by six order of magnitude, i.e. in (3.48) $\epsilon_{\mathsf{tol;r}} = 10^{-6}$. In contrast, other problems exist where the converged state utilising this relative criterion cannot be identified with an equilibrium state, so that an absolute criterion, as e.g. $(3.47)_1$ is more appropriate. Moreover, in case of very small initial norms (e.g. $||\mathbf{r}_{\mathsf{S}}(\mathbf{d}^{i=0}_{n+1})|| = 10^{-8}$), relative reduction by six order of magnitude cannot be reached, because current computers can handle in total only 16 numbers of decimal places. Consequently, before starting a simulation the convergence criteria should be treated very carefully.

For the application of exact Newton methods in conjunction with a consistent linearisation and good initial estimates chosen sufficiently close to the actual solution, the method converges quadratically. Consistent linearisation comprises the calculation of the tangential stiffness matrix in each iteration step as shown in (3.45) which can possibly leads to expensive simulations with high computational costs especially for large systems of equations with large numbers of DOFs. Hence, various alternative approaches exist, as e.g. quasi-Newton methods or modified Newton

methods, which are based on cheaper approximations of the stiffness matrix with the expense of the quadratic convergence behaviour. Beyond, strategies to enlarge the convergence radius are invented as the pseudo-transient continuation (ψTC) strategy for structural dynamics, see Gee et al. [46], which aims at higher robustness and possibly larger time steps compared to the exact Newton method with the expense of velocity. In summary, to achieve optimal convergence in a relative short time, exact Newton methods are exclusively applied in the present work.

3.4 Constitutive laws for the structural field

Previously, all basics for solving nonlinear structural dynamics with the FEM and a Newton-Raphson scheme have been presented. The only remaining open issue is the determination of the stresses to close the given structural problem. Hence, in the following, constitutive laws for isotropic, elastic as well as elastoplastic solids will be presented. Due to the exclusive use of isotropic materials, the thermodynamic principle of material symmetry is fulfilled, see section 2.4.1. Newton's method is utilised, thus the consistent linearisation of the stresses has to be performed and the so-called fourth-order material tangent $\mathscr{C}_{\mathsf{mat}}$ is obtained. Exemplarily, based on the second Piola-Kirchhoff stress tensor (2.96), the material tangent follows by

$$\mathscr{C}_{\mathsf{mat}} \;=\; \frac{\partial \boldsymbol{S}}{\partial \boldsymbol{E}_{\mathsf{GL}}} \;=\; \rho_0 \, \frac{\partial^2 \psi}{\partial \boldsymbol{E}_{\mathsf{GL}} \, \partial \boldsymbol{E}_{\mathsf{GL}}} \;=\; 2 \, \rho_0 \, \frac{\partial^2 \psi}{\partial \boldsymbol{C} \, \partial \boldsymbol{C}} \, . \tag{3.49}$$

Subsequently, stresses and their corresponding material tangent are specified for the two cases of elastic and elastoplastic materials, respectively.

3.4.1 Elasticity

Perfect elastic materials are described by (2.84) for the case that the inequation is equal to zero, i.e. the material version of (2.84) leads to

$$\mathcal{D}_{\mathsf{mech}} \;=\; \boldsymbol{S} : \dot{\boldsymbol{E}}_{\mathsf{GL}} \;-\; \rho_0 \, \dot{\psi} \;=\; \boldsymbol{S} : \frac{1}{2} \, \dot{\boldsymbol{C}} \;-\; \rho_0 \, \dot{\psi} \;=\; 0 \, , \tag{3.50}$$

where the existence of the thermodynamic potential ψ per unit reference volume is assumed. Consequently, so-called green-elastic or hyperelastic materials are presented, where a strain energy density function (SEF) Ψ is introduced by $\Psi := \rho_0 \, \psi$. For further details on SEF, the reader is referred, e.g. to Holzapfel [58] and Doll and Schweizerhof [35]. Exemplarily, two isotropic elastic constitutive models are presented, namely the Saint Venant-Kirchhoff (abbreviated to SVK) material and a compressible hyperelastic material model according to Simo and Miehe [122] (abbreviated to ESIMO). The SVK material is an isotropic, hyperelastic model based on the Helmholtz free energy

$$\rho_0 \, \psi_{\mathsf{SVK}}(\boldsymbol{E}_{\mathsf{GL}}) \;=\; \Psi_{\mathsf{SVK}}(\boldsymbol{E}_{\mathsf{GL}}) \;=\; \mu \, \boldsymbol{E}_{\mathsf{GL}} : \boldsymbol{E}_{\mathsf{GL}} \;+\; \frac{\lambda}{2} \, (\operatorname{tr} \boldsymbol{E}_{\mathsf{GL}})^2 \tag{3.51}$$

with the Lamé constants λ and μ, which can be expressed by

$$\mu \;=\; \frac{E}{2 \, (1 \,+\, \nu)} \, , \quad \lambda \;=\; \frac{E \, \nu}{(1 \,+\, \nu) \, (1 \,-\, 2 \, \nu)} \tag{3.52}$$

using Young's modulus and Poisson's ratio, E and ν, respectively. In contrast, the ESIMO material is an isotropic, hyperelastic model which is based on the Helmholtz free energy

$$\rho_0\,\psi_{\mathsf{ESIMO}}(\boldsymbol{C}) \;=\; \Psi_{\mathsf{ESIMO}}(\boldsymbol{B}) \;=\; \frac{K}{2}\left(\frac{1}{2}\,(J^2\,-\,1)\,-\,\ln J\right)\,+\,\frac{\mu}{2}\,(\operatorname{tr}\tilde{\boldsymbol{B}}\,-\,3)\,. \tag{3.53}$$

It is noted, that in contrast to Simo and Miehe [122], in the present work the pre-factor of the first term in (3.53) is assumed to $\frac{K}{2}$. Thus, for an one-dimensional analysis Hooke's law is recovered, which will be shown in section 7.1.1. Inserting the time derivation of (3.51) or (3.53) into (3.50) and assuming strain rates unequal to zero, (2.96) is recovered. Since (3.53) is described in the current deformation tensor $\boldsymbol{B}$, the Kirchhoff-stresses $\boldsymbol{\tau}_{\mathsf{ESIMO}}$ are determined by

$$\boldsymbol{\tau}_{\mathsf{ESIMO}} \;=\; 2\,\rho_0\,\frac{\partial\psi}{\partial\boldsymbol{B}} \;=\; \frac{K}{2}\,(J^2\,-\,1)\,\boldsymbol{I}\,+\,\mu\,\operatorname{dev}\tilde{\boldsymbol{B}}\,, \tag{3.54}$$

where (2.98) and (B.28) are used. Via pull-back of (3.54) the second Piola-Kirchhoff stresses are obtained. Consequently, the second Piola-Kirchhoff stresses are given for the two material models by:

$$\boldsymbol{S}_{\mathsf{SVK}} \;=\; 2\,\mu\,\boldsymbol{E}_{\mathsf{GL}}\,+\,\lambda\,\operatorname{tr}\boldsymbol{E}_{\mathsf{GL}}\,\boldsymbol{I}\,, \tag{3.55}$$

$$\boldsymbol{S}_{\mathsf{ESIMO}} \;=\; \boldsymbol{F}^{-1}\cdot\boldsymbol{\tau}_{\mathsf{ESIMO}}\cdot\boldsymbol{F}^{-\mathsf{T}} \;=\; \frac{K}{2}\,(J^2\,-\,1)\,\boldsymbol{C}^{-1}\,+\,\mu\,\boldsymbol{F}^{-1}\cdot(\operatorname{dev}\tilde{\boldsymbol{B}})\cdot\boldsymbol{F}^{-\mathsf{T}}\,. \tag{3.56}$$

Equation (3.55) shows that for the SVK material the second Piola-Kirchhoff stress depends linearly on the Green-Lagrange strain. In contrast, the Simo material (3.56) describes a nonlinear relation between stress and strain.

According to section 2.1.3, the deformation gradient $\boldsymbol{F}$ and the right Cauchy-Green deformation tensor $\boldsymbol{C}$ can be multiplicatively split, see (2.35) and (2.38). Similarly, e.g. for the Simo material, the potential (3.53) can also be split into these two contributions, yielding

$$\psi_{\mathsf{ESIMO}}(\boldsymbol{C}) \;=\; \underbrace{\psi_{\mathsf{ESIMO;iso}}(\tilde{\boldsymbol{C}})}_{\frac{1}{\rho_0}\,\hat{\mathbb{W}}(\tilde{\boldsymbol{C}})} + \underbrace{\psi_{\mathsf{ESIMO};v}(J)}_{\frac{1}{\rho_0}\,\hat{\mathbb{U}}(J)}\,, \tag{3.57}$$

where $\hat{\mathbb{U}}$ and $\hat{\mathbb{W}}$ are the volumetric and isochoric SEFs, respectively, for hyperelastic materials. Moreover, isochoric, deviatoric stresses and volumetric stresses follow as

$$\boldsymbol{S}_{\mathsf{ESIMO}} \;=\; \boldsymbol{S}_{\mathsf{ESIMO;iso}}(\tilde{\boldsymbol{C}}) \;+\; \boldsymbol{S}_{\mathsf{ESIMO};v}(J)\,, \tag{3.58}$$

and finally, the material tangent $\mathscr{C}_{\mathsf{mat}}$ is obtained equally.

3.4.2 Elastoplasticity

In section 2.4.2, the motivation for the constitutive theory has been drawn using the simple example of a steel bar subjected to an axial load. If the bar has been subjected to a larger axial strain and does not reach its initial state after unloading, the elasticity theory does no longer capture the observed deformation behaviour. Consequently, plasticity has to be included. In a first step, small strain elastoplasticity will be presented. For this case, the basic concepts of

plasticity will be explained. Subsequently, this small strain elastoplastic material is extended to continuum damage mechanics (CDM) and finally, a finite strain elastoplastic material model will be established.

In the context of plasticity, the second law of thermodynamics is no longer described by an equation (3.50), but via an inequality, e.g. in form of the material Clausius-Planck inequality obtained as pull-back of (2.84), yielding

$$\mathcal{D}_{\mathsf{mech}} = \boldsymbol{S} : \dot{\boldsymbol{E}} - \rho_0 \dot{\psi} \geq 0 \,. \tag{3.59}$$

3.4.2.1 Theory of plasticity

This section introduces the theory of plasticity. Following Hill [57], the theory of plasticity is defined as the mathematical study of stress and strain in plastically deformed solids, especially metals. Metals are part of crystalline materials, hence in a microscopic approach plasticity is caused by dislocations or movements of atomic layers relatively to each other, as depicted in Figure 3.1 for infinitesimal deformations. Here, the initially unloaded state is described by a

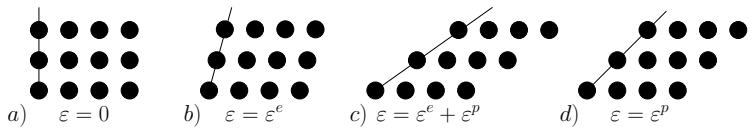

Figure 3.1: Dislocation of atomic layers for infinitesimal strains.

strain state $\varepsilon = 0$. Due to an applied load, the body deforms with an elastic strain ε^e. This load state is fully reversible, so that after unloading, the initial state $\varepsilon = 0$ is recovered. If a certain limit is exceeded, plastic deformations start to arise which is described by $\varepsilon^e + \varepsilon^p$ and shown in the Figure 3.1 $c)$. If the body is unloaded at this point, the initial state $\varepsilon = 0$ is not recovered. In contrast, the plastic strains ε^p describe the remaining, irreversible deformation of the body, see Figure 3.1 $d)$.

One-dimensional small strain elastoplastic model

In the present thesis, however, in contrast to a microscopic approach a continuum macroscopic (phenomenological) approach is pursued. Following the macroscopic procedure, internal variables are introduced to model the plasticity. To introduce the macroscopic procedure, a typical stress-strain curve of a steel bar under uniaxial tension is depicted in Figure 3.2. Due to the uniaxial load, it is allowed to reduce the fully three-dimensional problem to an one-dimensional one, where the scalar-valued strain and stress, ε and σ, respectively, are introduced. To restrict the introduction to the essential features of plasticity, the simple infinitesimal theory, i.e. the special case of small strains (see section 2.5) is assumed. Subsequently, in the infinitesimal strain case, the infinitesimal strain tensor ε replaces the deformation gradient $\boldsymbol{F}$ and the linearised stress tensor $\sigma_{\mathsf{lin}} = \sigma(\varepsilon)$ replaces the first Piola-Kirchhoff tensor $\boldsymbol{P}$. For the sake of lucidity, the index lin is omitted in the linearised stress tensor. The bar is subjected to an increasing load, so that the stress-free initial configuration (i.e. $\sigma = \varepsilon = 0$) is deformed. The behaviour can be described with linear elasticity until the stress $\sigma_{\mathsf{y};0}$ is reached, which is known as initial yield stress, and which marks the elastic limit. Further increase of load can be realized by plastic deformations

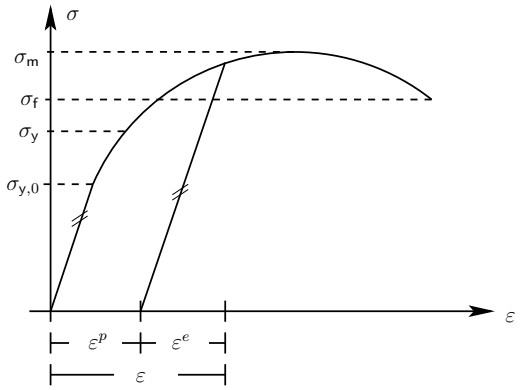

Figure 3.2: Characteristic stress-strain curve of steel bar.

ε^p, and material hardening possibly starts. The load can be increased until a maximal stress is reached, the so-called maximal tensile strength σ_m. Although stretching of the bar is still possible (ε is still increasing), softening takes place, i.e. the stress decreases, which is observable in experiments by necking of the steel bar. Softening occurs until a maximal strain ε_f is reaches and the bar fails. The stress at the failure point is denoted the failure stress σ_f.

Unloading of the bar during hardening shows elastic behaviour, which is depicted in Figure 3.2 by the two small lines indicating parallel elastic branches. As soon as the body is fully unloaded, the remaining strains ε^p are the permanent, irreversible part of the deformation. Motivated by Figure 3.2, the total strain ε can be additively split into fully reversible, elastic and irreversible, plastic strains, ε^e and ε^p, respectively, as

$$\varepsilon \;=\; \varepsilon^e \;+\; \varepsilon^p \,. \tag{3.60}$$

Following the well-known elastic uniaxial constitutive relation (Hooke's law), the stress can be expressed as

$$\sigma \;=\; E\,\varepsilon^e \;=\; E\,(\varepsilon \;-\; \varepsilon^p)\,, \tag{3.61}$$

where the additive split (3.60) and Young's modulus E are used. In order to define a constitutive model, phenomenological aspects need to be mathematically introduced into the model by appropriate equations. Previously, in the context of Figure 3.2, the existence of an elastic domain has been postulated which is delimited by the yield stress σ_y. With the introduction of the yield function Φ of the form

$$\Phi(\sigma, \sigma_\mathsf{y}) \;=\; |\sigma| \;-\; \sigma_\mathsf{y}\,, \tag{3.62}$$

the elastic domain can be defined for one-dimensional elastoplasticity by

$$\mathcal{E} \;=\; \{\sigma \,|\, \Phi(\sigma, \sigma_\mathsf{y}) \;<\; 0\} \tag{3.63}$$

with the boundary of the surface ($\Phi = 0$) denoted the so-called yield surface. It should be noted here, that a stress state above the current yield stress is plastically not admissible, i.e. stress states which lie inside the elastic domain ($\Phi < 0$) or on the boundary ($\Phi = 0$) are only admissible. Thus, the following restriction

$$\Phi(\sigma, \sigma_\mathsf{y}) \;\leq\; 0 \tag{3.64}$$

has to be satisfied. For a current stress state below the yield stress, which lies within the elastic domain, the plastic load state does not change, which can be expressed by

$$\Phi(\sigma, \sigma_{\mathsf{y}}) \, < \, 0 \quad \text{for} \quad \dot{\varepsilon}^p \, = \, 0 \, , \tag{3.65}$$

i.e. only elastic strains arise. The other plastically admissible load state is described by $\Phi = 0$, i.e. a stress state on the boundary, which can either describe elastic unloading and neutral loading or plastic loading. Hence, according to (3.65) this postulates

$$\Phi(\sigma, \sigma_{\mathsf{y}}) \, = \, 0 \quad \text{for} \quad \begin{cases} \dot{\varepsilon}^p \, = \, 0 & \text{: elastic unloading, neutral loading} \\ \dot{\varepsilon}^p \, \neq \, 0 & \text{: plastic loading} \end{cases} . \tag{3.66}$$

Equations (3.65) and (3.66) define the so-called yield criterion, because they define conditions when plastic straining occurs, i.e. $\dot{\varepsilon}^p \neq 0$. Assuming that under tension $\dot{\varepsilon}^p$ is positive and under compression negative, the so-called plastic flow rule can be established as

$$\dot{\varepsilon}^p \, = \, \dot{\gamma} \, \mathrm{sign}(\sigma) \, , \tag{3.67}$$

where sign denotes the signum function

$$\mathrm{sign}(\sigma) \, = \, \begin{cases} +1 \, \text{if} \, \sigma \, \geq \, 0 \\ -1 \, \text{if} \, \sigma \, < \, 0 \end{cases} , \tag{3.68}$$

and $\dot{\gamma}$ denotes the plastic multiplier. The plastic multiplier is non-negative, has to obey

$$\dot{\gamma} \, \leq \, 0 \, , \tag{3.69}$$

and has to satisfy the so-called complimentary equation $\dot{\Phi} \, \dot{\gamma} \, = \, 0$, which implies under plastic yielding (i.e. $\dot{\gamma} > 0$), the consistency condition

$$\dot{\Phi} \, = \, 0 \, . \tag{3.70}$$

The consistency condition guarantees, that in a plastic load step the stress state persists on the boundary of the yield surface. Consequently, equations (3.67), (3.69), (3.70) are used to define the loading/unloading conditions of an elastoplastic model also known as the Kuhn-Tucker conditions

$$\Phi \, \leq \, 0 \, , \quad \dot{\gamma} \, \geq \, 0 \, , \quad \Phi \, \dot{\gamma} \, = \, 0 \, . \tag{3.71}$$

Finally, to complete the basics of an uniaxial elastoplastic model, a hardening law has to be introduced, as shown in Figure 3.2: the yield stress σ_{y} is steadily increasing with the applied load from the initial value $\sigma_{\mathsf{y};0}$. Hence, so-called isotropic hardening occurs, which is expressed by an increasing yield stress while plastic strains evolve, i.e.

$$\sigma_{\mathsf{y}} \, = \, \sigma_{\mathsf{y}}(\bar{\varepsilon}^p) \, := \, \sigma_{\mathsf{y};0} \, + \, \kappa(\bar{\varepsilon}^p) \, , \tag{3.72}$$

where, according to (2.101), the scalar-valued thermodynamic force associated to isotropic hardening denotes κ and the scalar-valued internal variable is the accumulated plastic strain $\bar{\varepsilon}^p$. To fulfil the consistency condition (3.70), the derivative of the yield function (3.62) is taken as

$$\dot{\Phi} \, = \, \mathrm{sign}(\sigma) \, \dot{\sigma} \, - \, H^{\mathsf{iso}} \, \dot{\bar{\varepsilon}}^p \tag{3.73}$$

with the rate of the accumulated plastic strain $\dot{\bar{\varepsilon}}^p$, the isotropic hardening modulus H^{iso}, and the stress rate $\dot{\sigma}$, which are introduced by

$$\dot{\bar{\varepsilon}}^p = \dot{\gamma}\,, \tag{3.74}$$

$$H^{\mathsf{iso}} = H^{\mathsf{iso}}(\bar{\varepsilon}^p) = \frac{\mathrm{d}\sigma_{\mathsf{y}}}{\mathrm{d}\bar{\varepsilon}^p}\,, \tag{3.75}$$

$$\dot{\sigma} = E\,(\dot{\varepsilon} - \dot{\varepsilon^p}) =: E^{ep}\,\dot{\varepsilon}\,, \tag{3.76}$$

respectively. In (3.76), E^{ep} is the elastoplastic tangent modulus which relates the total strain rates $\dot{\varepsilon}$ with the total stress rate $\dot{\sigma}$ and which describes the slope of the stress-strain curve, e.g. in Figure 3.2. Since E^{ep} follows from the time continuous settings, it is frequently referred to as the continuum elastoplastic tangent modulus. Using the aforementioned relations, the plastic multiplier is determined by

$$\dot{\gamma} = \frac{E}{E + H^{\mathsf{iso}}}\,\mathrm{sign}(\sigma)\,\dot{\varepsilon} = \frac{E}{E + H^{\mathsf{iso}}}\,|\dot{\varepsilon}|\,, \tag{3.77}$$

where use has been made of (3.67), (3.68), and (3.74). Combining (3.76) and (3.77), the elastoplastic tangent is specified to

$$E^{ep} = \frac{E\,H^{\mathsf{iso}}}{E + H^{\mathsf{iso}}}\,. \tag{3.78}$$

So-called isotropic strain hardening can easily be included in the model by replacing, e.g. in (3.62) the constant value σ_{y} with $\sigma_{\mathsf{y}}(\bar{\varepsilon}^p)$. In contrast, isotropic work hardening exists which will not be used in the present work. For further insight, see e.g. de Souza Neto et al. [33].

Three-dimensional small strain elastoplastic model

The plasticity theory derived previously for the one-dimensional case can directly be extended to the general three-dimensional case. First, the scalar-valued strain ε is replaced with the total strain tensor $\boldsymbol{\varepsilon}$, see (2.107). According to (3.60), $\boldsymbol{\varepsilon}$ can be additively split into elastic and plastic strains as

$$\boldsymbol{\varepsilon} = \boldsymbol{\varepsilon}^e + \boldsymbol{\varepsilon}^p\,. \tag{3.79}$$

In compliance with (2.108) and (2.109), the infinitesimal elastic strains $\boldsymbol{\varepsilon}^e$ are additively split into isochoric deviatoric and volumetric contributions, $\boldsymbol{\varepsilon}^e_d$ and $\boldsymbol{\varepsilon}^e_v$, respectively. A thermodynamic potential ψ is assumed, based on section 2.4.4 and (2.89), to

$$\psi(\boldsymbol{\varepsilon}, \boldsymbol{\varepsilon}^p, \bar{\varepsilon}^p)\,, \tag{3.80}$$

where the general internal variables are specified to

$$\boldsymbol{\alpha}_{\mathsf{k}} = \{\boldsymbol{\varepsilon}^p, \bar{\varepsilon}^p\}\,. \tag{3.81}$$

Moreover, it is common to assume that

$$\psi = \psi^e(\boldsymbol{\varepsilon}^e) + \psi^p(\boldsymbol{\alpha}_{\mathsf{k}})\,, \tag{3.82}$$

motivated, e.g. by (3.57) or (3.79), i.e. the elastic contribution ψ^e depends only on the elastic strains, whereas the internal variables appear only in the plastic part ψ^p. Subsequently, the potential is inserted into (2.92) including (2.101), (3.79), (3.81), and (3.82), yielding

$$\left(\boldsymbol{\sigma} \,-\, \rho_0 \,\frac{\partial \psi^e}{\partial \boldsymbol{\varepsilon}^e}\right) : \dot{\boldsymbol{\varepsilon}}^e \,+\, \boldsymbol{\sigma} : \dot{\boldsymbol{\varepsilon}}^p \,-\, \kappa\, \dot{\bar{\varepsilon}}^p \,\geq\, 0\,. \tag{3.83}$$

Herein, based on (2.108), the strain rate is split additively, i.e.

$$\dot{\boldsymbol{\varepsilon}} \,=\, \dot{\boldsymbol{\varepsilon}}^e \,+\, \dot{\boldsymbol{\varepsilon}}^p\,, \tag{3.84}$$

so that, as in (2.97), the stress is determined by

$$\boldsymbol{\sigma} \,=\, \rho_0 \,\frac{\partial \psi}{\partial \boldsymbol{\varepsilon}^e} \,=\, \rho_0 \,\frac{\partial \psi^e}{\partial \boldsymbol{\varepsilon}^e}\,. \tag{3.85}$$

Furthermore, the general thermodynamic forces (2.101) are specified to

$$\boldsymbol{A}_{\mathsf{k}} = \{-\boldsymbol{\sigma}, \kappa\}\,, \tag{3.86}$$

where $-\boldsymbol{\sigma}$ and κ denote the thermodynamical forces conjugate to $\boldsymbol{\varepsilon}^p$ and $\bar{\varepsilon}^p$, respectively, so that the dissipation inequality (2.102) or for the present case (3.83) reduces to

$$\boldsymbol{\sigma} : \dot{\boldsymbol{\varepsilon}}^p \,-\, \kappa\, \dot{\bar{\varepsilon}}^p \,\geq\, 0\,. \tag{3.87}$$

Moreover, the yield function (3.62) is extended to the general three-dimensional case

$$\Phi(\boldsymbol{\sigma}, \boldsymbol{A}_{\mathsf{k}})\,, \tag{3.88}$$

now depending on the stress tensor $\boldsymbol{\sigma}$ and the set of forces $\boldsymbol{A}_{\mathsf{k}}$ associated to $\boldsymbol{\alpha}_{\mathsf{k}}$. The Kuhn-Tucker conditions (3.71) remains valid for the three-dimensional case and the elastic domain (3.63) is extended to

$$\mathcal{E} \,=\, \{\boldsymbol{\sigma} \,|\, \Phi(\boldsymbol{\sigma}, \boldsymbol{A}_{\mathsf{k}}) \,<\, 0\}\,, \tag{3.89}$$

where the yield surface describes the boundary of $\mathcal{E}$ via $\Phi(\boldsymbol{\sigma}, \boldsymbol{A}_{\mathsf{k}}) \,=\, 0$. To determine the internal variables, evolution equations are required, see $(2.105)_1$. The existence of the complementary dissipation potential ϕ^* is postulated to $\phi^* = \phi^*(\boldsymbol{\sigma}, \boldsymbol{A}_{\mathsf{k}})$. Since for the present work associative plasticity is assumed, the yield function and the dissipation potential coincide, i.e.

$$\phi^* = \phi^*(\boldsymbol{\sigma}, \boldsymbol{A}_{\mathsf{k}}) \,\equiv\, \Phi(\boldsymbol{\sigma}, \boldsymbol{A}_{\mathsf{k}})\,. \tag{3.90}$$

Associative plasticity is a valid assumption for various plasticity models and especially for the application to metals, as stated, e.g. in de Souza Neto et al. [33], Hill [57], and Simo and Hughes [120]. In contrast, non-associative plasticity models assume the dissipation potential to be unequal to the yield function, i.e. $\phi^* \,\neq\, \Phi$. For instance, associative plasticity guarantees that the plastic strain rate tensor $\dot{\boldsymbol{\varepsilon}}^p$ is normal to the yield surface in the stress space, see section 2.4.4 and depicted later on in Figure 3.3 (right). Furthermore, it can be shown, that associative laws can be derived from the so-called principle of maximum plastic dissipation. It postulates that a given state described by $(\boldsymbol{\sigma}, \boldsymbol{A}_{\mathsf{k}})$ maximises the dissipation function (2.103) or (3.87) for given rates of internal variables.

Based on (3.90), the plastic flow rule (3.67) and analogously the evolution equations for the internal variables for fully three-dimensions follow as

$$\dot{\boldsymbol{\varepsilon}}^p \;=\; \dot{\gamma}\,\boldsymbol{N}\,, \tag{3.91}$$

$$\dot{\boldsymbol{\alpha}}_{\mathsf{k}} \;=\; \dot{\gamma}\,\boldsymbol{H}\,, \tag{3.92}$$

where the flow vector $\boldsymbol{N}$ and the general hardening modulus $\boldsymbol{H}$ are defined by

$$\boldsymbol{N} \;=\; \boldsymbol{N}(\boldsymbol{\sigma}, \boldsymbol{A}_{\mathsf{k}}) \;:=\; \frac{\partial \Phi}{\partial \boldsymbol{\sigma}}\,, \tag{3.93}$$

$$\boldsymbol{H} \;=\; \boldsymbol{H}(\boldsymbol{\sigma}, \boldsymbol{A}_{\mathsf{k}}) \;:=\; -\frac{\partial \Phi}{\partial \boldsymbol{A}_{\mathsf{k}}}\,, \tag{3.94}$$

respectively. Specifying (3.92) for the internal variable $\dot{\varepsilon}^p$, the evolution equation yields $\dot{\varepsilon}^p = \dot{\gamma}$, i.e. (3.74) is recovered. Based on (3.76), the rate equation for the three-dimensional case reads

$$\dot{\boldsymbol{\sigma}} \;=\; \mathscr{C}^{ep}_{\mathsf{mat;c}} : \dot{\boldsymbol{\varepsilon}}\,, \tag{3.95}$$

where the three-dimensional continuum elastoplastic tangent modulus $\mathscr{C}^{ep}_{\mathsf{mat;c}}$ is included. Since $\mathscr{C}^{ep}_{\mathsf{mat;c}}$ is achieved from the time-continuum settings, the index c emphasizes the time-continuum tangent, in contrast to the consistent tangent operator which will be derived in section 3.4.2.2 based on the fully discretised equations.

Von Mises plasticity

Various approaches to model a phenomenological yield criterion in metal plasticity are available in literature, e.g. Drucker and Prager [37], Tresca [134], von Mises [140], or the Mohr-Coulomb model, see e.g. Crisfield [27]. Due to its simplicity, the so-called von Mises model, proposed by von Mises [140], is very common and hence will be applied in this work. Based on observed deformation behaviour of most metals whose volume remains constant during plastic yielding, the von Mises yield criterion assumes that plastic yielding depends only on the deviatoric part of the stress. This can be expressed with the second invariant of the stress deviator J_2 (see (B.23)) and the yield criterion is specified to

$$\Phi \;=\; \sqrt{3\,J_2(\boldsymbol{s})} \;-\; \sigma_{\mathsf{y}} \;=\; \sqrt{\frac{3}{2}\,(\boldsymbol{s} : \boldsymbol{s})} \;-\; \sigma_{\mathsf{y}} \;=\; \sqrt{\frac{3}{2}}\,||\boldsymbol{s}|| \;-\; \sigma_{\mathsf{y}}\,, \tag{3.96}$$

where $||\cdot||$ denotes the L^2-norm and $\boldsymbol{s}$ denotes the stress deviator (2.49). Accordingly, the von Mises yield criterion is also known as J_2-plasticity. The equivalent von Mises stress can be defined as

$$q \;=\; \sqrt{\frac{3}{2}}\,||\boldsymbol{s}||\,. \tag{3.97}$$

As plastic yielding is independent of the hydrostatic stresses, i.e. pressure-insensitive, plasticity depends only on the isochoric part of the deformation, so that

$$\operatorname{tr} \dot{\boldsymbol{\varepsilon}}^p \;=\; 0\,. \tag{3.98}$$

As a consequence of isochoric plasticity, it is common to split the potential into an elastic and a plastic part, compare (3.82). Subsequently, equations (3.82), (3.96), and (3.98) define the conditions of the so-called plastic incompressibility. For isotropic materials, the yield function can be stated in principle stresses denoted by σ_1, σ_2, σ_3. Thus, in the principle stress space the von Mises yield surface represents a circular cylinder with the hydrostatic axis $\sigma_1 = \sigma_2 = \sigma_3$ as its centre and the radius $r = \sqrt{\frac{2}{3}}\,\sigma_{\mathsf{y}}$, see Figure 3.3. Moreover, due to the pressure-insensitivity, the

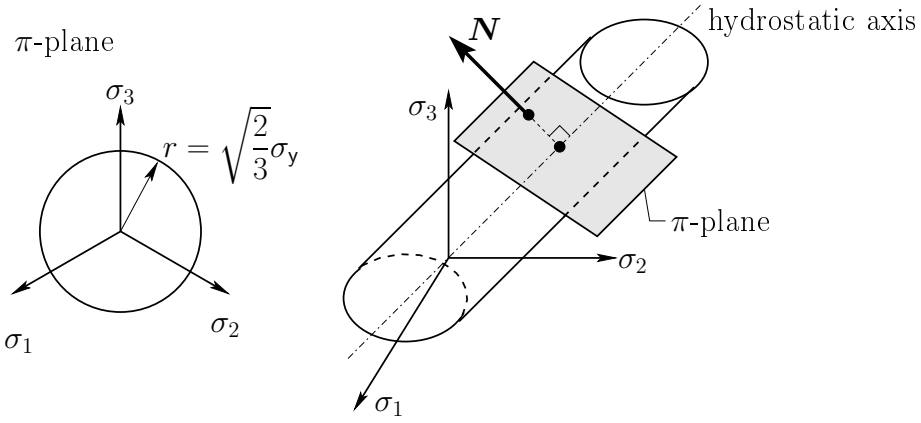

Figure 3.3: Von Mises yield surface in π-plane (left) and in principle stress space (right).

yield surface can be described by a deviatoric plane, the so-called π-plane, a plane perpendicular on the hydrostatic axis. In the π-plane, the von Mises yield surface is again represented by a circle. Hence, the advantage for computational plasticity arises because the yield surface of the von Mises criterion is smooth at each point which is, e.g. not valid for the Tresca model.

Exemplarily, the flow vector (3.93) is determined assuming the von Mises yield criterion (3.96), using $(\mathrm{C}.5)_2$, by

$$\boldsymbol{N}(\boldsymbol{\sigma}, \boldsymbol{A}_{\mathsf{k}}) \equiv \frac{\partial \Phi}{\partial \boldsymbol{\sigma}} = \frac{\partial}{\partial \boldsymbol{\sigma}} \Big[\sqrt{3\, J_2(\boldsymbol{s})} \Big] = \sqrt{\frac{3}{2}}\, \frac{\boldsymbol{s}}{||\boldsymbol{s}||}\,, \tag{3.99}$$

which is denoted the Prandtl-Reuss flow rule. This flow vector is said to be coaxial to the stress tensor $\boldsymbol{\sigma}$, i.e. the principle directions of $\boldsymbol{N}$ and $\boldsymbol{\sigma}$ coincide.

As mentioned previously in (3.72), the yield surface Φ is generally not constant, but can depend on the plastic history, i.e. hardens. Two types of hardening can be distinguished as depict in Figure 3.4: isotropic hardening and kinematic hardening. Isotropic hardening describes an extension of the yield surface, while kinematic hardening describes a translation of the yield surface. Furthermore, kinematic hardening is known as Bauschinger effect and is observed in cyclic loadings. While isotropic hardening is described by the scalar-valued thermodynamic conjugate variable κ, see (3.86), kinematic hardening is described by the tensor-valued symmetric deviatoric (stress-like) back stress $\boldsymbol{\beta}$. According to the geometric interpretation of the translation of the yield surface, $\boldsymbol{\beta}$ defines the translation of the centre of the yield surface. Finally, to conclude, in real experiments a mixture of both hardening effects occurs named mixed hardening. Apart from the two presented hardening types, a further load state is conceivable which is known as perfect plasticity. Perfect plasticity is described by a material model where the yield stress is independent of the plastic deformations and no hardening takes place. Consequently, the limit load

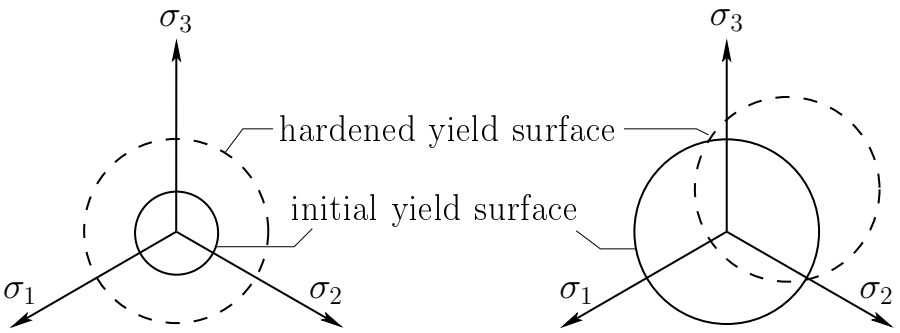

Figure 3.4: Representation of isotropic (left) and kinematic (right) hardening.

is constant and is characterized by $\sigma_{\mathrm{y};0}$. According to Figure 3.4, perfect plasticity is described by a fixed initial yield surface, or in Figure 3.2, by a horizontal stress-strain curve after passing the elastic limit.

3.4.2.2 Solution techniques for path-dependent materials

Constitutive initial value problem

In section 3.2, the continuous IBVP has been proposed which has been discretised in space and time to achieve the fully discrete equations of motion, e.g. given in terms of the one-step-θ scheme by (3.40). In case of plasticity, the deformation history further enters the IBVP. Thus, for path-dependent materials, as the present elastoplastic materials, the stress is no longer a function of the current strains only. Instead, the stress depends on the history of the strains to which the solid has been subjected. The history is introduced via the evolution equations (3.93) representing PDEs in time. Consequently, initial conditions for (3.93) are required

$$\boldsymbol{\alpha}_{\mathsf{k}}(t=0) \;=\; \boldsymbol{\alpha}_{\mathsf{k};0} \;=\; \hat{\boldsymbol{\alpha}}_{\mathsf{k};0} \quad \text{in } \Omega_0 \,. \tag{3.100}$$

As mentioned in section 3.2.2, the time continuous equations are partitioned into time intervals $[t_n, t_{n+1}]$. Equivalently, for a given time interval $[t_n, t_{n+1}]$ and a given set of interval variables $\boldsymbol{\alpha}_{\mathsf{k};n}$ at the known time t_n, the current strain tensor $\boldsymbol{\varepsilon}_{n+1}$ is used to determine the current stress tensor $\boldsymbol{\sigma}_{n+1}$ through an integration algorithm, as e.g. the Newton-Raphson scheme. For a discrete time step, the current solution $\boldsymbol{\sigma}_{n+1}$ is approximated using an incremental function $\check{\boldsymbol{\sigma}}_{n+1}$

$$\boldsymbol{\sigma}_{n+1} \;=\; \check{\boldsymbol{\sigma}}_{n+1}(\boldsymbol{\varepsilon}_{n+1}, \boldsymbol{\alpha}_{\mathsf{k};n}) \,. \tag{3.101}$$

Hence, for infinitesimal strain increments, the solution converges to the exact solution. In general, the stresses are nonlinear, whereas they can be assumed as path-independent within one time increment, because to determine $\boldsymbol{\sigma}_{n+1}$ the current strain state $\boldsymbol{\varepsilon}_{n+1}$ and the old solution of the internal variables $\boldsymbol{\alpha}_{\mathsf{k};n}$ are used.

As for the stress, the internal variables are achieved incrementally via

$$\boldsymbol{\alpha}_{\mathsf{k};n+1} \;=\; \check{\boldsymbol{\alpha}}_{\mathsf{k};n+1}(\boldsymbol{\varepsilon}_{n+1}, \boldsymbol{\alpha}_{\mathsf{k};n}) \,. \tag{3.102}$$

Introduction of the incremental functions into the element internal force vector for the infinitesimal case yields

$$\mathbf{f}^{(e)}_{\mathsf{int;S};n+1} \;=\; \int\limits_{\Omega_0^{(e)}} \delta\boldsymbol{\varepsilon}^{\mathsf{T}}_{n+1} : \check{\boldsymbol{\sigma}}_{n+1}(\boldsymbol{\varepsilon}_{n+1}, \boldsymbol{\alpha}_{\mathsf{k};n})\, \mathrm{d}V_0 \,. \tag{3.103}$$

For time discretisation of the rate quantities, included in the evolution equations (3.91) and (3.92), an implicit (backward) Euler scheme is chosen in this thesis leading to incremental quantities. Consequently, the incremental plastic multiplier $\Delta\gamma$ follows as

$$\dot{\gamma}(t) \;=\; \frac{\Delta\gamma}{\Delta t}\,, \tag{3.104}$$

which is inserted into the incremental evolution equations. Subsequently, time-discrete equations are established to determine the new unknown solution of the internal variables at time t_{n+1} by

$$\boldsymbol{\varepsilon}^{p}_{n+1} = \boldsymbol{\varepsilon}^{p}_{n} \;+\; \Delta\gamma\, \boldsymbol{N}(\boldsymbol{\sigma}_{n+1}, \boldsymbol{A}_{\mathsf{k};n+1})\,, \tag{3.105}$$

$$\boldsymbol{\alpha}_{\mathsf{k};n+1} = \boldsymbol{\alpha}_{\mathsf{k};n} \;+\; \Delta\gamma\, \boldsymbol{H}(\boldsymbol{\sigma}_{n+1}, \boldsymbol{A}_{\mathsf{k};n+1})\,. \tag{3.106}$$

Furthermore, the Kuhn-Tucker conditions in their incremental form read

$$\Phi(\boldsymbol{\sigma}_{n+1}, \boldsymbol{A}_{\mathsf{k};n+1}) \;\leq\; 0\,, \quad \frac{\Delta\gamma}{\Delta t} \;\geq\; 0\,, \quad \Phi(\boldsymbol{\sigma}_{n+1}, \boldsymbol{A}_{\mathsf{k};n+1})\, \frac{\Delta\gamma}{\Delta t} \;=\; 0\,, \tag{3.107}$$

and the thermodynamical forces are given by

$$\boldsymbol{\sigma}_{n+1} \;=\; \rho_0\, \frac{\partial\psi}{\partial\boldsymbol{\varepsilon}^{e}}\bigg|_{n+1}\,, \quad \boldsymbol{A}_{\mathsf{k};n+1} \;=\; \rho_0\, \frac{\partial\psi}{\partial\boldsymbol{\alpha}_{\mathsf{k}}}\bigg|_{n+1}\,. \tag{3.108}$$

Subsequently, using the relations above and (3.101), the associated discrete consistent material tangent is achieved as

$$\mathscr{C}_{\mathsf{mat}} \;=\; \mathscr{C}^{ep}_{\mathsf{mat}} \;\equiv\; \frac{\partial\check{\boldsymbol{\sigma}}_{n+1}}{\partial\boldsymbol{\varepsilon}_{n+1}}\bigg|_{\boldsymbol{\alpha}_{\mathsf{k};n}}\,. \tag{3.109}$$

To obtain good convergence behaviour and to preserve the quadratic rate of convergence of Newton's method, the consistent tangent operator (see Simo and Taylor [123]) is utilised based on the fully discretised incremental equations, in contrast to the continuum tangent operator $\mathscr{C}^{ep}_{\mathsf{mat;c}}$ (3.95), which is achieved from the time-continuum settings. The only difference between the two tangents lies in the terms with the incremental plastic multiplier $\Delta\gamma$, see de Souza Neto et al. [33], which emerge in the consistent tangent $\mathscr{C}^{ep}_{\mathsf{mat}}$. Especially, for large time steps with large values of the plastic multiplier $\Delta\gamma$, i.e. big differences between continuum and consistent tangent, computational time can be decisively reduced using $\mathscr{C}^{ep}_{\mathsf{mat}}$ due to a substantially faster convergence of the global Newton scheme.

Elastic predictor/plastic corrector algorithm

Due to the constraints (3.107), the solution of the incremental elastoplastic problem (3.104)-(3.108) cannot directly follow from the standard approach for IBVP. Instead a two-step algorithm, namely an elastic predictor/plastic corrector algorithm is applied, which is also known as

radial return-mapping method, originally invented by Wilkins [144] for perfect plasticity. The return-mapping algorithm is widely used in literature for elastoplasticity, see e.g. Armero and Simo [7], Caminero et al. [21], de Souza Neto et al. [33], Montáns and Bathe [95], Ortiz and Simo [101], Peric and de Souza Neto [104], Simo [118], and Simo and Taylor [123].

According to $(3.107)_2$, two values are admissible for the plastic multiplier, that is $\Delta\gamma = 0$ and $\Delta\gamma > 0$. A time interval $[t_n, t_{n+1}]$ is given and all values at time t_n are known. Subsequently, in a first step, which is named elastic trial step, the plastic multiplier is assumed to be equal to zero ($\Delta\gamma \equiv 0$), which significates that the load step is assumed to be completely elastic, and neither plastic flow ($\Delta\boldsymbol{\varepsilon}^p \equiv 0$) nor evolution of internal variables ($\Delta\boldsymbol{\alpha}_{\mathsf{k}} \equiv 0$) take place. Within the incremental equations, the rate quantities are transformed to increments, thus $\Delta(\cdot) = (\cdot)_{n+1} - (\cdot)_n$. For the determination of the trial elastic strains and the trial interval variables follows

$$\boldsymbol{\varepsilon}^{e;\mathsf{trial}}_{n+1} = \boldsymbol{\varepsilon}^{e}_{n} + \Delta\boldsymbol{\varepsilon}\,, \tag{3.110}$$

$$\boldsymbol{\varepsilon}^{p;\mathsf{trial}}_{n+1} = \boldsymbol{\varepsilon}^{p}_{n}\,, \tag{3.111}$$

$$\boldsymbol{\alpha}^{\mathsf{trial}}_{\mathsf{k};n+1} = \boldsymbol{\alpha}_{\mathsf{k};n}\,, \tag{3.112}$$

where the total strain increment for t_{n+1} is assumed to

$$\Delta\boldsymbol{\varepsilon} = \boldsymbol{\varepsilon}_{n+1} - \boldsymbol{\varepsilon}_{n}\,. \tag{3.113}$$

Hence, in the trial elastic step the stress and the thermodynamic force yield

$$\boldsymbol{\sigma}^{\mathsf{trial}}_{n+1} = \rho_0 \left.\frac{\partial\psi}{\partial\boldsymbol{\varepsilon}^e}\right|^{\mathsf{trial}}_{n+1}, \quad \boldsymbol{A}^{\mathsf{trial}}_{\mathsf{k};n+1} = \rho_0 \left.\frac{\partial\psi}{\partial\boldsymbol{\alpha}_{\mathsf{k}}}\right|^{\mathsf{trial}}_{n+1}. \tag{3.114}$$

It is noted, that the present trial state is only the actual solution if the Kuhn-Tucker condition $(3.107)_1$ holds, i.e.

$$\Phi^{\mathsf{trial}}_{n+1} \equiv \Phi(\boldsymbol{\sigma}^{\mathsf{trial}}_{n+1}, \boldsymbol{A}^{\mathsf{trial}}_{\mathsf{k};n+1}) \leq 0\,, \tag{3.115}$$

so that the stress state lies within the yield surface or on its boundary. In this case, the trial values are updated to the new values

$$(\cdot)_{n+1} := (\cdot)^{\mathsf{trial}}_{n+1}\,. \tag{3.116}$$

In contrast, if $(3.107)_1$ or (3.115) is violated, i.e. $\Phi^{\mathsf{trial}}_{n+1} > 0$, the current load step is not admissible and the second, so-called plastic corrector step or return-mapping algorithm is performed. For the return-mapping algorithm, the plastic multiplier is assumed to be greater than zero ($\Delta\gamma > 0$), so that plastic flow occurs and the interval variables change. Based on (3.105), (3.106) and the trial values (3.110)-(3.112), admissible final values at the end of the time step are computed for $\Delta\gamma > 0$ by

$$\boldsymbol{\varepsilon}^{e}_{n+1} = \boldsymbol{\varepsilon}^{e;\mathsf{trial}}_{n+1} - \Delta\gamma\,\boldsymbol{N}(\boldsymbol{\sigma}_{n+1}, \boldsymbol{A}_{\mathsf{k};n+1})\,, \tag{3.117}$$

$$\boldsymbol{\varepsilon}^{p}_{n+1} = \boldsymbol{\varepsilon}^{p;\mathsf{trial}}_{n+1} + \Delta\gamma\,\boldsymbol{N}(\boldsymbol{\sigma}_{n+1}, \boldsymbol{A}_{\mathsf{k};n+1})\,, \tag{3.118}$$

$$\boldsymbol{\alpha}_{\mathsf{k};n+1} = \boldsymbol{\alpha}^{\mathsf{trial}}_{\mathsf{k};n} + \Delta\gamma\,\boldsymbol{H}(\boldsymbol{\sigma}_{n+1}, \boldsymbol{A}_{\mathsf{k};n+1})\,, \tag{3.119}$$

where the only possible value of the yield surface arises to be

$$\Phi(\boldsymbol{\sigma}_{n+1}, \boldsymbol{A}_{\mathsf{k};n+1}) = 0 \tag{3.120}$$

for meeting the Kuhn-Tucker conditions.

To conclude, a solution of the overall elastoplastic problem is achieved, if the system of equations composed by (3.117)-(3.120) is solved. As stresses and state variables are computed at each Gauss point, an efficient solution strategy is required to circumvent high computational costs.

3.4.2.3 Small strain elastoplasticity

In the previous sections 3.4.2.1-3.4.2.2, the basics for an elastoplastic material have been introduced. In the following, a small strain elastoplastic material with mixed hardening, i.e. nonlinear isotropic and linear kinematic hardening, is presented which is based on the following potential

$$\rho_0\,\psi(\boldsymbol{\varepsilon}^e,\bar{\varepsilon}^p,\boldsymbol{Z}) \;=\; \rho_0\,\psi^e(\boldsymbol{\varepsilon}\;-\;\boldsymbol{\varepsilon}^p)\;+\;\rho_0\,\psi^p(\bar{\varepsilon}^p,\boldsymbol{Z}) \;=\; \rho_0\,\psi^e(\boldsymbol{\varepsilon}^e)\;+\;\rho_0\,\psi^p(\bar{\varepsilon}^p,\boldsymbol{Z})\,, \tag{3.121}$$

where $\boldsymbol{Z}$ is a second-order tensor-valued internal variable associated to the back stress $\boldsymbol{\beta}$ that models the kinematic hardening, while $\bar{\varepsilon}^p$ models the isotropic hardening. Hence, the internal variables and their conjugated thermodynamic forces are summarized by

$$\boldsymbol{\alpha}_{\mathsf{k}} \;=\; \{\boldsymbol{\varepsilon}^p,\boldsymbol{Z},\bar{\varepsilon}^p\}\,,\quad \boldsymbol{A}_{\mathsf{k}} \;=\; \{-\boldsymbol{\sigma},\boldsymbol{\beta},\kappa\}\,. \tag{3.122}$$

The potentials in (3.121) are specified for the present model to

$$\psi^e(\boldsymbol{\varepsilon}^e) = \psi^e_d(\boldsymbol{\varepsilon}^e_d)\;+\;\psi^e_v(\boldsymbol{\varepsilon}^e_v) \;=\; 2\,G\,\boldsymbol{\varepsilon}^e_d:\boldsymbol{\varepsilon}^e_d\;+\;K\,\boldsymbol{\varepsilon}^e_v:\boldsymbol{\varepsilon}^e_v\,, \tag{3.123}$$

$$\psi^p(\boldsymbol{Z},\bar{\varepsilon}^p) = \frac{1}{3}\,H^{\mathsf{kin}}\,\boldsymbol{Z}:\boldsymbol{Z}\;+\;\frac{1}{2}\,H^{\mathsf{iso}}\,\bar{\varepsilon}^{p\,2}\,, \tag{3.124}$$

where K and G denote the bulk and the shear modulus, respectively, and $\boldsymbol{\varepsilon}^e_d$ and ε^e_v are the deviatoric and the volumetric elastic strains, respectively, introduced in (2.109). Furthermore, the shear modulus is identical to the second Lamé constants μ (see (3.52)), i.e. $G \equiv \mu$. As for the Lamé constants (3.52), the bulk modulus can be expressed in E and ν as

$$K \;=\; \frac{E}{3\,(1\;-\;2\,\nu)}\,. \tag{3.125}$$

In (3.123), the elastic potential ψ^e is split into an elastic deviatoric and an elastic volumetric contribution according to (2.108) and (3.57). Hence, according to (3.85) using (2.48), the deviatoric stress and the hydrostatic pressure follow as

$$\boldsymbol{s} \;=\; 2\,G\,\boldsymbol{\varepsilon}^e_d\,,\quad p \;=\; K\,\varepsilon^e_v\,. \tag{3.126}$$

To approximate the nonlinear isotropic hardening, piecewise linear isotropic hardening is assumed. This means that any (arbitrary) nonlinear hardening curve can be approximated by choosing a sufficiently large number of sampling pairs $(\bar{\varepsilon}^p,\sigma_{\mathsf{y}})$ with linear interpolation between adjacent pairs. Subsequently, for a given load step the isotropic hardening slop reads

$$H^{\mathsf{iso}} := \left.\frac{\mathrm{d}\sigma_{\mathsf{y}}}{\mathrm{d}\bar{\varepsilon}^p}\right|_{\bar{\varepsilon}^p_n+\Delta\gamma}\,. \tag{3.127}$$

The yield function is determined by

$$\Phi(\boldsymbol{\sigma},\boldsymbol{\beta},\sigma_{\mathsf{y}}) \;=\; \sqrt{\frac{3}{2}}\,||(\boldsymbol{s}\;-\;\boldsymbol{\beta})||\;-\;\sigma_{\mathsf{y}} \;=\; \sqrt{\frac{3}{2}}\,||\boldsymbol{\eta}||\;-\;\sigma_{\mathsf{y}}(\bar{\varepsilon}^p) \;=\; \check{q}\;-\;\sigma_{\mathsf{y}}(\bar{\varepsilon}^p) \;\leq\; 0\,, \tag{3.128}$$

where the relative stress tensor $\boldsymbol{\eta}$ and based on (3.97), the relative effective equivalent von Mises yield stress $\check{q}$ are used. Herein,

$$\boldsymbol{\eta} \;=\; \boldsymbol{s} \;-\; \boldsymbol{\beta} \tag{3.129}$$

is deviatoric by definition, and $\check{q} = \sqrt{\frac{3}{2}}\,||\boldsymbol{\eta}||$. To satisfy the plastic consistency condition (3.70) for the yield surface (3.128), the time derivative is given by

$$\dot{\Phi} \;=\; \frac{\partial \Phi}{\partial \boldsymbol{\sigma}} : \dot{\boldsymbol{\sigma}} \;+\; \frac{\partial \Phi}{\partial \boldsymbol{\beta}} : \dot{\boldsymbol{\beta}} \;+\; \frac{\partial \Phi}{\partial \bar{\varepsilon}^p} : \dot{\bar{\varepsilon}}^p \;=\; 0\,, \tag{3.130}$$

i.e. due to the second term, an evolution equation for the back stress $\boldsymbol{\beta}$ is required. In the present model, so-called Prager-Ziegler's linear kinematic hardening law is used, which is defined as

$$\dot{\boldsymbol{\beta}} \;=\; \frac{2}{3}\, H^{\mathsf{kin}}\, \dot{\gamma}\, \check{\boldsymbol{N}} \tag{3.131}$$

with the constant linear kinematic hardening modulus H^{kin} and the unit flow vector $\check{\boldsymbol{N}} = \frac{\boldsymbol{\eta}}{||\boldsymbol{\eta}||}$. According to (3.131), the evolution law for the internal variable $\boldsymbol{Z}$ reduces to (3.91).

As explained in section 3.4.2.2, the two-step algorithm is used for the solution of the initial value problem at hand. Hence, the evolution equations have to be stated in incremental form according to (3.105) and (3.106). Moreover, the current back stresses $\boldsymbol{\beta}_{n+1}$ are determined using the incremental form of (3.131), leading to

$$\boldsymbol{\beta}_{n+1} \;=\; \boldsymbol{\beta}_n \;+\; \frac{2}{3}\, H^{\mathsf{kin}}\, \Delta\gamma\, \check{\boldsymbol{N}}_{n+1} \tag{3.132}$$

with the unit flow vector

$$\check{\boldsymbol{N}}_{n+1} \;=\; \frac{\boldsymbol{\eta}^{\mathsf{trial}}_{n+1}}{||\boldsymbol{\eta}^{\mathsf{trial}}_{n+1}||} \tag{3.133}$$

and the flow vector $\boldsymbol{N}_{n+1} \;=\; \sqrt{\frac{3}{2}}\check{\boldsymbol{N}}_{n+1}$. The present small strain elastoplastic model can be solved very efficiently. Instead of solving a system of equations in the return-mapping algorithm, the solution can be reduced to the evaluation of one single equation to determine the sole free parameter $\Delta\gamma$. For details, the interested reader is referred to, e.g. de Souza Neto et al. [33]. To determine $\Delta\gamma$, the consistency condition needs to be fulfilled for an admissible plastic state, i.e. at the end of the time step the stress state is returned to the yield surface, i.e.

$$\Phi(\Delta\gamma) \;=\; \sqrt{\frac{3}{2}}\,||\boldsymbol{\eta}^{\mathsf{trial}}_{n+1}|| \;-\; \Delta\gamma\,[3\,G \;+\; H^{\mathsf{kin}}] \;-\; \sigma_{\mathsf{y}}(\bar{\varepsilon}^p_n \;+\; \Delta\gamma) \;\stackrel{!}{=}\; 0\,, \tag{3.134}$$

where the accumulated plastic strains $\bar{\varepsilon}^p$ (3.74) are discretised using (3.104), yielding

$$\bar{\varepsilon}^p_{n+1} \;=\; \bar{\varepsilon}^p_n \;+\; \Delta\gamma\,. \tag{3.135}$$

Since (3.134) is nonlinear, a Newton-Raphson method, often denoted local Newton method, is utilised to determine $\Delta\gamma$, which is described in Algorithm 1. Based on the solution $\Delta\gamma$ computed within the local Newton, see Algorithm 1, all remaining quantities (i.e. e.g. κ_{n+1}, $\boldsymbol{\beta}_{n+1}$, $\boldsymbol{\sigma}_{n+1}$)

Algorithm 1 Local Newton-Raphson iteration algorithm for solution of the return-mapping equation of the von Mises model.

Initialise iteration index $m := 0$, set initial guess for $\Delta\gamma$
Predictor $\Delta\gamma^{m=0} := 0$
Calculate initial residual (yield function)
$r_\Phi^{m=0} := \Phi(\Delta\gamma = 0) = \sqrt{\frac{3}{2}}\,||\boldsymbol{\eta}_{n+1}^{\mathsf{trial}}|| + [3\,G + H^{\mathsf{kin}}] - \sigma_{\mathsf{y}}(\bar{\varepsilon}_n^p)$

Perform local Newton
for each iteration step $m = 0, ..., \mathsf{max}_{\mathsf{lociter}}$
Check for convergence of the local Newton
if $|r_\Phi^m| \leq \epsilon_{\mathsf{tol};p}$
finish local Newton with solution $\Delta\gamma = \Delta\gamma^m$

Calculate tangent/residual derivative: $K^m := \frac{\mathrm{d}r_\Phi^m}{\mathrm{d}\Delta\gamma^m}$
Update plastic multiplier: $\Delta\gamma^{m+1} := \Delta\gamma^m - \frac{r_\Phi^m}{K^m}$
Update accumulated plastic strain: $\bar{\varepsilon}_{n+1}^p = \bar{\varepsilon}_n^p + \Delta\gamma^{m+1}$

Calculate updated residual
$r_\Phi^{m+1} = \sqrt{\frac{3}{2}}\,||\boldsymbol{\eta}_{n+1}^{\mathsf{trial}}|| - \Delta\gamma^{m+1}\,[3\,G + H^{\mathsf{kin}}] - \sigma_{\mathsf{y}}(\bar{\varepsilon}_{n+1}^p)$

Update local Newton-Raphson iteration step $m = m + 1$

are updated to the final quantities at t_{n+1}. For instance the final result of stresses $\boldsymbol{\sigma}_{n+1}$ is based on the final deviatoric stresses, which are computed according to

$$\boldsymbol{s}_{n+1} = \boldsymbol{s}_{n+1}^{\mathsf{trial}} - 2\,G\,\Delta\gamma\,\boldsymbol{N}_{n+1}\,, \tag{3.136}$$

based on (2.108), (3.117), and (3.126). The hydrostatic pressure is not influenced by plastic deformations, i.e. $p_{n+1} = p_{n+1}^{\mathsf{trial}}$, thus the final stresses follow as

$$\boldsymbol{\sigma}_{n+1} = \boldsymbol{s}_{n+1} + p_{n+1}\,\boldsymbol{I}\,. \tag{3.137}$$

In Algorithm 2, the implicit elastic predictor/return-mapping algorithm for the present linear elastoplastic material model is presented. Subsequently, as stated at the beginning of section 3.4, the material tangent (3.49) has to be computed. For the given small strain elastoplastic material model, an incremental function of the stress is considered, as stated in de Souza Neto et al. [33]:

$$\boldsymbol{\sigma}_{n+1} = \left[\boldsymbol{\mathscr{C}}_{\mathsf{mat}}^e - \hat{H}(\Phi_{n+1}^{\mathsf{trial}})\,\frac{\Delta\gamma\,6\,G^2}{\check{q}_{n+1}^{\mathsf{trial}}}\boldsymbol{\mathscr{I}}_{\mathsf{d}}\right] : \boldsymbol{\varepsilon}_{n+1}^{e,\mathsf{trial}} + \hat{H}(\Phi_{n+1}^{\mathsf{trial}})\,\frac{\Delta\gamma\,3G}{\check{q}_{n+1}^{\mathsf{trial}}}\,\boldsymbol{\beta}_n\,, \tag{3.138}$$

where intermediate solutions of the elastic trial step $(\cdot)^{\mathsf{trial}}$, the back stresses of the old time $\boldsymbol{\beta}_n$, and the deviatoric symmetric fourth-order identity tensor $\boldsymbol{\mathscr{I}}_{\mathsf{d}}$ $(\mathrm{B}.30)_1$ are used to describe the current stresses $\boldsymbol{\sigma}_{n+1}$, see (3.101). Moreover, $\boldsymbol{\mathscr{C}}_{\mathsf{mat}}^e$ is the standard elastic tangent which is based on $(3.61)_1$. Since for the solution of the plasticity, the elastic predictor/plastic corrector scheme

Algorithm 2 Fully implicit elastic predictor/plastic corrector (return-mapping) algorithm for the von Mises model.

For time t_{n+1} a strain increment $\Delta\boldsymbol{\varepsilon}$ (3.113) is given, as well as the state variables at t_n

Elastic predictor
Evaluate the elastic trial state (3.110)-(3.112) using (3.126) and (2.108):
Evaluate strains
$\boldsymbol{\varepsilon}^{e;\mathsf{trial}}_{n+1} = \boldsymbol{\varepsilon}^{e}_{n} + \Delta\boldsymbol{\varepsilon}\ , \quad \boldsymbol{\varepsilon}^{p;\mathsf{trial}}_{n+1} = \boldsymbol{\varepsilon}^{p}_{n}\ , \quad \bar{\varepsilon}^{p;\mathsf{trial}}_{n+1} = \bar{\varepsilon}^{p;\mathsf{trial}}_{n}$
Evaluate stresses
$\boldsymbol{s}^{\mathsf{trial}}_{n+1} = 2\,G\,\boldsymbol{\varepsilon}^{e;\mathsf{trial}}_{d;n+1}\,, \quad p^{\mathsf{trial}}_{n+1} = K\,\varepsilon^{e;\mathsf{trial}}_{v;n+1},$
$\boldsymbol{\beta}^{\mathsf{trial}}_{n+1} = \boldsymbol{\beta}_{n}$

Check plastic admissibility
if $\Phi^{\mathsf{trial}}_{n+1} = \sqrt{\frac{3}{2}}\,||(\boldsymbol{s}^{\mathsf{trial}}_{n+1} - \boldsymbol{\beta}^{\mathsf{trial}}_{n+1})|| - \sigma^{\mathsf{trial}}_{\mathsf{y};n+1} \leq 0$
set $(\cdot)_{n+1} = (\cdot)^{\mathsf{trial}}$ and finish material call

Return-mapping
Solve consistency condition (3.134) according to local Newton (Algorithm 1) for $\Delta\gamma$
Calculate flow vector $\boldsymbol{N}_{n+1} = \sqrt{\frac{3}{2}}\,\frac{\eta^{\mathsf{trial}}_{n+1}}{||\eta^{\mathsf{trial}}_{n+1}||}$
Update state variables
Update stresses
$\boldsymbol{s}_{n+1} = \boldsymbol{s}^{\mathsf{trial}}_{n+1} - 2\,G\,\Delta\gamma\,\boldsymbol{N}_{n+1}, \quad p_{n+1} = p^{\mathsf{trial}}_{n+1}, \quad \boldsymbol{\sigma}_{n+1} = \boldsymbol{s}_{n+1} + p_{n+1}\,\boldsymbol{I}$
$\boldsymbol{\beta}_{n+1} = \boldsymbol{\beta}^{\mathsf{trial}}_{n+1} + \frac{2}{3}\,H^{\mathsf{kin}}\,\Delta\gamma\,\boldsymbol{N}_{n+1}$
Update strains
$\boldsymbol{\varepsilon}^{e}_{n+1} = \boldsymbol{\varepsilon}^{e;\mathsf{trial}}_{n+1} - \Delta\gamma\,\boldsymbol{N}_{n+1}\,, \quad \boldsymbol{\varepsilon}^{p}_{n+1} = \boldsymbol{\varepsilon}^{p;\mathsf{trial}}_{n+1} + \Delta\gamma\,\boldsymbol{N}_{n+1}\ , \quad \bar{\varepsilon}^{p;\mathsf{trial}}_{n+1} = \bar{\varepsilon}^{p;\mathsf{trial}}_{n} + \Delta\gamma$

Finish material call

is used, the stresses are naturally formulated in the elastic trial strain measures $\boldsymbol{\varepsilon}^{e;\mathsf{trial}}_{n+1}$. In this context, the relation

$$\boldsymbol{\varepsilon}^{e;\mathsf{trial}}_{n+1} = \boldsymbol{\varepsilon}_{n+1} - \boldsymbol{\varepsilon}^{p}_{n} \tag{3.139}$$

is used for the general elastoplastic tangent modulus (3.109). Hence, the elastoplastic material tangent is determined by consistent linearisation of the stresses (3.138) with respect to $\boldsymbol{\varepsilon}^{e,\mathsf{trial}}_{n+1}$ instead of the total strains as included in (3.109). Subsequently, the consistent elastoplastic tangent reads

$$\begin{aligned}\mathscr{C}^{ep}_{\mathsf{mat}} \;=\; \mathscr{C}^{e}_{\mathsf{mat}} + \hat{H}(\Phi^{\mathsf{trial}}_{n+1})\Big[- \frac{\Delta\gamma\,6\,G^2}{\check{q}^{\mathsf{trial}}_{n+1}}\,\mathscr{I}_{\mathsf{d}} + \\ + 6\,G^2\Big(\frac{\Delta\gamma}{\check{q}^{\mathsf{trial}}_{n+1}} - \frac{1}{3\,G + H^{\mathsf{iso}} + H^{\mathsf{kin}}}\Big)\check{\boldsymbol{N}}_{n+1}\otimes\check{\boldsymbol{N}}_{n+1}\Big]\,,\end{aligned} \tag{3.140}$$

which depends on the old values of the internal variables. The Heaviside function

$$\hat{H}(\Phi^{\mathsf{trial}}_{n+1}) = \begin{cases} 1 & \text{if} \quad \Phi^{\mathsf{trial}}_{n+1} > 0 \\ 0 & \text{if} \quad \Phi^{\mathsf{trial}}_{n+1} \leq 0 \end{cases} \tag{3.141}$$

is introduced to differentiate between an elastic or neutral load step, i.e. $\hat{H}(\Phi_{n+1}^{\mathsf{trial}}) = 0$, and a plastic load step, i.e. $\hat{H}(\Phi_{n+1}^{\mathsf{trial}}) = 1$. For an elastic unloading step ($\hat{H} = 0$), the elastoplastic tangent modulus reduces to the elastic tangent modulus, so that $\mathscr{C}_{\mathsf{mat}} := \mathscr{C}^{e}_{\mathsf{mat}}$. For a plastic load step ($\hat{H} = 1$), additional linearisations have to be considered for the tangent, leading to $\mathscr{C}_{\mathsf{mat}} := \mathscr{C}^{ep}_{\mathsf{mat}}$. In summary, a solution of the material model is found applying the Algorithm 2 with the local Newton in Algorithm 1.

3.4.2.4 Small strain elastoplasticity with ductile damage

The present material model is based on the continuum damage mechanics (CDM) concept, see for instance Lemaitre [75], where an internal damage variable D is introduced which describes the effective stress density of microvoids, microcavities and microcracks. The stresses are computed according to the concept of effective stresses (see e.g. Kachanov [64]). The concept is motivated by the damage behaviour in an uniaxial tensile test: the body is loaded by a tensile force f. If a certain load limit is passed, the body starts to damage which can be observed via microvoids, mircocracks or microcavities. The stress σ characterizes a load state of the body which is defined as the ratio between applied load f and total surface A. As soon as damage evolves, the so-called damaged area A_D can be defined, which corresponds to the part of the area A which includes, e.g. microcracks. Thus, the scalar-valued damage variable is defined as

$$D = \frac{A_D}{A}\,. \tag{3.142}$$

The effective stress then follows as the ratio between applied force and load-bearing, effective area A_{eff}, i.e.

$$\sigma_{\mathsf{eff}} = \frac{f}{A - A_D} = \frac{f}{A_{\mathsf{eff}}}\,. \tag{3.143}$$

The concept of effective stress can be easily extended to the fully three-dimensional test. Since isotropic behaviour is assumed, damage evolves in each direction equally. The resulting effective, undamaged stress tensor $\boldsymbol{\sigma}_{\mathsf{eff}}$ is defined as the stress of the remaining area where the damaged area is subtracted, hence using (3.142), $\boldsymbol{\sigma}_{\mathsf{eff}}$ results in

$$\boldsymbol{\sigma}_{\mathsf{eff}} = \frac{\boldsymbol{\sigma}}{1 - D}\,. \tag{3.144}$$

In contrast, for anisotropic damage, the damage is modelled via a higher-order, i.e. either a second-order or a fourth-order, damage tensor $\boldsymbol{D}$.

Based on de Souza Neto [30], Doghri [34], and Lemaitre and Desmorat [79], the present material model is understood as an extension of the elastoplastic material model presented in section 3.4.2.3 to include CDM. Hence, in the following a ductile isotropic damage model, the so-called Lemaitre ductile damage model according to Lemaitre [75, 76, 77] and Lemaitre and Desmorat [79] is presented.

It is common to rephrase the linear elasticity (3.61) when damage is included, so that

$$\boldsymbol{\sigma} = (1 - D)\mathscr{C}^{e}_{\mathsf{mat}} : \boldsymbol{\varepsilon}^{e}\,, \tag{3.145}$$

which can be split including (2.48) and (3.126) for the damaged case into

$$\boldsymbol{s} \;=\; (1 \,-\, D)\, 2\, G\, \boldsymbol{\varepsilon}_d^e\,, \quad p \;=\; (1 \,-\, D)\, K\, \varepsilon_v^e\,. \tag{3.146}$$

The Lemaitre model is assumed to be defined in the following internal variables and their corresponding thermodynamic forces

$$\boldsymbol{\alpha}_{\mathsf{k}} \;=\; \{\boldsymbol{\varepsilon}^p, R, D\}\,, \quad \boldsymbol{A}_{\mathsf{k}} \;=\; \{-\boldsymbol{\sigma}, \kappa, -Y\}\,, \tag{3.147}$$

respectively. Herein, R denotes the scalar-valued internal variable and the conjugated scalar-valued thermodynamic force is κ which describes isotropic hardening. Furthermore, the damage is introduced into the model via the scalar variable D which is related to the damage energy release rate Y. Exemplarily, the thermodynamic potential in form of the Helmholtz free energy postulates

$$\rho_0\, \psi(\boldsymbol{\varepsilon}^e, R, D) \;=\; \rho_0\, \psi^{ed}(\boldsymbol{\varepsilon}^e, D) \;+\; \rho_0\, \psi^p(R) \tag{3.148}$$

with the elastic damaged and the plastic potential,

$$\rho_0\, \psi^{ed}(\boldsymbol{\varepsilon}^e, D) = \frac{1}{2}\, \boldsymbol{\varepsilon}^e : [(1 \,-\, D)\, \mathscr{C}^e_{\mathsf{mat}}] : \boldsymbol{\varepsilon}^e\,, \tag{3.149}$$

$$\rho_0\, \psi^p(R) = \frac{1}{2}\, H^{\mathsf{iso}}\, R^2\,, \tag{3.150}$$

respectively. As for the purely elastoplastic model in section 3.4.2.3, nonlinear isotropic hardening is approximated by assuming piecewise linear isotropic hardening. Thus, sampling pairs (R, σ_{y}) are chosen with sufficiently large number of pairs for a correct interpolation of the real nonlinear hardening behaviour. Moreover, a relation for the variables R, $\dot{\gamma}$ and $\bar{\varepsilon}^p$ is drawn by

$$R \;=\; \dot{\gamma} \;=\; (1 \,-\, D)\, \bar{\varepsilon}^p \tag{3.151}$$

with $R = \dot{\gamma} = \bar{\varepsilon}^p$ for an undamaged load step, i.e. $D \equiv 0$. Subsequently, the von Mises yield function is assumed to

$$\Phi \;=\; \sqrt{\frac{3}{2}}\, ||\boldsymbol{s}_{\mathsf{eff}}|| \,-\, \sigma_{\mathsf{y}}(R) \;=\; q_{\mathsf{eff}} \,-\, \sigma_{\mathsf{y}}(R) \;\leq\; 0\,, \tag{3.152}$$

where based on (3.144), the effective deviatoric stress and the effective von Mises equivalent stress follow as

$$\boldsymbol{s}_{\mathsf{eff}} \;=\; \frac{1}{1 \,-\, D}\, \boldsymbol{s}\,, \quad q_{\mathsf{eff}} \;=\; \sqrt{\frac{3}{2}}\, ||\boldsymbol{s}_{\mathsf{eff}}||\,, \tag{3.153}$$

respectively, and based on (3.72) the yield stress is computed by

$$\sigma_{\mathsf{y}}(R) \;=\; \sigma_{\mathsf{y};0} + \kappa(R)\,. \tag{3.154}$$

Moreover, the flow vector (3.93) yields

$$\boldsymbol{N} = \frac{\partial \Phi}{\partial \boldsymbol{\sigma}_{\mathsf{eff}}} \;=\; \sqrt{\frac{3}{2}}\, \frac{\boldsymbol{s}_{\mathsf{eff}}}{||\boldsymbol{s}_{\mathsf{eff}}||}\,, \tag{3.155}$$

which is inserted, e.g. into (3.105) to compute the plastic strains. In addition to the elastoplastic material presented in section 3.4.2.3, an evolution equation for the damage variable is introduced by

$$\dot{D} \;=\; \dot{\gamma}\,\frac{\hat{H}(\bar{\varepsilon}^p \,-\, \bar{\varepsilon}^p_D)}{1 \,-\, D}\left(\frac{-Y}{r}\right)^S , \tag{3.156}$$

where r, S are experimentally determined material parameters and the energy-release rate Y is defined as

$$Y \;=\; \rho_0\,\frac{\partial \psi^{ed}}{\partial D} \;=\; \frac{-1}{2\,(1 \,-\, D)^2}\,\boldsymbol{\sigma} : \mathscr{C}^{e\,-1}_{\mathsf{mat}} : \boldsymbol{\sigma} \;=\; \frac{-q^2}{6\,G\,(1 \,-\, D)^2} \,+\, \frac{-p^2}{2\,K\,(1 \,-\, D)^2}\,. \tag{3.157}$$

As shown in (3.156), the present model includes a so-called damage threshold $\bar{\varepsilon}^p_D$. In experiments it can be observed that a body can bear a certain amount of plastic strains in which no damage is observed (described by $\hat{H} = 0$ for $\bar{\varepsilon}^p \leq \bar{\varepsilon}^p_D$). Passing this limit, i.e. $\bar{\varepsilon}^p > \bar{\varepsilon}^p_D$, damage evolves and the Heaviside function follows as $\hat{H} = 1$.

Summarizing, a solution for the given damage material is obtained, if the discretised constitutive initial value problem using a backward Euler time integration scheme, see section 3.4.2.2, satisfies all equations. This comprises the Kuhn-Tucker conditions (3.107) with the yield surface (3.152) and the evolution equations (3.151) and (3.156) utilising the two-step algorithm of section 3.4.2.2 for the given set of equations. Since the present model neglects kinematic hardening ($\boldsymbol{\beta} = \mathbf{0}$), the so-called simplified Lemaitre material model is considered which enables a very efficient solution approach. For this model, the number of equations can be reduced to one single equation. For details on the derivation of the one-equation return-mapping, the reader is referred to de Souza Neto et al. [33]. Subsequently, according to the Algorithm 2 for the undamaged elastoplastic materials, a solution of the damage material is achieved equally. Herein, in case of inadmissible values of $\Phi^{\mathsf{trial}}_{n+1}$, a return-mapping algorithm is applied in the plastic corrector step by solving solely

$$r_{\Phi;\mathsf{D}}(\Delta\gamma) \;\equiv\; \omega_{\mathsf{D}}(\Delta\gamma) \,-\, \omega_{\mathsf{D};n} \,+\, \frac{\Delta\gamma}{\omega_{\mathsf{D}}(\Delta\gamma)}\left(\frac{-Y(\Delta\gamma)}{r}\right)^S \;=\; 0 \tag{3.158}$$

to obtain a solution for $\Delta\gamma$. For convenience, the material integrity ω_{D} is introduced as $\omega_{\mathsf{D}} := 1 - D$. Since (3.158) describes a nonlinear equation, a local Newton is applied according to Algorithm 1 for the residual $r_{\Phi;\mathsf{D}}$. In this context it is noted, that the inclusion of damage into the material model worsens the convergence of Newton's method (for details see e.g. de Souza Neto et al. [33]). For this reason the initial guess or predictor $\Delta\gamma^{m=0}$ plays an important role. In de Souza Neto et al. [33], the authors showed that an initial guess

$$\Delta\gamma^{m=0} \;=\; \frac{q^{\mathsf{trial}}_{n+1} \,-\, \sigma_{\mathsf{y}}(R_n)\,\omega_{\mathsf{D};n}}{3\,G} \tag{3.159}$$

leads to improved convergence compared to the default initial guess of $\Delta\gamma^{m=0} = 0$. Thus, this predictor is adopted in the present work as well. Subsequently, with the solution $\Delta\gamma$, all remaining quantities, such as κ_{n+1}, D_{n+1}, $\boldsymbol{\sigma}_{n+1}$, can be updated equivalently to Algorithm 2.

Finally, the material tangent is required, which results in the damaged elastoplastic tangent

$$\begin{aligned}\boldsymbol{\mathscr{C}}_{\mathsf{mat}}^{edp} \;=\; & \frac{2\,G\,\omega_{\mathsf{D}}\,\sigma_{\mathsf{y}}(R)}{q_{\mathsf{eff}}^{\mathsf{trial}}}\,\boldsymbol{\mathscr{I}}_d \;+\; 2\,G\left[a_1\,H^{\mathsf{iso}}\,\omega_{\mathsf{D}} \;+\; a_4\,\sigma_{\mathsf{y}}(R) \;-\; \frac{\omega_{\mathsf{D}}\,\sigma_{\mathsf{y}}(R)}{q_{\mathsf{eff}}^{\mathsf{trial}}}\right]\check{\boldsymbol{N}}\otimes\check{\boldsymbol{N}} + \\ & + K\,\sqrt{\frac{2}{3}}\,[a_2\,H^{\mathsf{iso}}\,\omega_{\mathsf{D}} \;+\; a_3\,\sigma_{\mathsf{y}}(R)]\,\check{\boldsymbol{N}}\otimes\boldsymbol{I} + \\ & + 2\,G\,\sqrt{\frac{3}{2}}\,p_{\mathsf{eff}}\,a_4\,\boldsymbol{I}\otimes\check{\boldsymbol{N}} \;+\; K\,(\omega_{\mathsf{D}} \;+\; a_3\,p_{\mathsf{eff}})\,\boldsymbol{I}\otimes\boldsymbol{I}\end{aligned} \tag{3.160}$$

with H^{iso} defined in (3.75), the unit flow vector $\check{\boldsymbol{N}} = \sqrt{\frac{2}{3}}\boldsymbol{N}$ based on (3.155), and the coefficient $a_1 - a_4$ which are given as

$$a_1 = \left(\frac{\mathrm{d}r_{\Phi;\mathsf{D}}}{\mathrm{d}\Delta\gamma}\right)^{-1}\left[\frac{\omega_{\mathsf{D}}}{q_{\mathsf{eff}}^{\mathsf{trial}} \;-\; \sigma_{\mathsf{y}}(R)} \;-\; \frac{1}{3\,G}\left(\frac{-Y}{r}\right)^{S}\right], \tag{3.161}$$

$$a_2 = -\frac{S\,p_{\mathsf{eff}}\,(q_{\mathsf{eff}}^{\mathsf{trial}} \;-\; \sigma_{\mathsf{y}}(R))}{3\,G\,r\,K\,\frac{\mathrm{d}r_{\Phi;\mathsf{D}}}{\mathrm{d}\Delta\gamma}}\left(\frac{-Y}{r}\right)^{S-1}, \tag{3.162}$$

$$a_3 = a_2\,\frac{\mathrm{d}\omega_{\mathsf{D}}}{\mathrm{d}\Delta\gamma}, \tag{3.163}$$

$$a_4 = a_1\,\frac{\mathrm{d}\omega_{\mathsf{D}}}{\mathrm{d}\Delta\gamma} \;-\; \frac{\omega_{\mathsf{D}}}{q_{\mathsf{eff}}^{\mathsf{trial}} \;-\; \sigma_{\mathsf{y}}(R)}. \tag{3.164}$$

Herein, the derivation of (3.158) $\frac{\mathrm{d}r_{\Phi;\mathsf{D}}}{\mathrm{d}\Delta\gamma}$ and the derivative of the integrity $\dfrac{\mathrm{d}\omega_{\mathsf{D}}}{\mathrm{d}\Delta\gamma}$ with respect to the plastic multiplier are included. The latter yields

$$\frac{\mathrm{d}\omega_{\mathsf{D}}}{\mathrm{d}\Delta\gamma} \;=\; \frac{3\,G \;+\; \omega_{\mathsf{D}}\,H^{\mathsf{iso}}}{q_{\mathsf{eff}}^{\mathsf{trial}} \;-\; \sigma_{\mathsf{y}}(R)}. \tag{3.165}$$

For the sake of lucidity, the index $n+1$ has been omitted in $\boldsymbol{\mathscr{C}}_{\mathsf{mat}}^{edp}$. As the coefficients of $\check{\boldsymbol{N}}\otimes\boldsymbol{I}$ and $\boldsymbol{I}\otimes\check{\boldsymbol{N}}$ in (3.160) are different, the resulting material tangent $\boldsymbol{\mathscr{C}}_{\mathsf{mat}}^{edp}$ is unsymmetric. The full Lemaitre model is obtained by introducing the back stress into the system which is presented in the appendix D.1.

3.4.2.5 Finite strain elastoplasticity

The present model is based on Simo and Miehe [122] and represents an extension of the hyperelastic material model presented in section 3.4.1. As it describes the elastoplastic extension it is named "EPSIMO". It represents a common finite strain hyperelastoplastic material model with J_2-plasticity which is utilised in various publications, as e.g. Simo and Hughes [120] and de Souza Neto et al. [33].

As usual in finite elastoplasticity, the solid kinematics is constitutively based on a multiplicative split of the deformation gradient

$$\boldsymbol{F} \;=\; \boldsymbol{F}^e\cdot\boldsymbol{F}^p, \tag{3.166}$$

where $\boldsymbol{F}^e$ and $\boldsymbol{F}^p$ denote elastic and plastic contributions, respectively. Herein, $\boldsymbol{F}^e$ can be understood as an external variable, whereas $\boldsymbol{F}^p$ has the character of an internal variable, which cannot be determined from the overall process but has to be determined within the process via additional evolution equations. The intermediate configuration $\check{\Omega}$, depicted in Figure 3.5, describes

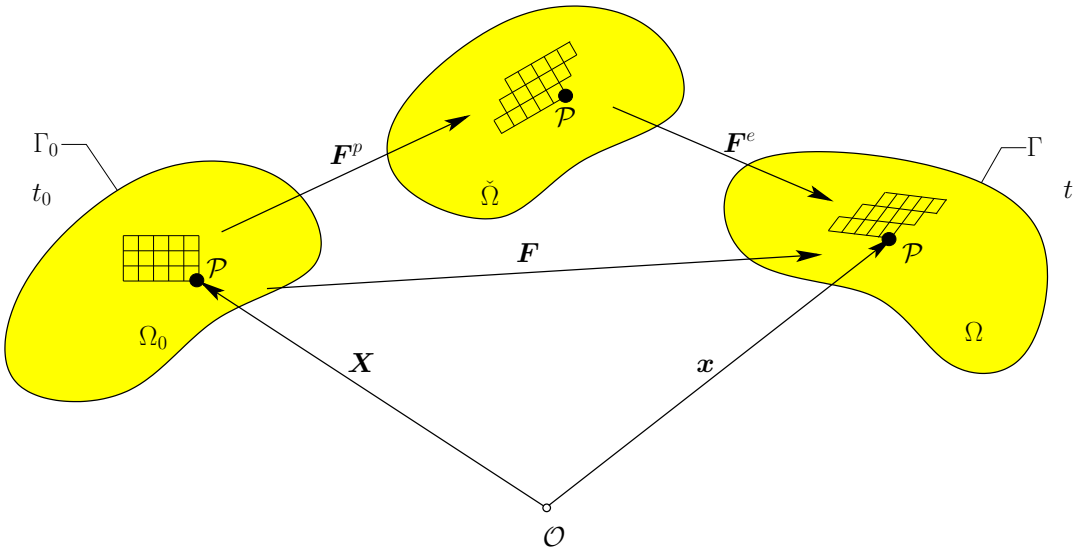

Figure 3.5: Reference, intermediate and current configuration.

a stress-free locally-unloaded configuration which is connected to the reference configuration Ω_0 via the plastic deformation $\boldsymbol{F}^p$ and to the current configuration Ω via the elastic deformation $\boldsymbol{F}^e$, respectively. The split can further be interpreted from a micromechanical point of view. As shown in Figure 3.5, $\boldsymbol{F}^p$ is related to the slip of atomic layers and $\boldsymbol{F}^e$ to the lattice distortion. The parts $\boldsymbol{F}^e$ and $\boldsymbol{F}^p$ can no longer be referred to the gradient of the displacement field (2.3). In contrast, they rather describe a local, pointwise partition of $\boldsymbol{F}$. According to (2.12), (2.14) and (3.166), the elastic right and left Cauchy-Green deformation tensors as well as the plastic right Cauchy-Green deformation tensors are given by

$$\check{\boldsymbol{C}}^e = \boldsymbol{F}^{e\,\mathsf{T}} \cdot \boldsymbol{F}^e \,, \tag{3.167}$$

$$\boldsymbol{B}^e = \boldsymbol{F}^e \cdot \boldsymbol{F}^{e\,\mathsf{T}} \,, \tag{3.168}$$

$$\boldsymbol{C}^p = \boldsymbol{F}^{p\,\mathsf{T}} \cdot \boldsymbol{F}^p \,. \tag{3.169}$$

Since J_2-plasticity comprises isochoric plastic deformations (i.e. $\det \boldsymbol{F}^p = 1$), the Jacobi determinant postulates

$$\det \boldsymbol{F} = J = \det(\boldsymbol{F}^e \cdot \boldsymbol{F}^p) = \det \boldsymbol{F}^e \, \det \boldsymbol{F}^p = \det \boldsymbol{F}^e \,, \tag{3.170}$$

so that the total and the elastic Jacobi determinants, J and J^e, respectively, coincide. Thus, applying (2.35) to (3.168) and considering (3.170), subsequently the tensor $\boldsymbol{B}^e$ is multiplicatively split into

$$\boldsymbol{B}^e = \boldsymbol{B}^e_v \cdot \tilde{\boldsymbol{B}}^e \,, \tag{3.171}$$

leading to volumetric and isochoric contributions, $\boldsymbol{B}^e_v = (J^{\frac{2}{3}}\,\boldsymbol{I})$ and

$$\tilde{\boldsymbol{B}}^e = J^{-\frac{2}{3}}\,\boldsymbol{F}^e \cdot \boldsymbol{F}^{e\,\mathsf{T}} = J^{-\frac{2}{3}}\,\boldsymbol{B}^e \,, \tag{3.172}$$

respectively. Moreover, for the present finite strain elastoplastic material the internal variables are specified to

$$\boldsymbol{\alpha}_{\mathsf{k}} \;=\; \{\boldsymbol{F}^p, \bar{\varepsilon}^p\}\,. \tag{3.173}$$

Via

$$\boldsymbol{F}^p \;=\; \boldsymbol{F}^{e\,-1} \cdot \boldsymbol{F}\,, \tag{3.174}$$

the plastic deformation gradient $\boldsymbol{F}^p$ can be computed from the total and the elastic deformation gradient. Hence, the Helmholtz free energy (2.89) reduces form $\psi(\boldsymbol{F}^e, \boldsymbol{F}^p, \bar{\varepsilon}^p)$ to $\psi(\boldsymbol{F}^e, \bar{\varepsilon}^p)$. Based on the hyperelastic version (3.53), the present hyperelasto-plastic potential is postulated with the elastic left Cauchy-Green deformation tensor $\boldsymbol{B}^e$ (3.168) instead of the deformation gradient. Subsequently, the potential per unit reference volume reads

$$\begin{aligned}
\rho_0\,\psi_{\mathsf{EPSIMO}}(\boldsymbol{B}^e, \bar{\varepsilon}^p) \;&:=\; \underbrace{\hat{\mathbb{U}}(J) \,+\, \hat{\mathbb{W}}(\tilde{\boldsymbol{B}}^e)}_{\rho_0\,\psi^e_{\mathsf{EPSIMO}}(J,\tilde{\boldsymbol{B}}^e)} + \quad \underbrace{\hat{\mathbb{K}}(\bar{\varepsilon}^p)}_{\rho_0\,\psi^p_{\mathsf{EPSIMO}}(\bar{\varepsilon}^p)} \\
&=\; \underbrace{\frac{K}{2}\left[\frac{1}{2}\,(J^2 \,-\, 1) - \ln J\right]}_{\hat{\mathbb{U}}(J)} + \underbrace{\frac{1}{2}\,\mu\left[\operatorname{tr}\tilde{\boldsymbol{B}}^e \,-\, 3\right]}_{\hat{\mathbb{W}}(\tilde{\boldsymbol{B}}^e)} + \\
&\quad + \underbrace{\frac{1}{2}\,H^{\mathsf{iso}}\,\bar{\varepsilon}^{p\,2} \,+\, (\sigma_{\mathsf{y};\infty} \,-\, \sigma_{\mathsf{y};0})\,\hat{\mathbb{H}}(\bar{\varepsilon}^p)}_{\hat{\mathbb{K}}(\bar{\varepsilon}^p)}\,,
\end{aligned} \tag{3.175}$$

where the constant material parameters for isotropic hardening H^{iso}, saturation hardening stress $\sigma_{\mathsf{y};\infty}$, and initial yield stress $\sigma_{\mathsf{y};0}$ are used. The hardening potential is further specified to

$$\hat{\mathbb{H}}(\bar{\varepsilon}^p) \;=\; \begin{cases} \bar{\varepsilon}^p \,-\, \left[1 \,-\, \exp(-\delta\,\bar{\varepsilon}^p)\right]\dfrac{1}{\delta} & \text{for} \quad \delta \,\neq\, 0 \\ 0 & \qquad\quad\;\; \delta \,=\, 0 \end{cases} \tag{3.176}$$

with the hardening exponent δ. The split (3.171) is employed in (3.175) so that $\hat{\mathbb{U}}(J)$ and $\hat{\mathbb{W}}(\tilde{\boldsymbol{B}}^e)$ can be identified with the hyperelastic volumetric and isochoric SEF, respectively. The isotropic hardening potential $\hat{\mathbb{K}}(\bar{\varepsilon}^p)$ enables to show exponential isotropic hardening as well as linear softening. As usual, the second law of thermodynamics has to be satisfied. Hence, according to the previous approaches, the time derivative of (3.175) is inserted into the Clausius-Planck inequality (2.84). Herein, the rate of $\boldsymbol{B}^e$ evolves, which is defined as

$$\dot{\boldsymbol{B}}^e \;=\; \boldsymbol{B}^{e\,\mathsf{T}}\,\boldsymbol{L} \,+\, \boldsymbol{B}^e\,\boldsymbol{L}^{\mathsf{T}} \,+\, \mathcal{L}_t(\boldsymbol{B}^e) \tag{3.177}$$

with the spatial velocity gradient $\boldsymbol{L}$ (2.24) and the objective material time derivative of $\boldsymbol{B}^e$ (see (2.27)) given by

$$\mathcal{L}_t(\boldsymbol{B}^e) \;=\; \boldsymbol{F} \cdot \dot{\boldsymbol{C}}^{p\,-1} \cdot \boldsymbol{F}^{\mathsf{T}}\,, \tag{3.178}$$

i.e. as the push-forward of the rate of the inverse plastic right Cauchy-Green deformation tensor $\dot{\boldsymbol{C}}^{p\,-1}$, based on (3.169). Furthermore, including (2.25) as well as the assumption of isotropy

$$\begin{aligned}
\frac{\partial\psi_{\mathsf{EPSIMO}}}{\partial\boldsymbol{B}^e} : \dot{\boldsymbol{B}}^e \;&=\; \frac{\partial\psi_{\mathsf{EPSIMO}}}{\partial\boldsymbol{B}^e} \cdot \boldsymbol{B}^e : \left[2\,\boldsymbol{D} \,+\, \mathcal{L}_t(\boldsymbol{B}^e) \cdot \boldsymbol{B}^{e\,-1}\right] \\
&=\; \boldsymbol{B}^e \cdot \frac{\partial\psi_{\mathsf{EPSIMO}}}{\partial\boldsymbol{B}^e} : \left[2\,\boldsymbol{D} \,+\, \mathcal{L}_t(\boldsymbol{B}^e) \cdot \boldsymbol{B}^{e\,-1}\right],
\end{aligned} \tag{3.179}$$

obtaining the constraints for the given problem. For instance, the Kirchhoff stresses yield

$$\boldsymbol{\tau} \;=\; 2\,\rho_0\,\frac{\partial \psi_{\mathsf{EPSIMO}}}{\partial \boldsymbol{B}^e}\cdot\boldsymbol{B}^e\,. \tag{3.180}$$

Finally, including (3.175) and (3.180), the Kirchhoff and the Cauchy stresses are expressed as

$$\boldsymbol{\tau} \;=\; \underbrace{\frac{K}{2}\,(J^2\,-\,1)}_{\boldsymbol{\tau}_v} \;+\; \underbrace{\mu\,\mathrm{dev}\tilde{\boldsymbol{B}}^e}_{\tilde{\boldsymbol{\tau}}} \;=\; J\,\boldsymbol{\sigma}\,, \tag{3.181}$$

where according to (3.58), volumetric and isochoric parts of the Kirchhoff stress tensor, $\boldsymbol{\tau}_v$ and $\tilde{\boldsymbol{\tau}}$, respectively, are distinguished. Consequently, including all previous relations into the second law of thermodynamics (3.59), the dissipation inequality reads

$$\mathcal{D}_{\mathsf{mech}} \;:=\; \boldsymbol{\tau}\;:\;\Big(-\frac{1}{2}\,\mathcal{L}_t(\boldsymbol{B}^e)\Big)\cdot\boldsymbol{B}^{e\,-1}\;-\;\kappa(\bar{\varepsilon}^p)\cdot\dot{\bar{\varepsilon}}^p\;\geq\;0\,, \tag{3.182}$$

where the thermodynamic force associated to isotropic hardening according to (2.101) reads

$$\kappa(\bar{\varepsilon}^p) \;=\; \rho_0\,\frac{\partial\psi}{\partial\bar{\varepsilon}^p} \;=\; H_{\mathsf{iso}}\,\bar{\varepsilon}^p \;+\; [\sigma_{\mathsf{y};\infty}\;-\;\sigma_{\mathsf{y};0}]\,[1\;-\;\exp(-\delta\,\bar{\varepsilon}^p)]\,. \tag{3.183}$$

According to (3.89), the elastic domain follows as

$$\mathcal{E} \;=\; \{\boldsymbol{\tau}\,|\,\check{\Phi}(\boldsymbol{\tau},\kappa)\;<\;0\}\,, \tag{3.184}$$

where the von Mises yield criterion is assumed to

$$\check{\Phi} \;:=\; ||\boldsymbol{s}||\;-\;\sqrt{\frac{2}{3}}\,\sigma_{\mathsf{y}}(\bar{\varepsilon}^p)\;\leq\;0 \tag{3.185}$$

with the yield surface $\check{\Phi}$, the deviator of the Kirchhoff stress based on (3.180)

$$\boldsymbol{s} \;:=\; \mathrm{dev}\,\boldsymbol{\tau} \;=\; \tilde{\boldsymbol{\tau}}\,, \tag{3.186}$$

and the yield stress σ_{y} corresponding to (3.72), i.e. $\sigma_{\mathsf{y}} = \sigma_{\mathsf{y};0} + \kappa(\bar{\varepsilon}^p)$. The present yield criterion (3.185) represents a common alternative but equivalent form of (3.96). Based on (3.185) and (3.92), the accumulated plastic strain is defined as

$$\dot{\bar{\varepsilon}}^p \;=\; \sqrt{\frac{2}{3}}\,\dot{\gamma}\,. \tag{3.187}$$

According to (3.91), a plastic flow rule is required for the present finite strain material material, yielding

$$-\frac{1}{2}\,\mathcal{L}_t(\boldsymbol{B}^e) = \;\dot{\gamma}\,\frac{\partial\check{\Phi}}{\partial\boldsymbol{\tau}}\cdot\boldsymbol{B}^e \;=\; \dot{\gamma}\,\boldsymbol{N}_{\mathsf{cur}}\cdot\boldsymbol{B}^e\,, \tag{3.188}$$

where the spatial flow vector

$$\boldsymbol{N}_{\mathsf{cur}} \;=\; \frac{\partial\check{\Phi}}{\partial\boldsymbol{\tau}} \;=\; \frac{\boldsymbol{s}}{||\boldsymbol{s}||} \tag{3.189}$$

is introduced. The index $(\cdot)_{\mathsf{cur}}$ indicates that the quantity is expressed with respect to the current configuration. As stated in Glaser [51], Miehe [88], and Simo and Miehe [122], (3.188) can be simplified for the application to metals. Thus, in a first step $\boldsymbol{B}^e$ is replaced with its corresponding isochoric, volumetric counterparts according to (3.171). Subsequently, the isochoric part of $\boldsymbol{B}^e$ is split into its deviatoric and volumetric or spherical parts according to (B.16), so that (3.188) results in

$$\mathcal{L}_t\, \boldsymbol{B}^e \;=\; -2\,\dot\gamma\, \boldsymbol{N}_{\mathsf{cur}}\, J^{\frac{2}{3}}\, \tilde{\boldsymbol{B}}^e \;=\; -2\,\dot\gamma\, J^{\frac{2}{3}}\, \frac{\boldsymbol{s}}{||\boldsymbol{s}||}\, \Big(\operatorname{dev} \tilde{\boldsymbol{B}}^e \,+\, \frac{1}{3}\operatorname{tr} \tilde{\boldsymbol{B}}^e\, \boldsymbol{I}\Big)\,. \tag{3.190}$$

Introducing $\tilde{\boldsymbol{\tau}}$ (3.181) and reformulating (3.190) yields

$$\begin{aligned} \mathcal{L}_t\, \boldsymbol{B}^e \;&=\; -2\,\dot\gamma\, J^{\frac{2}{3}}\, \Big(\boldsymbol{N}_{\mathsf{cur}}\, \frac{\boldsymbol{s}}{\mu} \,+\, \frac{\boldsymbol{s}}{||\boldsymbol{s}||}\, \frac{1}{3}\operatorname{tr} \tilde{\boldsymbol{B}}^e \cdot \boldsymbol{I}\Big) \\ &=\; -2\,\dot\gamma\, J^{\frac{2}{3}}\, \Big(\boldsymbol{N}_{\mathsf{cur}}^2\, \frac{||\boldsymbol{s}||}{\mu} \,+\, \frac{\boldsymbol{s}}{||\boldsymbol{s}||}\, \frac{1}{3}\operatorname{tr} \tilde{\boldsymbol{B}}^e \cdot \boldsymbol{I}\Big)\,. \end{aligned} \tag{3.191}$$

For instance in Miehe [88] and Simo and Miehe [122], the second term of (3.191) is assumed to $\frac{||\boldsymbol{s}||}{\mu_0} \,\cong\, 10^{-3}$, hence for most metals this term can be neglected.

As the material or total Lagrangian formulation is chosen, the aforementioned relations are expressed in the following with respect to the reference configuration. Consequently, instead of the elastic left Cauchy-Green deformation tensor $\boldsymbol{B}^e$ the inverse of the plastic right Cauchy-Green deformation tensor $\boldsymbol{C}^{p\,-1}$ (3.169) is used which is the material equivalent to $\boldsymbol{B}^e$ or the pull-back of $\boldsymbol{B}^e$, i.e.

$$\boldsymbol{C}^{p\,-1} \;=\; \boldsymbol{F}^{-1} \cdot \boldsymbol{B}^e \cdot \boldsymbol{F}^{-\mathsf{T}}\,. \tag{3.192}$$

Furthermore, by including all aforementioned relations and transforming (3.191) to the reference configuration using (3.178), the flow rule is finally reduced to

$$\dot{\boldsymbol{C}}^{p\,-1} \;=\; -2\, J^{\frac{2}{3}}\, \dot\gamma\, \frac{1}{3}\operatorname{tr} \tilde{\boldsymbol{B}}^e\, \boldsymbol{F}^{-1} \cdot \boldsymbol{N}_{\mathsf{cur}} \cdot \boldsymbol{F}^{-\mathsf{T}} \;=\; -2\, J^{\frac{2}{3}}\, \dot\gamma\, \frac{1}{3}\operatorname{tr} \tilde{\boldsymbol{B}}^e\, \boldsymbol{N}\,, \tag{3.193}$$

where via pull-back of $\boldsymbol{N}_{\mathsf{cur}}$ the material flow vector $\boldsymbol{N}$ is introduced. Moreover, using (2.46), (3.192), (3.193), the material expression of the dissipation (3.182) follows as

$$\mathcal{D}_{\mathsf{mech}} \;:=\; \boldsymbol{C} \cdot \boldsymbol{S} : \Big(-\frac{1}{2}\, \dot{\boldsymbol{C}}^{p\,-1}\Big) \cdot \boldsymbol{C}^p \;-\; \kappa(\bar\varepsilon^p)\, \dot{\bar\varepsilon}_p \;\geq\; 0\,. \tag{3.194}$$

An admissible plastic load step is characterized by $\overset{\circ}{\Phi} \;=\; 0$, see e.g. $(3.71)_3$. Thus, it is valid to write

$$||\boldsymbol{s}|| \;=\; \sqrt{\frac{2}{3}}\, \sigma_{\mathsf{y}}(\bar\varepsilon^p)\,. \tag{3.195}$$

The stress term of the dissipation inequality (3.194) can be expressed by

$$\boldsymbol{C} \cdot \boldsymbol{S} : \Big(-\frac{1}{2}\, \dot{\boldsymbol{C}}^{p\,-1}\Big) \cdot \boldsymbol{C}^p \;=\; \boldsymbol{\tau} : \Big(-\frac{1}{2}\, \mathcal{L}_t(\boldsymbol{B}^e)\Big) \cdot \boldsymbol{B}^{e\,-1} \;=\; \boldsymbol{\tau} : (\dot\gamma\, \boldsymbol{N}_{\mathsf{cur}})\,. \tag{3.196}$$

Since $\boldsymbol{N}_{\mathsf{cur}}$ is purely deviatoric, the Kirchhoff stress $\boldsymbol{\tau}$ in the dot product (3.196) reduces to the deviatoric component $\boldsymbol{s}$. Moreover, $\boldsymbol{s}$ and $\boldsymbol{N}_{\mathsf{cur}}$ are collinear and the flow vector is a normalized vector, so that

$$\boldsymbol{s} : \dot\gamma\, \boldsymbol{N}_{\mathsf{cur}} \;=\; \dot\gamma\, \boldsymbol{s} : \frac{\boldsymbol{s}}{||\boldsymbol{s}||} \;=\; \dot\gamma\, ||\boldsymbol{s}||\, \underbrace{||\boldsymbol{N}_{\mathsf{cur}}||}_{=1} \;=\; \dot\gamma\, ||\boldsymbol{s}||\,. \tag{3.197}$$

Subsequently, using (3.197) and integrating (3.195) therein, the dissipation can be reduced to

$$\begin{aligned} \mathcal{D}_{\mathsf{mech}} &= \dot{\gamma}\left(||\boldsymbol{s}|| - \sqrt{\frac{2}{3}}\,\kappa(\bar{\varepsilon}^p)\right) = \dot{\gamma}\left(\sqrt{\frac{2}{3}}\,\sigma_{\mathsf{y}}(\bar{\varepsilon}^p) - \sqrt{\frac{2}{3}}\,\kappa(\bar{\varepsilon}^p)\right) \\ &= \dot{\gamma}\left[\sqrt{\frac{2}{3}}\left(\sigma_{\mathsf{y};0} + \kappa(\bar{\varepsilon}^p)\right) - \sqrt{\frac{2}{3}}\,\kappa(\bar{\varepsilon}^p)\right], \end{aligned} \tag{3.198}$$

which finally results in

$$\mathcal{D}_{\mathsf{mech}} = \dot{\gamma}\sqrt{\frac{2}{3}}\,\sigma_{\mathsf{y};0}\,, \tag{3.199}$$

i.e. $\mathcal{D}_{\mathsf{mech}}$ follows to depend only on the plastic multiplier $\dot{\gamma}$ and the initial yield stress $\sigma_{\mathsf{y};0}$.

All required relations are specified for the given material. Thus, as a next step, the evolution equations are discretised in time using a backward Euler time integration which are then solved with a return-mapping algorithm, see section 3.4.2.2. The return-mapping algorithm was first established for finite strains elastoplasticity in Simo [125, 126] and still represents the default solution strategy in the literature. For more details on return-mapping within the finite strain regime, the interested reader is referred to the literature, as e.g. de Souza Neto et al. [33], Simo and Hughes [120] and Simo [125, 126]. Since the procedure for setting up the final discrete equations is equal to the small strain case, the detailed derivations are spared here.

Subsequently, the consistent material tangent is established. The representation is restricted to the important results, because full derivations of the material tangent $\boldsymbol{\mathscr{C}}_{\mathsf{mat}}$ are reported in the literature, as e.g. in Holzapfel [58], Simo and Hughes [120], and Simo and Miehe [122]. For more details, the interested reader is referred to these publications. The present material model is described in a spatial approach using Kirchhoff stresses $\boldsymbol{\tau}$. Hence, the Kirchhoff stresses are linearised with respect to a spatial deformation measure. As proposed in Simo [125], the linearisations of the Kirchhoff stresses are performed with respect to the Euler-Almansi strain tensor $\boldsymbol{E}_{\mathsf{EA}}$ (2.18) leading to a spatial tangent modulus $c^{ep}_{\mathsf{mat};ijkl}$. Via pull-back, the spatial tangent can be transformed to the material tangent, which yields the well-known relation

$$\mathscr{C}_{\mathsf{mat};IJKL} = F_{Ii}\,F_{Jj}\,F_{Kk}\,F_{Ll}\left(\frac{\partial \tau_{ij}}{\partial E_{\mathsf{EA};kl}}\right) = F_{Ii}\,F_{Jj}\,F_{Kk}\,F_{Ll}\,c_{\mathsf{mat};ijkl} \tag{3.200}$$

given in index notation. Based on the volumetric-isochoric split (3.181), the material tangent $\boldsymbol{\mathscr{C}}_{\mathsf{mat}}$ also consists of two terms, i.e.

$$\boldsymbol{\mathscr{C}}^{ep}_{\mathsf{mat}} = \boldsymbol{\mathscr{C}}^{e}_{\mathsf{mat};v} + \tilde{\boldsymbol{\mathscr{C}}}^{ep}_{\mathsf{mat}}\,, \tag{3.201}$$

where $\boldsymbol{\mathscr{C}}^{e}_{\mathsf{mat};v}$ is the volumetric and $\tilde{\boldsymbol{\mathscr{C}}}^{ep}_{\mathsf{mat}}$ is the isochoric tangent. The elastic volumetric tangent follows as

$$\boldsymbol{\mathscr{C}}^{e}_{\mathsf{mat};v} = K\,J^2\,(\boldsymbol{C}^{-1}\otimes\boldsymbol{C}^{-1}) - K\,(J^2 - 1)\,(\boldsymbol{C}^{-1}\odot\boldsymbol{C}^{-1})\,, \tag{3.202}$$

where $\odot$, $\otimes$ are tensor products according to (B.33) and (B.34). The isochoric part $\tilde{\boldsymbol{\mathscr{C}}}^{ep}_{\mathsf{mat}}$ is computed within the return-mapping algorithm in a plastic load step. To determine $\tilde{\boldsymbol{\mathscr{C}}}^{ep}_{\mathsf{mat}}$, first the final solution of the deviatoric stresses at t_{n+1} is utilised which is computed according to Algorithm 2 using (3.189) and (3.190) by

$$\boldsymbol{s}_{n+1} = \boldsymbol{s}^{\mathsf{trial}}_{n+1} - 2\,\tilde{\mu}\,\Delta\gamma\,\boldsymbol{N}_{\mathsf{cur}} \tag{3.203}$$

with

$$\tilde{\mu} \;=\; \frac{1}{3}\,\mu\,\mathrm{tr}\,\tilde{\boldsymbol{B}}^{e;\mathsf{trial}}\,, \quad \boldsymbol{N}_{\mathsf{cur}} \;=\; \frac{\boldsymbol{s}^{\mathsf{trial}}_{n+1}}{||\boldsymbol{s}^{\mathsf{trial}}_{n+1}||}\,. \tag{3.204}$$

Linearising (3.203) and applying the product rule, then postulates the isochoric tangent as pull-back, i.e.

$$\tilde{\mathscr{C}}^{ep}_{\mathsf{mat}} \;=\; \tilde{\mathscr{C}}^{e;\mathsf{trial}}_{\mathsf{mat}} \;+\; \tilde{\mathscr{C}}^{p}_{\mathsf{mat}} \tag{3.205}$$

with the trial elastic and the plastic tangents, $\tilde{\mathscr{C}}^{e;\mathsf{trial}}_{\mathsf{mat}}$ and $\tilde{\mathscr{C}}^{p}_{\mathsf{mat}}$, respectively. Herein, the elastic trial material tangent follows as a result of the linearisation of the trial stresses with respect to the deformation by

$$\tilde{\mathscr{C}}^{e;\mathsf{trial}}_{\mathsf{mat}} \;=\; 2\,\tilde{\mu}\,(\boldsymbol{C}^{-1}\odot\boldsymbol{C}^{-1} \;-\; \frac{1}{3}\,\boldsymbol{C}^{-1}\otimes\boldsymbol{C}^{-1}) \;-\; \frac{2}{3}\,||\boldsymbol{s}^{\mathsf{trial}}_{n+1}||\,(\boldsymbol{C}^{-1}\otimes\boldsymbol{N} \;+\; \boldsymbol{C}^{-1}\otimes\boldsymbol{N})\,. \tag{3.206}$$

The plastic corrector tangent $\tilde{\mathscr{C}}^{p}_{\mathsf{mat}}$ is obtained as pull-back of $\tilde{c}^{p}_{\mathsf{mat};ijkl}$. Based on (3.203), the following linearisations

$$\Big[\frac{\partial||\boldsymbol{s}^{\mathsf{trial}}_{n+1}||}{\partial\boldsymbol{E}_{\mathsf{EA};n+1}}\Big] \;=\; 2\,\tilde{\mu}\,\boldsymbol{N}_{\mathsf{cur}} \;+\; 2\,||\boldsymbol{s}^{\mathsf{trial}}_{n+1}||\,\mathrm{dev}[\boldsymbol{N}^2_{\mathsf{cur}}]\,, \tag{3.207}$$

$$\Big[\frac{\partial\tilde{\mu}}{\partial\boldsymbol{E}_{\mathsf{EA};n+1}}\Big] \;=\; \frac{2}{3}\,||\boldsymbol{s}^{\mathsf{trial}}_{n+1}||\,\boldsymbol{N}_{\mathsf{cur}}\,, \tag{3.208}$$

$$\Big[\frac{\partial\Delta\gamma}{\partial\boldsymbol{E}_{\mathsf{EA};n+1}}\Big] \;=\; \frac{1}{\beta_0}\,\Big[\Big(1 \;-\; \frac{2\,||\boldsymbol{s}^{\mathsf{trial}}_{n+1}||\,\Delta\gamma}{3\,\tilde{\mu}}\Big)\,\boldsymbol{N}_{\mathsf{cur}} \;+\; \frac{||\boldsymbol{s}^{\mathsf{trial}}_{n+1}||}{\tilde{\mu}}\,\mathrm{dev}[\boldsymbol{N}^2_{\mathsf{cur}}]\Big]\,, \tag{3.209}$$

$$\Big[\frac{\partial\boldsymbol{N}_{\mathsf{cur}}}{\partial\boldsymbol{E}_{\mathsf{EA};n+1}}\Big] \;=\; \frac{1}{||\boldsymbol{s}^{\mathsf{trial}}_{n+1}||}\,\Big\{\tilde{\boldsymbol{c}}^{e;\mathsf{trial}}_{\mathsf{mat}} \;-\; \boldsymbol{N}_{\mathsf{cur}}\otimes\Big[2\,\tilde{\mu}\boldsymbol{N}_{\mathsf{cur}} \;+\; 2\,||\boldsymbol{s}^{\mathsf{trial}}_{n+1}||\,\mathrm{dev}[\boldsymbol{N}^2_{\mathsf{cur}}]\Big]\Big\}\,, \tag{3.210}$$

respectively, arise within the return-mapping algorithm. In (3.210), the spatial trial elastic material tangent $\tilde{\boldsymbol{c}}^{e;\mathsf{trial}}_{\mathsf{mat}}$ is included which is the push-forward of (3.206). Subsequently, $\tilde{\mathscr{C}}^{p}_{\mathsf{mat}}$ is given as

$$\begin{aligned}
\tilde{\mathscr{C}}^{p}_{\mathsf{mat}} \;=\;& -2\,\Delta\gamma\,\frac{2}{3}\,||\boldsymbol{s}^{\mathsf{trial}}_{n+1}||\,\boldsymbol{N}\otimes\boldsymbol{N} \;-\\
& -2\,\tilde{\mu}\,\frac{1}{\beta_0}\,\Big[\Big(1 \;-\; \frac{2\,||\boldsymbol{s}^{\mathsf{trial}}_{n+1}||\,\Delta\gamma}{3\,\tilde{\mu}}\Big)\,\boldsymbol{N} \;+\\
& \quad +\,\frac{||\boldsymbol{s}^{\mathsf{trial}}_{n+1}||}{\tilde{\mu}}\,\boldsymbol{F}^{-1}\cdot\mathrm{dev}[\boldsymbol{N}^2_{\mathsf{cur}}]\cdot\boldsymbol{F}^{-\mathsf{T}}\Big]\otimes\boldsymbol{N} \;-\\
& -2\,\tilde{\mu}\,\Delta\gamma\,\Big(\frac{1}{||\boldsymbol{s}^{\mathsf{trial}}_{n+1}||}\,\Big\{\tilde{\mathscr{C}}^{e;\mathsf{trial}}_{\mathsf{mat}} \;-\\
& \quad -\,\boldsymbol{N}\otimes\Big[2\,\tilde{\mu}\boldsymbol{N} \;+\; 2\,||\boldsymbol{s}^{\mathsf{trial}}_{n+1}||\,\boldsymbol{F}^{-1}\cdot\mathrm{dev}[\boldsymbol{N}^2_{\mathsf{cur}}]\cdot\boldsymbol{F}^{-\mathsf{T}}\Big]\Big\}\Big)\,.
\end{aligned} \tag{3.211}$$

Finally, the elastoplastic isochoric tangent is obtained via reformulations of (3.206) and (3.211), so that

$$\begin{aligned}\tilde{\mathscr{C}}^{ep}_{\mathsf{mat}} \;=\; & \Big(1 \,-\, \hat{H}(\check{\Phi}^{\mathsf{trial}}_{n+1})\,\beta_1\Big)\Big[2\,\tilde{\mu}\,(\boldsymbol{C}^{-1}\odot\boldsymbol{C}^{-1} \,-\, \frac{1}{3}\,\boldsymbol{C}^{-1}\otimes\boldsymbol{C}^{-1}) - \\ & - \frac{2}{3}\,||\boldsymbol{s}^{\mathsf{trial}}_{n+1}||\,(\boldsymbol{C}^{-1}\otimes\boldsymbol{N} \,+\, \boldsymbol{C}^{-1}\otimes\boldsymbol{N})\Big] \,-\, \hat{H}(\check{\Phi}^{\mathsf{trial}}_{n+1})\,2\,\tilde{\mu}\,\beta_3\,\boldsymbol{N}\otimes\boldsymbol{N} - \\ & - \hat{H}(\check{\Phi}^{\mathsf{trial}}_{n+1})\,2\,\tilde{\mu}\,\beta_4\,\boldsymbol{N}\otimes\Big(\boldsymbol{F}^{-1}\cdot\mathrm{dev}[\boldsymbol{N}^2_{\mathsf{cur}}]\cdot\boldsymbol{F}^{-\mathsf{T}}\Big)\,,\end{aligned} \tag{3.212}$$

where $\hat{H}(\check{\Phi}^{\mathsf{trial}}_{n+1})$ is the Heaviside function (3.141) and the scaling factors β_i are assumed as

$$\beta_0 = 1 \,+\, \frac{1}{3\,\tilde{\mu}}\,\frac{\partial\kappa_{n+1}}{\partial\bar{\varepsilon}^p_{n+1}}\,, \tag{3.213}$$

$$\beta_1 = \frac{2\,\tilde{\mu}}{||\boldsymbol{s}^{\mathsf{trial}}_{n+1}||}\,\Delta\gamma\,, \tag{3.214}$$

$$\beta_2 = \frac{2}{3}\,\frac{\Delta\gamma}{\tilde{\mu}}\,||\boldsymbol{s}^{\mathsf{trial}}_{n+1}||\,\Big(1 \,-\, \frac{1}{\beta_0}\Big)\,, \tag{3.215}$$

$$\beta_3 = \Big(\frac{1}{\beta_0} \,-\, \beta_1 \,+\, \beta_2\Big)\,, \tag{3.216}$$

$$\beta_4 = \Big(\frac{1}{\beta_0} \,-\, \beta_1\Big)\,\frac{||\boldsymbol{s}^{\mathsf{trial}}_{n+1}||}{\tilde{\mu}}\,. \tag{3.217}$$

For β_0 the derivative of κ_{n+1} with respect to $\bar{\varepsilon}^p_{n+1}$ is included, which results in

$$\frac{\partial\kappa(\bar{\varepsilon}^p_{n+1})}{\partial\bar{\varepsilon}^p_{n+1}} \;=\; H^{\mathsf{iso}} \,+\, [\sigma_{\mathsf{y};\infty} \,-\, \sigma_{\mathsf{y};0}]\,[-\exp(-\delta\,\bar{\varepsilon}^p_{n+1})\,(-\delta)]\,. \tag{3.218}$$

Finally, according to (3.201), the complete material tangent $\mathscr{C}_{\mathsf{mat}}$ follows as sum of the elastic volumetric and the isochoric part (3.202) and (3.212), respectively. Further derivations about this material model are summarized in the Appendix D.2.

3.5 Solution techniques for linear equations

Inserting one of the previously presented constitutive laws of section 3.4 into (3.45), the system is closed and hence a solution can be computed with the Newton-Raphson method. One important aspect of the Newton-Raphson method is an efficient and robust solution approach of the linear system (3.45). Especially for large finite element models (with large numbers of DOFs), the solution of the linear system may represent for a time step n the computationally most expensive part of the whole solution procedure. Thus, in the following, the focus is set on solution techniques for linear systems which are abstractly assumed to

$$\mathbf{A}\,\mathbf{x} \;=\; \mathbf{b} \tag{3.219}$$

with the matrix $\mathbf{A}$, the unknown solution vector $\mathbf{x}$, and the right-hand side vector $\mathbf{b}$, respectively.

A good overview on the topic of solution strategies of linear systems can be found in Küttler [70] and the references therein, as e.g. Quarteroni et al. [107]. For the solution of linear systems two different approaches are distinguished: direct and iterative solvers. Direct linear solvers, e.g. based on a LU-decomposition of the matrix $\mathbf{A}$, are suitable for small linear system of equations but loose their efficiency for large and sparse linear system of equations. For instance, within the Gauss-elimination the sparsity pattern gets lost, because the zero-entries are filled leading to a full matrix, which consumes high memory and which is computationally very costly due to the increased number of calculations. Moreover, parallelization of direct solvers can be realised but is complicated and demands high communication between the processors. In contrast, for large and sparse system of equations, iterative solvers are commonly utilised which enable an efficient solution at the expense of exactness of the obtained solution. Starting from an initial guess $\mathbf{x}^0$, the exact solution

$$\mathbf{x} \;=\; \mathbf{A}^{-1}\,\mathbf{b} \tag{3.220}$$

is approximated iteratively until a prescribed user-defined convergence criterion ϵ_{lin} is fulfilled for the residual $\mathbf{r}^j$, i.e.

$$||\mathbf{r}^j_{\mathsf{lin}}|| \;=\; ||\mathbf{b} \;-\; \mathbf{A}^{-1}\,\mathbf{x}^j|| \;\leq\; \epsilon_{\mathsf{lin}} \tag{3.221}$$

with the iteration index of the linear solver denoted by j.

For the present thesis, a Krylov subspace method in the form of the generalised minimum residual (GMRES) approach with preconditioning is used. For a detailed description on GMRES methods, the interested reader is referred particularly to Saad and Schultz [113]. In the present thesis, the GMRES provided by the open-source package AZTEC (see Tuminaro et al. [138]) is employed.

As preconditioning is very important, the condition number of a matrix is introduced here, which is defined as the ratio of the largest to the smallest eigenvalue of $\mathbf{A}$. Small condition numbers refer to a fast convergence, whereas high condition numbers signify slow convergence or even no solution of the linear system. Thus, preconditioning strategies are employed to improve the convergence behaviour by reducing the condition number of the matrix. For instance, scaling of (3.219) with a preconditioning matrix $\mathbf{M}_{\mathsf{R}}$ yields

$$\mathbf{A}\,\mathbf{M}_{\mathsf{R}}^{-1}\,\underbrace{\mathbf{M}_{\mathsf{R}}\,\mathbf{x}}_{\check{\mathbf{x}}} \;=\; \mathbf{b}\,, \tag{3.222}$$

where the index $(\cdot)_{\mathsf{R}}$ indicates the use of a right preconditioning matrix and $\check{\mathbf{x}}$ is the intermediate solution vector. Right preconditioning is used exclusively in this thesis, because the right-hand side or residual vector $\mathbf{b}$, which is used for convergence checking among other things, is not scaled (see (3.222)) as compared with left preconditioning (i.e. $\mathbf{M}_{\mathsf{L}}^{-1}\mathbf{A}\mathbf{x} \;=\; \mathbf{M}_{\mathsf{L}}^{-1}\,\mathbf{b}$). This simplifies the convergence check, because the convergence of the given problem can be directly evaluated by checking the norm of the residual (3.47) or (3.221) without additional computations. To determine the solution $\mathbf{x}$, first the intermediate system

$$\mathbf{A}\,\mathbf{M}_{\mathsf{R}}^{-1}\,\check{\mathbf{x}} \;=\; \mathbf{b} \tag{3.223}$$

is solved iteratively with the GMRES. This solution method aims at minimizing for every iteration j the norm of the residual vector $||\mathbf{r}^j_{\mathsf{lin}}||$ over the Krylov subspaces given by

$$\mathcal{K}^k(\mathbf{A}, \mathbf{r}^0_{\mathsf{lin}}) \;=\; \mathrm{span}\,(\mathbf{r}^0_{\mathsf{lin}}, \mathbf{A}\,\mathbf{r}^0_{\mathsf{lin}}, \mathbf{A}^2\,\mathbf{r}^0_{\mathsf{lin}}, ..., \mathbf{A}^{k-1}\,\mathbf{r}^0_{\mathsf{lin}})\,, \tag{3.224}$$

where $\mathbf{r}_{\text{lin}}^{0}$ is the initial residual. Subsequently, the original solution is computed via

$$\mathbf{x} \;=\; \mathbf{M}_{\text{R}}^{-1}\,\check{\mathbf{x}}\,. \tag{3.225}$$

Hence, the solution process involves the application of the inverse preconditioner on different vectors $\mathbf{y}$, representing either a vector of the Krylov space or the intermediate solution vector, which is used to determine the arbitrary solution vector $\mathbf{z}$. Instead of solving any matrix-vector products, e.g. (3.225), the corresponding linear system

$$\mathbf{M}_{\text{R}}\,\mathbf{z} \;=\; \mathbf{y} \tag{3.226}$$

is computed iteratively using, e.g. a stationary Richardson iteration. Solving (3.226) circumvents the inverting of $\mathbf{M}_{\text{R}}$. As (3.226) can be called solution of the corresponding linear system, see e.g. Wiechert [143], the distinction between "solver" and "preconditioner" is generally not straightforward. While the preconditioner can be interpreted as the solver, the Krylov method accelerates the method only.

Subsequently, within an effective and efficient preconditioning process, the condition number should be reduced to accelerate the convergence, and moreover, the preconditioning matrix $\mathbf{M}_{\text{R}}$ should approximate the matrix of the target problem well ($\mathbf{M}_{\text{R}} \approx \mathbf{A}$), while being invertible with as little effort as possible. Consequently, standard preconditioner, as e.g. Jacobi and Gauss-Seidel methods, or algebraic multigrid (AMG) methods, can be used. However, for an efficient solution, problem-specific preconditioners are required. For instance, in Küttler [70] or Wiechert [143], special preconditioners are presented for the surface-coupled problem of fluid-structure interaction problem. Further details on special preconditioners for the target TSI problem within a monolithic framework will be presented in section 6.3.

4 Thermo field

For the development of the thermomechanical models, appropriate for the target application to rocket nozzles, the temperature field needs to be considered. This section provides an overview of the governing equations required to describe a temperature field with the finite element method (FEM). A more detailed representation on this topic can be found in the literature, e.g. in Holzapfel [58], Lemaitre and Chaboche [78], and Polifke and Kopitz [105]. The procedure to establish a fully discrete system of equations for the thermal field is comparable to the one for the structural field in chapter 3. Moreover, the basics of nonlinear continuum thermodynamics have already been featured in chapter 2. Consequently, the detailed derivation are skipped in this chapter.

In a first step, the balance equations for the thermal field will be established. Then, in a second step the thermal initial boundary value problem (IBVP) will be presented followed by the numerical solution technique. Latter requires a weak form of the thermal balance equation which will be fully discretised using the FEM for space discretisation and the finite difference method for time discretisation. To finish, the residual and the tangential system matrix will be introduced to enable the application of a Newton-Raphson method.

4.1 Governing equations

Based on the general model presented in section 2.4.3, the balance equations for the temperature field are obtained as special case by neglecting all mechanical terms, which finally leads to the instationary heat conduction equation. Hence, the energy balance (2.70) reduces to

$$\rho_0 \left(\dot{\psi} \, + \, \dot{T} \, \eta \, + \, T \, \dot{\eta} \right) \, = \, - \operatorname{Div} \boldsymbol{Q} \, + \, \rho_0 \, r \quad \text{in } \Omega_0 \, , \tag{4.1}$$

where all mechanical terms are neglected and the rate of the internal energy $\dot{e}$ is replaced using (2.81). The target application of the present thesis is on coupled generally nonlinear thermo-structure interaction (TSI) problems, where the initial and the current domains are not equal, i.e. $\Omega_0 \neq \Omega$. Thus, for the sake of simplicity and in view of the later coupled TSI problem, all following relations are expressed in material quantities.

A purely thermal analysis is independent of the deformation, so that reference and current configuration are identical and the domain remains constant, i.e. $\Omega_0 \equiv \Omega$. Consequently, for a purely thermal analysis, the equations can be treated similar to a geometrically linear analysis, where e.g. the deformation gradient $\boldsymbol{F}$ reduces to the identity tensor $\boldsymbol{I}$ so that $\boldsymbol{F} \equiv \boldsymbol{I}$. As a next step, the general potential (2.88) is reduced to the thermal terms, resulting in

$$\psi(T, \operatorname{Grad} T) \, , \tag{4.2}$$

where the potential ψ depends only on the temperatures T and the temperature gradients $\operatorname{Grad} T$. To describe thermodynamically admissible processes, the second law of thermodynamics, for

instance in form (2.94), neglecting again all mechanical terms, has to be satisfied. Subsequently, time derivation of (4.2) reads

$$\dot{\psi} \;=\; \frac{\partial \psi}{\partial T}\,\dot{T} \;+\; \frac{\partial \psi}{\partial \mathrm{Grad}\, T} \cdot (\mathrm{Grad}\, T)^{\cdot}\,. \tag{4.3}$$

Introducing (4.3) into the reduced form of (2.94) then yields

$$-\,\rho_0 \left(\frac{\partial \psi}{\partial T} \;+\; \eta\right) \dot{T} \;-\; \rho_0\, \frac{\partial \psi}{\partial \mathrm{Grad}\, T} \cdot (\mathrm{Grad}\, T)^{\cdot} \;-\; \frac{1}{T}\, \boldsymbol{Q} \cdot \mathrm{Grad}\, T \;\;\geq\; 0\,, \tag{4.4}$$

where the entropy η is defined by the first term of (4.4) or by (2.99). In contrast to the purely mechanical theory in chapter 3, the entropy η cannot be neglected for the thermal field but represents a variable of the problem at hand. Moreover, the second term of (4.4) is determined according to (2.100). Hence, the entropy inequality reduces to the heat conduction dissipation $\mathcal{D}_{\mathsf{cond}}$ introduced in its spatial version in (2.82). Accordingly, the material version follows as

$$\mathcal{D}_{\mathsf{cond}} \;=:\; -\,\frac{1}{T}\, \boldsymbol{Q} \cdot \mathrm{Grad}\, T \;\;\geq\; 0\,. \tag{4.5}$$

Next, the specific heat C_{V} is established and is defined according to the thermodynamical principles as the amount of heat required to change a unit mass of a substance by one degree in temperature, i.e.

$$C_{\mathsf{V}} \;=\; \frac{\partial e}{\partial T}\,. \tag{4.6}$$

The index $(\cdot)_{\mathsf{V}}$ denotes that C_{V} is measured at constant volume. Using the International System of Units (SI), C_{V} is expressed in joules per kelvin. Substituting the internal energy using the Legendre transformation (2.80) and (2.99), the specific heat at constant volume follows as

$$C_{\mathsf{V}} \;=\; -\frac{\partial^2 \psi}{\partial T^2}\, T \;=\; \frac{\partial \eta}{\partial T}\, T\,. \tag{4.7}$$

Exemplarily, the Helmholtz free energy (4.2) per unit reference volume is chosen to

$$\rho_0\, \psi(T) \;=\; -\rho_0\, C_{\mathsf{V}} \left[(T \;-\; T_0) \;-\, T \ln\left(\frac{T}{T_0}\right)\right], \tag{4.8}$$

where T_0 and C_{V} denote the constant initial temperature and the constant specific heat, respectively. In general, the heat capacity depends on the deformation and on the temperature. However, for the application to elastomers, see for instance Netz [96], the heat capacity C_{V} can be assumed to depend only on the temperature. Furthermore, for the application to metals, a constant specific heat capacity (i.e. $C_{\mathsf{V}} = const.$) is a valid assumption, utilised e.g. in Adam and Ponthot [1], Ghadiani [48], Ibrahimbegovic and Chorfi [61], and Simo and Miehe [122]. Accordingly, the heat capacity is also assumed to be constant (i.e. $C_{\mathsf{V}} = const.$), since focus in this work is on the application to metals. Subsequently, the entropy and its time derivative yield

$$\eta(T) = \; -\frac{\partial \psi}{\partial T} \;=\; C_{\mathsf{V}} \ln\left(\frac{T}{T_0}\right), \tag{4.9}$$

$$\dot{\eta}(T) = \; \frac{\partial \eta}{\partial T}\, \dot{T} \;=\; -\frac{\partial^2 \psi}{\partial T^2}\, \dot{T} \;=\; C_{\mathsf{V}}\, \frac{1}{T}\, \dot{T}\,. \tag{4.10}$$

Including (4.2)-(4.10) into (4.1) and reformulating, postulates the strong form of the instationary heat equation via

$$\rho_0 \, C_{\mathsf{V}} \, \dot{T} \;=\; -\mathrm{Div}\, \boldsymbol{Q} \;+\; \rho_0 \, r \quad \text{in } \Omega_0 \,. \tag{4.11}$$

As previously mentioned, in a purely thermal analysis the deformation is neglected, consequently the material and spatial heat flux coincide, that is $\boldsymbol{Q} \equiv \boldsymbol{q}$, which is also valid for the material and spatial gradient, hence $\mathrm{Grad}\, T \equiv \mathrm{grad}\, T$. Subsequently, to satisfy (4.5), a constitutive law for the heat flux has to be chosen associating the heat flux $\boldsymbol{q}$ with its dual variable $\mathrm{grad}\, T$ and the temperature T. Accordingly, so-called Fourier's law proposed by Fourier [41], which is linear and isotropic is utilised, which is defined as

$$\boldsymbol{q} \;=\; -k \, \mathrm{grad}\, T \,. \tag{4.12}$$

Herein, the thermal conductivity k is assumed constant and positive that is $k \geq 0$. Thus, heat is conducted in the direction of decreasing temperatures. Apart from Fourier's law, different constitutive laws for the heat flux are available in the literature, as e.g. Duhamel's law of heat conduction (see e.g. Holzapfel [58]) which uses a positive semi-definite second-order tensor $\boldsymbol{k}$ instead of the constant conductivity k. If Duhamel's law is restricted to thermally isotropic behaviour (i.e. no preferred direction), the conductivity tensor reduces to $\boldsymbol{k} \;=\; k \, \boldsymbol{I}$. If a constant heat conductivity $k \;=\; const.$ is assumed, Fourier's law is recovered as a special form of Duhamel's law. Moreover, e.g. in Holzapfel and Simo [59] and Sherief and Abd El-Latief [117], a variable conductivity ($k \neq const.$) is assumed in the context of elastomers. In Bargmann and Steinmann [13] and Bargmann et al. [14], three different constitutive laws for the heat flux $\boldsymbol{q}$ are proposed based on the Green-Naghdi's non-classical theory. Nevertheless, for the present work Fourier's law as stated in (4.12) yields physical results and hence is exclusively considered in this thesis.

4.2 Finite element formulation and solution schemes

The IBVP of the thermal field is described by the equations (4.11) and (4.12) combined with the kinematic relations presented in section 2.1, as well as with a set of initial conditions and boundary conditions. The boundary $\partial\Omega_0$ is divided into pairwise disjoint boundary parts $\partial\Omega_0 = \Gamma_{0;\mathsf{D};\mathsf{T}} \cup \Gamma_{0;\mathsf{N};\mathsf{T}}$ where the index T represents the boundary of the thermo problem. Dirichlet and Neumann boundary conditions are prescribed on $\Gamma_{0;\mathsf{D};\mathsf{T}}$ and $\Gamma_{0;\mathsf{N};\mathsf{T}}$, respectively, as follows:

$$T = \hat{T} \quad \text{on } \Gamma_{0;\mathsf{D};\mathsf{T}} \,, \tag{4.13}$$

$$-\boldsymbol{Q} \cdot \boldsymbol{n}_0 = \hat{Q} \quad \text{on } \Gamma_{0;\mathsf{N};\mathsf{T}} \,. \tag{4.14}$$

Herein, $\hat{Q}$ is defined as the heat flux in opposite or negative direction of the outward normal vector indicated by the negative value of $-\boldsymbol{Q} \cdot \boldsymbol{n}_0$, i.e. inflow into the body is postulated to be positive. On a specific part $\Gamma_{0;\mathsf{C};\mathsf{T}}$ of the Neumann boundary $\Gamma_{0;\mathsf{N};\mathsf{T}}$, a heat flux according to Newton's law of heat dissipation, so-called heat convection boundary conditions, can be prescribed in the following form:

$$-\boldsymbol{Q} \cdot \boldsymbol{n}_0 \;=\; -(-k \, \mathrm{Grad}\, T) \cdot \boldsymbol{n}_0 \;=:\; \hat{Q}_{\mathsf{C}} \;=\; h \, (T \;-\; T_\infty) \quad \text{on } \Gamma_{0;\mathsf{C};\mathsf{T}} \tag{4.15}$$

with linear heat transfer coefficient h and ambient temperature T_∞ of the surrounding. Given the initial temperature field T_0, the initial condition at $t = 0$ reads

$$T_0 \;=\; T(\boldsymbol{X}, t = 0) \;=\; \hat{T}_0 \quad \text{in } \Omega_0 \,. \tag{4.16}$$

A weak form of the instationary heat conduction equation is obtained by multiplication of (4.11) and (4.14) with the virtual temperatures δT followed by integration by parts as

$$\begin{aligned} &\int_{\Omega_0} \rho_0 \, C_{\mathsf{V}} \, \dot{T} \, \delta T \, \mathrm{d}V_0 \;-\; \int_{\Omega_0} \boldsymbol{Q} \cdot \mathrm{Grad}\, \delta T \, \mathrm{d}V_0 \\ &- \int_{\Gamma_{0;\mathsf{N};\mathsf{T}} \setminus \Gamma_{0;\mathsf{C};\mathsf{T}}} \hat{Q} \, \delta T \, \mathrm{d}A_0 \;-\; \int_{\Gamma_{0;\mathsf{C};\mathsf{T}}} \hat{Q}_{\mathsf{C}} \, \delta T \, \mathrm{d}A_0 \;-\; \int_{\Omega_0} \rho_0 \, r \, \delta T \, \mathrm{d}V_0 \;=\; 0 \,, \end{aligned} \tag{4.17}$$

where the virtual temperatures δT are assumed to $\delta T = 0$ on $\Gamma_{0;\mathsf{D};\mathsf{T}}$. In contrast to the weak form of the structural field (3.11) which describes virtual works $\delta \mathcal{W}$, the weak form of the thermal field (4.17) describes the rate of virtual work, i.e. a virtual power $\delta \mathcal{P}$.

4.2.1 Space discretisation

The FEM is applied for spatial discretisation of the thermal equation (4.17). The present derivations are based on the corresponding explanations for the structural field, see section 3.2.1.1. Thus, as for the structural field, the isoparametric concept is applied for the thermal field as well. In accordance with (3.14) for the displacements, the discrete temperatures for an element e are introduced by

$$T^{(e)}(\boldsymbol{X}, t) \;\approx\; T^{(e);h}(\boldsymbol{X}, t) \;=\; \sum_{I=1}^{\mathsf{nnod}} \check{N}_I(\boldsymbol{X}) \, \mathbf{T}_I(t) \,, \tag{4.18}$$

where I and nnod are the current node and the total number of nodes per elements, respectively. The shape function denotes $\check{N}$ and $\mathbf{T}$ is the nodal temperature vector. The temperature rates $\dot{T}$ and the virtual temperatures δT are discretised equally. The Bubnov-Galerkin approach is used for the thermo field as well, thus the same shape functions for the temperature T and its virtual counterpart δT are used. Furthermore, polynomials are used for the shape functions. Depending on the number of nodes and the order of the polynomial, different finite element shapes are constructed. Exemplarily, for three-dimensions eight-noded hexahedral elements (named Hex8), or 27-noded hexahedral elements (named Hex27) can be mentioned. While Hex8 elements use linear polynomials in each direction, Hex27 use quadratic polynomials in each direction.

For evaluation of the weak form (4.17), the Gauss quadrature is used as numerical integration technique. Consequently, the element is expressed in local coordinates $\boldsymbol{\xi}$ by mapping the global quantities into the parameter space, see (3.15), yielding for the temperatures

$$T^{(e);h}(\boldsymbol{\xi}, t) \;=\; \sum_{I=1}^{\mathsf{nnod}} N_I(\boldsymbol{\xi}) \, \mathbf{T}_I(t) \,, \tag{4.19}$$

where N defines the shape functions in the parameter space. Subsequently, based on (3.17), all elementwise contributions are assembled, which leads to the semi-discrete weak form of the

instationary heat conduction equation

$$\delta\mathbf{T}\,[\mathbf{C}\,\dot{\mathbf{T}} \,+\, \mathbf{f}_{\mathsf{int;T}}(\mathbf{T}) \,-\, \mathbf{f}_{\mathsf{ext;T}}(\mathbf{T})] \,=\, 0\,, \tag{4.20}$$

with the capacity matrix $\mathbf{C}$, the internal force vector $\mathbf{f}_{\mathsf{int;T}}$, the external force vector $\mathbf{f}_{\mathsf{ext;T}}$, and the global vectors of virtual temperatures $\delta\mathbf{T}$, temperature rates $\dot{\mathbf{T}}$, and temperatures $\mathbf{T}$, respectively. It is noted here, that the heat convection boundary term (4.15), which depends on the current temperature T, is part of the external force vector, hence $\mathbf{f}_{\mathsf{ext;T}}(\mathbf{T})$ depends on the solution vector $\mathbf{T}$. By assuming arbitrary virtual temperatures $\delta\mathbf{T}$, (4.20) can equivalently be rewritten to

$$\mathbf{C}\,\dot{\mathbf{T}} \,+\, \mathbf{f}_{\mathsf{int;T}}(\mathbf{T}) \,-\, \mathbf{f}_{\mathsf{ext;T}}(\mathbf{T}) \,=\, \mathbf{0}\,. \tag{4.21}$$

Equation (4.21) describes the semi-discrete thermal system of equation. Since it is still continuous in time, in the following time discretisation is performed.

4.2.2 Time discretisation

The fully discrete thermal equation is obtained by applying a finite difference scheme to (4.21). As for the structural field, different time integration schemes are available for the thermal field: explicit schemes in the form of a forward Euler time integration and implicit schemes, as e.g. the generalised-α method and the one-step-θ method. For the target application to thermo-fluid-structure interaction (TFSI), explicit schemes are applicable due to very small time steps required in the flow solver. For details on the present TFSI approach, see e.g. Hammerl et al. [53]. The present thesis aims at pure TSI, thus implicit schemes are the method of choice due to improved stability behaviour and due to allowing larger time steps. Moreover, according to the structural field, a quasi-static approach for the thermal field can be realised by neglecting the capacity term ($\mathbf{C}\,\dot{\mathbf{T}}$). However, in contrast to the structural field, this represents a special rare case.

In the following, the presentation is restricted to the generalised-α method, because the one-step-θ scheme can be derived as a special case of it. For the thermal field, the method is based on the work of Jansen et al. [63]. Following the approach for the second-order structural system of equation in Chung and Hulbert [25] (see section 3.2.2.1), they developed the generalised-α method for first-order systems of equations, such as the Navier-Stokes equation in fluid dynamics or the present thermo field. Equivalently to (3.26), the endpoint solutions for the temperature rates at t_{n+1} can be expressed as

$$\dot{\mathbf{T}}_{n+1} \,\approx\, \mathbf{t}_{n+1} \,=\, \frac{\mathbf{T}_{n+1} \,-\, \mathbf{T}_n}{\gamma_{\mathsf{T}}\,\Delta t} \,-\, \frac{1 \,-\, \gamma_{\mathsf{T}}}{\gamma_{\mathsf{T}}}\,\dot{\mathbf{T}}_n \tag{4.22}$$

introducing the approximated thermal rate vector $\mathbf{t}_{n+1}$ and using the unknown primary variable $\mathbf{T}_{n+1}$, known quantities at t_n, and the algorithmic parameter $\gamma_{\mathsf{T}} \in [0,\,1]$. Subsequently, utilising the generalised-α method, the evaluation point of the first-order thermal equation is shifted from t_{n+1} to the generalised mid-points $t_{n+\alpha_{\mathsf{m;T}}}$ and $t_{n+\alpha_{\mathsf{f;T}}}$ (in contrast to the generalised midpoints of the structural equation $t_{n+1-\alpha_{\mathsf{m}}}$ and $t_{n+1-\alpha_{\mathsf{f}}}$). Herein, the index T emphasizes the thermal field. Thus, the discrete quantities for temperatures and temperature rates follow as

$$\mathbf{T}_{n+\alpha_{\mathsf{f;T}}} \,=\, \alpha_{\mathsf{f;T}}\,\mathbf{T}_{n+1} \,+\, (1 \,-\, \alpha_{\mathsf{f;T}})\,\mathbf{T}_n\,, \tag{4.23}$$

$$\mathbf{t}_{n+\alpha_{\mathsf{m;T}}} \,=\, \alpha_{\mathsf{m;T}}\,\mathbf{t}_{n+1} \,+\, (1 \,-\, \alpha_{\mathsf{m;T}})\,\mathbf{t}_n\,, \tag{4.24}$$

respectively, with the two additional generalised-α parameters $\alpha_{\mathsf{m};\mathsf{T}} \in [0,\,1]$ and $\alpha_{\mathsf{f};\mathsf{T}} \in [0,\,1]$. Corresponding values at the end of the time interval t_{n+1} are expressed by a linear interpolation

$$\mathbf{T}_{n+1} \;=\; \mathbf{T}_n \;+\; \Delta t \left[\gamma_{\mathsf{T}}\, \mathbf{t}_{n+1} \;+\; (1 \;-\; \gamma_{\mathsf{T}})\, \mathbf{t}_n\right]. \tag{4.25}$$

Moreover, according to Jansen et al. [63], an optimal set of parameter is given by

$$\gamma_{\mathsf{T}} \;=\; 0.5 \;+\; \alpha_{\mathsf{m};\mathsf{T}} \;-\; \alpha_{\mathsf{f};\mathsf{T}}\,, \quad \alpha_{\mathsf{m};\mathsf{T}} \;\geq\; \alpha_{\mathsf{f};\mathsf{T}} \;\geq\; 0.5\,, \tag{4.26}$$

which defines a stable and second-order accurate time integration scheme. The maximal spectral radius $\rho_{\infty;\mathsf{T}}$ can be used as sole free algorithmic parameter, equivalent to (3.33), (3.34), and to Jansen et al. [63]. Hence, a second-order accurate scheme is given by the three generalised-α parameters

$$\alpha_{\mathsf{f};\mathsf{T}} = \frac{1}{\rho_{\infty;\mathsf{T}} \;+\; 1}\,, \quad \alpha_{\mathsf{m};\mathsf{T}} = \frac{1}{2}\,\frac{3 \;-\; \rho_{\infty;\mathsf{T}}}{\rho_{\infty;\mathsf{T}} \;+\; 1}\,, \quad \gamma_{\mathsf{T}} \;=\; \frac{1}{2} \;+\; \alpha_{\mathsf{m};\mathsf{T}} \;-\; \alpha_{\mathsf{f};\mathsf{T}}\,. \tag{4.27}$$

For the approximation of the force vectors $\mathbf{f}_{\mathsf{int};\mathsf{T};n+\alpha_{\mathsf{f};\mathsf{T}}}$ and $\mathbf{f}_{\mathsf{ext};\mathsf{T};n+\alpha_{\mathsf{f};\mathsf{T}}}$, a so-called tr-like approach is chosen as in (3.32). Thus, exemplarily the internal force vector is interpolated between solutions at t_n and t_{n+1}

$$\begin{aligned} \mathbf{f}_{\mathsf{int};\mathsf{T};n+\alpha_{\mathsf{f}}} \;&=\; \alpha_{\mathsf{f};\mathsf{T}}\, \mathbf{f}_{\mathsf{int};\mathsf{T};n+1} \;+\; (1 \;-\; \alpha_{\mathsf{f};\mathsf{T}})\, \mathbf{f}_{\mathsf{int};\mathsf{T};n} \\ &=\; \alpha_{\mathsf{f};\mathsf{T}}\, \mathbf{f}_{\mathsf{int};\mathsf{T}}(\mathbf{T}_{n+1}) \;+\; (1 \;-\; \alpha_{\mathsf{f};\mathsf{T}})\, \mathbf{f}_{\mathsf{int};\mathsf{T}}(\mathbf{T}_n)\,. \end{aligned} \tag{4.28}$$

The external force vector is interpolated equivalently. By including the results of this subsection into (4.21), the fully discrete equation of heat conduction is obtained as

$$\mathbf{C}\, \mathbf{t}_{n+\alpha_{\mathsf{m};\mathsf{T}}} \;+\; \mathbf{f}_{\mathsf{int};\mathsf{T}}(\mathbf{T}_{n+\alpha_{\mathsf{f};\mathsf{T}}}) \;-\; \mathbf{f}_{\mathsf{ext};\mathsf{T}}(\mathbf{T}_{n+\alpha_{\mathsf{f};\mathsf{T}}}) \;=\; \mathbf{0}\,. \tag{4.29}$$

Furthermore, for $\theta_{\mathsf{T}} := \gamma_{\mathsf{T}}$ and $\alpha_{\mathsf{m};\mathsf{T}} = \alpha_{\mathsf{f};\mathsf{T}} = 1$, the so-called generalised trapezoidal rule (or one-step-θ scheme) is obtained as a special case of the generalised-α method. Unconditionally stable fully implicit schemes of the one-step-θ time integration, as desired in this work, can only be realised for parameter $\theta_{\mathsf{T}} \in [0.5,\,1]$. Subsequently, the corresponding fully discrete thermo equation applying an one-step-θ scheme follows as

$$\begin{aligned} \mathbf{C}\, \frac{\mathbf{T}_{n+1} - \mathbf{T}_n}{\Delta t} \;&+\; \theta_{\mathsf{T}} \Big[\mathbf{f}_{\mathsf{int};\mathsf{T}}(\mathbf{T}_{n+1}) \;-\; \mathbf{f}_{\mathsf{ext};\mathsf{T}}(\mathbf{T}_{n+1})\Big] \;+ \\ &+\; (1 - \theta_{\mathsf{T}}) \Big[\mathbf{f}_{\mathsf{int};\mathsf{T}}(\mathbf{T}_n) \;-\; \mathbf{f}_{\mathsf{ext};\mathsf{T}}(\mathbf{T}_n)\Big] \;=\; \mathbf{0}\,, \end{aligned} \tag{4.30}$$

which corresponds to the structural form (3.39).

4.3 Linearisation and solution techniques for nonlinear equations

The fully discrete instationary heat conduction equation (4.29) describes a linear system of equations. However, due to the coupling terms emerging in the final TSI framework (see chapter 5),

the target TSI system of equation will be nonlinear, so that the solution will require an iterative method as the Newton-Raphson iteration scheme.

To provide the thermal field as general as possible, even the pure thermo problem is rewritten in incremental form. Subsequently, the residual is defined for a given Newton iteration step i as

$$\mathbf{r}_{\mathsf{T}}(\mathbf{T}^{i}_{n+1}) \;=\; \mathbf{C}\,\mathbf{t}^{i}_{n+\alpha_{\mathsf{m;T}}} \;+\; \mathbf{f}_{\mathsf{int;T}}(\mathbf{T}^{i}_{n+\alpha_{\mathsf{f;T}}}) \;-\; \mathbf{f}_{\mathsf{ext;T}}(\mathbf{T}^{i}_{n+\alpha_{\mathsf{f;T}}})\,. \tag{4.31}$$

Based on the structural linear system (3.45) and the thermal residual (4.31), the thermal linear system yields

$$\mathbf{K}_{\mathsf{TT}}(\mathbf{T}^{i}_{n+1})\,\Delta\mathbf{T}^{i+1}_{n+1} \;=\; -\mathbf{r}_{\mathsf{T}}(\mathbf{T}^{i}_{n+1})\,, \tag{4.32}$$

where $\mathbf{K}_{\mathsf{TT}}$ and $\Delta\mathbf{T}^{i+1}_{n+1}$ denote the thermal dynamic effective tangential matrix and the incremental temperature vector, respectively. The temperature vector can be updated via

$$\mathbf{T}^{i+1}_{n+1} \;=\; \mathbf{T}^{i}_{n+1} \;+\; \Delta\mathbf{T}^{i+1}_{n+1}\,. \tag{4.33}$$

The Newton loop is aborted if prescribed user-defined convergence criteria for solution vector and residual, see (3.47) and (3.48), are fulfilled. Hence, the temperature solution $\mathbf{T}_{n+1} \;=\; \mathbf{T}^{i+1}_{n+1}$ is found. Since the present purely thermal problem is linear, a solution of (4.32) is achieved for $\Delta\mathbf{T}^{i+1}_{n+1}$ after one single iteration.

In the context of heat convection boundary condition it is noted, that two versions exist for the heat convection boundary conditions $\hat{Q}_{\mathsf{C}}$. Based on (4.15), $\hat{Q}_{\mathsf{C}}$ can either be discretised using the old converged solution $\mathbf{T}_n$ or the current temperatures $\mathbf{T}_{n+1}$. The first simplified version $\hat{Q}_{\mathsf{C}}(\mathbf{T}_n)$ does not contribute to the linearisation, whereas the second version $\hat{Q}_{\mathsf{C}}(\mathbf{T}_{n+1})$ requires linearisation with respect to $\mathbf{T}_{n+1}$ so that terms for $\mathbf{K}_{\mathsf{TT}}$ arise. Subsequently, in case of heat convection boundary conditions, the full version, i.e. $\hat{Q}_{\mathsf{C}}(\mathbf{T}_{n+1})$ is utilised.

4.4 Solution techniques for linear equations

Finally, a solver has to be chosen for the solution of thermal linear system (4.32). According to section 3.5, direct and iterative solvers introduced for the solution of the structural field can be utilised equally for the thermal field. The reader is referred to this section 3.5 for details on the available solvers.

5 Thermo-structure interaction

The problem of thermo-structure interaction (TSI) is the actual topic of interest of this thesis. It describes a coupled problem of the two physical fields structure and thermo. In particular, the TSI problem is a volume-coupled problem, i.e. at each point of the domain the two fields are coupled. This is in contrast to surface-coupled problems, as for instance fluid-structure interaction (FSI) problems, which are only coupled at the interface between the fluid and the structural domain. Based on the procedure of setting up the system of equations for the single fields structure and thermo, see chapter 3 and chapter 4, respectively, the coupled TSI problem is derived. Moreover, the nonlinear continuum thermodynamics (see chapter 2) provides further basic relations.

Metals show isotropic behaviour due to thermal loads. This means, that a temperature change causes purely volumetric deformations which are equal in each direction. The temperature is inserted into solid mechanics by temperature-dependent stresses. These thermal stresses can be introduced in two forms: firstly by thermal strains and secondly by a thermomechanical potential. The assumption of thermal strains is common in infinitesimal thermo-elasto-plasticity with the total strain tensor $\boldsymbol{\varepsilon}$ being split into

$$\boldsymbol{\varepsilon} \;=\; \boldsymbol{\varepsilon}^e \;+\; \boldsymbol{\varepsilon}^p \;+\; \boldsymbol{\varepsilon}^t \,, \tag{5.1}$$

i.e. in addition to elastic and plastic strains, $\boldsymbol{\varepsilon}^e$ and $\boldsymbol{\varepsilon}^p$, respectively, thermal strains $\boldsymbol{\varepsilon}^t$ arise. They are defined as

$$\boldsymbol{\varepsilon}^t \;=\; \alpha_{\mathsf{T}}\, \Delta T\, \boldsymbol{I} \tag{5.2}$$

with the coefficient of thermal expansion (CTE) α_{T} and the temperature difference ΔT which is defined as the difference between the current temperature T and the initial temperature T_0, that is $\Delta T = T - T_0$. Thus, for linear thermoelasticity, assuming Hooke's law, the stress yields $\boldsymbol{\sigma} \;=\; E\,\boldsymbol{\varepsilon}^e \;=\; E\,\boldsymbol{\varepsilon} - E\,\alpha_{\mathsf{T}}\,\Delta T\,\boldsymbol{I}$, where (5.1) and (5.2) are used and $\boldsymbol{\varepsilon}^p \equiv 0$. This approach is used, e.g. in André [5], Bornemann and Wall [18, 19], and Kuhl et al. [69]. The second possibility, namely a thermomechanical potential, represents the default strategy in finite deformation thermomechanical analysis, see for instance Adam and Ponthot [1], Bargmann and Steinmann [13], Glaser [50], Holzapfel [58], Ibrahimbegovic and Chorfi [61], and Simo and Miehe [122]. Here, the temperature T is included in the constitutive law. Following the setup of finite strain plasticity in the general non-isothermal case, in addition to the plastic intermediate configuration $\breve{\Omega}$ depicted in Figure 3.5, a thermal intermediate configuration has to be considered, cf. e.g. Erbts and Düster [38], Glaser [51], Hartmann [54], Holzapfel [58], Miehe [87], and Netz [96], i.e.

$$\boldsymbol{F} \;=\; \boldsymbol{F}^t \cdot \boldsymbol{F}^e \cdot \boldsymbol{F}^p \,. \tag{5.3}$$

Alternatively, for instance in Holzapfel [58] and Hartmann [54], the opposite order compared to (5.3), that is $\boldsymbol{F} \;=\; \boldsymbol{F}^e \cdot \boldsymbol{F}^t$ is employed for the study of thermoelastic elastomers. For the application to isotropic thermal expansion, Hartmann [54] showed that both order yielded the

same expressions for stress and entropy. Since the present work does not investigate elastomers, the multiplicative split (5.3) is exclusively considered in this work.

In contrast to the thermal deformations which are solely volumetric, for most metals the volume remains constant during plastic deformations. Hence, plastic deformations are assumed isochoric ($J^p = \det \boldsymbol{F}^p = 1$, see (2.37)). Subsequently, based on (5.3) the Jacobi determinant (2.7) can be used to further express volumetric deformations as

$$J \;=\; J^t \, J^e \,. \tag{5.4}$$

This corresponds to the so-called Duhamel-Neumann hypothesis for the theory of finite deformations, i.e. to (5.1) for linear thermoelasticity where $\boldsymbol{\varepsilon}^p = \boldsymbol{0}$. According to Lu and Pister [81], the thermal expansion is assumed to be

$$J^t \;=\; \frac{\mathrm{d}V}{\mathrm{d}V_0} \;=\; \exp\left(3\,\alpha_\mathsf{T}\,\Delta T\right). \tag{5.5}$$

Linearisation of (5.5) with respect to the initial configuration yields for isotropic materials $J^t \;=\; 1 \,+\, 3\,\alpha_\mathsf{T}\,\Delta T$, which corresponds to the infinitesimal linear theory. Thus, instead of a multiplicative split shown in (5.4), in the following the volumetric deformation is expressed by

$$J^e \;=\; J^e(T) \;=\; J\,J^{t\,-1}\,. \tag{5.6}$$

Consequently, the additional thermal intermediate configuration can be omitted and volumetric deformations are described only by J^e. For instance, if thermal stresses arise due to a temperature change, elastic strains balance the body which implicitly correspond to thermal strains according to (5.6). For further details on the derivation of (5.6), the reader is referred to the literature mentioned above and Willner [145].

5.1 Governing equations

The target of the present work is to establish a general approach for TSI. Hence, based on the general framework for a constitutive model, presented in section 2.4.3, with the general TSI potential (2.89), which comprises mechanical, thermal, and thermomechanical terms, the general approach is subsequently specified for the application to small and finite strain TSI. Since thermal loads lead to purely volumetric and plastic loads to purely isochoric deformation, respectively, the complete deformation behaviour can be described as a sum of the thermoelastic and the plastic contribution. Thus, according to (3.57), (3.82) or (3.175), the constitutive TSI law postulates a potential

$$\psi(\boldsymbol{F}, T, \operatorname{grad} T, \boldsymbol{\alpha}_\mathsf{k}, \boldsymbol{X}) \;=\; \psi^e(\boldsymbol{F}, T, \operatorname{grad} T, \boldsymbol{X}) \;+\; \psi^p(\boldsymbol{F}, T, \boldsymbol{\alpha}_\mathsf{k}, \boldsymbol{X}) \tag{5.7}$$

with the thermoelastic and plastic potentials, ψ^e and ψ^p, respectively. Since ψ^p, can possibly include temperature-dependent material parameters, the temperature T enters the plastic potential. As explained in Stainier and Ortiz [128], for metals it is valid to assume that the elastic deformation behaviour and the purely thermal energy are independent of the internal, i.e. plastic processes. Hence, the energy ψ is decomposed additively into uncoupled contributions of

the single effects. To emphasize this additive decomposition, the Helmholtz free energy ψ in (5.7) is expressed with respect to the reference volume, so that ψ is reformulated using potential functions according to

$$\rho_0\,\psi(\boldsymbol{F},T,\operatorname{grad}T,\boldsymbol{\alpha}_{\mathsf{k}},\boldsymbol{X}) := \hat{\mathbb{U}}(J^e) + \hat{\mathbb{W}}(\tilde{\boldsymbol{F}}) + \hat{\mathbb{M}}(J^e,T) + \hat{\mathbb{T}}(T) + \hat{\mathbb{K}}(\boldsymbol{\alpha}_{\mathsf{k}},T)\,, \quad (5.8)$$

where in contrast to the deformation gradient $\boldsymbol{F}$, the Jacobi-determinant J^e (5.6) and the isochoric deformation gradient $\tilde{\boldsymbol{F}}$ (2.36) are applied. $\hat{\mathbb{U}}$ and $\hat{\mathbb{W}}$ can be identified with the standard hyperelastic materials potentials according to (3.57), whereas $\hat{\mathbb{M}}(J^e,T)$ describes the thermomechanical coupling potential. The potential $\hat{\mathbb{T}}(T)$ represents the purely thermal potential and is assumed identical to (4.8). Finally, $\hat{\mathbb{K}}(\boldsymbol{\alpha}_{\mathsf{k}},T)$ is the convex plastic potential. Subsequently, based on the potential functions, the coupling of the two fields structure and thermo can be explained: the temperature enters the structural field via additional thermal stresses and possibly moreover via temperature-dependent material parameters. Herein, $\hat{\mathbb{M}}(J^e,T)$ characterizes the thermomechanical coupling potential, leading to thermal stresses and moreover to thermal expansion and dilatation, whereas $\hat{\mathbb{K}}(\boldsymbol{\alpha}_{\mathsf{k}},T)$ being temperature-dependent and therefore enables exemplarily von Mises plasticity combined with temperature-dependent isotropic hardening and thermal softening. This is in accordance to Agelet de Saracibar et al. [2], Ibrahimbegovic and Chorfi [61], but in contrast to Simo and Miehe [122], who assumed an isothermal plastic potential $\hat{\mathbb{K}}_{\mathsf{Simo}}(\boldsymbol{\alpha}_{\mathsf{k}})$. In contrast, the structure enters the thermal field via coupling terms, arising from $\hat{\mathbb{M}}(J^e,T)$ and $\hat{\mathbb{K}}(\boldsymbol{\alpha}_{\mathsf{k}},T)$, in addition to the purely thermal energy (4.8). Thus, coupling terms as the internal or mechanical dissipation $\mathcal{D}_{\mathsf{mech}}$ may emerge in the thermal balance equation. Furthermore, for finite deformation TSI, where the initial domain Ω_0 deforms to Ω, so that $\Omega \neq \Omega_0$, and a Lagrangian formulation is used, the deformation enters the thermal field additionally due to the mapping of all quantities in the balance equations to the reference configuration.

In the following, the corresponding balance equations for a general nonlinear TSI problems are established. In this context, equilibrium of the overall TSI problem is achieved if the balance of linear momentum and the nonlinear instationary heat equation are solved for the displacements $\boldsymbol{u}$ and the temperatures T.

5.1.1 Structural field

The balance of linear momentum, utilised to describe the mechanical field of a thermomechanical solid within the TSI framework, is described by the strong or the weak form, (3.1) and (3.11), respectively. Since in TSI the potential is defined by (5.7), the structural balance equation modifies to

$$\int_{\Omega_0}\rho_0\,\ddot{\boldsymbol{u}}\cdot\delta\boldsymbol{u}\,\mathrm{d}V_0 + \int_{\Omega_0}\delta\boldsymbol{E}^{\mathsf{T}}_{\mathsf{GL}} : \boldsymbol{S}(\boldsymbol{F},T,\boldsymbol{\alpha}_{\mathsf{k}},\boldsymbol{X})\,\mathrm{d}V_0 - \int_{\Omega_0}\hat{\boldsymbol{b}}_0\cdot\delta\boldsymbol{u}\,\mathrm{d}V_0 - \int_{\Gamma_{0;\mathsf{N};\mathsf{S}}}\hat{\boldsymbol{t}}_0\cdot\delta\boldsymbol{u}\,\mathrm{d}A_0 = 0\,, \quad (5.9)$$

where the stresses $\boldsymbol{S}$ depend on mechanical variables $(\boldsymbol{F},\boldsymbol{\alpha}_{\mathsf{k}})$ and on the temperature T. The mechanical initial boundary value problem (IBVP) is described by (5.9), the boundary and initial conditions (3.2)-(3.6), and finally by a constitutive law for the stresses, which will be specified later in section 5.3.

5.1.2 Thermo field

The nonlinear instationary heat conduction equation, utilised for modelling the temperature field of coupled TSI, can be obtained following the procedure presented in chapter 4 where instead of the potential (4.8), the thermomechanical potential (5.8) is used. As the second law of thermodynamics must be satisfied, (2.95), (2.99), (2.101), and (2.102) must be valid. The first term of (2.102), i.e. the mechanical dissipation $\mathcal{D}_{\mathsf{mech}}$ is given, e.g. by (3.194), whereas the second term of (2.102) represents the heat conductivity dissipation $\mathcal{D}_{\mathsf{cond}}$ which associates the material heat flux $\boldsymbol{Q}$ with the material temperature gradient $\mathrm{Grad}\, T$. Taking into account (4.12), the material heat flux $\boldsymbol{Q}$ is obtained as pull-back of the spatial heat flux $\boldsymbol{q}$ (4.12), i.e.

$$\boldsymbol{Q} \;=\; -k_0\, \boldsymbol{C}^{-1} \cdot \mathrm{Grad}\, T \tag{5.10}$$

with the reference thermal conductivity k_0 and the inverse of the right Cauchy-Green deformation tensor $\boldsymbol{C}^{-1}$, see (2.12). Furthermore, $k_0 := Jk$ and it is assumed to be constant and positive, whereas k is the deformation-dependent thermal conductivity. Subsequently, the entropy (4.9) and its rate (4.10) are required, as shown in chapter 4. Hence, by assuming (5.8)

$$\begin{aligned} \eta(\boldsymbol{F}, T, \boldsymbol{\alpha}_{\mathsf{k}}) \;&=\; -\frac{\partial \psi}{\partial T} \;=\; -\frac{1}{\rho_0}\Big(\frac{\partial \hat{\mathbb{M}}(J^e, T)}{\partial T} \;-\; \frac{\partial \hat{\mathbb{T}}(T)}{\partial T} \;-\; \frac{\partial \hat{\mathbb{K}}(\boldsymbol{\alpha}_{\mathsf{k}}, T)}{\partial T}\Big) \\ &=\; C_{\mathsf{V}} \ln\Big(\frac{T}{T_0}\Big) \;-\; \frac{1}{\rho_0}\Big(\frac{\partial \hat{\mathbb{M}}(J^e, T)}{\partial T} \;+\; \frac{\partial \hat{\mathbb{K}}(\boldsymbol{\alpha}_{\mathsf{k}}, T)}{\partial T}\Big)\,, \end{aligned} \tag{5.11}$$

$$\begin{aligned} \dot{\eta}(\boldsymbol{F}, T, \boldsymbol{\alpha}_{\mathsf{k}}) \;&=\; C_{\mathsf{V}}\, \frac{1}{T}\, \dot{T} \;-\; \frac{1}{\rho_0}\Big(\frac{\partial^2 \hat{\mathbb{M}}(J^e, T)}{\partial T\, \partial J^e}\, \dot{J}^e \;+\; \frac{\partial^2 \hat{\mathbb{M}}(J^e, T)}{\partial T^2}\, \dot{T} + \\ &\quad + \frac{\partial^2 \hat{\mathbb{K}}(\boldsymbol{\alpha}_{\mathsf{k}}, T)}{\partial T^2}\, \dot{T} \;+\; \frac{\partial^2 \hat{\mathbb{K}}(\boldsymbol{\alpha}_{\mathsf{k}}, T)}{\partial T\, \partial \boldsymbol{\alpha}_{\mathsf{k}}} \star \dot{\boldsymbol{\alpha}}_{\mathsf{k}}\Big)\,, \end{aligned} \tag{5.12}$$

where C_{V} denotes the constant heat capacity, see (4.7), and $\dot{J}^e$ is the rate of the elastic Jacobi determinant, see (5.6). Based on (5.12), the so-called thermo-elasto-plastic heating term or Gough-Joule effect $\mathcal{H}^{ep}$ is defined as

$$\mathcal{H}^{ep} := T\, \frac{1}{\rho_0}\Big(\frac{\partial^2 \hat{\mathbb{M}}(J^e, T)}{\partial T\, \partial J^e}\, \dot{J}^e + \frac{\partial^2 \hat{\mathbb{M}}(J^e, T)}{\partial T^2}\, \dot{T} + \frac{\partial^2 \hat{\mathbb{K}}(\boldsymbol{\alpha}_{\mathsf{k}}, T)}{\partial T^2}\, \dot{T} + \frac{\partial^2 \hat{\mathbb{K}}(\boldsymbol{\alpha}_{\mathsf{k}}, T)}{\partial T\, \partial \boldsymbol{\alpha}_{\mathsf{k}}} \star \dot{\boldsymbol{\alpha}}_{\mathsf{k}}\Big)\,, \tag{5.13}$$

which represents a further coupling term for the thermal equation in addition to $\mathcal{D}_{\mathsf{mech}}$. Since the given potential (5.8) describes a general thermo-elasto-plastic material, the index $(\cdot)^{ep}$ indicates that the term is defined by elastic and plastic terms. In contrast in case of thermoelasticity, this term reduces to the thermoelastic heating term $\mathcal{H}^e$.

By combining the aforementioned results with the first law of thermodynamics, the change in temperature can be determined by

$$\rho_0\, C_{\mathsf{V}}\, \dot{T} \;+\; \mathrm{Div}\, \boldsymbol{Q} \;-\; \rho_0\, r \;-\; \mathcal{D}_{\mathsf{mech}} \;-\; \mathcal{H}^{ep} \;=\; 0 \quad \text{in } \Omega_0\,, \tag{5.14}$$

denoting the strong form of the thermomechanically instationary heat conduction equation. Thus, the thermal IBVP of TSI is given by (5.10), (5.14), and by the boundary and initial conditions (4.13)-(4.16). Analogous to (4.17), the weak form is established based on (5.14) and (4.14), by

introducing virtual temperatures δT and applying integration by parts. Hence, the weak form reads

$$\int_{\Omega_0} \rho_0 \, C_{\mathsf{V}} \, \dot{T} \, \delta T \, \mathrm{d}V_0 \; - \int_{\Omega_0} \boldsymbol{Q} \cdot \mathrm{Grad} \, \delta T \, \mathrm{d}V_0 \; - \int_{\Omega_0} \mathcal{D}_{\mathsf{mech}} \, \delta T \, \mathrm{d}V_0 \; - \int_{\Omega_0} \mathcal{H}^{ep} \, \delta T \, \mathrm{d}V_0 \; - \\ - \int_{\Gamma_{0;\mathsf{N};\mathsf{T}} \setminus \Gamma_{0;\mathsf{C};\mathsf{T}}} \hat{Q} \, \delta T \, \mathrm{d}A_0 \; - \int_{\Gamma_{0;\mathsf{C};\mathsf{T}}} \hat{Q}_{\mathsf{C}} \, \delta T \, \mathrm{d}A_0 \; - \int_{\Omega_0} \rho_0 \, r \, \delta T \, \mathrm{d}V_0 \; = \; 0 \, . \tag{5.15}$$

In the following, the boundary of the heat convection is further investigated. Within the purely thermal analysis in chapter 4, the deformation was neglected as $\boldsymbol{F} \equiv \boldsymbol{I}$, so that a material version of the heat convection boundary was given by (4.15). This is also valid for a geometrically linear TSI analysis. In contrast, for the given general geometrically nonlinear TSI case, the pull-back of (4.15) using Nanson's formula (2.10) results in the fully material version, i.e.

$$\begin{aligned} -\boldsymbol{q} \cdot \boldsymbol{n} \, \mathrm{d}A \; &= \; h \, (T \, - \, T_\infty) \, \mathrm{d}A \; = \; \hat{q}_{\mathsf{C}} \, \mathrm{d}A \\ &= \; h \, (T \, - \, T_\infty) \, J \, \sqrt{\boldsymbol{n}_0^{\mathsf{T}} \cdot \boldsymbol{C}^{-1} \cdot \boldsymbol{n}_0} \, \mathrm{d}A_0 \; =: \; \hat{Q}_{\mathsf{C}} \, \mathrm{d}A_0 \, , \end{aligned} \tag{5.16}$$

where the pull-back of the infinitesimal area element of the current configuration $\mathrm{d}A$ is utilised, defined as

$$\mathrm{d}A \; = \; J \, \sqrt{\boldsymbol{n}_0^{\mathsf{T}} \cdot \boldsymbol{C}^{-1} \cdot \boldsymbol{n}_0} \, \mathrm{d}A_0 \, , \tag{5.17}$$

leading to the material equivalent $\mathrm{d}A_0$. As previously mentioned, material versions of balance equations still describe equilibrium with respect to the current configuration. Via pull-back to the reference configuration the terms can be expressed in its material form, which usually simplifies the equation. For instance, the reference domain Ω_0 is known and constant, subsequently the differentials $\mathrm{d}\Omega_0$ in the weak form are independent of the deformation, so that they do not contribute to the linearisation process. Thus, for solving the integral terms in the weak form, the terms are mapped from the reference configuration to the parameter space and evaluated afterwards using, e.g. Gauss quadrature as introduced in section 3.2.1.1. As depicted in (5.16), the material form of heat convection boundary conditions is more complicated compared to its spatial form. Hence, instead of the standard procedure described above, the procedure of curvilinear coordinates, proposed in section 2.1.2, is adopted here for the coupled nonlinear heat convection boundary conditions. Instead of performing a pull-back of $\hat{q}_{\mathsf{C}} \, \mathrm{d}A$ from current to the reference configuration (via φ^{-1}) and from reference into the parameter space (via ζ^{-1}), the mapping $(\varphi \circ \zeta)^{-1}$ is directly performed, i.e. the term is directly mapped from the current configuration into the parameter space and computed there afterwards using Gauss quadrature. Subsequently, the boundary term is evaluated by

$$\int_{\Gamma_{\mathsf{C}}} \hat{q}_{\mathsf{C}} \, \mathrm{d}A \; = \int_{\Gamma_{\mathsf{C}}} h \, (T \, - \, T_\infty) \, \mathrm{d}A \; = \int_{-1}^{1} \int_{-1}^{1} h \, (T \, - \, T_\infty) \, |\check{\boldsymbol{n}}| \, \mathrm{d}\xi^1 \, \mathrm{d}\xi^2 \, , \tag{5.18}$$

where the scalar-valued physical infinitesimal area element of the current configuration $\mathrm{d}A$ according to (2.34) is utilised which is part of the boundary Γ_c. As the current infinitesimal area $\mathrm{d}A$ is deformation-dependent, the term contributes to the consistent linearisation process. In contrast

to the material term in (5.17), this linearisation can easier be performed. Consequently, the weak form of the thermo problem is expressed by

$$\begin{aligned} &\int_{\Omega_0} \rho_0\, C_{\mathsf{V}}\, \dot{T}\, \delta T \,\mathrm{d}V_0 \;-\; \int_{\Omega_0} \boldsymbol{Q} \cdot \mathrm{Grad}\, \delta T \,\mathrm{d}V_0 \;-\; \int_{\Omega_0} \mathcal{D}_{\mathsf{mech}}\, \delta T \,\mathrm{d}V_0 \;- \\ &- \int_{\Omega_0} \mathcal{H}^{ep}\, \delta T \,\mathrm{d}V_0 \;-\; \int_{\Gamma_{0;\mathsf{N};\mathsf{T}} \setminus \Gamma_{0;\mathsf{C};\mathsf{T}}} \hat{Q}\, \delta T \,\mathrm{d}A_0 \;-\; \int_{\varphi(\Gamma_{0;\mathsf{C};\mathsf{T}})} \hat{q}_{\mathsf{C}}\, \delta T \,\mathrm{d}A \;-\; \int_{\Omega_0} \rho_0\, r\, \delta T \,\mathrm{d}V_0 \;=\; 0\,, \end{aligned} \tag{5.19}$$

where $\varphi(\Gamma_{0;\mathsf{C};\mathsf{T}})$ denotes the mapping of the boundary $\Gamma_{0;\mathsf{C};\mathsf{T}}$ to the current configuration according to Figure 2.1.

5.2 Space and time discretisation

After having defined the weak forms of the balance equations for TSI, i.e. (5.9) and (5.19), utilising a Lagrangian description, a numerical solution is obtained by applying the finite element method (FEM) for spatial discretisation and a finite difference method for temporal discretisation, resulting in the fully discrete TSI equations.

In this context, it is worth mentioning that the Lagrangian approach is advantageous for the whole nonlinear TSI problem. For instance considering the structural field whose domain is deformed as a result of an applied deformation: due to the volume-coupling, the domain of the thermo field has to experience the same deformation, yielding the same deformed domain. A Lagrangian description refers all quantities to the initial domain Ω_0, which is per definition identical for both fields. Hence, no additional effort is required to transform the thermal domain according to the structural domain. In contrast, using an Euler approach for the thermo field would require additional effort since transformation operations would be necessary to get the deformed thermal domain.

In the present thesis, a conforming element approach is employed for the TSI problem, i.e. the spatial discretisation of both fields structure and thermo are identical. However, since the TSI is based on separate discretisations for both fields, a non-conforming element approach can also be realised. Ongoing work is concerned which this aspect which will contribute to increase the efficiency and the flexibility of the TSI solution. Thus, it will be possible to choose different meshes due to the physical requirements of the single field. For instance a fine mesh will be applied for thermo field at regions where high heat fluxes will be excepted whereas a coarse mesh will be sufficient for the corresponding structure. Subsequently, the computational costs will be reduced since, e.g. less structural element evaluations need to be performed.

The procedure of setting up the system of equation for TSI comprises the procedure of the single fields, thus the present explanations are based on sections 3.2.1 and 4.2 for the structural and thermal field, respectively. Consequently, the global semi-discrete equations of the TSI problem follow as

$$\mathbf{M}\,\ddot{\mathbf{d}} \;+\; \mathbf{D}\,\dot{\mathbf{d}} \;+\; \mathbf{f}_{\mathsf{int};\mathsf{S}}(\mathbf{d},\mathbf{T}) \;-\; \mathbf{f}_{\mathsf{ext};\mathsf{S}} \;=\; \mathbf{0}\,, \tag{5.20}$$

$$\mathbf{C}\,\dot{\mathbf{T}} \;+\; \mathbf{f}_{\mathsf{int};\mathsf{T}}(\mathbf{T},\mathbf{d}) \;-\; \mathbf{f}_{\mathsf{ext};\mathsf{T}}(\mathbf{T},\mathbf{d}) \;=\; \mathbf{0}\,, \tag{5.21}$$

with the global mass and damping matrix $\mathbf{M}$ and $\mathbf{D}$, the structural internal and external force vector $\mathbf{f}_{\mathsf{int};\mathsf{S}}$ and $\mathbf{f}_{\mathsf{ext};\mathsf{S}}$, and the global acceleration, velocity and displacement vectors $\ddot{\mathbf{d}}$, $\dot{\mathbf{d}}$ and $\mathbf{d}$,

respectively. Moreover, $\mathbf{C}$ denotes the capacity matrix, $\mathbf{f}_{\mathsf{int;T}}$ and $\mathbf{f}_{\mathsf{ext;T}}$ denote the thermal internal and external force vector, and $\dot{\mathbf{T}}$ and $\mathbf{T}$ are the global vectors of temperature rate and temperature, respectively. In (5.20) and (5.21), the coupling is established. For instance, in the structural equation (5.20), the structural internal force vector $\mathbf{f}_{\mathsf{int;S}}(\mathbf{d}, \mathbf{T})$ is temperature-dependent and in the thermal equation (5.21), the thermal internal and external force vectors, $\mathbf{f}_{\mathsf{int;T}}(\mathbf{T}, \mathbf{d})$ and $\mathbf{f}_{\mathsf{ext;T}}(\mathbf{T}, \mathbf{d})$, are both deformation-dependent.

The given equations are discretised with standard finite elements (FEs) where the order of the polynomial is chosen according to the requirements of the problem. In the context of thermo-plastic modelling at finite strains, different FE approaches are available. As explained in section 3.2.1.2 for a purely mechanical analysis with isothermal finite strain plasticity, volumetric locking arises for standard linear displacement-based FE elements (as e.g. (tri-)linearly interpolated hexahedral elements) due to the incompressibility constraint. Hence, the F-bar method has been introduced to circumvent the emerging volumetric locking. Subsequently, for TSI with finite strain thermo-elasto-plasticity, the approach of section 3.2.1.2 is extended. Consequently, the F-bar method is applied to the whole structural equation (5.20), i.e. the element technology is applied to the mechanical and the thermal stresses, further details are explained in Appendix D.2. In contrast, standard FE elements are chosen for the thermal field. Choosing different kinds of element technology for the structural field and standard FE elements for the thermal field represents a common strategy in literature, see for instance Adam and Ponthot [1], Glaser [51], Miehe [90], and Miehe et al. [92]. In contrast, approaches exist where element technology is extended to both fields, as e.g. in Ibrahimbegovic and Chorfi [61], Simo and Miehe [122]. Moreover, as an alternative to circumvent locking, quadratic elements as the 27-noded (tri-)quadratically interpolated hexahedral elements are utilised which are applied for both fields equally.

Subsequently, the fully discrete system of equation for TSI is obtained by time discretisation of (5.20) and (5.21) according to sections 3.2.2 and 4.2.2. Consequently, using an one-step-θ scheme, the TSI system results in

$$\begin{aligned} \mathbf{M}\,\frac{\mathbf{v}_{n+1}-\mathbf{v}_n}{\Delta t} \;&+\; \theta_{\mathsf{S}}\left[\mathbf{D}\,\mathbf{v}_{n+1} + \mathbf{f}_{\mathsf{int;S}}(\mathbf{d}_{n+1},\mathbf{T}_{n+1}) - \mathbf{f}_{\mathsf{ext;S};n+1}\right] + \\ &+\; (1-\theta_{\mathsf{S}})\left[\mathbf{D}\,\mathbf{v}_n + \mathbf{f}_{\mathsf{int;S}}(\mathbf{d}_n,\mathbf{T}_n) - \mathbf{f}_{\mathsf{ext;S};n}\right] = \mathbf{0}\,, \end{aligned} \tag{5.22}$$

$$\begin{aligned} \mathbf{C}\,\frac{\mathbf{T}_{n+1}-\mathbf{T}_n}{\Delta t} \;&+\; \theta_{\mathsf{T}}\left[\mathbf{f}_{\mathsf{int;T}}(\mathbf{T}_{n+1},\mathbf{d}_{n+1}) - \mathbf{f}_{\mathsf{ext;T}}(\mathbf{T}_{n+1},\mathbf{d}_{n+1})\right] + \\ &+\; (1-\theta_{\mathsf{T}})\left[\mathbf{f}_{\mathsf{int;T}}(\mathbf{T}_n,\mathbf{d}_n) - \mathbf{f}_{\mathsf{ext;T}}(\mathbf{T}_n,\mathbf{d}_n)\right] = \mathbf{0}\,, \end{aligned} \tag{5.23}$$

or in

$$\mathbf{M}\,\mathbf{a}_{n+1-\alpha_{\mathsf{m;S}}} + \mathbf{D}\,\mathbf{v}_{n+1-\alpha_{\mathsf{f;S}}} + \mathbf{f}_{\mathsf{int;S;n+1}-\alpha_{\mathsf{f;S}}}(\mathbf{d},\mathbf{T}) - \mathbf{f}_{\mathsf{ext;S};n+1-\alpha_{\mathsf{f;S}}} = \mathbf{0}\,, \tag{5.24}$$

$$\mathbf{C}\,\mathbf{t}_{n+\alpha_{\mathsf{m;T}}} + \mathbf{f}_{\mathsf{int;T;n}+\alpha_{\mathsf{f;T}}}(\mathbf{T},\mathbf{d}) - \mathbf{f}_{\mathsf{ext;T}}(\mathbf{T}_{n+\alpha_{\mathsf{f;T}}}) = \mathbf{0}\,, \tag{5.25}$$

using a generalised-α method. For the sake of clarity, the indices S and T differentiate the algorithmic parameter of the structural and thermal field, respectively. It is worth mentioning, that in a coupled problem, the time integration plays an important role. A consistent solution is only established if the coupled fields are evaluated at the same point in time. Otherwise, this may cause problems leading to possibly unphysical solutions. Details on this topics will be drawn in section 6 where the different solution techniques for the TSI problem will be presented.

5.3 Constitutive laws for thermo-structure interaction problems

As noted above, constitutive laws have to be chosen to close the thermomechanical problem at hand while fulfilling the second law of thermodynamics. According to (2.82) or (2.104), two sub-potentials are necessary. Firstly, to satisfy the thermal dissipation $\mathcal{D}_{\mathsf{cond}}$, Fourier's law (4.12) is exclusively utilised to determine the heat fluxes. Secondly, a thermomechanical potential is necessary which must fulfil the mechanical dissipation $\mathcal{D}_{\mathsf{mech}}$ and which is used to determine the stresses, the entropy and the coupling terms of the thermo equation arising in TSI, i.e. $\mathcal{D}_{\mathsf{mech}}$ and $\mathcal{H}^{ep}$. Based on the mechanical potentials introduced in section 3.4 and the thermal potential (4.8), in the following extended thermomechanical potentials will be presented. As the TSI problem will be solved with an exact Newton method, a consistent linearisation of the whole problem is required. Subsequently, in addition to the stresses, the material tangent $\mathscr{C}_{\mathsf{mat}}$ will be determined which is a fourth-order tensor. Since the stresses will include mechanical and thermal parts, a thermal material tangent $\boldsymbol{C}_{\mathsf{T}}$ may further arise according to

$$\boldsymbol{C}_{\mathsf{T}} = \frac{\partial \boldsymbol{S}}{\partial T}\,, \tag{5.26}$$

which represents a second-order tensor. For TSI, two kinds of thermomechanical materials are generally distinguished, namely thermoelastic and thermo-elasto-plastic materials. These two kinds will be explained in the following sections based on the corresponding isothermal structural materials presented in section 3.4.

5.3.1 Thermoelasticity

In the following, two isotropic thermo-hyperelastic constitutive models are proposed based on the elastic material models of section 3.4.1, which are extended to temperature-dependence. Hence, a thermomechanical potential is described as the sum of different potentials, which comprises a mechanical potential given in (3.53) or (3.51), the thermal potential (4.8) and a coupling potential. Thus, the temperature-dependent Saint Venant-Kirchhoff (TSVK) material utilised, e.g. in Glaser [51], and the compressible thermo-hyperelastic material model based on Simo and Miehe [122] are established. The Helmholtz free energy per unit reference volume for these two materials postulates

$$\begin{aligned}\rho_0\,\psi_{\mathsf{TSVK}}(\boldsymbol{E}_{\mathsf{GL}},T) = \Psi_{\mathsf{TSVK}} &= \underbrace{\mu(T)\,\boldsymbol{E}_{\mathsf{GL}}:\boldsymbol{E}_{\mathsf{GL}} + \frac{\lambda(T)}{2}\,(\operatorname{tr}\boldsymbol{E}_{\mathsf{GL}})^2}_{\hat{\mathbb{U}}(\boldsymbol{E}_{\mathsf{GL}},T)+\hat{\mathbb{W}}(\boldsymbol{E}_{\mathsf{GL}},T)} \\ &\quad \underbrace{+\,m_0(T)\,\Delta T\,(\operatorname{tr}\boldsymbol{E}_{\mathsf{GL}})}_{\hat{\mathbb{M}}(\boldsymbol{E}_{\mathsf{GL}},T)} \underbrace{-\,\rho_0\,C_{\mathsf{V}}\left(T\ln\frac{T}{T_0} - \Delta T\right)}_{\hat{\mathbb{T}}(T)}\,,\end{aligned} \tag{5.27}$$

$$\rho_0\,\psi_{\mathsf{TESIMO}}(\boldsymbol{B},T) \;=\; \Psi_{\mathsf{TESIMO}} \;=\; \underbrace{\frac{K}{2}\left(\frac{1}{2}\left(J^{e\,2}\;-\;1\right)\;-\;\ln\,J^{e\,2}\right)}_{\hat{\mathbb{U}}(J^e)} + \underbrace{\frac{\mu}{2}\left(\operatorname{tr}\tilde{\boldsymbol{B}}\;-\;3\right)}_{\hat{\mathbb{W}}(\tilde{\boldsymbol{B}})} + \\ + \underbrace{\frac{m_0}{2}\,\Delta T\left(\frac{J^{e\,2}\;-\;1}{J^e}\right)}_{\hat{\mathbb{M}}(J^e,T)}\;\underbrace{-\rho_0\,C_{\mathsf{V}}\left(T\ln\frac{T}{T_0}\;-\;\Delta T\right)}_{\hat{\mathbb{T}}(T)}\,, \tag{5.28}$$

where the abbreviation "TESIMO" represent the thermoelastic version of the model in Simo and Miehe [122]. Moreover, the corresponding potential functions per reference volume Ψ_{TSVK} and Ψ_{TESIMO} are included in (5.27) and (5.28), respectively. In (5.28), the stress-temperature modulus defined as

$$m_0 \;=\; -\,(2\,\mu\;+\;3\,\lambda)\,\alpha_{\mathsf{T}}\,, \tag{5.29}$$

the Lamé constants λ and μ (see (3.52)), and the bulk modulus K (see (3.125)) are used. As homogeneous bodies are treated $\alpha_{\mathsf{T}} = const.$, see Parkus [103]. The TSVK material includes a temperature-dependent Young's modulus $E(T)$ which can be approximated using a polynomial function. Consequently, for this material the Lamé constants, the bulk modulus, and hence the stress-temperature modulus are also temperature-dependent, i.e. $\mu(T)$, $\lambda(T)$, $K(T)$, and $m_0(T)$, respectively. In contrast, for the TESIMO material the parameters are constants. Based on the potentials (5.27) and (5.28), and including equation (2.96), (3.55), and (3.56), the second Piola-Kirchhoff stresses follow as

$$\boldsymbol{S}_{\mathsf{TSVK}} = \underbrace{2\,\mu(T)\,\boldsymbol{E}_{\mathsf{GL}}\;+\;\lambda(T)\operatorname{tr}\boldsymbol{E}_{\mathsf{GL}}\,\boldsymbol{I}}_{\boldsymbol{S}_{\mathsf{dT}}} + \underbrace{m_0\,\Delta T\,\boldsymbol{I}}_{\boldsymbol{S}_{\mathsf{T}}}\,, \tag{5.30}$$

$$\boldsymbol{S}_{\mathsf{TESIMO}} = \underbrace{\frac{K}{2}\left(J^{e\,2}\;-\;1\right)\boldsymbol{C}^{-1}\;+\;\boldsymbol{F}^{-1}\cdot\left(\mu\,\operatorname{dev}\tilde{\boldsymbol{B}}\right)\cdot\boldsymbol{F}^{-\mathsf{T}}}_{\boldsymbol{S}_{\mathsf{d}}} + \underbrace{\frac{m_0}{2}\,\Delta T\,\frac{\left(J^{e\,2}\;+\;1\right)}{J^e}\,\boldsymbol{C}^{-1}}_{\boldsymbol{S}_{\mathsf{dT}}}\,. \tag{5.31}$$

Herein, the stresses can be additively split. For the TSVK material, thermomechanical and purely thermal stresses can be distinguished, i.e. $\boldsymbol{S}_{\mathsf{dT}}$ and $\boldsymbol{S}_{\mathsf{T}}$, while for the TESIMO material model, purely mechanical and thermomechanical stresses, $\boldsymbol{S}_{\mathsf{d}}$ and $\boldsymbol{S}_{\mathsf{dT}}$, respectively are distinguished. Subsequently, the material tangents are determined. While the determination of $\mathscr{C}_{\mathsf{mat}}$ follows standard procedures, the thermal tangent is specified for the two materials, based on (5.26), to

$$\boldsymbol{C}_{\mathsf{T;TSVK}} \;=\; 2\,\frac{\partial\mu(T)}{\partial T}\,\boldsymbol{E}_{\mathsf{GL}}\;+\;\frac{\partial\lambda(T)}{\partial T}\operatorname{tr}\boldsymbol{E}_{\mathsf{GL}}\,\boldsymbol{I}\;+\;m_0\,\boldsymbol{I}\,, \tag{5.32}$$

$$\boldsymbol{C}_{\mathsf{T;TESIMO}} \;=\; \frac{m_0}{2}\,\frac{\left(J^{e\,2}\;+\;1\right)}{J^e}\,\boldsymbol{C}^{-1}\,. \tag{5.33}$$

In the following, the thermoelastic coupling term $\mathcal{H}^e$ is determined according to (5.13), leading for the TSVK and the TESIMO material to

$$\mathcal{H}^e_{\mathsf{TSVK}} \;=\; T\,m_0\operatorname{tr}\dot{\boldsymbol{E}}_{\mathsf{GL}}\,, \tag{5.34}$$

$$\mathcal{H}^e_{\mathsf{TESIMO}} \;=\; T\,\frac{m_0}{2}\,\frac{J^{e\,2}\;+\;1}{J^e}\,\boldsymbol{C}^{-1}:\dot{\boldsymbol{E}}_{\mathsf{GL}}\,, \tag{5.35}$$

respectively. Thermoelastic materials are treated here, i.e. no energy is dissipated, which implies that the dissipation in (5.19) vanishes and $\mathcal{D}_{\mathsf{mech}} \equiv 0$.

5.3.2 Thermo-elasto-plasticity

Based on the elastoplastic materials in section 3.4.2, in the following thermo-elasto-plastic materials will be presented. For the small strain regime, two thermo-elasto-plastic material models will be distinguished. First, a von Mises thermo-elasto-plastic material model with mixed hardening will be developed which is based on the elastoplastic material model of section 3.4.2.3. This material model is used, e.g. in Kuhl et al. [69] in a slightly modified version. Subsequently, the so-called Robinson's viscoplastic material model, originally proposed by Robinson and Swindeman [110] and extended to the non-isothermal case, e.g. in Bornemann and Wall [18], will be established. Finally, in the context of finite strains, the thermo-hyperelasto-plastic material model of Simo and Miehe [122] will be developed.

As introduced in section 2.4, the phenomenological approach to thermodynamics with internal variables is applied in the following. Hence, based on a chosen energy potential ψ, the stresses and the entropy can be determined. Hereby, the equilibrium contributions belong to the thermoelastic response, while the non-equilibrium contributions belong to the plastic response of the material, so that irreversible, dissipative effects are described via the evolution of the internal variables, i.e. by $\dot{\boldsymbol{\alpha}}_{\mathsf{k}}$. As a stress-free initial configuration is assumed, at $t = 0$ all internal variables $\boldsymbol{\alpha}_{\mathsf{k}}$ vanish. If the evolution equations for the internal variables $\boldsymbol{\alpha}_{\mathsf{k}}$ are fulfilled together with the balance equations, a thermodynamical equilibrium is achieved.

Since in plasticity irreversible processes are described, energy dissipates to heat leading to a dissipation $\mathcal{D} \geq 0$. Hence, apart from stresses and the thermo-elasto-plastic heating term $\mathcal{H}^{ep}$, the mechanical dissipation $\mathcal{D}_{\mathsf{mech}}$ will be determined for each material model.

Thermo-elasto-plasticity is solved using an elastic predictor/plastic corrector solution strategy, as proposed in section 3.4.2.2. Instead of an elastic predictor, the predictor comprises an thermoelastic predictor phase followed by a plastic corrector phase. This strategy is used, e.g. in Kuhl [68] and Kuhl et al. [69] for small strain thermoplasticity and in Simo and Miehe [122] and Fritsch [44] for finite strain thermoplasticity.

5.3.2.1 Linear thermo-elasto-plastic material

As mentioned above, the present linear thermo-elasto-plastic material model represents an extension of the linear isothermal elastoplastic material model of section 3.4.2.3. In addition to the purely mechanical model, where mechanical stresses are described by (3.138), thermal stresses arise, so that the total stress yields

$$\boldsymbol{\sigma}_{n+1} = \underbrace{\left[\boldsymbol{\mathscr{C}}^{e}_{\mathsf{mat}} - \hat{H}(\Phi^{\mathsf{trial}})\,\frac{\Delta\gamma\,6\,G^2}{\bar{q}^{\mathsf{trial}}_{n+1}}\,\boldsymbol{\mathscr{I}}_{\mathsf{d}}\right] : \boldsymbol{\varepsilon}^{e;\mathsf{trial}}_{n+1} + \hat{H}(\Phi^{\mathsf{trial}})\,\frac{\Delta\gamma\,3\,G}{\bar{q}^{\mathsf{trial}}_{n+1}}\,\boldsymbol{\beta}_n}_{\boldsymbol{\sigma}_{\mathsf{d}}} + \underbrace{m_0\,\Delta T\,\boldsymbol{I}}_{\boldsymbol{\sigma}_{\mathsf{T}}} . \tag{5.36}$$

Herein, equivalent to (5.7) and (5.8), the linear stress can be additively decomposed into mechanically elastoplastic and thermal stresses, $\boldsymbol{\sigma}_{\mathsf{d}}$ and $\boldsymbol{\sigma}_{\mathsf{T}}$, respectively. This thermo-elasto-plastic material model is able to show mixed hardening, i.e. nonlinear isotropic hardening and linear kinematic hardening, as well as temperature-dependent stresses. While the mechanical material tangent is described by (3.140), the thermal tangent follows as

$$\boldsymbol{C}_{\mathsf{T}} = m_0\,\boldsymbol{I} . \tag{5.37}$$

Subsequently, the thermo-elasto-plastic heating term and the mechanical dissipation follow as

$$\mathcal{H}^e = T\, m_0 \operatorname{tr} \dot{\boldsymbol{\varepsilon}}^e \tag{5.38}$$

$$\mathcal{D}_{\mathsf{mech}} = \boldsymbol{\eta} : \dot{\boldsymbol{\varepsilon}}^p - \kappa(\bar{\varepsilon}^p)\, \dot{\bar{\varepsilon}}^p\,, \tag{5.39}$$

respectively. It is noted here, that due to the chosen linear Prager-Ziegler's law (3.132), the influence of the kinematic hardening in $\mathcal{H}^{ep}$ vanishes, consequently $\mathcal{H}^{ep} \equiv \mathcal{H}^e$, i.e. the thermo-elasto-plastic heating terms reduces to the thermoelastic heating term.

5.3.2.2 Robinson's viscoplastic material

In this section, the so-called Robinson's viscoplastic material proposed by Arya [8, 9] and Arya and Arnold [10] and adopted by Bornemann and Wall [18, 19] is presented. The basic version of the viscoplastic Robinson's material model in Robinson and Swindeman [110] describes a purely mechanical material. Subsequently, this model is extended to the non-isothermal case, e.g. in Arya and Arnold [10], Bornemann and Wall [18, 19], and moreover in Providakis [106] for a boundary element method (BEM). Motivated by the application to rocket thrust chambers in the publications of Arya, this material is established for the present thesis as well. For instance in Arya [8], Robinson's material is used in the context of unified viscoplastic finite element stress-strain analysis where it is compared to experiments on thrust chambers composed of NARloy-Z. NARloy-Z is a copper-based alloy. In this context unified means, that the inelastic strains cover plasticity, creep, relaxation, etc.. Different version of Robinson's material exist. In the present thesis, the version of Arya and Arnold [10] is utilised. The presentation is restricted to the main equations. For further details on the Robinson's material, the reader is referred to the literature mentioned above.

Robinson's material is an isotropic viscoplastic material model which includes kinematic hardening. Hence, the inelastic strains $\boldsymbol{\varepsilon}^p$ and the back stress $\boldsymbol{\beta}$ are the internal variables of this model, i.e. $\boldsymbol{\alpha}_{\mathsf{k}} = \{\boldsymbol{\varepsilon}^p, \boldsymbol{\beta}\}$. The material model is based on the additive split of strains according to (5.1) with the thermal strains $\boldsymbol{\varepsilon}^t$ (5.2) and the viscoplastic strains $\boldsymbol{\varepsilon}^p$, so that the total strain rate follows as

$$\dot{\boldsymbol{\varepsilon}} = \dot{\boldsymbol{\varepsilon}}^e + \dot{\boldsymbol{\varepsilon}}^p + \dot{\boldsymbol{\varepsilon}}^t\,. \tag{5.40}$$

According to Hooke's law (3.61), the elastic strain rates $\dot{\boldsymbol{\varepsilon}}^e$ are related to the stress rates $\dot{\boldsymbol{\sigma}}$ by

$$\dot{\boldsymbol{\varepsilon}}^e = \boldsymbol{\mathscr{C}}_{\mathsf{mat}}^{e\,-1} : \dot{\boldsymbol{\sigma}}\,, \tag{5.41}$$

where $\boldsymbol{\mathscr{C}}_{\mathsf{mat}}^{e\,-1}$ is the inverse of Hooke's elastic material tangent. Based on the notation proposed in Freed et al. [42], Robinson's material can be handled in a thermodynamically consistent way. Therefore, the Gibbs free enthalpy ζ is introduced, in contrast to the Helmholtz free energy ψ or the internal energy e, which represents an energy in the variables stress and temperature. Via Legendre-transformation

$$\zeta(\boldsymbol{\sigma}, T) = e - T\,\eta - \frac{1}{\rho_0}\,\boldsymbol{\sigma} : \boldsymbol{\varepsilon}^e\,, \tag{5.42}$$

i.e. the enthalpy can be related to the internal energy $e(\boldsymbol{\varepsilon}, \eta)$. Moreover, ζ is the mechanical complementary energy to the Helmholtz free energy $\psi(\boldsymbol{\varepsilon}, T)$. Subsequently, the Gibbs free enthalpy can be used to define a potential for the given Robinson material by

$$\zeta(\boldsymbol{\sigma}, T, \boldsymbol{\varepsilon}^p) = \zeta^e(\boldsymbol{\sigma}, T) + \zeta^p(\boldsymbol{\sigma}, T, \boldsymbol{\varepsilon}^p)\,, \tag{5.43}$$

where the thermoelastic free enthalpy of Hooke-like material and the plastic contributions are assumed as

$$\begin{aligned}\rho_0\,\zeta^e(\boldsymbol{\sigma},T) \;&=\; \frac{\rho_0}{2}\,\boldsymbol{\sigma}:\boldsymbol{\mathscr{C}}^{e\,-1}_{\mathsf{mat}}:\boldsymbol{\sigma}\;+\;\rho_0\,\alpha_{\mathsf{T}}\,\boldsymbol{I}:\boldsymbol{\sigma}\,\Delta T\;+\;\eta_0\,\Delta T\,-\\ &\quad-\rho_0\,C_{\mathsf{V}}\left(T_0\ln\frac{T}{T_0}\;-\;\Delta T\right),\end{aligned}\tag{5.44}$$

$$\rho_0\,\zeta^p(\boldsymbol{\sigma},T,\boldsymbol{\varepsilon}^p)=\;\frac{1}{3}\,H^{\mathsf{kin}}\,\boldsymbol{\varepsilon}^p:\boldsymbol{\varepsilon}^p\tag{5.45}$$

with the initial entropy value η_0 and the kinematic hardening modulus H^{kin}. Using (5.44), the elastic strains and the entropy result in

$$\boldsymbol{\varepsilon}^e=\;-\rho_0\,\frac{\partial\zeta}{\partial\boldsymbol{\sigma}}\;=\boldsymbol{\mathscr{C}}^{e\,-1}_{\mathsf{mat}}:\boldsymbol{\sigma}\;+\;\Delta T\,\alpha_{\mathsf{T}}\,\boldsymbol{I}\,,\tag{5.46}$$

$$\eta=\;-\frac{\partial\zeta}{\partial T}\;=\;\rho_0\,\alpha_{\mathsf{T}}\,\boldsymbol{I}:\boldsymbol{\sigma}\;+\;\eta_0\;-\;\rho_0\,C_{\mathsf{V}}\left(\frac{T_0}{T}\;-\;1\right),\tag{5.47}$$

where (5.46) can be transformed such that an equation for the stresses $\boldsymbol{\sigma}$ depending on elastic strains $\boldsymbol{\varepsilon}^e$ and the temperature increment ΔT follows as

$$\boldsymbol{\sigma}\;=\;\boldsymbol{\mathscr{C}}^{e}_{\mathsf{mat}}:(\boldsymbol{\varepsilon}^e\;-\;\alpha_{\mathsf{T}}\,\Delta T\,\boldsymbol{I})\,.\tag{5.48}$$

To determine the unified plastic strains, the yield function is first assumed to

$$\Phi\;=\;\frac{J_2(\boldsymbol{\eta})}{K^2}\;-\;1\,,\tag{5.49}$$

where $K\;=\;K(T)$ is a temperature-dependent material parameter, $\boldsymbol{\eta}$ is the relative stress or overstress (3.129) using the deviatoric stress $\boldsymbol{s}$ (2.49), and $J_2(\boldsymbol{\eta})$ is the second invariant of the effective stress according to (B.23). According to the Kuhn-Tucker conditions (3.71), plasticity can only occur in the Robinson material if the two conditions are fulfilled, namely the yield function (5.49) and the scalar product of deviatoric and back stresses have to be both greater than zero, i.e.

$$\Phi\;\overset{!}{>}\;0\quad\text{and}\quad\boldsymbol{s}:\boldsymbol{\eta}\;\overset{!}{>}\;0\,.\tag{5.50}$$

Hence, the plastic flow postulates

$$\dot{\boldsymbol{\varepsilon}}^p\;=\;\boldsymbol{f}^p(\boldsymbol{u},\boldsymbol{\varepsilon}^p,\boldsymbol{\beta},T)\;=\;\frac{A\,\Phi^a}{\sqrt{J_2(\boldsymbol{\eta})}}\,\boldsymbol{\eta}\,,\tag{5.51}$$

including the material constants a and A. If the two conditions are not valid, no plastic flow takes place, i.e. $\dot{\boldsymbol{\varepsilon}}^p\equiv\boldsymbol{0}$. To determine the back stresses a second evolution equation is required which is assumed to

$$\dot{\boldsymbol{\beta}}\;=\;\boldsymbol{f}^{\beta}(\boldsymbol{u},\boldsymbol{\varepsilon}^p,\boldsymbol{\beta},T)\;=\;h(\boldsymbol{\beta})\,\dot{\boldsymbol{\varepsilon}}^p\;-\;r(\boldsymbol{\beta})\,\boldsymbol{\beta}\tag{5.52}$$

with h corresponding to the evolution of the accumulated deformation, i.e. is connected with the viscous strain rate $\dot{\boldsymbol{\varepsilon}}^p$, and r corresponding to the recovery or softening process. In (5.51)

and (5.52), the tensor $\boldsymbol{f}$ summarizes the evolution equations in a function, which is used later for the solution of the local plasticity problem. The evolution law (5.52) is further known as the so-called Bailey-Orowan law, see Arya and Kaufmann [11]. It postulates that at elevated temperatures the deformation is governed by the two competing processes: hardening h and softening r. Introducing

$$G \;=\; \frac{J_2(\boldsymbol{\beta})}{K_0^2}\,, \quad R \;=\; R_0 \exp\Big[Q_0\,\Big(\frac{1}{\Theta_0} \;-\; \frac{1}{T}\Big)\Big]\,, \tag{5.53}$$

where $J_2(\boldsymbol{\beta})$ is the second invariant of the deviatoric back stress according to (B.23) and G_0 and G are the constant and the deformation-dependent shear threshold, respectively. Furthermore, K_0^2 is the Bingham-Prager shear stress threshold and R is the recovery term for which the activation energy Q_0, the recovery or softening factor R_0, and the activation temperature Θ_0 are used. Thus, for the case $G > G_0$ and $\boldsymbol{s} : \boldsymbol{\beta} > 0$, h and r are expressed by

$$h(\boldsymbol{\beta}) \;=\; \frac{H}{G^{\beta}}\,, \quad r(\boldsymbol{\beta}) \;=\; \frac{R\,G^{m-\beta}}{\sqrt{J_2(\boldsymbol{\beta})}}\,, \tag{5.54}$$

whereas for the remaining cases $G \leq G_0$ and $\boldsymbol{s} : \boldsymbol{\beta} \leq 0$

$$h(\boldsymbol{\beta}) \;=\; \frac{H}{G_0^{\beta}}\,, \quad r(\boldsymbol{\beta}) \;=\; \frac{R\,G_0^{m-\beta}}{\sqrt{J_2(\boldsymbol{\beta})}}\,. \tag{5.55}$$

Summarizing, in (5.54) and (5.55) the following material parameters are used: $H \;=\; H(T)$, $\beta \;=\; \beta(T)$, and $R_0 \;=\; R_0(T)$ are temperature-dependent variables, whereas m is a constant material parameter. At steady state, they balance each other, so that in (5.52) $\dot{\boldsymbol{\beta}} \equiv 0$ follows.

As mentioned previously, an equilibrium state is obtained if the balance equations and in addition the evolution equations (5.51) and (5.52) at Gauss point level are solved. Therefore, the evolution equations are firstly discretised in time using a backward Euler time integration scheme and secondly are computed at each Gauss point gp for the current time step $n+1$. In contrast to all other plastic materials, the Robinson's material is not solved using an elastic predictor/plastic corrector schemes (as presented in section 3.4.2.2). Instead, the internal variables $\boldsymbol{\varepsilon}^p$ and $\boldsymbol{\beta}$ are locally defined, so that they are understood discontinuous across element boundaries. It this context it is common to discretise the internal variables by an interpolation with polynomials that are equal to 1 at a Gauss point gp. Hence, the discrete internal variables $\boldsymbol{\varepsilon}^{p;(e);\mathsf{gp}}$ and $\boldsymbol{\beta}^{(e);\mathsf{gp}}$ are associated to each Gauss point of an element (e). Due to the local definition, their elementwise contribution is decoupled in the global system. Consequently, the increments of the internal variables $\Delta\boldsymbol{\varepsilon}^{p;(e)}$ and $\Delta\boldsymbol{\beta}^{(e)}$ depend only on the displacement increment $\Delta\mathbf{d}^{(e)}$ of this element (e). Thus, a relatively easy local static condensation is enabled which eliminates the internal variables on the global level. To realise the static condensation, in a first step residuals of the evolution equations are defined as

$$\mathbf{r}_{\boldsymbol{\varepsilon}^p}^{(e);\mathsf{gp}} := \dot{\boldsymbol{\varepsilon}}^{p;(e);\mathsf{gp}} \;-\; \mathbf{f}^{p}(\mathbf{d}^{(e)}, \boldsymbol{\varepsilon}^{p;(e);\mathsf{gp}}, \boldsymbol{\beta}^{(e);\mathsf{gp}}, \mathbf{T}^{(e)}) \;=\; \mathbf{0}\,, \tag{5.56}$$

$$\mathbf{r}_{\boldsymbol{\beta}}^{(e);\mathsf{gp}} := \dot{\boldsymbol{\beta}}^{(e);\mathsf{gp}} \;-\; \mathbf{f}^{\beta}(\mathbf{d}^{(e)}, \boldsymbol{\varepsilon}^{p;(e);\mathsf{gp}}, \boldsymbol{\beta}^{(e);\mathsf{gp}}, \mathbf{T}^{(e)}) \;=\; \mathbf{0}\,. \tag{5.57}$$

Subsequently, these residuals are discretised in time using a backward Euler time integration scheme, yielding

$$\mathbf{r}^{(e);\mathsf{gp}}_{\boldsymbol{\varepsilon}^p;n+1} := \frac{\boldsymbol{\varepsilon}^{p;(e);\mathsf{gp}}_{n+1} - \boldsymbol{\varepsilon}^{p;(e);\mathsf{gp}}_{n}}{\Delta t} - \mathbf{f}^p(\mathbf{d}^{(e)}_{n+1}, \boldsymbol{\varepsilon}^{p;(e);\mathsf{gp}}_{n+1}, \boldsymbol{\beta}^{(e);\mathsf{gp}}_{n+1}, \mathbf{T}^{(e)}_{n+1}) = \mathbf{0}\,, \tag{5.58}$$

$$\mathbf{r}^{(e);\mathsf{gp}}_{\boldsymbol{\beta};n+1} := \frac{\boldsymbol{\beta}^{(e);\mathsf{gp}}_{n+1} - \boldsymbol{\beta}^{(e);\mathsf{gp}}_{n}}{\Delta t} - \mathbf{f}^\beta(\mathbf{d}^{(e)}_{n+1}, \boldsymbol{\varepsilon}^{p;(e);\mathsf{gp}}_{n+1}, \boldsymbol{\beta}^{(e);\mathsf{gp}}_{n+1}, \mathbf{T}^{(e)}_{n+1}) = \mathbf{0}\,. \tag{5.59}$$

The structural field is solved if the displacements and the internal variables are determined within the Newton-Raphson iteration. In the present material model, static condensation of the material variables is performed at each Gauss point, i.e. no global material response is achieved. Instead, condensed stresses and condensed stiffness contributions, $\boldsymbol{\sigma}_{\mathsf{red}}$ and $\mathscr{C}_{\mathsf{mat;red}}$, respectively, are computed at Gauss point level, which are then inserted elementwisely into the global system. Based on initial values $\mathbf{d}^i$, $\mathbf{T}^i$ and $\boldsymbol{\varepsilon}^{p;(e);\mathsf{gp};i}$, $\boldsymbol{\beta}^{(e);\mathsf{gp};i}$ for iteration step i, $\boldsymbol{\sigma}^{(e);\mathsf{gp}}_{\mathsf{red}}$ and $\mathscr{C}^{(e);\mathsf{gp}}_{\mathsf{mat;red}}$ are obtained from linearisation of the material by

$$\mathsf{Lin}\left[\begin{array}{c}\boldsymbol{\sigma}\\ \hdashline \mathbf{r}^{\boldsymbol{\varepsilon}^p}\\ \mathbf{r}^{\boldsymbol{\beta}}\end{array}\right]^{(e);\mathsf{gp}}_{n+1} = \left[\begin{array}{c}\boldsymbol{\sigma}\\ \hdashline \mathbf{r}^{\boldsymbol{\varepsilon}^p}\\ \mathbf{r}^{\boldsymbol{\beta}}\end{array}\right]^{(e);\mathsf{gp};i}_{n+1} + \left[\begin{array}{c|cc} \dfrac{\partial\boldsymbol{\sigma}}{\partial\boldsymbol{\varepsilon}} & \dfrac{\partial\boldsymbol{\sigma}}{\partial\boldsymbol{\varepsilon}^p} & \dfrac{\partial\boldsymbol{\sigma}}{\partial\boldsymbol{\beta}} \\ \hdashline \dfrac{\partial\mathbf{r}^{\boldsymbol{\varepsilon}^p}}{\partial\boldsymbol{\varepsilon}} & \dfrac{\partial\mathbf{r}^{\boldsymbol{\varepsilon}^p}}{\partial\boldsymbol{\varepsilon}^p} & \dfrac{\partial\mathbf{r}^{\boldsymbol{\varepsilon}^p}}{\partial\boldsymbol{\beta}} \\ \dfrac{\partial\mathbf{r}^{\boldsymbol{\beta}}}{\partial\boldsymbol{\varepsilon}} & \dfrac{\partial\mathbf{r}^{\boldsymbol{\beta}}}{\partial\boldsymbol{\varepsilon}^p} & \dfrac{\partial\mathbf{r}^{\boldsymbol{\beta}}}{\partial\boldsymbol{\beta}} \end{array}\right]^{(e);\mathsf{gp};i}_{n+1} \left[\begin{array}{c}\Delta\boldsymbol{\varepsilon}\\ \hdashline \Delta\boldsymbol{\varepsilon}^p\\ \Delta\boldsymbol{\beta}\end{array}\right]^{(e);\mathsf{gp};i}_{n+1}, \tag{5.60}$$

where the internal variables are computed for a given strain increment $\Delta\boldsymbol{\varepsilon}$ via static condensation of the two lower rows by

$$\left[\begin{array}{c}\Delta\boldsymbol{\varepsilon}^p\\ \Delta\boldsymbol{\beta}\end{array}\right]^{\mathsf{gp};i}_{n+1} = \left[\begin{array}{c|c} \dfrac{\partial\mathbf{r}^{\boldsymbol{\varepsilon}^p}}{\partial\boldsymbol{\varepsilon}^p} & \dfrac{\partial\mathbf{r}^{\boldsymbol{\varepsilon}^p}}{\partial\boldsymbol{\beta}} \\ \dfrac{\partial\mathbf{r}^{\boldsymbol{\beta}}}{\partial\boldsymbol{\varepsilon}^p} & \dfrac{\partial\mathbf{r}^{\boldsymbol{\beta}}}{\partial\boldsymbol{\beta}} \end{array}\right]^{\mathsf{gp};i;-1}_{n+1} \left(- \left[\begin{array}{c}\mathbf{r}^{\boldsymbol{\varepsilon}^p}\\ \mathbf{r}^{\boldsymbol{\beta}}\end{array}\right] - \left[\begin{array}{c}\dfrac{\partial\mathbf{r}^{\boldsymbol{\varepsilon}^p}}{\partial\boldsymbol{\varepsilon}}\\ \dfrac{\partial\mathbf{r}^{\boldsymbol{\beta}}}{\partial\boldsymbol{\varepsilon}}\end{array}\right] \Delta\boldsymbol{\varepsilon} \right)^{\mathsf{gp};i}_{n+1}. \tag{5.61}$$

Inserting (5.61) into (5.60), the linearisation of the stresses $\boldsymbol{\sigma}$ with respect to the strains $\boldsymbol{\varepsilon}$ is given as

$$\mathsf{Lin}\,\boldsymbol{\sigma} = \boldsymbol{\sigma} + \frac{\partial\boldsymbol{\sigma}}{\partial\boldsymbol{\varepsilon}} : \Delta\boldsymbol{\varepsilon} + \left[\begin{array}{cc} \dfrac{\partial\boldsymbol{\sigma}}{\partial\boldsymbol{\varepsilon}^p} & \dfrac{\partial\boldsymbol{\sigma}}{\partial\boldsymbol{\beta}} \end{array}\right] : \left[\begin{array}{c}\Delta\boldsymbol{\varepsilon}^p\\ \Delta\boldsymbol{\beta}\end{array}\right], \tag{5.62}$$

where the indices are omitted for the sake of clarity. Reformulating (5.62) yields

$$\begin{aligned}\mathsf{Lin}\,\boldsymbol{\sigma} = {} & \boldsymbol{\sigma} + \frac{\partial\boldsymbol{\sigma}}{\partial\boldsymbol{\varepsilon}} : \Delta\boldsymbol{\varepsilon} + \\ & + \left[\begin{array}{cc} \dfrac{\partial\boldsymbol{\sigma}}{\partial\boldsymbol{\varepsilon}^p} & \dfrac{\partial\boldsymbol{\sigma}}{\partial\boldsymbol{\beta}} \end{array}\right] \left[\begin{array}{c|c} \dfrac{\partial\mathbf{r}^{\boldsymbol{\varepsilon}^p}}{\partial\boldsymbol{\varepsilon}^p} & \dfrac{\partial\mathbf{r}^{\boldsymbol{\varepsilon}^p}}{\partial\boldsymbol{\beta}} \\ \dfrac{\partial\mathbf{r}^{\boldsymbol{\beta}}}{\partial\boldsymbol{\varepsilon}^p} & \dfrac{\partial\mathbf{r}^{\boldsymbol{\beta}}}{\partial\boldsymbol{\beta}} \end{array}\right]^{-1} \left(- \left[\begin{array}{c}\mathbf{r}^{\boldsymbol{\varepsilon}^p}\\ \mathbf{r}^{\boldsymbol{\beta}}\end{array}\right] - \left[\begin{array}{c}\dfrac{\partial\mathbf{r}^{\boldsymbol{\varepsilon}^p}}{\partial\boldsymbol{\varepsilon}}\\ \dfrac{\partial\mathbf{r}^{\boldsymbol{\beta}}}{\partial\boldsymbol{\varepsilon}}\end{array}\right] \Delta\boldsymbol{\varepsilon} \right), \end{aligned} \tag{5.63}$$

and

$$\begin{aligned}\mathsf{Lin}\,\boldsymbol{\sigma} \;=\; & \underbrace{\left\{\boldsymbol{\sigma} - \begin{bmatrix} \dfrac{\partial \boldsymbol{\sigma}}{\partial \boldsymbol{\varepsilon}^p} & \dfrac{\partial \boldsymbol{\sigma}}{\partial \boldsymbol{\beta}} \end{bmatrix} \begin{bmatrix} \dfrac{\partial \mathbf{r}^{\boldsymbol{\varepsilon}^p}}{\partial \boldsymbol{\varepsilon}^p} & \dfrac{\partial \mathbf{r}^{\boldsymbol{\varepsilon}^p}}{\partial \boldsymbol{\beta}} \\ \dfrac{\partial \mathbf{r}^{\boldsymbol{\beta}}}{\partial \boldsymbol{\varepsilon}^p} & \dfrac{\partial \mathbf{r}^{\boldsymbol{\beta}}}{\partial \boldsymbol{\beta}} \end{bmatrix}^{-1} \begin{bmatrix} \mathbf{r}^{\boldsymbol{\varepsilon}^p} \\ \mathbf{r}^{\boldsymbol{\beta}} \end{bmatrix}\right\}}_{\boldsymbol{\sigma}_{\mathsf{red}}} + \\ & + \underbrace{\left\{\frac{\partial \boldsymbol{\sigma}}{\partial \boldsymbol{\varepsilon}} - \begin{bmatrix} \dfrac{\partial \mathbf{r}^{\boldsymbol{\varepsilon}^p}}{\partial \boldsymbol{\varepsilon}^p} & \dfrac{\partial \mathbf{r}^{\boldsymbol{\varepsilon}^p}}{\partial \boldsymbol{\beta}} \\ \dfrac{\partial \mathbf{r}^{\boldsymbol{\beta}}}{\partial \boldsymbol{\varepsilon}^p} & \dfrac{\partial \mathbf{r}^{\boldsymbol{\beta}}}{\partial \boldsymbol{\beta}} \end{bmatrix}^{-1} \begin{bmatrix} \dfrac{\partial \boldsymbol{\varepsilon}^p}{\partial \boldsymbol{\varepsilon}} & \dfrac{\partial \boldsymbol{\beta}}{\partial \boldsymbol{\varepsilon}} \end{bmatrix}\right\}}_{\mathscr{C}_{\mathsf{mat;red}}} \Delta\boldsymbol{\varepsilon}\,,\end{aligned} \tag{5.64}$$

which is finally summarized to

$$\mathsf{Lin}\,\boldsymbol{\sigma} \;=:\; \boldsymbol{\sigma}_{\mathsf{red}} + \mathscr{C}_{\mathsf{mat;red}} : \Delta\boldsymbol{\varepsilon}\,. \tag{5.65}$$

Consequently, the condensed reduced stresses and tangent, $\boldsymbol{\sigma}_{\mathsf{red}}$ and $\mathscr{C}_{\mathsf{mat;red}}$, respectively, follow as results of the linearisation and the elimination of the internal variables.

Subsequently, based on (5.65) a solution of the target linear system (6.3) can be computed after assembly of the elementwise terms. Therefore, the global internal force vector is composed of $\boldsymbol{\sigma}_{\mathsf{red}}$ at each Gauss point, i.e.

$$\mathbf{f}_{\mathsf{int;S};n+1}(\mathbf{d}^i, \mathbf{T}^i) \;=\; \sum_{e=1}^{\mathsf{nele}} \Big[\sum_{\mathsf{gp}}^{\mathsf{ngp}} \int\limits_{\Omega_0^{(e)}} \Big(\frac{\partial \boldsymbol{\varepsilon}}{\partial \mathbf{d}}\Big)^{\mathsf{T}} : \boldsymbol{\sigma}_{\mathsf{red}}(\mathbf{d}, \boldsymbol{\varepsilon}^p, \boldsymbol{\beta}, \mathbf{T})\, \mathrm{d}V_0 \Big]_{n+1}^{(e);\mathsf{gp};i} \tag{5.66}$$

and accordingly, the global tangential matrix $\mathbf{K}_{\mathsf{SS}}$ is composed of the matrices $\mathscr{C}_{\mathsf{mat;red}}$ at each Gauss point by

$$\mathbf{K}_{\mathsf{int;SS}}(\mathbf{d}, \mathbf{T}) \;=\; \sum_{e=1}^{\mathsf{nele}} \Big\{ \sum_{\mathsf{gp}}^{\mathsf{ngp}} \Big[\int\limits_{\Omega_0^{(e)}} \Big(\frac{\partial \boldsymbol{\varepsilon}}{\partial \mathbf{d}}\Big)^{\mathsf{T}} : \mathscr{C}_{\mathsf{mat;red}} : \Big(\frac{\partial \boldsymbol{\varepsilon}}{\partial \mathbf{d}}\Big)\, \mathrm{d}V_0 \Big]^{(e);\mathsf{gp}} \Big\}\,. \tag{5.67}$$

Since a Newton method is utilised which solves for incremental values $\Delta\mathbf{d}$, incremental solutions of the internal variables are computed. The final solution of the internal variables at the end of time step $n+1$ at each Gauss point gp of each element (e) are obtained by updating

$$\begin{bmatrix} \boldsymbol{\varepsilon}^p \\ \boldsymbol{\beta} \end{bmatrix}_{n+1}^{i+1} = \begin{bmatrix} \boldsymbol{\varepsilon}^p \\ \boldsymbol{\beta} \end{bmatrix}_{n+1}^{i} + \begin{bmatrix} \Delta\boldsymbol{\varepsilon}^p \\ \Delta\boldsymbol{\beta} \end{bmatrix}_{n+1}^{i+1}. \tag{5.68}$$

To summarize, Algorithm 3 describes a solution approach with a Newton-Raphson scheme using Robinson's material with static condensation.

Based on the entropy equation (5.47), the thermo-elasto-plastic heating terms vanishes ($\mathcal{H}^{ep} \equiv 0$). Moreover, based on Freed et al. [42], the mechanical Dissipation follows as

$$\mathcal{D}_{\mathsf{mech}} \;=\; \boldsymbol{\eta} : \dot{\boldsymbol{\varepsilon}}^p\,. \tag{5.69}$$

Algorithm 3 Solution procedure for the structural subproblem (5.22) of a TSI problem using Robinson's viscoplastic material model.

Time loop
for time step $n = 0, ..., t_{\mathsf{max}}$
  Predictor $\mathbf{x}_{n+1}^{i=0} = \mathbf{x}_n$ with $\mathbf{x} = \{\mathbf{d}, \mathbf{T}, \boldsymbol{\varepsilon}^{p;(e);\mathsf{gp}}, \boldsymbol{\beta}^{(e);\mathsf{gp}}\}$
  Calculate initial global residual $\mathbf{r}_{\mathsf{S};n+1}^{i=0}$ with $\mathbf{x}_{n+1}^{i=0}$ and element internal force vector $\mathbf{f}_{\mathsf{int;S};n+1}^{i=0}$

  # Newton-Raphson iteration
  for each iteration step $i = 0, ..., \mathsf{max}_{\mathsf{nlniter}}$
    # Check for convergence of Newton-Raphson iteration
    if $||\mathbf{r}_{\mathsf{S};n+1}^{i}|| \leq \epsilon$
      stop Newton-Raphson iteration
    Calculate $\mathbf{r}_{\mathsf{S};n+1}^{i} = \mathbf{r}_{\mathsf{S}}(\mathbf{x}_{n+1}^{i})$ with $\mathbf{f}_{\mathsf{int;S}}(\mathbf{d}, \mathbf{T})$ (5.66) and $\mathbf{T}^{i} = const.$
    Calculate $\mathbf{K}_{\mathsf{S};n+1}^{i} = \mathbf{K}_{\mathsf{S}}(\mathbf{x}_{n+1}^{i})$ according (5.67)

    # Solve linear system $\Delta\mathbf{d}_{n+1}^{i+1} = -(\mathbf{K}_{\mathsf{S};n+1}^{i})^{-1}\,\mathbf{r}_{\mathsf{d};n+1}^{i}$

      # At Gauss point gp start material call
      for Gauss point $l = 0, ..., \mathsf{ngp}$
      Given is $\Delta\boldsymbol{\varepsilon}_{n+1}^{i+1;l}$, $T_{n+1}^{i+1;l}$ and all state variables at t_n
      Update internal variables $\boldsymbol{\varepsilon}_{n+1}^{p;i+1;l}$, $\boldsymbol{\beta}_{n+1}^{i+1;l}$ according to (5.68)
      Calculate $\boldsymbol{\varepsilon}_{n+1}^{e;i+1;l}$ based on (5.1)
      Calculate the incremental solution vectors of the internal variables
      $\Delta\boldsymbol{\varepsilon}_{n+1}^{p;i+1;l}$, $\Delta\boldsymbol{\beta}_{n+1}^{i+1;l}$ according to (5.61) using $\Delta\boldsymbol{\varepsilon}(\Delta\mathbf{d}_{n+1}^{i+1})$
      Calculate $\boldsymbol{\sigma}_{\mathsf{red}}$ and $\mathscr{C}_{\mathsf{mat;red}}$ according to (5.64)
      # Finish material call

    # Update solution vectors
    $\mathbf{d}_{n+1}^{i+1} = \mathbf{d}_{n+1}^{i} + \Delta\mathbf{d}_{n+1}^{i+1}$
    Update Newton-Raphson iteration step $i = i + 1$

  Update time $t = t + \Delta t$ and step $n = n + 1$

5.3.2.3 Finite strain thermo-hyperelasto-plastic material model

The previously presented material models are based on small strains. In contrast, the present material model is formulated in finite strains. It is based on Simo and Miehe [122] and has been introduced for purely mechanical analyses in section 3.4.2.5. Extensions of the model of Simo and Miehe [122] is realised in numerous publications, for instance in Miehe and Schröder [91] and Reese and Govindjee [108].

In addition to the purely mechanical finite strain elastoplastic material model, temperature-dependence is introduced in the yield stress and additional thermal stresses. Thus, the present model describes a finite strain isotropic thermo-hyperelasto-plastic material with J_2-plasticity and nonlinear isotropic hardening. The thermoelastic domain is presented by the von Mises yield function (3.185), where the yield function is temperature-dependent, i.e. $\sigma_{\mathsf{y}}(\bar{\varepsilon}^p, T)$. The Helmholtz free energy ψ given in (5.8) is specified by determining the internal variables according to (3.173) and by using the elastic left Cauchy-Green deformation tensor $\boldsymbol{B}^e$, see (3.168) and especially (3.171), so that the potential yields

$$
\begin{aligned}
\rho_0\,\psi(\boldsymbol{B}^e, T, \bar{\varepsilon}^p) \;&=\; \hat{\mathbb{U}}(J^e) \,+\, \hat{\mathbb{W}}(\tilde{\boldsymbol{B}}^e) \,+\, \hat{\mathbb{M}}(J^e, T) \,+\, \hat{\mathbb{T}}(T) \,+\, \hat{\mathbb{K}}(\bar{\varepsilon}^p, T) \\
&=\; \underbrace{\frac{K}{2}\left[\frac{1}{2}\,(J^{e\,2} \,-\, 1) - \ln\, J^e\right]}_{\hat{\mathbb{U}}(J^e)} + \underbrace{\frac{1}{2}\,\mu\,(\operatorname{tr}\tilde{\boldsymbol{B}}^e \,-\, 3)}_{\hat{\mathbb{W}}(\tilde{\boldsymbol{B}}^e)} + \\
&\quad + \underbrace{\frac{m_0}{2}\,\Delta T\left(\frac{J^{e\,2}\,-\,1}{J^e}\right)}_{\hat{\mathbb{M}}(J^e,T)} \underbrace{-\,\rho_0\,C_{\mathsf{V}}\left(T\,\ln\,\frac{T}{T_0} \,-\, \Delta T\right)}_{\hat{\mathbb{T}}(T)} + \\
&\quad + \underbrace{\frac{1}{2}\,H^{\mathsf{iso}}\,\bar{\varepsilon}^{p\,2} \,+\, [\sigma_{\mathsf{y};\infty}(T) \,-\, \sigma_{\mathsf{y};0}(T)]\,\hat{\mathbb{H}}(\bar{\varepsilon}^p)}_{\hat{\mathbb{K}}(\bar{\varepsilon}^p,T)}
\end{aligned}
\tag{5.70}
$$

with the hardening potential $\hat{\mathbb{H}}$ (3.176). In contrast to Simo and Miehe [122], a plastic potential $\hat{\mathbb{K}}(\bar{\varepsilon}^p, T)$ is assumed which depends not only on the accumulated plastic strain $\bar{\varepsilon}^p$ but also on the temperature T. Consequently, the hardening potential $\hat{\mathbb{K}}$ enables von Mises plasticity with isotropic temperature-dependent nonlinear hardening, so that saturation strain hardening combined with linear thermoplastic softening is enabled. The proposed version of $\hat{\mathbb{K}}$ is in agreement with approaches in literature, e.g. Agelet de Saracibar et al. [2], Ibrahimbegovic and Chorfi [61], and with the final function used for the yield stress in the numerical example section of Simo and Miehe [122]. In Simo and Miehe [122], the mechanical dissipation term derived in the theory is not used for the numerical examples. Instead they redefine the mechanical dissipation by introducing a non-physical dissipation factor and by utilising the total yield function so that temperature-dependence is further introduced. In the work of Stainier and Ortiz [128], the authors explain that an a-priori definition of this constant dissipation factor is in general not capable to reproduce real material behaviour which has further been confirmed by various experimental works. Consequently, they do not use this restricted form for the dissipation, instead they use the expression directly following from their variational framework. Accordingly, in the present work the term derived in the theory is utilised.

To enable thermal softening, the yield stresses and the isotropic hardening modulus are assumed temperature-dependent, yielding

$$\sigma_{\mathsf{y};0}(T) = \sigma_{\mathsf{y};0}(T_0)\,[1 - \omega_0\,(T - T_0)]\,, \tag{5.71}$$
$$\sigma_{\mathsf{y};\infty}(T) = \sigma_{\mathsf{y};\infty}(T_0)\,[1 - \omega_\mathsf{h}\,(T - T_0)]\,, \tag{5.72}$$
$$H^{\mathsf{iso}}(T) = H^{\mathsf{iso}}(T_0)\,[1 - \omega_\mathsf{h}\,(T - T_0)]\,, \tag{5.73}$$

with the thermal softening parameter ω_0 for the initial yield stress and the thermal softening parameter ω_h for the hardening modulus and the saturation stress. Derivations of (5.70) are used within the second law of thermodynamics, see section 2.4.3, to determine the stresses based on (5.31), leading to

$$\boldsymbol{S} = \underbrace{\frac{K}{2}\,(J^{e\,2} - 1)\,\boldsymbol{C}^{-1}}_{\boldsymbol{S}_\mathsf{d}} + \underbrace{\boldsymbol{F}^{-1}\cdot(\mu\,\mathrm{dev}\,\tilde{\boldsymbol{B}}^e)\cdot\boldsymbol{F}^{-\mathsf{T}} + \frac{m_0}{2}\,\Delta T\left(\frac{J^{e\,2}+1}{J^e}\right)\boldsymbol{C}^{-1}}_{\boldsymbol{S}_{\mathsf{dT}}}, \tag{5.74}$$

where in contrast to (5.31), the deviatoric plastic stresses are temperature-dependent due to (5.71)-(5.73) which enter the stress calculation in the return-mapping. To compute the coupling terms, the mechanical dissipation $\mathcal{D}_{\mathsf{mech}}$ is expressed by (3.199) where according to (5.71), the mechanical dissipation follows to be temperature-dependent which is shown by

$$\mathcal{D}_{\mathsf{mech}} = \dot\gamma\,\sqrt{\frac{2}{3}}\,\sigma_{\mathsf{y};0}(T)\,. \tag{5.75}$$

Moreover, $\mathcal{H}^{ep}$ is derived from (5.13) and (5.70), leading to

$$\mathcal{H}^{ep} = T\left(\frac{m_0}{2}\,\frac{J^{e\,2}+1}{J^e}\,\boldsymbol{C}^{-1} : \dot{\boldsymbol{E}}_{\mathsf{GL}} + \frac{\partial\kappa(\bar\varepsilon^p,T)}{\partial T}\,\dot{\bar\varepsilon}^p\right), \tag{5.76}$$

where $\kappa(\bar\varepsilon^p,T)$ is the thermodynamical force associated to isotropic hardening based on (3.183). In contrast to the constant terms in (3.183), the present κ includes temperature-dependent terms (see (5.71)-(5.73)). In (5.76), the derivative of κ with respect to the temperature is included which is computed using the chain rule by

$$\frac{\mathrm{d}\kappa(\bar\varepsilon^p,T)}{\mathrm{d}T} = \frac{\partial\kappa(\bar\varepsilon^p,T)}{\partial T} + \frac{\partial\kappa(\bar\varepsilon^p,T)}{\partial\bar\varepsilon^p}\,\frac{\partial\bar\varepsilon^p}{\partial\Delta\gamma}\,\frac{\partial\Delta\gamma}{\partial T}\,, \tag{5.77}$$

where a temperature-dependent plastic multiplier $\Delta\gamma(T)$ is assumed. Based on (3.187), the partial derivation yields

$$\frac{\partial\bar\varepsilon^p}{\partial\Delta\gamma} = \sqrt{\frac{2}{3}}\,. \tag{5.78}$$

A result of $\frac{\partial\Delta\gamma}{\partial T}$ is achieved by linearising the consistency condition with respect to the temperatures and subsequently reordering the result, which gives

$$\frac{\partial\Delta\gamma}{\partial T} = -\sqrt{\frac{2}{3}}\,\frac{\dfrac{\partial\sigma_{\mathsf{y};0}(T)}{\partial T} + \dfrac{\partial\kappa(\bar\varepsilon^p,T)}{\partial T}}{2\,\bar\mu\,\beta_0} \tag{5.79}$$

with the coefficient β_0 introduced for the purely structural case in (3.213) including (3.218), which is here temperature-dependent due to (5.77). For the sake of clarity, it is noted that the total temperature derivation of the thermodynamical force (5.77) is split in (5.79) into its partial derivations: while the first term of the right-hand side is included in the numerator, the second term is part of the denominator included in β_0. Subsequently, the partial derivations of the yield stresses follow as

$$\frac{\partial \sigma_{\mathsf{y};0}(T)}{\partial T} = \sigma_{\mathsf{y};0}(T_0)\,(-\omega_0)\,, \tag{5.80}$$

$$\frac{\partial \kappa(\bar{\varepsilon}^p, T)}{\partial T} = -H^{\mathsf{iso}}(T_0)\,\omega_{\mathsf{h}}\,\bar{\varepsilon}^p + [-\omega_{\mathsf{h}}\,\sigma_{\mathsf{y};\infty}(T_0) + \omega_0\,\sigma_{\mathsf{y};0}(T_0)]\,[1 - \exp(-\delta\,\bar{\varepsilon}^p)]\,, \tag{5.81}$$

$$\frac{\partial \kappa(\bar{\varepsilon}^p, T)}{\partial \bar{\varepsilon}^p} = H^{\mathsf{iso}}(T) + [\sigma_{\mathsf{y};\infty}(T) - \sigma_{\mathsf{y};0}(T)]\,[-\exp(-\delta\,\bar{\varepsilon}^p)\,(-\delta)]\,, \tag{5.82}$$

so that the total derivative of κ (5.77) is composed of (5.78), (5.81), and (5.82). The thermal derivation of $\Delta\gamma$ (5.79) is determined using (5.80) and (5.81). Further details are shown in Appendix D.2.

Based on (3.201), the material tangent for the thermo-elasto-plastic material $\mathscr{C}^{ep}_{\mathsf{mat}}$ consists of a volumetric and an isochoric part

$$\mathscr{C}^{ep}_{\mathsf{mat}} = \mathscr{C}^{e}_{\mathsf{mat};v} + \tilde{\mathscr{C}}^{ep}_{\mathsf{mat}} \tag{5.83}$$

with the isochoric tangent $\tilde{\mathscr{C}}^{ep}_{\mathsf{mat}}$ (3.212) and the volumetric thermoelastic tangent

$$\mathscr{C}^{e}_{\mathsf{mat};v} = \mathscr{C}^{e}_{\mathsf{mat};v;\mathsf{S}} + \mathscr{C}^{e}_{\mathsf{mat};v;\mathsf{T}}\,, \tag{5.84}$$

where $\mathscr{C}^{e}_{\mathsf{mat};v;\mathsf{S}}$ corresponds to (3.202) and $\mathscr{C}^{e}_{\mathsf{mat};v;\mathsf{T}}$ to the volumetric thermoelastic part, defined as

$$\mathscr{C}^{e}_{\mathsf{mat};v;\mathsf{T}} = \Delta T\,\frac{m_0}{2}\left[\left(J^e - \frac{1}{J^e}\right)(\boldsymbol{C}^{-1}\otimes\boldsymbol{C}^{-1}) - 2\left(J^e + \frac{1}{J^e}\right)(\boldsymbol{C}^{-1}\odot\boldsymbol{C}^{-1})\right]. \tag{5.85}$$

Subsequently, the thermal tangent $\boldsymbol{C}_{\mathsf{T}}$ (5.26) is established. The linearisation of the thermomechanical stresses $\boldsymbol{S}_{\mathsf{dT}}$ in (5.74) with respect to the temperatures T yields two terms, one as a result of the volumetric thermal stresses and one as a result of the temperature-dependence of the yield stresses, see (5.71) and (5.72), which is determined within the return-mapping algorithm. Thus, the thermal tangent reads

$$\boldsymbol{C}_{\mathsf{T}} = \frac{\partial \boldsymbol{S}}{\partial T} = \frac{\partial \boldsymbol{S}_v}{\partial T} + \frac{\partial \tilde{\boldsymbol{S}}}{\partial T} = \boldsymbol{C}_{\mathsf{T};v} + \tilde{\boldsymbol{C}}_{\mathsf{T}} \tag{5.86}$$

with the volumetric thermal tangent

$$\boldsymbol{C}_{\mathsf{T};v} = \frac{\partial \boldsymbol{S}_v}{\partial T} = \frac{m_0}{2}\left(\frac{J^{e\,2}+1}{J^e}\right)\boldsymbol{C}^{-1}\,. \tag{5.87}$$

The isochoric thermal tangent $\tilde{\boldsymbol{C}}_{\mathsf{T}}$ is determined by the result of the linearisation of the final deviatoric stresses $\boldsymbol{s}_{n+1}$ (3.203) with respect to T. The only temperature-dependent term in (3.203) represents the plastic multiplier according to (5.79). Hence, the isochoric thermal tangent yields

$$\tilde{\boldsymbol{C}}_{\mathsf{T}} = \frac{\partial \tilde{\boldsymbol{S}}}{\partial T} = -2\,\tilde{\mu}\,\frac{\partial \Delta\gamma}{\partial T}\,\boldsymbol{N} \tag{5.88}$$

with the isothermal constant $\tilde{\mu}$, see (3.204), and the material flow vector $\boldsymbol{N}$ introduced as pull-back of (3.193).

Finally, based on (5.87), the thermo-elasto-plastic heating terms (5.76) reduces to

$$\mathcal{H}^{ep} \;=\; T\left(\boldsymbol{C}_{\mathsf{T};v} \;:\; \dot{\boldsymbol{E}}_{\mathsf{GL}} \;+\; \frac{\partial \kappa(\bar{\varepsilon}^p, T)}{\partial T}\,\dot{\bar{\varepsilon}}^p\right), \tag{5.89}$$

hence recovering the original relation of $\mathcal{H}^{ep}$ towards the temperature-dependent stresses included via $\hat{\mathbb{M}}(J^e, T)$ in (5.13).

6 Solution approaches for thermo-structure interaction

This chapter draws an overview of the different solution techniques available for thermo-structure interaction (TSI) problems and subsequently explains in detail the methods utilised in this thesis for solving a TSI problem.

In the literature, various approaches exist to solve a coupled problem. In this context field elimination, operator splitting, fractional-step method, staggered solution method, partitioned solution method, and finally the monolithic solution method can be distinguished. For a general introduction to coupled problems, available solution approaches, and especially to the surface-coupled problem of fluid-structure interaction (FSI), the reader is referred, e.g. to Felippa et al. [40], Küttler [70], Löhner et al. [80], Mok [93], Wall [141], and the references therein.

In the following, the different solution methods for coupled problems are explained. First, solution with field elimination implies, that the field variables of one field are eliminated and are introduced into the other field, which is solved subsequently. The elimination destroys the sparsity pattern of the system matrix, so that a solution can only be realised with the expense of possibly high computational costs. Thus, this method is restricted to small linear problems. Since the present work investigates also large problem sizes, the method of field elimination is not further pursued. Next, as described, e.g. in Armero and Simo [6] and Wall [141], the two methods partitioned and staggered can be used synonymously, hence they are summarized to the sole partitioned solution method. A partitioned method is characterized by a separation of the coupled problem in different partitions, so that the individual physical fields can be solved independently. In general, a partition is understood as a separation of the spatial discretisation, while a separation of the time discretisation is generally known as splitting, as shown in Felippa et al. [40]. In contrast, for TSI problems it is common to interpret a partitioned solution approach as a product formula which is known as operator splitting or synonymously as fractional-step method. Thus, for thermomechanical problems the latter two solution methods can also be integrated into the partitioned approach.

Consequently, fully coupled thermomechanical systems can be solved with both partitioned and monolithic coupling algorithms. In current literature, usually partitioned algorithms are considered, since they are very flexible with respect to the formulation and solution methods of the individual fields. Each partition may even be treated, for example, by existing field-specific software packages, so that commercial and non-commercial software packages can be combined. The coupling informations are passed as “external loads” with known values from one field to another. Separating the total problem into smaller blocks enables reductions concerning complexity and memory requirements, while computing time in general increases. Loosely (“one-way staggered”) and strongly (“iterative staggered”) coupled partitioned algorithms can be distinguished. Loosely coupled schemes accept that the coupling conditions are not fulfilled exactly at any point within a time step. In contrast, strongly coupled schemes aim at achieving

equilibrium of the overall TSI system of equations at any point within a time step through iterations between the partitioned fields (i.e. an equilibrium state is achieved with respect to a given exactness criterion ϵ_{out}). Hence, these strongly coupled schemes imply that at the end of the time step the coupling conditions are fulfilled with respect to ϵ_{out}. A significant problem of partitioned algorithms is either their conditional stability (for loosely coupled schemes) or their potentially very slow convergence or even divergence (for strongly coupled schemes). Various stabilisation techniques have been proposed to retain unconditional stability properties and acceleration techniques to improve convergence behaviour, respectively. For instance, as an acceleration technique relaxation in form of an Aitken Δ^2 method, as proposed in Irons and Tuck [62] and Mok and Wall [94] can be considered. This kind of relaxation is simple to implement and leads in many applications to a faster convergence of the problem. Aitken relaxation is applied for the coupled problem of FSI, e.g. in Küttler and Wall [71, 72], where it is said to be a proper choice for many FSI problems. For instance in Danowski et al. [29], Erbts and Düster [38], the Aitken Δ^2 method was applied to strongly coupled partitioned TSI algorithms.

As previously mentioned, a partitioned approach to TSI can be interpreted as a product formula. In literature, mainly three different operator splits can be distinguished for TSI: isothermal, adiabatic, and isentropic split. The definition of the operator split refers to the predictor step, which is then followed by a corrector step. The traditional way in loosely coupled TSI is the isothermal split, presented in Armero and Simo [6] for linear thermoelasticity and Erbts and Düster [38], Miehe [89] for finite strain thermoelasticity. Additionally, in Adam and Ponthot [1], Canadija and Brnic [22], Simo and Miehe [122], and Wriggers et al. [146] an isothermal split was utilised for finite strain thermo-elasto-plasticity. To simulate finite strain thermo-elasto-plasticity including phase change, the isothermal split was considered in Agelet de Saracibar et al. [2], while it was considered in Srikanth and Zabaras [127] for finite strain thermo-elasto-plasticity including damage, and in Miehe et al. [92] for finite strain thermo-visco-plasticity neglecting the so-called structural thermo-elasto-plastic heating term $\mathcal{H}^{ep}$. The implementation of the isothermal split is rather easy, but a maximal time-step size has to be obeyed and the split is only conditionally stable. This split implies, that the field equations are divided into a mechanical phase solved at constant temperature, i.e. isothermal, followed by a purely thermal phase. In contrast in the adiabatic split, as e.g. in Armero and Simo [6], the structural thermoelastic heating term $\mathcal{H}^{e}$ is included into the mechanical phase, leading to a temperature change in the mechanical phase that enforces the entropy η to remain constant, i.e. $\dot{\eta} = 0$. In the isentropic split, the first subproblem corresponds to an isentropic (adiabatic) elastodynamic phase with fixed entropy followed by a heat conduction phase with fixed motion and velocity. In Armero and Simo [6], an unconditionally stable algorithm based on an adiabatic split was presented for linear thermoelasticity or in Armero and Simo [7] for finite strain thermoplasticity, whereas in Armero and Simo [7], Holzapfel and Simo [59] an unconditionally stable isentropic operator split was proposed. Moreover, in Agelet de Saracibar et al. [2] finite strain thermo-elasto-plasticity using an isothermal as well as an isentropic split was presented. In addition to the isothermal split, an isentropic operator split was considered in Miehe [89] for finite strain thermoelasticity and in Agelet de Saracibar et al. [2] for finite strain thermo-elasto-plasticity with phase change. In Farhat et al. [39], an unconditionally stable second-order-accurate loosely coupled partitioned procedure was proposed for the fully coupled linear elastic thermomechanical system, assuming that the stress term in the temperature equation depends on the initial temperature T_0 instead of the current temperature T. In Bornemann and Wall [19], a partitioned TSI approach was presented neglect-

ing $\mathcal{H}^{ep}$. In Erbts and Düster [38], an isothermal fully implicit partitioned coupling scheme for thermoelasticity at finite deformation was presented utilising different strategies to accelerate the convergence of the outer iteration loop, utilising backward Euler time integration, and considering all coupling terms in the model. In Ibrahimbegovic and Chorfi [61], fully coupled finite strain viscoplasticity was solved using the commercial finite element (FE) program FEAP (see Taylor [131]). New consistent time integration algorithms for finite strain thermoelasticity were developed in Romero [112] which were applied to a fractional step method in time in Romero [111].

In the context of the surface-coupled problem of FSI, it was recently pointed out, e.g. in Gee et al. [47] that well-designed monolithic algorithms are superior to iterative staggered schemes, even if acceleration procedures are utilised in the latter. Especially if the problem is physically strongly coupled, monolithic solutions are very efficient and robust and within the discretisation an exact solution is achieved. Monolithic algorithms solve the coupled nonlinear multiphysics system simultaneously. They do not assume any approximation or assumption for the solution as it is common in partitioned schemes, for instance by choosing an operator split. Predominantly, implicit schemes are applied to achieve good stability properties. Compared to partitioned approaches, standard and unmodified single field solvers, e.g. in the form of commercial software packages, cannot be used in most cases. A particular challenge for monolithic algorithms is the efficient solution of the large system of equations, including potential nonlinearities or unsymmetries. One essential aspect for efficient solvers for large-scale problems is a good preconditioning technique. Various preconditioners based on algebraic multigrid (AMG) methods were proposed in Gee et al. [47], Heil [55], Klöppel et al. [67] for monolithic solution schemes for FSI problems based on matching and non-matching grids, respectively. If properly designed, those schemes were shown to enable fast, efficient, and robust solutions of the fully coupled problem.

Few monolithic approaches to TSI problems can be found in the literature, and most of them have been based on simplifying assumptions. For instance, monolithic algorithms were applied to the fully coupled linear thermomechanical problem along with a boundary element method (BEM) in Tanaka et al. [130], assuming that the linear stress term depends on the initial temperature T_0 instead of the current temperature T, as was also done in Farhat et al. [39]. That assumption avoided a linearisation with respect to the temperatures, so that the coupling term could be interpreted as an external load. By contrast, in the present work, the current temperature T, i.e. a full coupling will be considered. In Carter and Booker [24], a symmetric TSI system was constructed for small strain thermoelastic problems which was then solved in a fully coupled monolithic way. In Glaser [51], monolithic algorithms were developed for the calculation of thin-walled structures using shell elements and an arc-length method for the TSI solution. While all coupling terms were considered, only a simplified mechanical dissipation was included where the hardening power was neglected. In contrast, the present approach included all emerging dissipation terms. An effective monolithic approach based on a variational formulation of the fully coupled thermomechanical boundary-value problem for general dissipative solids was established in Yang et al. [147] and Stainier and Ortiz [128]. They showed that the proposed variational formulation was able to correctly predict the dissipated energy that was converted into heat by comparison with experimental data. Subsequently, their work was further proceeded in Canadija and Mosler [23], for instance with respect to account for kinematic hardening.

In the following, partitioned and monolithic solution techniques for coupled TSI problems will be specified. While in section 6.1 the target coupled system will be first summarized, in

section 6.2 loosely and strongly coupled partitioned schemes with different predictors will be presented. Subsequently, in section 6.3 a monolithic scheme with block Gauss-Seidel (BGS) preconditioner and AMG methods will be established.

6.1 Linearisation and solution techniques for nonlinear equations

Previously, partitioned and monolithic solution strategies for TSI problems have been introduced. Since both strategies apply a Newton-Raphson method to iteratively solve the coupled TSI system of nonlinear algebraic equations, in the following, the corresponding linear systems will be deduced. Based on section 3.3 and 4.3 for the single fields, the fully discrete equations for the structure (5.24) and the thermo (5.25) are considered, where exemplarily a generalised-α time integration scheme is used. Subsequently, residuals of the coupled problem can be defined for a given (Newton) iteration step i as

$$\mathbf{r}_{\mathsf{S}}(\mathbf{d}^i_{n+1}, \mathbf{T}^i_{n+1}) = \mathbf{M}\,\mathbf{a}^i_{n+1-\alpha_{\mathsf{m;S}}} + \mathbf{D}\,\mathbf{v}^i_{n+1-\alpha_{\mathsf{f;S}}} + \mathbf{f}_{\mathsf{int;S};n+1-\alpha_{\mathsf{f;S}}}(\mathbf{d}^i, \mathbf{T}^i) - \mathbf{f}_{\mathsf{ext;S};n+1-\alpha_{\mathsf{f;S}}}\,, \tag{6.1}$$

$$\mathbf{r}_{\mathsf{T}}(\mathbf{T}^i_{n+1}, \mathbf{d}^i_{n+1}) = \mathbf{C}\,\mathbf{t}^i_{n+\alpha_{\mathsf{m;T}}} + \mathbf{f}_{\mathsf{int;T};n+\alpha_{\mathsf{f;T}}}(\mathbf{T}^i, \mathbf{d}^i) - \mathbf{f}_{\mathsf{ext;T;n}+\alpha_{\mathsf{f;T}}}(\mathbf{T}^i, \mathbf{d}^i)\,. \tag{6.2}$$

Equation (6.1) and (6.2) represent the corresponding coupled residuals of the single fields structure (3.41) and thermo (4.31). Once the residuals are available, the linear systems of equations follow by

$$\mathbf{K}_{\mathsf{SS}}(\mathbf{d}^i_{n+1}, \mathbf{T}^i_{n+1})\,\Delta\mathbf{d}^{i+1}_{n+1} + \mathbf{K}_{\mathsf{ST}}(\mathbf{d}^i_{n+1}, \mathbf{T}^i_{n+1})\,\Delta\mathbf{T}^{i+1}_{n+1} = -\mathbf{r}^i_{\mathsf{S};n+1}\,, \tag{6.3}$$

$$\mathbf{K}_{\mathsf{TT}}(\mathbf{T}^i_{n+1}, \mathbf{d}^i_{n+1})\,\Delta\mathbf{T}^{i+1}_{n+1} + \mathbf{K}_{\mathsf{TS}}(\mathbf{T}^i_{n+1}, \mathbf{d}^i_{n+1})\,\Delta\mathbf{d}^{i+1}_{n+1} = -\mathbf{r}^i_{\mathsf{T};n+1}\,, \tag{6.4}$$

where due to the coupling effects the matrices $\mathbf{K}_{\mathsf{ST}}$ and $\mathbf{K}_{\mathsf{TS}}$ emerge. While $\mathbf{K}_{\mathsf{ST}}$ includes the linearisation of the structural equations with respect to the temperatures (as e.g. the linearisation of the thermal stresses with respect to the temperatures), the matrix $\mathbf{K}_{\mathsf{TS}}$ includes the linearisation of the thermal equations with respect to the displacements (as e.g. the linearisation of the thermoelastic heating term $\mathcal{H}^e$ (5.35) with respect to the displacements). For the sake of completeness, the diagonal matrices $\mathbf{K}_{\mathsf{SS}}$ and $\mathbf{K}_{\mathsf{TT}}$ correspond to the tangential matrices (3.45) and (4.32), respectively, which can include additional terms due to the coupling, as described e.g. in (5.84). Since $\mathbf{K}_{\mathsf{ST}} \neq \mathbf{K}^{\mathsf{T}}_{\mathsf{TS}}$, the TSI system is non-symmetric. Equation (6.3) and (6.4) can be summarized in matrix notation to

$$\begin{bmatrix} \mathbf{K}_{\mathsf{SS}} & \mathbf{K}_{\mathsf{ST}} \\ \mathbf{K}_{\mathsf{TS}} & \mathbf{K}_{\mathsf{TT}} \end{bmatrix}^i_{n+1} \begin{bmatrix} \Delta\mathbf{d} \\ \Delta\mathbf{T} \end{bmatrix}^{i+1}_{n+1} = - \begin{bmatrix} \mathbf{r}_{\mathsf{S}} \\ \mathbf{r}_{\mathsf{T}} \end{bmatrix}^i_{n+1}\,. \tag{6.5}$$

If a converged solution is achieved, the solution vectors for both fields at t_{n+1} are computed by (3.46) and (4.33), respectively.

6.2 Partitioned solution approach

In the present section, the different partitioned TSI algorithms will be presented. Based on section 6.1, (6.3) and (6.4) describe the system of equations which is solved using a partitioned

algorithm. As mentioned in the introduction of this chapter, the coupling variables are passed in partitioned algorithms as "external loads" with known values from one field to another. Consequently, the matrices K_{ST} and K_{TS} vanish. Subsequently, based on (6.5), the partitioned TSI system follows as

$$\begin{bmatrix} \mathsf{K}_{\mathsf{SS}} & \mathbf{0} \\ \mathbf{0} & \mathsf{K}_{\mathsf{TT}} \end{bmatrix}_{n+1}^{i} \begin{bmatrix} \Delta \mathbf{d} \\ \Delta \mathbf{T} \end{bmatrix}_{n+1}^{i+1} = - \begin{bmatrix} \hat{\mathbf{r}}_{\mathsf{S}} \\ \hat{\mathbf{r}}_{\mathsf{T}} \end{bmatrix}_{n+1}^{i} , \tag{6.6}$$

where the two fields are decoupled, so that each can apply its own Newton method. The $\hat{(\cdot)}$ in the residuals indicates that the residuals include coupling information in the form of external loads.

In the following, the well-known isothermal split is considered as coupling strategy. To enable a common representation of the partitioned TSI approach used in various references, for instance in Armero and Simo [6], Erbts and Düster [38], and Simo and Miehe [122], alternatively to the representation of the fully discrete problem in (6.6), a nonlinear operator

$$\mathcal{A}(\boldsymbol{u}(\boldsymbol{X},t), \dot{\boldsymbol{u}}(\boldsymbol{X},t), T(\boldsymbol{X},t)) = \left\{ \begin{array}{l} \dot{\boldsymbol{u}} \\ \rho_0 \, \ddot{\boldsymbol{u}} - \operatorname{Div} \boldsymbol{P}(\boldsymbol{u},T) - \hat{\boldsymbol{b}}_0 \\ \rho_0 \, C_{\mathsf{V}} \dot{T} + \operatorname{Div} \boldsymbol{Q} - \rho_0 \, r - \mathcal{D}_{\mathsf{mech}} - \mathcal{H}^{ep} \end{array} \right\} \tag{6.7}$$

is introduced for the continuous TSI problem, where the variables are summarized in $\boldsymbol{s} = \{\boldsymbol{u}(\boldsymbol{X},t), \dot{\boldsymbol{u}}(\boldsymbol{X},t), T(\boldsymbol{X},t)\}$. Subsequently, for the isothermal split, the operator $\mathcal{A}$ is split into the two following subproblems

$$\begin{aligned} \mathcal{A}_{\mathsf{S}}^{1}(\boldsymbol{s}) &= \left\{ \begin{array}{l} \dot{\boldsymbol{u}} \\ \rho_0 \, \dot{\boldsymbol{u}} - \operatorname{Div} \boldsymbol{P}(\boldsymbol{u},T) - \hat{\boldsymbol{b}}_0 = \mathbf{0} \\ 0 \end{array} \right\} , \\ \mathcal{A}_{\mathsf{T}}^{2}(\boldsymbol{s}) &= \left\{ \begin{array}{l} \mathbf{0} \\ \mathbf{0} \\ \rho_0 \, C_{\mathsf{V}} \dot{T} + \operatorname{Div} \boldsymbol{Q} - \rho_0 \, r - \mathcal{D}_{\mathsf{mech}} - \mathcal{H}^{ep} = 0 \end{array} \right\} , \end{aligned} \tag{6.8}$$

where $\mathcal{A}_{\mathsf{S}}^{1}(\boldsymbol{s})$ corresponds to the purely mechanical, isothermal and $\mathcal{A}_{\mathsf{T}}^{2}(\boldsymbol{s})$ to the purely thermal, heat conduction phase, respectively. According to this split, the sub-problems $\mathcal{A}_{\mathsf{S}}^{1}$ and $\mathcal{A}_{\mathsf{T}}^{2}$, which represent the predictor and the corrector phase, respectively, are decoupled. The continuous subproblems are first fully discretised in space and time, as previously presented in chapter 5.2, and subsequently can be solved successively within one time step leading to a two step solution procedure. The two step procedure implies, that the isothermal subproblem $\mathcal{A}_{\mathsf{S}}^{1}(\boldsymbol{s})$ is solved for the displacements first (i.e. predictor), which are then passed to $\mathcal{A}_{\mathsf{T}}^{2}$ to compute the temperatures (i.e. corrector).

In the following, the different solution procedures available in this thesis for partitioned TSI problems are presented. The most trivial coupling strategies are depicted in Figure 6.1. Herein, one-way or unidirectional loosely coupling schemes are shown, i.e. the coupling information is passed from one field to the other, but not vice versa. The horizontal arrows in Figure 6.1 indicate the solution in time. Hence, the first row describes the temperature solution in time and the second row the corresponding displacement solution in time. The vertical arrows indicate the exchange of coupling information. Using this coupling scheme, a TSI simulation can be realised in which one field is completely decoupled from the other. For instance in Figure 6.1

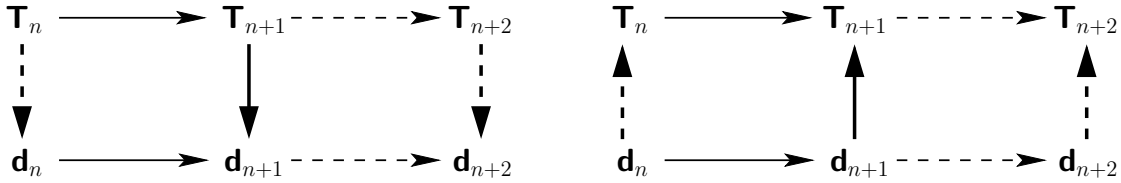

Figure 6.1: Unidirectional, one-way loosely coupled TSI with temperature (left) and displacement (right) as coupling variable.

(left), within time step t_{n+1} first the temperatures $\mathbf{T}_{n+1}$ are computed, subsequently $\mathbf{T}_{n+1}$ is passed to the structural field and is then used with $\mathbf{d}_n$ to compute the displacement solution $\mathbf{d}_{n+1}$. For instance, this coupling strategy (cf. Figure 6.1 (left)) can be used to simulate an example with purely thermal external loads resulting in temperature changes and, due to the coupling, in deformations, i.e. thermal expansion. In contrast, the deformation does not enter the thermo field. Consequently, it comprises the solution of the thermal field (4.21) and the coupled structural equation (5.20). Furthermore, Figure 6.1 (right) enables problems, as e.g. compression of a bar leading to heating due to dissipation neglecting thermal expansion.

The previously presented coupling schemes enable an one-way coupled TSI simulation. However, the thesis aims at fully coupled TSI, so that unidirectional coupling is not sufficient. Thus, as shown in Figure 6.2, two-way loosely and strongly coupled TSI algorithms are established. Exemplarily, a mechanical predictor is chosen which further contributes to improve the solution procedure. The mechanical predictor is indicated in Figure 6.2 by the inclined arrows. Alternatively, a thermal predictor can be applied so that, e.g. a corresponding two-way cou-

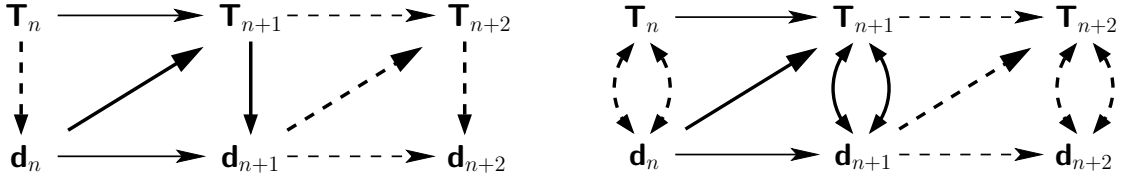

Figure 6.2: Two-way loosely (left) and strongly (right) coupled schemes with mechanical predictor.

pled algorithm based on Figure 6.1 (right) can be established via additional inclined arrows from top to bottom.

Both coupling strategies in Figure 6.2 describe a full coupling, i.e. both fields are influenced by a coupling effect. For instance in Figure 6.2 (left), within the mechanical predictor the coupling information of the old time step $\mathbf{d}_n$ is passed to the thermal field to compute the new temperature solution $\mathbf{T}_{n+1}$. Subsequently, the temperature $\mathbf{T}_{n+1}$ is passed to the structural field, so that two-way or bi-directional full coupling is realised. Figure 6.2 (left) depicts a loosely coupling, i.e. a time offset of the coupling effects arises. At the end of a time step equilibrium is not achieved. In contrast, in the strong coupling shown in Figure 6.2 (right), within one time step the coupling variables are exchanged in both directions. Equilibrium of the overall TSI system is achieved with respect to a given exactness criterion ϵ_{out} by iteration between the fields known as the so-called outer iteration loop. As mentioned at the beginning of this section and in the introduction (cf. section 1.2), strongly coupled partitioned algorithm may have the draw-

back of possibly slow convergence. Consequently, to accelerate the convergence behaviour, fix or dynamic relaxation can be integrated in strongly coupled partitioned TSI schemes. Numerical relaxation is a common method in computational mechanics to accelerate the convergence of the outer iteration loop (with iteration index l) by modifying the current solution vectors before passing them to the other field in the next iteration step. In this context, acceleration is meant to reduce the number of iterations in the outer iteration loop and to stabilize the partitioned coupling procedure. To explain the relaxation techniques applied in the present work, an abstract vector $\mathbf{y}$ is considered which can either represent the displacement or the temperature solution vector which subsequently is relaxed. For instance, relaxing the displacements, i.e. $\mathbf{y} = \mathbf{d}$, relaxation comprises that within the outer iteration loop iteration between the fields structure and thermo (indicated in Figure 6.2 (right) by the curved arrows), the current relaxed displacement solution $\mathbf{d}^{l+1}$ is passed to the thermal field as new coupling variable.

In the following, fix and dynamic relaxation strategies are presented. Both relaxation strategies are based on known iterative solution vectors $\mathbf{y}^{l-p}$ with ($p = 0, 1, 2, ... \leq l$ and $l = 0, 1, 2, ..., l_{\mathsf{max}}$), which are used to compute a new iterative solution $\check{\mathbf{y}}^{l+1}$. Instead of $\check{\mathbf{y}}^{l+1}$, a relaxed solution vector $\mathbf{y}^{l+1}$ is passed to the coupling field. The first and most trivial form is a fix relaxation which is characterized by

$$\mathbf{y}^{l+1} = \mathbf{y}^{l} + \omega \, \Delta\mathbf{y}^{l+1} \,, \tag{6.9}$$

where ω denotes the fix relaxation parameter, i.e. $\omega = const.$ and $\Delta\mathbf{y}^{l+1} = \check{\mathbf{y}}^{l+1} - \mathbf{y}^{l}$. Furthermore, in the context of dynamic relaxation, the Aitken Δ^2 method is applied, as proposed by Irons and Tuck [62] which was utilised for FSI, e.g. in Küttler [70], Küttler and Wall [71, 72], and Mok [93], and for TSI with an isothermal split, e.g in Danowski et al. [29] and Erbts and Düster [38]. Based on known iterative solution vectors $\mathbf{y}^{l-p}$, a new iterative solution $\check{\mathbf{y}}^{l+1}$ is computed within the Aitken Δ^2 method. In contrast to fix relaxation, the Aitken relaxation parameter ω^{Ait} is recalculated in each iteration. For $l \geq 1$, first the so-called Aitken factor μ is extrapolated via

$$\mu^{l} = \mu^{l-1} + (\mu^{l-1} - 1) \, \frac{[\Delta\mathbf{y}^{l+1} - \Delta\mathbf{y}^{l}]^{\mathsf{T}} \cdot (-\Delta\mathbf{y}^{l+1})}{(\Delta\mathbf{y}^{l+1} - \Delta\mathbf{y}^{l})^2} \tag{6.10}$$

with initial guess $\mu^{l=0} = 0$. Subsequently, the Aitken relaxation parameter follows as

$$\omega^{\mathsf{Ait};l} = 1 - \mu^{l} \,, \tag{6.11}$$

which is used to calculate the relaxed new solution vector, according to (6.9), by

$$\mathbf{y}^{l+1} = \mathbf{y}^{l} + \omega^{\mathsf{Ait};l} \, \Delta\mathbf{y}^{l+1} \,. \tag{6.12}$$

Since in (6.10) three solution vectors $\mathbf{y}^{l+1}$, $\mathbf{y}^{l}$ and $\mathbf{y}^{l-1}$ are required to calculate the Aitken factor μ^{l}, and moreover the initial values are chosen to $\mu^{0} = 0$ or $\omega^{\mathsf{Ait};0} = 0$, the first iterative solution $\mathbf{y}^{1}$ is not relaxed. Apart from this initial guess for the first time step, as proposed in Irons and Tuck [62] and utilised in Mok [93], the initial guess for the next time step $n+1$ and $l = 0$ is set to $\mu^{0}_{n+1} = \mu^{l_{\mathsf{max}}}_{n}$, i.e. to the latest relaxation parameter of the last time step. Moreover, as observed in Küttler [70] in the context of FSI, it is recommended to limit the relaxation parameter. In case of too large relaxation parameters the solution may diverge. Hence, to circumvent divergence,

the present approach includes a problem-dependent maximal relaxation parameter ω^{max} which limits the largest possible relaxation parameter for the new time step via

$$\omega_{n+1}^{\mathsf{Ait};0} \;=\; \min(\omega_{n}^{\mathsf{Ait};l_{\mathsf{max}}}\,,\,\omega^{\mathsf{max}})\,. \tag{6.13}$$

As described previously, convergence of the outer iteration loop is achieved if a prescribed tolerance ϵ_{out} is met. Herein, either relative or absolute criteria are possible, i.e. exemplarily for the displacements it follows

$$\frac{||\Delta\mathbf{d}_{n+1}^{l+1}||}{||\mathbf{d}_{n}||} \;<\; \epsilon_{\mathsf{out}}\,, \quad \text{or } ||\Delta\mathbf{d}_{n+1}^{l+1}|| \;<\; \epsilon_{\mathsf{out}}\,, \tag{6.14}$$

where for the norm $||\cdot||$ it is common to use the L^2-norm. Equation $(6.14)_1$ describes a relative criterion with respect to a known, converged solution $\mathbf{d}_n$. Furthermore, the relative criterion can refer to the solution of the last iteration step of the outer iteration loop $\mathbf{d}_{n+1}^{l}$ for the current time t_{n+1}. This can be critical, since convergence may be achieved based on a bad initial solution $\mathbf{d}_{n+1}^{l}$. Consequently, although the solution may be said to be converged and equilibrium may be said to be achieved, the results may be completely unphysical. Thus, one should decide carefully which is the most suitable convergence criterion for a given problem. Finally, equilibrium of strongly coupled partitioned TSI algorithms is said to be achieved if (6.14) is fulfilled for both displacements and temperatures.

In Erbts and Düster [38], a fully thermomechanical coupling for finite strain thermoelasticity is presented where weakly and strongly physical coupling are described dependent on the value of the coefficient of thermal expansion, so that loosely and strongly coupled solution approaches become necessary. They show that the isothermal split can achieve a converged and stable solution for their examples even if strong physical coupling is considered. Moreover, dynamic relaxation of the displacements is utilised, but they do not mention the treatment of the velocities in detail, so that it is not clear how they treat the velocities, i.e. either the velocities are relaxed according to the displacements or the velocities are recalculated after having relaxed the displacements. For the case of neglecting the velocities within the relaxation process, the resulting velocities do not fit to the displacements, so that a judgement of the results is difficult. In contrast, in this thesis in case of relaxing the displacements (i.e. $\mathbf{y} = \mathbf{d}$), the velocities are recalculated after having relaxed the displacements, so that displacements and velocities correlate. This may have an influence for the coupling, since the velocities are required, e.g. for the coupling term $\mathcal{H}^{ep}$. Moreover, the present work enables in addition the relaxation of the temperatures, i.e. $\mathbf{y} = \mathbf{T}$. To conclude, it is recommended to relax the coupling variable which is not directly influenced by the external loads. Hence, for instance in a tension or compression test where a purely mechanical load is applied, it is recommended to relax the temperatures, whereas, e.g. heating of a body, i.e. applying a purely thermal load, the displacements should be relaxed. Thus, in addition to the external loads, the body experiences, due to the relaxation, only a part of the coupling load.

As stated in the introduction of this chapter, one advantage of partitioned approaches is their flexibility. Exemplarily, different time integration schemes can be used for the coupling fields while consistent time integration is guaranteed in all cases. Even if the evaluation point of the equilibrium equation for structure and thermo are different (e.g. generalised-α for the structure and one-step-θ for the thermo), a consistent time integration is achieved because the coupling

information are exchanged at the end of the time step, i.e. at t_{n+1} by interpolating the solution vectors. A very common assumption in TSI is a quasi-static time integration, i.e. the structure is solved neglecting the inertia effects whereas the thermo field is solved dynamically. Since, for instance the coupling term $\mathcal{H}^{ep}$ requires the velocities, the velocities in a quasi-static TSI approach are calculated in this work using a finite difference scheme according to

$$\dot{\mathbf{d}}_{n+1} = \frac{\mathbf{d}_{n+1} - \mathbf{d}_n}{\Delta t}, \tag{6.15}$$

which corresponds to a backward Euler.

6.3 Monolithic solution approach

In the following, a monolithic solution scheme for the TSI problem will be presented which is based on Danowski et al. [29]. The fully coupled non-symmetric TSI system resulting from above derivations and (6.1)-(6.4) or (6.5) is

$$\underbrace{\begin{bmatrix} \mathsf{K}_{\mathsf{SS}} & \mathsf{K}_{\mathsf{ST}} \\ \mathsf{K}_{\mathsf{TS}} & \mathsf{K}_{\mathsf{TT}} \end{bmatrix}_{n+1}^{i}}_{\mathsf{K}_{n+1}^{\mathsf{TSI};i}} \underbrace{\begin{bmatrix} \Delta\mathbf{d} \\ \Delta\mathbf{T} \end{bmatrix}_{n+1}^{i+1}}_{\mathsf{x}_{n+1}^{i+1}} = \underbrace{-\begin{bmatrix} \mathbf{r}_{\mathsf{S}} \\ \mathbf{r}_{\mathsf{T}} \end{bmatrix}_{n+1}^{i}}_{-\mathsf{r}_{n+1}^{\mathsf{TSI};i}}. \tag{6.16}$$

After preconditioning, the coupled linear system (6.16) for time step $n+1$ and iteration step $i+1$ reads

$$\mathsf{K}^{\mathsf{TSI}}\,\mathsf{M}_{\mathsf{R}}^{-1}\,\mathsf{M}_{\mathsf{R}}\,\mathsf{x} = -\mathsf{r}^{\mathsf{TSI}}, \tag{6.17}$$

where M_{R} is the right preconditioning matrix. As stated in section 3.5, right preconditioning is used here exclusively. For the sake of simplicity, the Newton and time iteration indices are omitted in the following. Again, for an effective and efficient preconditioning process, the preconditioner matrix M_{R} should approximate the tangent matrix of the coupled TSI system (or Jacobian of the TSI problem) well ($\mathsf{M}_{\mathsf{R}} \approx \mathsf{K}^{\mathsf{TSI}}$), while being invertible with as little effort as possible.

Based on the abstract linear system (3.226) with the vectors y and z, the linear TSI system is iteratively solved performing a stationary Richardson iteration, i.e.

$$\mathsf{z}^{j+1} = \mathsf{z}^{j} + \omega_{\mathsf{BGS}}\,\Delta\mathsf{z}^{j+1} \quad \text{with} \quad \Delta\mathsf{z}^{j+1} = \mathsf{M}_{\mathsf{R}}^{-1}\,\underbrace{(\mathsf{y} - \mathsf{K}^{\mathsf{TSI}}\,\mathsf{z}^{j})}_{\check{\mathsf{r}}^{j}}, \tag{6.18}$$

with the iteration residual $\check{\mathsf{r}}^{j}$, the Richardson iteration index j, and the potential parameter $\omega_{\mathsf{BGS}} \in (0, 1]$, which can be interpreted as a relaxation parameter for the update of z^{j+1} (cf. (6.9)).

Since the properties of the individual blocks (structural and thermal submatrices) in the monolithic system (6.16) differ considerably, standard preconditioners cannot be applied. Alternatively, a BGS preconditioner is employed here. In this case, the different equation blocks of the linear system are solved successively within the two-step Gauss-Seidel iteration process. For each step, just as for partitioned schemes, efficient field-specific solvers like the algebraic multigrid (AMG) method can be used. As demonstrated for FSI in Gee et al. [47], the sequence of solution blocks in the preconditioner is physically motivated. In TSI, it is common to assume that

the effect of the structure on the thermal field is less important than the opposite effect. Thus, to enable an efficient solution, the preconditioning matrix is chosen to be

$$\mathbf{M}_{\mathsf{R}} = \begin{bmatrix} \mathbf{K}_{\mathsf{SS}} & \omega_{\mathsf{BGS}}\,\mathbf{K}_{\mathsf{ST}} \\ \mathbf{0} & \mathbf{K}_{\mathsf{TT}} \end{bmatrix}, \tag{6.19}$$

assuming that the effect of thermal expansion has a higher influence than the thermoelastic heating. In the first step, the solution of the thermal field is determined from

$$\mathbf{K}^{i}_{\mathsf{TT}}\,\Delta\mathbf{z}^{T;j+1} = \check{\mathbf{r}}^{j}_{\mathsf{T}} = \mathbf{y}_{\mathsf{T}} - \mathbf{K}^{i}_{\mathsf{TT}}\,\mathbf{z}^{T;j} - \mathbf{K}^{i}_{\mathsf{TS}}\,\mathbf{z}^{d;j}\,, \tag{6.20}$$

using the displacement and temperature values $\mathbf{z}^{d;j}$ and $\mathbf{z}^{T;j}$, respectively, resulting from the previous block Gauss-Seidel iteration step j. The update of the temperature solution vector is realised according to

$$\mathbf{z}^{T;j+1} = \mathbf{z}^{T;j} + \omega_{\mathsf{BGS}}\,\Delta\mathbf{z}^{T;j+1}\,. \tag{6.21}$$

In the second step, the update of the structural field is computed by solving

$$\mathbf{K}_{\mathsf{SS}}\,\Delta\mathbf{z}^{d;j+1} = \check{\mathbf{r}}^{d;j} - \omega_{\mathsf{BGS}}\,\mathbf{K}_{\mathsf{ST}}\,\mathbf{z}^{T;j+1} = \mathbf{y}_{\mathsf{S}} - \mathbf{K}_{\mathsf{SS}}\,\mathbf{z}^{d;j} - \omega_{\mathsf{BGS}}\,\mathbf{K}_{\mathsf{ST}}\,\mathbf{z}^{T;j+1}\,, \tag{6.22}$$

with the new temperature values $\mathbf{z}^{T;j+1}$ and

$$\mathbf{z}^{d;j+1} = \mathbf{z}^{d;j} + \omega_{\mathsf{BGS}}\,\Delta\mathbf{z}^{d;j+1}\,. \tag{6.23}$$

For the approximate solution of (6.20) and (6.22), again AMG methods are utilised as proposed in Gee et al. [47].

In case of inclusion of plasticity into the TSI problem, in contrast to (6.19), the opposite sequence may be more appropriate. Due to plasticity, dissipation arises and may have a significant impact on the thermo solution. Hence, instead of the procedure (6.19)-(6.23), the preconditioning matrix may be assumed to

$$\mathbf{M}_{\mathsf{R}} = \begin{bmatrix} \mathbf{K}_{\mathsf{SS}} & \mathbf{0} \\ \omega_{\mathsf{BGS}}\,\mathbf{K}_{\mathsf{TS}} & \mathbf{K}_{\mathsf{TT}} \end{bmatrix}, \tag{6.24}$$

so that the solution is obtained via firstly solving the structural field, and secondly updating the thermo field while applying the recently computed displacements $\mathbf{z}^{d;j+1}$. Consequently, for each TSI problem the appropriate sequence within the preconditioner has to be chosen according to the requirements. According to Gee et al. [47], the procedure (6.19)-(6.23) constitutes a backward BGS preconditioner, whereas the corresponding procedure utilising (6.24) constitutes a forward BGS preconditioner.

To summarize the proposed preconditioning method, a BGS preconditioner with independent AMG preconditioners for the respective diagonal blocks is used as given in Algorithm 4. As in Gee et al. [47], this preconditioning is named "BGS(AMG)". Both the open-source package AZTEC (see Tuminaro et al. [138]) and the ML package (see Gee et al. [45]) developed by Sandia National Laboratories are used for the solution procedure. To finish this section, the proposed monolithic TSI solution procedure is summarized in Algorithm 5.

In Algorithm 5, for convergence of the Newton-Raphson scheme the norm of the TSI residual $||\mathbf{r}^{\mathsf{TSI};i}_{n+1}||$ and the norm of the TSI vector $||\mathbf{x}^{\mathsf{TSI};i}_{n+1}||$ are tested. Beyond, the single fields can be

Algorithm 4 Relaxed block Gauss-Seidel iteration process employed as approximate solver for the abstract TSI problem based on (3.226) using (6.18) and (6.19).

for each iteration step j
  Compute thermal solution increment $\Delta \mathbf{z}^{T,j+1}$ from (6.20)
  Update thermal solution $\mathbf{z}^{T,j+1}$ utilising (6.21)
  Compute structural solution increment $\Delta \mathbf{z}^{d,j+1}$ from (6.22)
  Update structural solution $\mathbf{z}^{d,j+1}$ utilising (6.23)

tested for convergence separately. Hence, the strictest convergence criterion for the Newton-Raphson comprises the check for convergence of the coupled TSI problem and of the single fields structure and thermo, in which for each both the residual and the increment are tested. Moreover, as mentioned in section 3.3, the chosen convergence norm has a high influence, i.e. a simulation may converge or even diverge dependent on the chosen norm. It is common to use the L^2-norm or the root mean square (RMS) norm. While these norms consider all entries, an extreme single peak in the solution of one single DOF is not noticed but balanced out with the values of all other DOFs. In contrast, an infinity norm L^∞ gives the absolute value of the largest component of the vector, hence a single high peak can lead to an inadmissible norm so that the whole simulation can diverge.

Another important aspect arises in a challenging TSI problem using an iterative solver: here, the interaction between the nonlinear solver (Newton-Raphson iteration scheme) and the linear solver (an iterative solver, as the GMRES) is very important and has to be treated very carefully. The difficulty of this aspect is emphasized in the following by means of two possible convergence settings. Based on Table 6.1, an equilibrium state is achieved if all three prescribed tolerances

	Nonlinear solver residual	Nonlinear solver increment	Linear solver
1.	$\|\|\mathbf{r}^{\mathsf{TSI};i}\|\|/\|\|\mathbf{r}^{\mathsf{TSI};i=0}\| \| \leq 10^{-6}$	$\|\|\mathbf{x}^{\mathsf{TSI};i}\| \| \leq 10^{-8}$	$\|\|\mathbf{r}^{j+1}\|\|/\|\|\mathbf{r}^{j=0}\| \| \leq 10^{-4}$
2.	$\|\|\mathbf{r}^{\mathsf{TSI};i}\|\|/\|\|\mathbf{r}^{\mathsf{TSI};i=0}\| \| \leq 10^{-6}$	$\|\|\mathbf{x}^{\mathsf{TSI};i}\| \| \leq 10^{-8}$	$\|\|\mathbf{r}^{j+1}\|\|/\|\|\mathbf{r}^{j=0}\| \| \leq 10^{-8}$

Table 6.1: Two different solver settings using relative and absolute convergence criteria for the Newton-Raphson scheme (i.e. nonlinear solver) and a relative criterion for the iterative, linear solver.

in the nonlinear and in the linear solver are met. The only difference between the two settings in Table 6.1 is the criterion for the linear solver ϵ_{lin}. As mentioned above, an iterative solver approximates the solution with respect to ϵ_{lin}. In case of a too coarse criterion ϵ_{lin}, the solution of the overall problem is approximated only roughly and may lie outside the convergence radius of the Newton-Raphson. Consequently, possibly no solution may be found since the prescribed descendent direction may no fit. Thus, to ensure a correct Newton direction, it is recommended to first choose appropriate Newton criteria $\epsilon_{r^{\mathsf{TSI}}}$ and $\epsilon_{x^{\mathsf{TSI}}}$, and subsequently the criterion ϵ_{lin} for the linear solver, which in general should be of the same order of magnitude or even stricter than the criterion $\epsilon_{r^{\mathsf{TSI}}}$.

For the check of the coupled TSI vectors, i.e. residual $\mathbf{r}^{\mathsf{TSI}}$ and increment $\mathbf{x}^{\mathsf{TSI}}$, it is noted, that the vectors need to be scaled with the total number of DOFs. For instance in a three-dimensional

Algorithm 5 Solution procedure for TSI problem (6.16) with right preconditioned Newton-Krylov approach.

Time loop
for time step $n = 0, ..., t_{\max}$
  Predictor $\mathbf{x}_{n+1}^0 = \mathbf{x}_n$

  # Newton-Raphson iteration
  for each iteration step $i = 0, ..., \max_{\text{nlniter}}$
    # Check for convergence of Newton-Raphson iteration
    if $||\mathbf{r}_{n+1}^{\text{TSI};i}|| \leq \epsilon_{r^{\text{TSI}}}$ **and if** $||\mathbf{x}_{n+1}^{\text{TSI};i}|| \leq \epsilon_{x^{\text{TSI}}}$
      stop Newton-Raphson iteration
    Calculate $\mathbf{r}_{n+1}^{\text{TSI};i+1} = \mathbf{r}^{\text{TSI}}(\mathbf{x}_{n+1}^{i+1})$

    Initial guess $\check{\mathbf{x}}^0 = \mathbf{x}_{n+1}^{i+1;j=0}$
    # Calculate linear residual vector $\mathbf{r}^{j=0} = \mathbf{r}^0$
    $\mathbf{r}^0 = \Delta\mathbf{r}^0 = \mathbf{r}_{n+1}^{\text{TSI};i+1;j=0} - \mathbf{K}_{n+1}^{\text{TSI};i}\,\check{\mathbf{x}}^0$

    # Krylov iteration
    for each iteration step $j = 0, ..., \max_{\text{liniter}}$
      Apply block preconditioner $\mathbf{p}^{j+1} = \mathbf{M}_{\text{R}}^{-1}\,\Delta\mathbf{r}^j$ $\rightsquigarrow$ use Algorithm 4

      # Solve for Krylov increment $\Delta\check{\mathbf{x}}^{j+1}$ using $\mathbf{p}^{j+1}$ (e.g. with GMRES)
      Calculate $\Delta\check{\mathbf{x}}^{j+1} = \sum_k^{j+1} \Delta\check{\mathbf{x}}^k$ with $0 \leq k \leq j$ using $\mathbf{M}_{\text{R}}^{-1}$
      Update $\check{\mathbf{x}}^{j+1} = \check{\mathbf{x}}^j + \Delta\check{\mathbf{x}}^{j+1}$ and $\mathbf{r}^{j+1} = \mathbf{r}^{\text{TSI};j} - \mathbf{K}^{\text{TSI}}\,\check{\mathbf{x}}^{j+1}$
      # Check for convergence of Krylov iteration
      if $||\mathbf{r}^{j+1}||/||\mathbf{r}^0|| \leq \epsilon_{\text{lin}}$
        stop Krylov iteration

    Calculate solution vector $\mathbf{x}^{j+1} = \mathbf{M}_{\text{R}}^{-1}\,\check{\mathbf{x}}^{j+1}$ for time step $n+1$ and Newton iteration step $i+1$ $\rightsquigarrow$ use Algorithm 4

    Update solution vectors $\mathbf{x}_{n+1}^{i+1} = \mathbf{x}_{n+1}^i + \Delta\mathbf{x}_{n+1}^{i+1}$
    Update Newton-Raphson iteration step $i = i + 1$

  Update time $t = t + \Delta t$ and step $n = n + 1$

problem, the structure has three DOFs per node whereas the thermo has one DOF per node. Hence, within the TSI system the structure is weighted by a factor of three compared to the thermo field. To circumvent this issue, for convergence check of the TSI vectors the RMS norm is recommended which is defined as a L^2-norm scaled with the square root of the length of the vector, i.e. the total number of DOFs.

Another important issue arises for the TSI system because of the inclusion of units. SI-units are metre, seconds, kelvin, kilogram. For a TSI simulation the SI-units may not be appropriate. For instance, a deformed body is described by a temperature change of about $\Delta T = 300\ \mathrm{K}$ and a deformation in the range of millimetres. Thus, the solution vector includes (temperature) increments of 300 and (displacement) increments of 10^{-3} spanning in total 5 order of magnitude. Moreover, the condition of the system is deteriorated since terms of the tangent matrix and the solution vector differ by a factor of 10^{14} (e.g. Young's modulus of steel is $2.1 \cdot 10^{11} \frac{\mathrm{N}}{\mathrm{m}^2}$ with displacement increments of about $1\ \mathrm{mm} = 0.001\ \mathrm{m}$). Improvements are realised by choosing, for instance the following units $[\mathrm{mm}, \mathrm{ms}, \mathrm{K}, \mathrm{kg}]$. For this choice, the condition of the system is improved as the matrix entries and the displacement increments only span 2 order of magnitude (matrix entries $\approx 210\ \mathrm{GPa}$ with increments $\approx 1\ \mathrm{mm}$ leading to a range of $\approx 10^2$).

In Mayr et al. [86], a consistent time integration for the surface-coupled problem of FSI is presented. They show that optimal temporal convergence is achieved by interpolating consistently the coupling fields and the coupling conditions. Hence, for the choice of generalised-α scheme for the structural field and one-step-θ scheme for the fluid field (which is commonly utilised in FSI, as e.g. in Klöppel et al. [67] and Küttler and Wall [71]), optimal convergence is achieved. In this thesis, consistent time integration for the present monolithic TSI approach is realised by restricting the choice of time integration schemes for both fields to the same scheme with the same parameters. For instance, using generalised-α time integration for TSI, as shown in (5.24) and (5.25), the same spectral radius ρ_∞ is assumed for both fields, i.e. $\rho_\infty = \rho_{\infty;\mathsf{S}} = \rho_{\infty;\mathsf{T}}$. Furthermore, for the choice of one-step-θ time integration, in (5.22) and (5.23) the parameters θ are chosen to $\theta = \theta_\mathsf{S} = \theta_\mathsf{T}$.

In the context of monolithic solution approaches and large deformation TSI, heat convection boundary conditions require a special treatment for the tangent matrix. Since they depend on both the temperatures and the displacements, full linearisation leads on the one hand to the well-known contributions for the matrix $\mathbf{K}_{\mathsf{TT}}$ due to linearisation with respect to the temperatures and on the other hand to contributions for $\mathbf{K}_{\mathsf{TS}}$ due to linearisation with respect to the displacements. While the derivations for $\mathbf{K}_{\mathsf{TT}}$ are straight-forward, focus is set on the derivation for $\mathbf{K}_{\mathsf{TS}}$ which arises only in a monolithic approach (in contrast, in partitioned approaches $\mathbf{K}_{\mathsf{TS}}$ is neglected, see (6.6)). As previously discussed in section 5.1.2, a spatial approach for this thermal boundary condition is advantageous. Hence, further nonlinearities are introduced into the problem by use of the current area element $\mathrm{d}A$. Moreover, time discretisation with an one-step-θ method is exemplarily assumed in the following. According to (5.16), using the index notation, the boundary condition at node I is given by

$$\theta \cdot (\mathsf{f}_{\mathsf{ext};\mathsf{T};I})_{n+1}^{(e);i} \;=\; -\theta \Big(\int\limits_{\varphi(\Gamma_\mathsf{C}^{(e)})} -\boldsymbol{q} \cdot \boldsymbol{n}\, \mathrm{d}A \Big)_{n+1}^{(e);i} \;=\; -\theta \Big(\int\limits_{\varphi(\Gamma_\mathsf{C}^{(e)})} h\,(T - T_\infty)\, \mathrm{d}A \Big)_{n+1}^{(e);i}, \quad (6.25)$$

so that the overall contribution to the matrix K_{TS} is obtained as

$$\left(\mathsf{K}_{\mathsf{TS};I;(J;r)}\right)_{n+1}^{(e);i} \;=\; -\theta \int\limits_{\varphi(\Gamma_{\mathsf{C}}^{(e)})} \mathsf{N}_{\mathsf{T}}^{\mathsf{T}}\, h\,(\mathsf{N}_{\mathsf{T}}\,\mathsf{T}_{n+1}^{i} \;-\; T_{\infty})\,\mathrm{d}A^{(e)} \left(\frac{\partial A}{\partial \mathsf{d}_{J;r}}\right)_{n+1}^{(e);i}, \tag{6.26}$$

where r denotes the respective coordinate direction. Recalling that the area of an arbitrary curved surface (cf. section 2.1.2) is given as

$$A^{(e)} \;=\; \int_{-1}^{1}\int_{-1}^{1} \sqrt{\check{n}_1 \;+\; \check{n}_2 \;+\; \check{n}_3}\,\mathrm{d}\xi_1\,\mathrm{d}\xi_2 \;=\; \int_{-1}^{1}\int_{-1}^{1} |\check{\mathbf{n}}|\,\mathrm{d}\xi_1\,\mathrm{d}\xi_2\,, \tag{6.27}$$

thus the derivation of the area with respect to the displacement in r-direction at node I reads

$$\begin{aligned}\left(\frac{\partial A}{\partial \mathbf{d}}\right)_{n+1}^{(e);i} \;&=\; \left(\frac{\partial A}{\partial \mathsf{d}_{I;r}}\right)^{(e)} \\ &=\; \int_{-1}^{1}\int_{-1}^{1} \frac{\partial |\check{\mathbf{n}}|}{\partial \mathsf{d}_{I;r}}\,\mathrm{d}\xi_1\,\mathrm{d}\xi_2 \;=\; \int_{-1}^{1}\int_{-1}^{1} \frac{1}{|\check{\mathbf{n}}|}\left(\check{n}_s\,\frac{\partial \check{n}_s}{\partial \mathsf{d}_{I;r}} \;+\; \check{n}_t\,\frac{\partial \check{n}_t}{\partial \mathsf{d}_{I;r}}\right)\mathrm{d}\xi_1\,\mathrm{d}\xi_2\,,\end{aligned} \tag{6.28}$$

where the direction $r, s, t \in 1, 2, 3$ are mutually distinct, i.e. $r \neq s$, $s \neq t$, $t \neq r$. For the sake of lucidity the indices are omitted. The derivation of the current normal vector with respect to the displacements included in (6.28) results in

$$\frac{\partial \check{n}_s}{\partial \mathsf{d}_{I;r}} \;=\; \mathcal{E}_{rst}\,\frac{\partial}{\partial \mathsf{d}_{I;r}}\left(\frac{\partial x_r}{\partial \xi_1}\,\frac{\partial x_t}{\partial \xi_2} \;-\; \frac{\partial x_r}{\partial \xi_2}\,\frac{\partial x_t}{\partial \xi_1}\right) \tag{6.29}$$

with the so-called "Levi-Civita" permutation symbol

$$\mathcal{E}_{rst} \;=\; \begin{cases} +1 & \text{if } \{r,s,t\} \;=\; \{1,2,3\},\{3,1,2\},\{2,3,1\} \text{ (even permutation)} \\ \;0 & \text{if } r \;=\; s \quad \text{or } s \;=\; t \quad \text{or } t \;=\; r \\ -1 & \text{if } \{r,s,t\} \;=\; \{3,2,1\},\{2,1,3\},\{1,3,2\} \text{ (odd permutation)} \end{cases}. \tag{6.30}$$

In contrast to section 2.1.2, the distinction between co- and contravariant components is omitted here since a Cartesian coordinate system is assumed. Moreover, the derivation $\frac{\partial x_r}{\partial \xi_l}$ with $l \in 1, 2$ is introduced as

$$\frac{\partial x_r}{\partial \xi_l} \;=\; \sum_{J=1}^{\mathsf{nnod}} \left[\frac{\partial N_J}{\partial \xi_l}\,\mathsf{x}_{J;r}\right] \;=\; \sum_{J=1}^{\mathsf{nnod}} \left[\frac{\partial N_J}{\partial \xi_l}\,(\mathsf{X}_{J;r} \;+\; \mathsf{d}_{J;r})\right], \tag{6.31}$$

so that the differentiation of $\check{n}_s$ (6.29) follows as

$$\begin{aligned}\frac{\partial \check{n}_s}{\partial \mathsf{d}_{I;r}} \;&=\; \mathcal{E}_{rst}\left\{\frac{\partial N_I}{\partial \xi_1}\sum_{J=1}^{\mathsf{nnod}}\left[\frac{\partial N_J}{\partial \xi_2}\,(\mathsf{X}_{J;t} \;+\; \mathsf{d}_{J;t})\right] \;-\; \frac{\partial N_I}{\partial \xi_2}\sum_{J=1}^{\mathsf{nnod}}\left[\frac{\partial N_J}{\partial \xi_1}\,(\mathsf{X}_{J;t} \;+\; \mathsf{d}_{J;t})\right]\right\} \\ &=\; \mathcal{E}_{rst}\left\{\frac{\partial N_I}{\partial \xi_1}\sum_{J=1}^{\mathsf{nnod}}\left[\frac{\partial N_J}{\partial \xi_2}\,\mathsf{x}_{J;t}\right] \;-\; \frac{\partial N_I}{\partial \xi_2}\sum_{J=1}^{\mathsf{nnod}}\left[\frac{\partial N_J}{\partial \xi_1}\,\mathsf{x}_{J;t}\right]\right\}.\end{aligned} \tag{6.32}$$

The differentiation of $\check{n}_t$ with respect to $\mathsf{d}_{I;r}$ follows equivalently. Consequently, the linearisation yields

$$(\mathbf{K}_{\mathsf{TS};I;(J;r)})_{n+1}^{(e);i} = \left[-\theta \int_{-1}^{1} \int_{-1}^{1} \mathbf{N}_{\mathsf{T}}^{\mathsf{T}} \, h \, (\mathbf{N}_{\mathsf{T}} \, \mathbf{T} \, - \, T_{\infty}) \, \frac{1}{|\check{\mathbf{n}}|} \left(\check{n}_s \, \frac{\partial \check{n}_s}{\partial \mathsf{d}_{I;r}} \, + \, \check{n}_t \, \frac{\partial \check{n}_t}{\partial \mathsf{d}_{I;r}} \right) \mathrm{d}\xi_1 \, \mathrm{d}\xi_2 \right]_{n+1}^{(e);i} \tag{6.33}$$

and assembly of all elementwise matrices (6.33) completes the global matrix $\mathbf{K}_{\mathsf{TS}}$.

In practice, the structural index pairs $(J;r)$ utilised above are substituted by global numbers of DOFs. For instance, for a three-dimensional problem with $\mathsf{ndim} = 3$, the global ID z follows from $(J;r)$ via

$$(J;r) \rightarrow z \; = \; \mathsf{ndim} \cdot J \; + \; r \, . \tag{6.34}$$

Finally, with regard to the three-dimensional numerical example of a rotationally symmetric subscale thrust chamber, which will be presented in section 7.2, so-called inclined structural Dirichlet boundary conditions need to be introduced into the monolithic TSI system. Inclined structural Dirichlet boundary conditions are enabled in the monolithic algorithm by introducing a transformation matrix $\mathbf{T}$ into the linear system (6.16) as follows

$$\underbrace{\begin{bmatrix} \mathbf{T}\,\mathbf{K}_{\mathsf{SS}} & \mathbf{T}\,\mathbf{K}_{\mathsf{ST}} \\ \mathbf{K}_{\mathsf{TS}} & \mathbf{K}_{\mathsf{TT}} \end{bmatrix}_{n+1}^{i}}_{\mathbf{K}_{n+1}^{\mathsf{TSI};i}} \underbrace{\begin{bmatrix} \Delta\mathbf{d} \\ \Delta\mathbf{T} \end{bmatrix}_{n+1}^{i+1}}_{\mathbf{x}_{n+1}^{i+1}} = \underbrace{- \begin{bmatrix} \mathbf{T}\,\mathbf{r}_{\mathsf{S}} \\ \mathbf{r}_{\mathsf{T}} \end{bmatrix}_{n+1}^{i}}_{-\mathbf{r}_{n+1}^{\mathsf{TSI};i}} , \tag{6.35}$$

where the transformation matrix $\mathbf{T}$ is applied to each block of the structural equation.

In general, if a DOF is defined to have a Dirichlet boundary condition, the row which corresponds to this DOF in the system of equations is treated as follows: the tangent matrix $\mathbf{K}$ has a single one at the diagonal while all remaining entries are blanked. Furthermore, the Dirichlet value is set on the right-hand side of this DOF. Since the DOFs of the structural field are split into DOFs in x-, y-, and z-direction, respectively, inclined Dirichlet boundary conditions are realised by transformations, i.e. all DOFs of this node are rotated from a global xyz-coordinate system into a local coordinate system such that finally the directions corresponds to the inclined plane, described by two in plane directions, i.e. tangential- and normal-direction, t and n, respectively, as well as by a third out-of-plane direction $\check{z}$. Subsequently, a structural Dirichlet boundary condition can be defined which constraints for instance the movements of a certain node in normal direction of the inclined plane.

Since structural Dirichlet boundary conditions influence only the structural equation, the application of the transformation matrix $\mathbf{T}$ is reduced to the structural blocks, i.e. to $\mathbf{K}_{\mathsf{SS}}$ and $\mathbf{K}_{\mathsf{ST}}$. Hereby, for a DOF which has a structural Dirichlet boundary condition, the mentioned single one is set at the diagonal entry of $\mathbf{K}_{\mathsf{SS}}$, whereas the corresponding row of the block $\mathbf{K}_{\mathsf{ST}}$ is blanked. Furthermore, the thermal blocks of the tangent matrix are not influenced by a structural boundary condition, so that no special treatment is required for $\mathbf{K}_{\mathsf{TT}}$ or $\mathbf{K}_{\mathsf{TS}}$.

The transformation matrix $\mathbf{T}$ is a sparse matrix, which has zeros at the off-diagonal terms and an one at the diagonal entries, i.e. multiplication with $\mathbf{T}$ does not change the structural blocks. In contrast, at a certain node which has inclined Dirichlet boundary conditions, $\mathbf{T}$ has a 3×3 nonzero block, i.e. all x-, y-, and z-DOFs of this nodes are transformed such that finally in the local rotated system the inclined DOF is correctly described.

For the numerical example in section 7.2, the presented inclined structural Dirichlet boundary conditions will be used within the monolithic TSI algorithm to realise symmetry boundary conditions due to reduction of the symmetrical cylindrical thrust chamber to a computational model which comprises only $1/80^{\mathrm{th}}$ of the whole rotationally symmetric body.

7 Examples

In this chapter, the proposed computational method is tested for several different numerical examples, demonstrating that it is robust and provides accurate results. Since the present work aims at improving the understanding of the functionality of rocket nozzles in all working stages, the thermo-structure interaction (TSI) model has to be well verified and validated to enable reliable computational results. Hence, a series of validation examples is performed, in which each numerical example focuses on a different aspect of both the mathematical modelling and the computational approach. The variety of the considered examples illustrates that a broad spectrum of capabilities is realised. Some of the following examples have been published in Danowski et al. [29], whereas additional examples can be found in this work.

The remainder of this chapter is organized as follows. In section 7.1, the first examples will be considered for validating the different (temperature-dependent) elastoplastic material models for small and finite strain, respectively, possibly including ductile damage. For instance in section 7.1.1, the plastic materials will be tested in a very simple one element cyclic loading test which will aim at verifying the different effects of perfect plasticity and isotropic or kinematic hardening. Moreover, in section 7.1.2, the Robinson's viscoplastic material will be validated with results obtained in Arya and Kaufmann [11] by simulating a thick-walled cylinder subjected to an internal pressure under isothermal conditions. Then, in section 7.1.3, a cylindrical notched specimen will be computed to validate the linear elastoplastic material including ductile damage. Obtained results will be compared with the results of de Souza Neto et al. [33]. Subsequently, in section 7.1.4, the finite strain thermo-hyperelasto-plastic material model on the basis of the theory developed in section 5.3.2.3 will be validated for the simulation of thermally induced necking. The computed results will then be compared to the ones of Simo and Miehe [122]. After focusing on the validation of the different material models, the coupled TSI approach will be investigated in section 7.1.5. For the so-called second Danilovskaya problem, the partitioned and monolithic approaches are validated using a linear thermoelastic material. Furthermore, these two TSI algorithms will be compared with each other and the results will be discussed. In this context, the influence of different material parameters will be investigated for partitioned and monolithic solution algorithms, and the limits of partitioned TSI will be demonstrated. Finally, a fully three-dimensional simulation of a subscale rocket nozzle will be presented in section 7.2, which will demonstrate that high performance, fully parallel computing can also be realised. Furthermore, this example shall provide the reader with an overview of the huge variety of simulations which can be realised with the present TSI approach.

In this chapter, all numerical values are given in terms of the basic units millimetre, millisecond, kilogram and kelvin if the contrary is not explicitly indicated. Details on the material parameters and their units are summarized in Appendix A. The numerical simulations are performed by using our in-house parallel multiphysics research code BACI, see Wall and Gee [142]. Within the block Gauss-Seidel (BGS) preconditioner of the monolithic TSI algorithm, the default value of the potential parameter ω_{BGS} is chosen to be equal to one, which results in a conserva-

tive rating of the proposed approach. In case of other values, the respective value is stated in the corresponding section.

7.1 Validation examples

7.1.1 One element under cyclic loading

Within this first rather simple example, the different hardening effects and their correct representation by the numerical implementation will be demonstrated for all proposed (thermo-)elastoplastic materials presented in sections 3.4.2 and 5.3.2. Based on section 3.4.2, the small strain elastoplastic material model and the Lemaitre material will be distinguished by "PlLin" and "Damage". Moreover, the small strain thermo-elasto-plastic model, see 5.3.2.1, and the finite strain thermo-elasto-plastic model, introduced in section 5.3.2.3 and originally proposed by Simo and Miehe [122], will be denoted by "TPlLin" and "SIMO", respectively.

A cube of unit size, i.e. $x \times y \times z = 1\,\mathrm{m} \times 1\,\mathrm{m} \times 1\,\mathrm{m}$ is simulated under cyclic, displacement-controlled load $\hat{u}(\check{t})$, leading to tension and compression loading according to Figure 7.1. Hence, the initially stress-free body, is first elongated, then compressed, elongated, and finally compressed, so that at the end the prescribed elongation is reduced to zero, i.e. $\hat{u} = 0$. To avoid volumetric locking effects during plastic deformations, the lateral displacement is left unconstrained. Thus, structural Dirichlet boundary conditions are applied at the cube such that one single corner node is fixed in all three directions and the remaining edges around this node are fixed according to symmetry conditions.

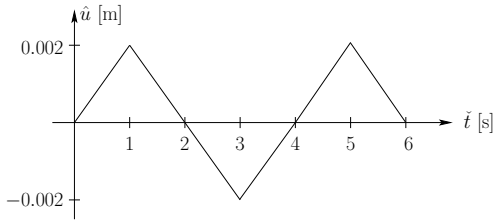

Figure 7.1: One element under cyclic loading: displacement-controlled load cycle under pseudo-time $\check{t}$.

The material parameters are chosen to a Young's modulus $E = 100\ \mathrm{Pa}$, a Poisson's ratio $\nu = 0.29$, an initial yield stress $\sigma_{\mathrm{y};0} = 0.1\ \mathrm{Pa}$, and varying linear hardening moduli H^{iso} and H^{kin}. To enable the correct deformation behaviour of pure elastoplasticity for all considered (thermo-)elastoplastic material models, the additional physical effects of the individual material models are neglected by choosing the corresponding material parameters to be equal to zero. This implies for the Lemaitre material model that the damage exponent and denominator, S and r, respectively, are set to zero. Furthermore, to omit damage, the damage threshold (3.156) is chosen to an extreme value of $\bar{\varepsilon}^p_D = 1.0 \cdot 10^4$. Thus, damage starts to occur only at an extreme plastic deformation state characterized by current accumulated plastic strains $\bar{\varepsilon}^p_{n+1}$ which are equal to or exceed the damage threshold $\bar{\varepsilon}^p_D$, i.e. $\bar{\varepsilon}^p_{n+1} \geq \bar{\varepsilon}^p_D = 1.0 \cdot 10^4$. For the thermoplastic material models, the coefficient of thermal expansion and the initial temperature are assumed to $\alpha_{\mathsf{T}} = 0$ and $T_0 = 0$, respectively. Beyond, the SIMO material includes the additional parameters

δ, ω_{h}, and ω_0, which corresponds to the hardening exponent and the two softening parameters, respectively. They are each chosen to be equal to zero. Finally, the saturation hardening stress $\sigma_{\mathsf{y};\infty}$ is set to $\sigma_{\mathsf{y};\infty} = \sigma_{\mathsf{y};0}$.

Spatial discretisation is realised by a single (tri-)linearly interpolated hexahedral element (i.e. one Hex8 element). Due to the bearing, which allows free movements in lateral directions, the appearance of volumetric locking is circumvented. However, in case of finite strain plasticity, i.e. the SIMO material, one Hex8 element with the F-bar method is used. The results of this simulation can be used to confirm the absence of volumetric locking for the given example. For time integration a quasi-static scheme is chosen, thus the pseudo-time $\check{t}$ is utilised. The strains remain small in the present example, hence the differentiation between the different stress and strain measures can be omitted. Consequently, in Figure 7.2 only the terms "stress" and "strain" are used. Since locking is expected not to cause problems and since stress and strain remain small, identical results are likely to occur for all proposed materials.

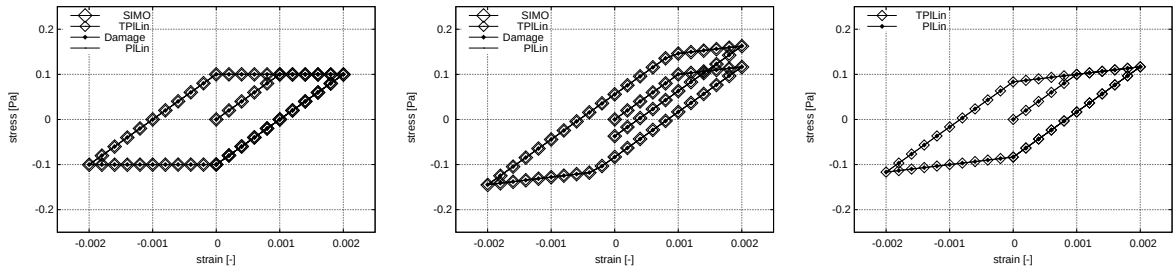

Figure 7.2: One element under cyclic loading: stress-strain curve for different hardening types: perfect plasticity (left), isotropic hardening $H^{\mathsf{iso}} = 20$ Pa (middle), and kinematic hardening $H^{\mathsf{kin}} = 20$ Pa (right).

Figure 7.2 depicts the results for the cases perfect plasticity (left) (i.e. $H^{\mathsf{iso}} = H^{\mathsf{kin}} = 0$), pure isotropic hardening (middle) (i.e. $H^{\mathsf{iso}} = 20$ Pa and $H^{\mathsf{kin}} = 0$), and pure kinematic hardening (right) (i.e. $H^{\mathsf{kin}} = 20$ Pa and $H^{\mathsf{iso}} = 0$), respectively. As introduced at the beginning of this example, these abbreviations of the material models are utilised in Figure 7.2. Up to now, kinematic hardening is integrated in the small strain (thermo-)elasto-plastic material models "TPlLin" and "PlLin". Consequently, results for pure kinematic hardening are provided only for these two materials, see Figure 7.2 (right).

Hooke's law is perfectly recovered, so that the slope of the stress-strain curve in the elastic regime is identified as the Young's modulus E. For the case of perfect plasticity, i.e. no hardening takes place, the uniaxial stress σ is strictly limited by the yield stress $\sigma_{\mathsf{y};0}$. Thus, the computed results are in perfect agreement to the theoretical derivations in section 3.4.2.1. Pure isotropic hardening, which implies $H^{\mathsf{iso}} = 20$ Pa and $H^{\mathsf{kin}} = 0$, results in a homogeneous extension of the elastic domain, i.e. $\sigma > \sigma_{\mathsf{y};0}$, around the stress-free state $\sigma = 0$. For the case of kinematic hardening, the centre of the elastic region is translated in the direction of the plastic flow, that is the resistance to plastic yielding is reduced for compression which takes place after pulling the body so that plasticity starts earlier i.e. for absolute stress values $|\sigma| < |\sigma_{\mathsf{y};0}|$. In Figure 7.3, the hardening effects are further illustrated by showing the stress distribution versus pseudo time $\check{t}$ for pure isotropic (left) and pure kinematic hardening (right). Consequently, the presented results reproduce the analytical solution for small strain plasticity. The results indicate that in

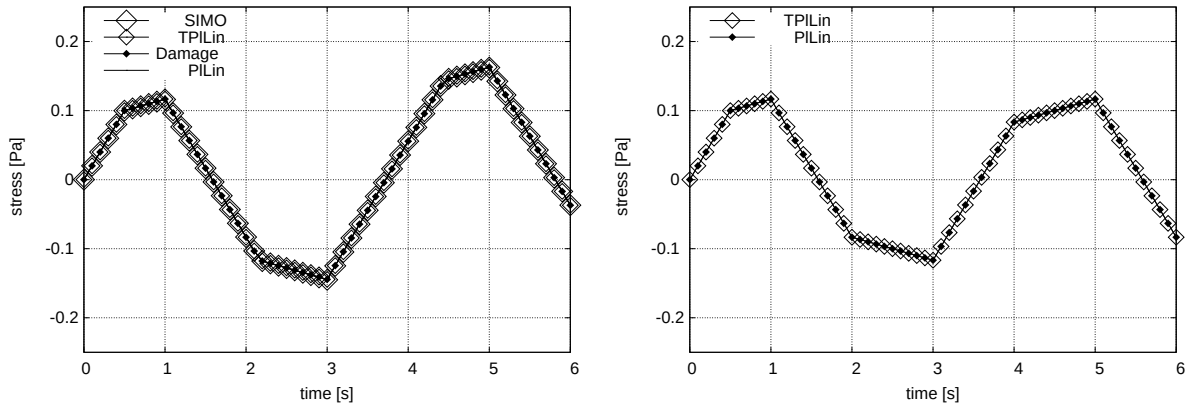

Figure 7.3: One element under cyclic loading: evolution of stress σ over pseudo time $\check{t}$ for pure isotropic (left) and pure kinematic hardening (right) using the proposed materials.

the elastic regime the slope is identified with the Young's modulus E (3.61). In the case of isotropic hardening, the slope corresponds to the elastoplastic tangent $E^{ep;\mathsf{iso}}$ (3.78), and finally, e.g. according to Sedlácek [115], for pure kinematic hardening, the slope can be identified with the elastoplastic tangent $E^{ep;\mathsf{kin}}$ given as

$$E^{ep;\mathsf{kin}} = \frac{\sigma_{\mathsf{max}} - \sigma_{\mathsf{y};0}}{\varepsilon - \frac{\sigma_{\mathsf{max}}}{E}}, \tag{7.1}$$

where σ_{max} denotes the maximal stress value and ε describes the total strain.

7.1.2 Internal pressurised thick-walled cylinder

In order to verify Robinson's viscoplastic material introduced in section 5.3.2.2, an internal pressurised cylinder is considered as proposed in Arya and Kaufmann [11]. As shown in Figure 7.4,

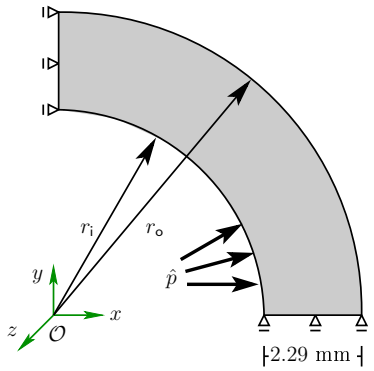

Figure 7.4: Internal pressurised cylinder: initial geometry and prescribed pressure boundary condition.

the thick-walled cylinder is subjected to an internal pressure $\hat{p} = 25.17\ \mathrm{MPa}$ under isothermal conditions, i.e. the temperature is held constant at $T = 699.8\ \mathrm{K}$. Due to symmetry, the cylinder is reduced to a quarter of a circular ring with corresponding symmetry boundary conditions as

depicted in Figure 7.4. The inner and outer radius are $r_i = 4.06$ mm and $r_o = 6.35$ mm, respectively. The cylinder is composed of a 2 1/4 Cr–1 Mo steel alloy. According to Arya and Kaufmann [11] and Bornemann and Wall [18], the material parameters for the present example are provided in Table 7.1. Herein, values for Young's modulus E, Poisson's ratio ν and coefficient of thermal

$E = 139.5$ GPa	$\nu = 0.296$	$\rho = 7,850\ \frac{\text{kg}}{\text{m}^3}$	$\alpha_\text{T} = 0.0$
$G_0 = 0.14$	$A = 2.468 \cdot 10^{-13}\ \frac{1}{\text{s}}$	$m = 7.73$	$a = 4$
$H = 68.2$ GPa	$R_0 = 6.37 \cdot 10^{-8}\ \frac{\text{N}}{\text{m}^2\,\text{s}}$	$Q_0 = 0.0$	$\Theta_0 = 1.0$ K
$\beta = 1.5$	$K_0^2 = 31.96$ MPa^2		$K^2 = 31.96$ MPa^2

Table 7.1: Internal pressurised cylinder: material parameters.

expansion α_T are summarized. In addition, the density ρ and the specific material parameters of the Robinson's material are outlined. For the present numerical example, the specific Robinson's parameters are all assumed to be temperature-independent.

The computational model is discretised with $45 \times 15 \times 1$ Hex8 elements in circumferential, radial and z-direction, respectively. For time discretisation an one-step-θ scheme is chosen with $\theta = 0.5$ resulting in a Crank-Nicolson scheme. The simulation time is $\check{t} = 1,985$ s with a time step $\Delta t = 0.1$ s. To enable a smooth application of the internal pressure load $\hat{p}$, the pressure $\hat{p}(\check{t})$ is increased linearly within the first five seconds. Thus, at $\check{t} = 5$ s, the complete value $\hat{p}(\check{t} = 5\ \text{s}) = 25.17$ MPa is applied to the cylinder, which in turn defines the initial value of the evaluation time t. After $\check{t} = 5$ s which is identical to $t = 0$, the pressure is held constant at $\hat{p} = 25.17$ MPa. For comparison of the present results with the results in the literature the evaluation time t is used.

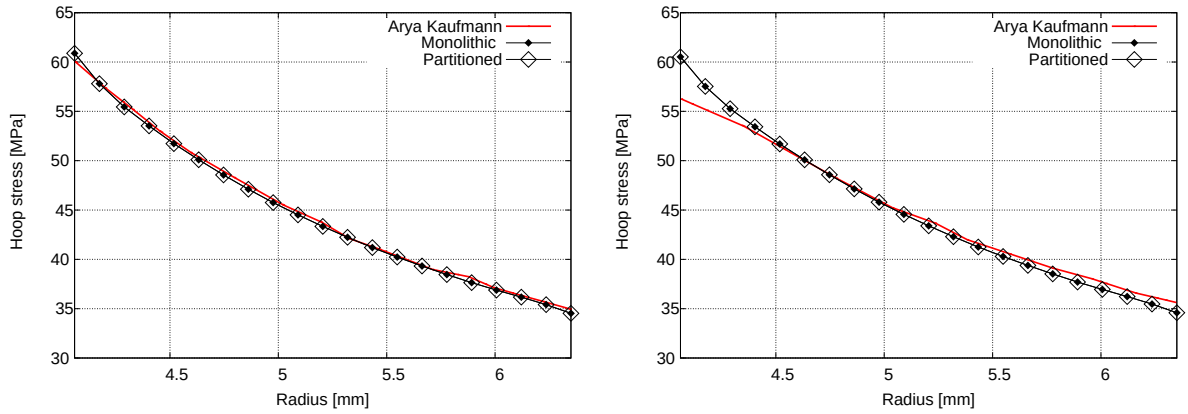

Figure 7.5: Internal pressurised cylinder: stress distribution over radius using Robinson's material model at time $t = 0$ s (left) and $t = 2.5$ s (right).

The example is simulated with the strongly coupled partitioned and the monolithic TSI algorithms. As expected, identical results are obtained for both solution algorithms as shown in Figure 7.5 and 7.6, where the naming "Monolithic" and "Partitioned" corresponds to the monolithic and the partitioned solution scheme, respectively. These Figures show the circumferential

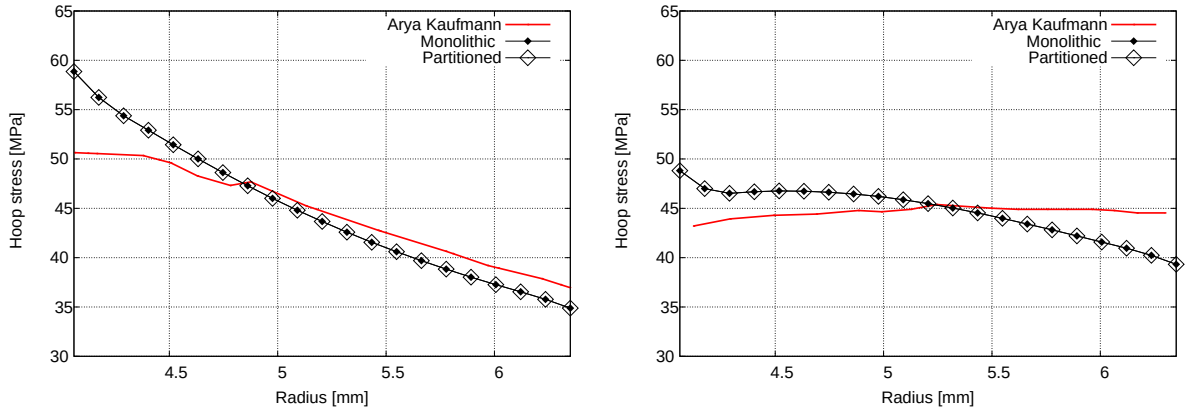

Figure 7.6: Internal pressurised cylinder: stress distribution over radius using Robinson's viscoplastic material model at time $t = 21.6$ s (left) and $t = 1,980$ s (right).

(hoop) stress distribution over the radius of the cylinder at different times as well as the results of Arya and Kaufmann [11] denoted by "Arya Kaufmann". Good agreement of the present results with the results in literature is achieved. Since the pressure is held constant at 25.17 MPa, the stresses decrease with time, i.e. the body relaxes and approaches a steady state. In Figure 7.5, the results are all in excellent agreement. A larger discrepancy is recognizable in the results shown in Figure 7.6. While the general development is still reproduced, namely that the hoop stresses decrease at the inner surface and increase at the outer surface with time, the resulting stresses are too high compared to the results of Arya and Kaufmann [11]. In contrast, the kink which is depicted in the left curve of "Arya Kaufmann" in Figure 7.6 seems to occur in the present results later in the simulation, as depicted in the right picture. The discrepancy can further be explained by the different evolution term h in the present approach $(5.54)_1$ compared to the one in Arya and Kaufmann [11]. However, the present h is in accordance to the one in Bornemann and Wall [18].

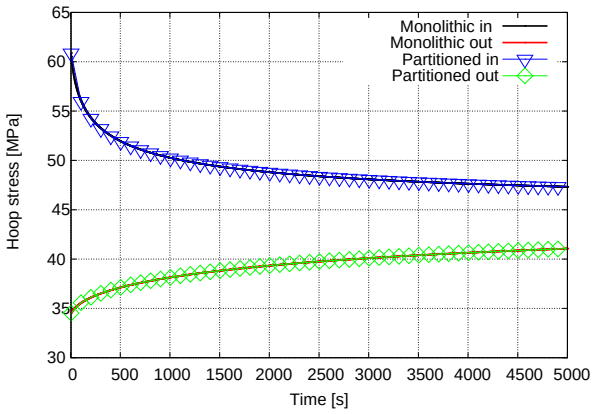

Figure 7.7: Internal pressurised cylinder: hoop stress distribution over time using Robinson's viscoplastic material model for one point at the inner side and another at the outer side of the cylinder using partitioned and monolithic schemes.

Apart from comparison with Arya and Kaufmann [11], a simulation was performed with long run times, i.e. $\check{t}_{\mathsf{max}} = 13,500$ s. Figure 7.7 depicts the hoop stress evolution over time for the first $5,000$ s, for which partitioned and monolithic TSI are utilised for two positions namely one at the outer and one at the inner side of the cylinder described by "out" and "in", respectively. In this Figure 7.7, the approximation of the body to a steady state is noticeable. It is emphasized that Figure 7.7 shows the results only for the first $5,000$ s, because at this time the partitioned algorithm diverges. In contrast, the monolithic algorithm reaches the maximal time $\check{t}_{\mathsf{max}} = 13,500$ s. The evolution of the hoop stress over time $\check{t}$ is exemplarily depicted in Figure 7.8 for the outer side. It is obvious, that after $\check{t}_{\mathsf{max}}$ the steady state is still not achieved. However, since the target of

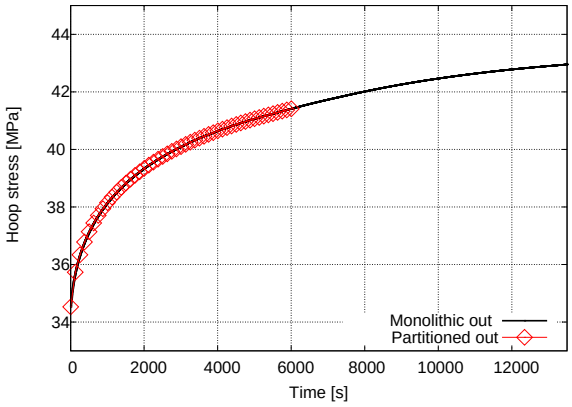

Figure 7.8: Internal pressurised cylinder: hoop stress distribution over long time up to $\check{t}_{\mathsf{max}} = 13,500$ s using Robinson's viscoplastic material model at a point on the outer surface.

this numerical example is on the validation of the physical behaviour of the present Robinson's viscoplastic material model which has been successfully conducted, a longer run is out of scope of the present thesis, and consequently is not further pursued.

7.1.3 Fracturing of a cylindrical notched specimen

The present numerical example is used to validate Lemaitre's material model of coupled plasticity and ductile damage introduced in section 3.4.2.4, which is also presented in Andrade Pires et al. [3] and de Souza Neto et al. [33]. A cylindrical pre-notched bar is subjected to monotonic axial stretching until the body fails. As a result of the monotonic axial stretching, isotropic hardening fully captures the deformation behaviour, i.e. the influence of kinematic hardening vanishes.

The bar is said to be failed as soon as the integrity ω_{D} at any Gauss point gp reaches an inadmissible value, i.e. $\omega_{\mathsf{D}} < 0$ or equivalently $D > 1$. For post-processing, the damage is visualised as an elementwise quantity, i.e.

$$D^{(e)} = \frac{1}{\mathsf{ngp}} \sum_{\mathsf{gp}}^{\mathsf{ngp}} D \,, \tag{7.2}$$

where D and ngp denote the damage value at Gauss point gp and the total number of Gauss points per element, respectively. Consequently, the damage value $D^{(e)}$ at the end of the simulation is expected to be less than 1.

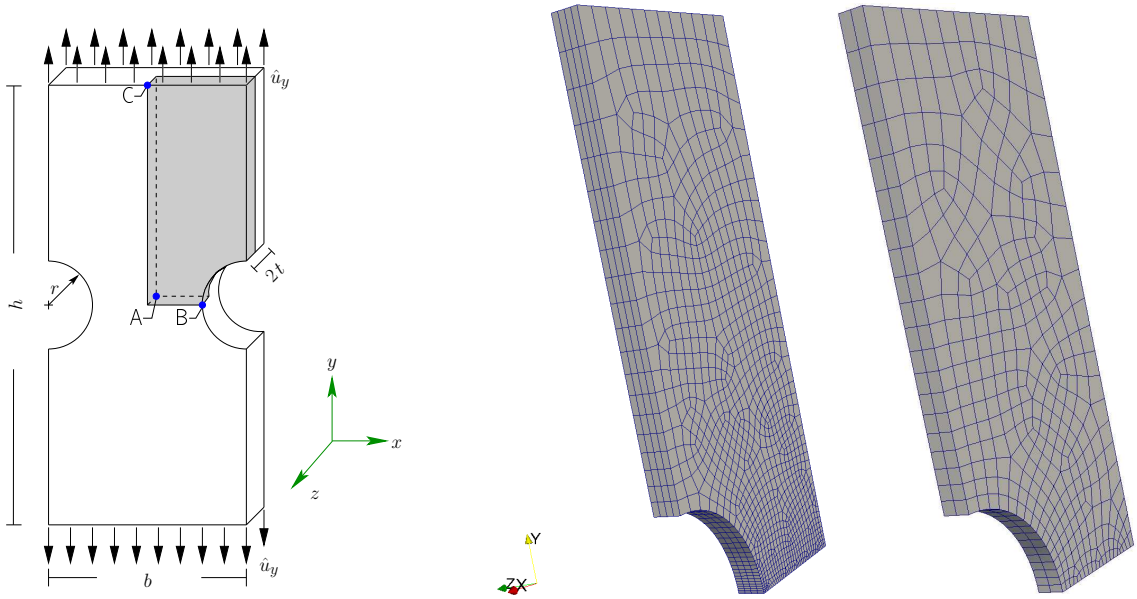

Figure 7.9: Cylindrical notched bar: geometry and boundary conditions (left) and the two used meshes (right).

In Figure 7.9 (left), the geometry and the boundary conditions of the problem are summarized. The body has a height $h = 40$ mm, a width $b = 18$ mm, a radius $r = 4$ mm, and a depth $t = 1$ mm. The loading consists of a prescribed monotonically increasing displacement $\hat{u}_y(t)$ at the top and the bottom surfaces of the body until the body fails. Due to symmetry only one eighth of the body is simulated which is depicted in Figure 7.9 (left) by the grey body. Hence, appropriate symmetry boundary conditions need to be imposed. Moreover, at the top load surface, the displacement in x- and z-direction are unconstrained. The evaluation points are illustrated in Figure 7.9 (left). While point A corresponds to the centre of the body, point B is located at root of the notch, which corresponds to the location where necking is likely to occur. Furthermore, point C is located at the top, where the displacement-controlled load $\hat{u}_y(t)$ is applied. The material parameter for Lemaitre's material are given in Table 7.2. For time integration, a

$E = 210$ GPa	$\nu = 0.3$	$\rho = 7,850\ \frac{\text{kg}}{\text{m}^3}$	$\sigma_{\text{y};0} = 0.62$ GPa
$\sigma_{\text{y};\infty} = 3.3$ GPa	$\delta = 0.4$	$S = 1.0$	$r = 3.5$ MPa

Table 7.2: Cylindrical notched bar: material parameters.

quasi-static analysis is chosen with a quasi-time step t. In Figure 7.9 (right), the two chosen unstructured meshes using (tri-)quadratically interpolated hexahedral elements (Hex27) are shown. For the fine mesh, $3,892$ elements with $36,297$ nodes and for the coarse mesh, 698 elements with $7,415$ nodes are used. To enable a correct resolution of the damage evolution, the mesh is refined in the bottom region surrounding the smallest cross section which in turn corresponds to the region where damage is likely to occur.

The failure of the body is observed in experiments in the centre of the specimen. Thus, the present simulation approach is aimed to reproduce this point of failure as well. Figure 7.10 il-

lustrates the damage distribution at the final deformed configuration. For visualisation purposes, the simulation results are reflected to cover the full length of the actual body. Figure 7.10 (left) shows that the coarse mesh is not able to reproduce the physical damage behaviour. In contrast,

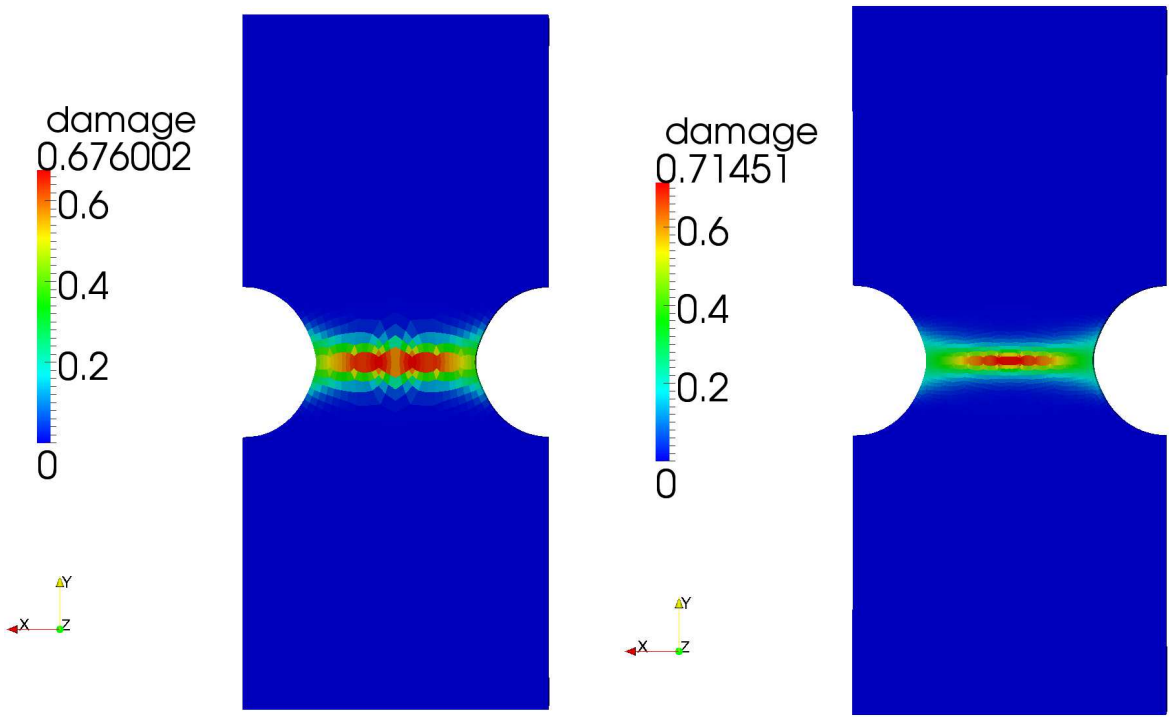

Figure 7.10: Cylindrical notched bar: damage contribution of mid-plane at final deformed configuration utilising the coarse (left) and fine mesh (right).

Figure 7.10 (right) depicts the results using the fine mesh. This simulation is able to capture the physics and the failure state correctly. It is worth repeating, that the damage variable $D^{(e)}$, e.g. in Figure 7.10 represents an elementwise measure, so that the maximal value is less than 1. However, a simulation is stopped due to exceeding an admissible value D at Gauss point level, i.e. $D > 1$.

The coarse mesh can bear more stretching with a maximal elongation $\hat{u}_{y;\mathsf{max}}^{\mathsf{coarse}} = 0.47\,\mathrm{mm}$, before fracturing with a final damage value $D_{\mathsf{max}}^{(e);\mathsf{coarse}} = 0.6760$ and the corresponding Gauss point value of $D_{\mathsf{max}}^{\mathsf{coarse}} = 1.0073$. For the fine mesh, an inadmissible value of $D_{\mathsf{max}}^{\mathsf{fine}} = 1.0040$ at the Gauss point and corresponding elementwise damage value of $D_{\mathsf{max}}^{(e);\mathsf{fine}} = 0.7145$ are reached at the centre of the body at an elongation $\hat{u}_{y;\mathsf{max}}^{\mathsf{fine}} = 0.348\,\mathrm{mm}$. This elongation $\hat{u}_{y;\mathsf{max}}^{\mathsf{fine}} = 0.348\,\mathrm{mm}$ leads to failure of the body and hence to the end of the simulation and is computed earlier compared to the coarse mesh (with $\hat{u}_{y;\mathsf{max}}^{\mathsf{coarse}} = 0.47\,\mathrm{mm}$).

Figure 7.11 depicts on the left side for both meshes the damage evolution $D_{\mathsf{max}}^{(e)}$ of the element at the centre point A over the elongation $\hat{u}_y$. Since the failure point for the coarse mesh is not the centre, a third curve is included in Figure 7.11 (left). The third curve is labelled "698 ele $\mathrm{D}_{\mathsf{max}}^{(e)}$" and presents the results for the failure point applying the coarse mesh, i.e. with 698 elements. At the beginning, all curves are equal to zero. Then damage starts to develop: for the fine mesh at point A at $\hat{u}_y^{\mathsf{fine}} = 0.0597\,\mathrm{mm}$ and for the coarse mesh at $\hat{u}_y^{\mathsf{coarse}} = 0.0053\,\mathrm{mm}$. In the middle

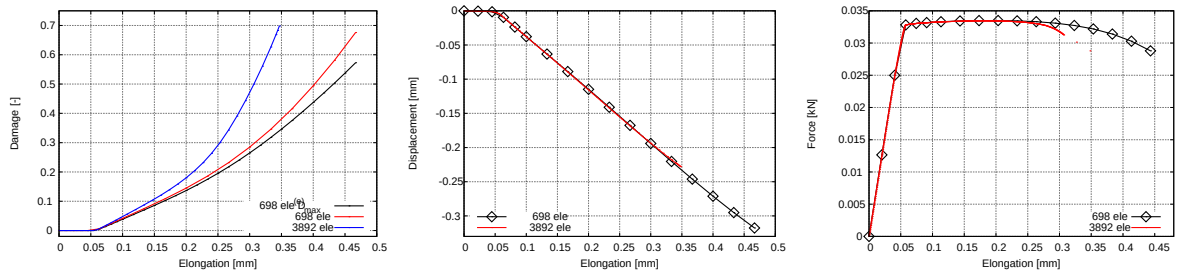

Figure 7.11: Cylindrical notched bar: evolution of the damage variable $D^{(e)}$ at centre point A over elongation $\hat{u}_y$ (left), necking at point B over elongation $\hat{u}_y$ (middle), and reaction force over elongation $\hat{u}_y$ (right).

of Figure 7.11, the necking radius at point B for both meshes over elongation $\hat{u}_y$ are shown. Finally, the rightmost plot of Figure 7.11 depicts the real reaction force of the notched specimen over the elongation. Since the computational model corresponds to a quarter of the real notched specimen, the real reaction force corresponds to four times of the computed reaction force.

Subsequently, Figure 7.12 illustrates the damage evolution at different load states using the fine mesh which is able to represent the physics correctly. While damage first starts to evolve at the bottom root of the notch, damage develops towards the middle of the body and finally leads to the failure of the whole body due to $D_{\mathsf{max}}^{(e);\mathsf{fine}} = 0.7145$ in the centre. Moreover, Figure 7.13 depicts the deformed three-dimensional body at failure state and emphasizes the fracture point at the centre. The colour represents the final damage distribution and the maximal value is reached at the centre and decrease in thickness direction.

In the following, the present results are compared to the results of de Souza Neto et al. [33]. A discrepancy between the results is observed: while the maximal displacement applied to the bar in the present model is $u_{y;\mathsf{max}}^{\mathsf{fine}} = 0.348\ \mathrm{mm}$, in de Souza Neto et al. [33] a larger value $u_{y;\mathsf{max}} = 0.576\ \mathrm{mm}$ is reached. The discrepancies can be justified by the fact that the present approach is fully three-dimensional (see in particular Figure 7.13) in contrast to the study of de Souza Neto et al. [33] who performed a two-dimensional fracturing only. Since damage evolution depends on the total current stress state, see (3.156) and (3.152), the z-components are considered additionally in this work. Hence, higher von Mises equivalent stress values are computed leading to higher plasticity and higher damage in the present approach, which in turn implies that the critical damage value is reached earlier.

Based on Appendix B.3, Figure 7.14 depicts on the left the von Mises stresses σ_{vM} for the evaluation points A-C. Here, the largest decrease of stresses during elongation is observed at the centre point A, whereas the stresses at the other two points remain nearly constant. The plot in the middle shows the von Mises stresses σ_{vM} and the von Mises strains $\varepsilon_{\mathsf{vM}}$, respectively, over elongation at the centre point A. Furthermore, on the right side, the stress-strain curve for the normal stresses σ_{yy} and normal strains ε_{yy} is shown. It can be seen, that in the first $0.05\ \mathrm{mm}$ of elongation in y-direction, the bar deforms elastically, which is identified by the linear stress-strain slope in Figure 7.14 (right). While the elastic strains ε_{yy}^{e} cover only a very small part of the total strain ε_{yy}, the much larger part is composed of plastic strains ε_{yy}^{p}.

Summarizing the previous results, fracture initiation is expected at the centre of the specimen and propagates radially towards the notch (cf. e.g. Figure 7.12 bottom right). This is in agreement

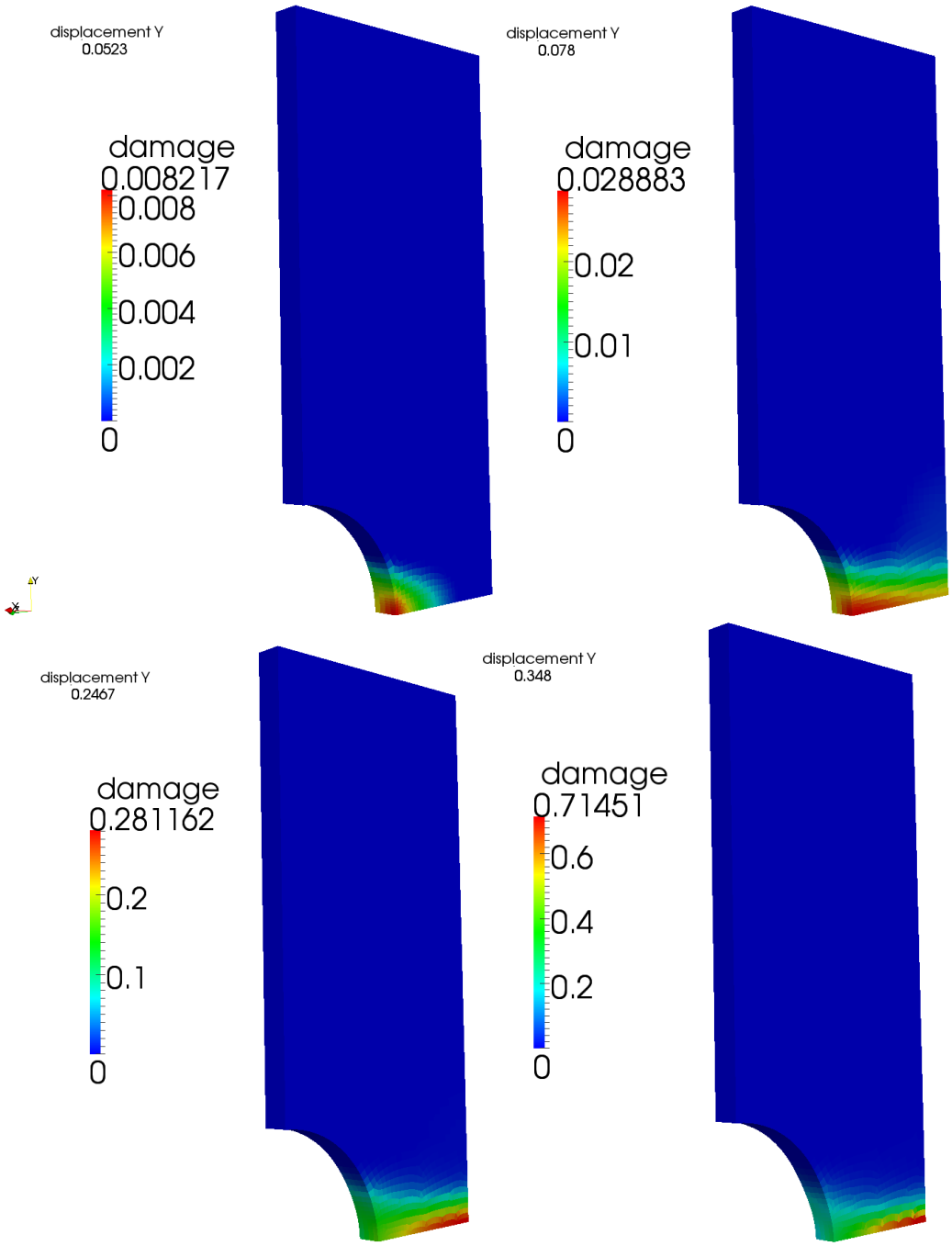

Figure 7.12: Cylindrical notched bar: damage contour plots at different deformation states using the fine mesh with $3,892$ elements.

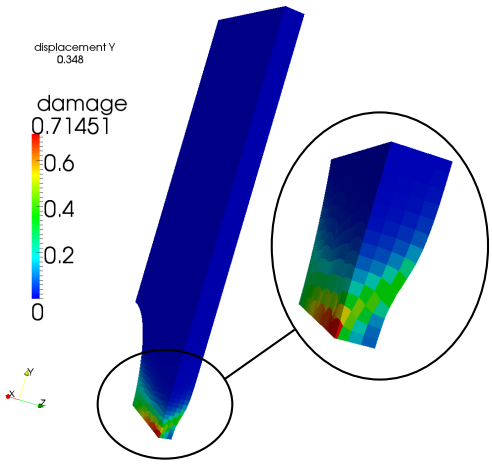

Figure 7.13: Cylindrical notched bar: three-dimensional damage contour plots of the fine mesh with $3,892$ elements at failure state.

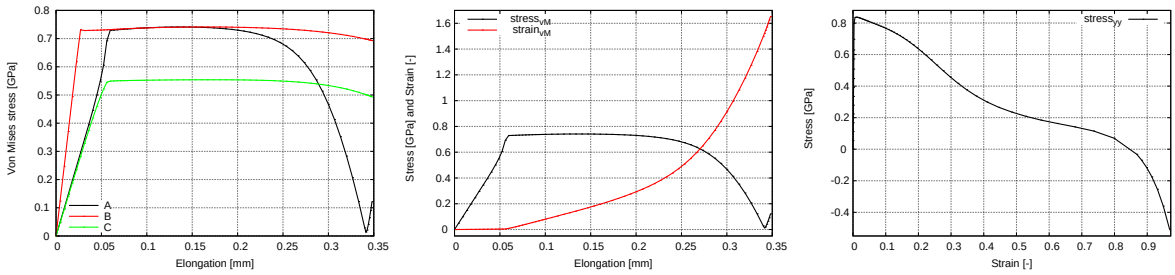

Figure 7.14: Cylindrical notched bar: von Mises stress σ_{vM} versus elongation $\hat{u}_y$ at centre point A, and points B and C (left), von Mises stress σ_{vM} and von Mises strain $\varepsilon_{\mathsf{vM}}$ versus elongation $\hat{u}_y$ at centre point A (middle), and stress-strain curve for normal stress $\boldsymbol{\sigma}_{yy}$ and normal strain $\boldsymbol{\varepsilon}_{yy}$ (right). For all results the fine mesh with $3,892$ elements is applied.

to the literature, as e.g. de Souza Neto et al. [33], where damage growth in ductile metals is described as strongly dependent on the stress triaxiality ratio. The stress triaxiality ratio $\frac{p}{q}$ is defined as the ratio between pressure p and von Mises equivalent stress q. Herein, decreasing ductility of a material leads to increasing values of the stress triaxiality ratio. For the present simulation, the absolute maximal value of the stress triaxiality ratio is computed at the centre of the specimen with $(\frac{p}{q})_{\mathsf{A}} = -3.6560$, which in turn represents the location for fracture initiation. For the sake of completeness, the corresponding values at the root of the notch point B and at the top edge point C are $(\frac{p}{q})_{\mathsf{B}} = -0.20615$ and $(\frac{p}{q})_{\mathsf{C}} = 0.20708$, respectively. Hence, absolute value of the stress triaxiality is maximal at point A which corresponds to the point of fracture initiation.

The importance of including ductile damage into the present example of a notched specimen can further be emphasized by assessing the results presented in Figure 7.14 and, in particular, the von Mises stresses at the three points depicted on the left side. The highest stresses are computed for evaluation point B. If the results are obtained from a simulation of the notched specimen applying a purely elastoplastic material without ductile damage according to section 3.4.2.3, this

point B would represent the point of largest plasticity and not point A. This is in agreement to de Souza Neto et al. [33]. They showed that simulating the notched specimen applying a purely elastoplastic material without ductile damage and defining a critical value of the accumulated plastic strains as the fracture criterion instead, fracture or crack initiation is predicted at the root of the notch B instead of the centre A. Consequently, to predict the correct physical behaviour, the inclusion of damage for instance in form of Lemaitre's material model is essential.

7.1.4 Thermally induced necking of a cylindrical bar

In the following, the finite strain thermo-hyperelasto-plastic material (see section 5.3.2.3) is validated. Therefore, the well-known benchmark example of necking of a cylindrical bar is considered. This example represents the common benchmark in the literature to show robustness and accuracy of a plastic formulation, and the utilised finite element (FE) technology of incompressible materials. Necking is simulated, for instance in Andrade Pires et al. [4], Caminero et al. [21], Montáns and Bathe [95], and Simo and Ju [121] for purely mechanical analyses, and e.g. in Canadija and Brnic [22], Ibrahimbegovic and Chorfi [61], Lehmann and Blix [74], Miehe [90], Simo and Miehe [122], and Wriggers et al. [146] for the extension to thermal effects. The present necking example represents the thermally triggered version and is based on the corresponding example of Simo and Miehe [122]. Hence, the results of the present example are compared to the results of Simo and Miehe [122]. In this context, it is important to note, that differences of the present results are expected due to differences of the material model, but the physical effects must be captured. For more details on the theory, the reader is referred to section 5.3.2.3.

The cylinder is characterized by a radius $r = 6.413$ mm and a length $l = 53.334$ mm. A total elongation of $2\,\hat{u}_z = 16$ mm is simulated by stretching the specimen with a constant velocity $2\,\hat{\hat{u}}_z = 2\ \frac{\text{mm}}{\text{s}}$. Mechanical Dirichlet boundary conditions applied at each end allow free contraction of the body leading to an initially homogeneous stress state in the absence of imperfections. A constant initial temperature T_0 is assumed for the whole body with $T_0 = 293\,\text{K}$. Moreover, thermal heat convection boundary conditions $\hat{Q}_\mathsf{C}$ according to (5.16) with $T_\infty = T_0 = 293$ K and $h = 1.75 \cdot 10^{-8}\ \frac{\text{kg}}{\text{ms}^2\,\text{K}}$ are applied on the entire boundary of the specimen, i.e. on the top surfaces and the circumference. The bar is composed of metal with the material parameters given in Table 7.3. The present thermomechanical necking example is triggered by

$K = 164.206$ GPa	$\mu = 80.1938$ GPa	$\rho = 7800\ \frac{\text{kg}}{\text{m}^3}$
$k_0 = 45\ \frac{\text{W}}{\text{m K}}$	$C_\mathsf{V} = 460\ \frac{\text{J}}{\text{kg K}}$	$\alpha_\mathsf{T} = 1.0 \cdot 10^{-5}\ \frac{1}{\text{K}}$
$H^{\mathsf{iso}} = 0.12924$ GPa	$\sigma_{\mathsf{y};0} = 0.45$ GPa	$\sigma_{\mathsf{y};\infty} = 0.715$ GPa
$\delta = 16.93$	$\omega_0 = 0.002$	$\omega_\mathsf{h} = 0.002$

Table 7.3: Thermally induced necking: material parameters.

a non-homogeneity in the temperature field. Plastic deformations lead to mechanical dissipation so that heat is generated. Due to the applied heat convection boundary conditions $\hat{Q}_\mathsf{C}$ at the

surrounding surfaces, the generated heat is released to the surrounding medium. Hence, thermal diffusion starts, leading to an inhomogeneous temperature field. This inhomogeneity results in non-uniform thermal strains and, since linear thermal softening is considered, the temperature-dependent material parameters change (for instance the yield stress $\sigma_{\mathrm{y};0}$ according to (5.71)). The generated heat breaks the symmetry of the problem and thus triggers the necking of the initially cylindrical bar.

The inclusion of the thermo-elasto-plastic heating $\mathcal{H}^{ep}$ leads to cooling of a body due to expansion. This term is especially important in the elastic regime, while its influence diminishes decisively compared to the increasing influence of the plastic mechanical dissipation. Since elastic behaviour captures only a small part of the whole deformation, the cooling is not noticed in the following Figure 7.16.

To circumvent overshooting of the temperature solution in particular at the top of the specimen, which then would lead to necking at the wrong side, i.e. at the top, the standard meshes used for purely mechanical necking analyses, e.g. in de Souza Neto et al. [33] with high aspect ratio (i.e. large elements at the top and very small elements in the necking zone) are not applicable here. In contrast, a mesh with smaller elements at the top needs to be used as shown in Figure 7.15 and confirmed in Simo and Miehe [122].

In this context it is worth mentioning, that the predictor plays a decisive role in a displacement-controlled simulation. A constant predictor updates the solution vectors only for the degrees of freedom (DOFs) which have Dirichlet boundary conditions, i.e. the new prescribed deformation $\hat{u}_{z;n+1}$ is fully applied to the Dirichlet DOFs only. Thus, the largest stress state is predicted at these Dirichlet DOFs and plasticity is likely to occur at the top. By contrast, the so-called TangDis predictors of the structural field extrapolate the new prescribed deformation $\hat{u}_{z;n+1}$ to the whole domain, so that the stresses are not concentrated only at the top. Consequently, to ensure correct physical prediction of plastic necking in the middle, which is caused by maximal stresses in the middle, the TangDis predictors need to be employed.

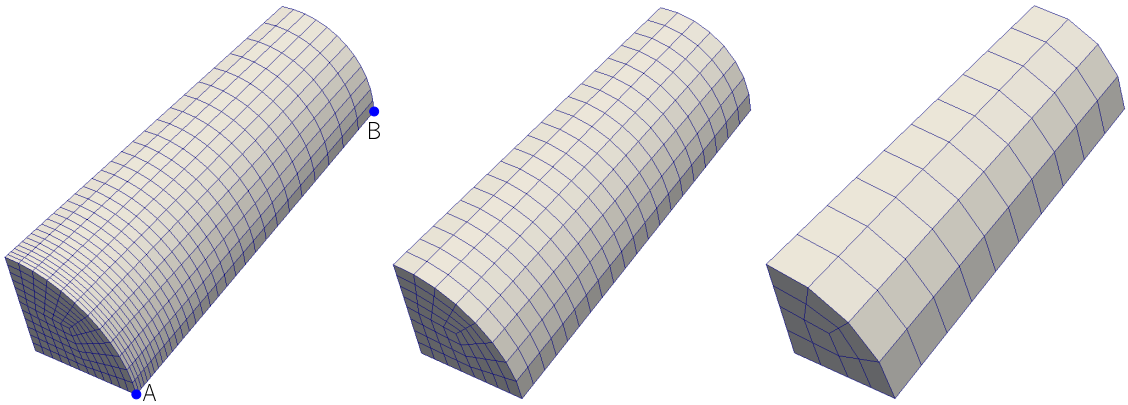

Figure 7.15: Thermally induced necking: applied finite element mesh with $3,240$ elements and evaluation points A and B (left), mesh with 960 elements (middle), and the mesh with 120 elements (right).

Subsequently, due to symmetry of the problem, only one eighth of the cylinder is modelled. Hence, corresponding symmetry boundary conditions are applied. To ensure a constant applied velocity $\hat{\dot{u}}_z = 1\,\frac{\mathrm{mm}}{\mathrm{s}}$, the simulation time is $t = 8\,\mathrm{s}$. The cylinder is discretised in space with F-bar

elements. As depicted in Figure 7.15, three different meshes are chosen, one with 120 elements, one with 960 elements, and the third one with $3,240$ elements. Moreover, in Figure 7.15 (left) the two evaluation points are indicated. While point A is located on boundary at the middle of the bar where necking is likely to occur, point B lies at the top surface where the load is applied. The numerical simulation is performed with the monolithic TSI algorithm and for time discretisation an one-step-θ scheme with $\theta = 0.5$ is chosen for both fields structure and thermo, resulting in a Crank-Nicolson scheme.

Figure 7.16 depicts the computational results for the temperature distribution. The bar is initially heated homogeneously. As soon as the symmetry of the bar is broken, the necking process is triggered at the bottom of the computational model. The circular bar plastifies strongly in the necking area. As mentioned above, mechanical dissipation is connected with the plastic deformations: the higher the plastic deformations the stronger the heating. Hence, the temperature rises the most in the necking zone.

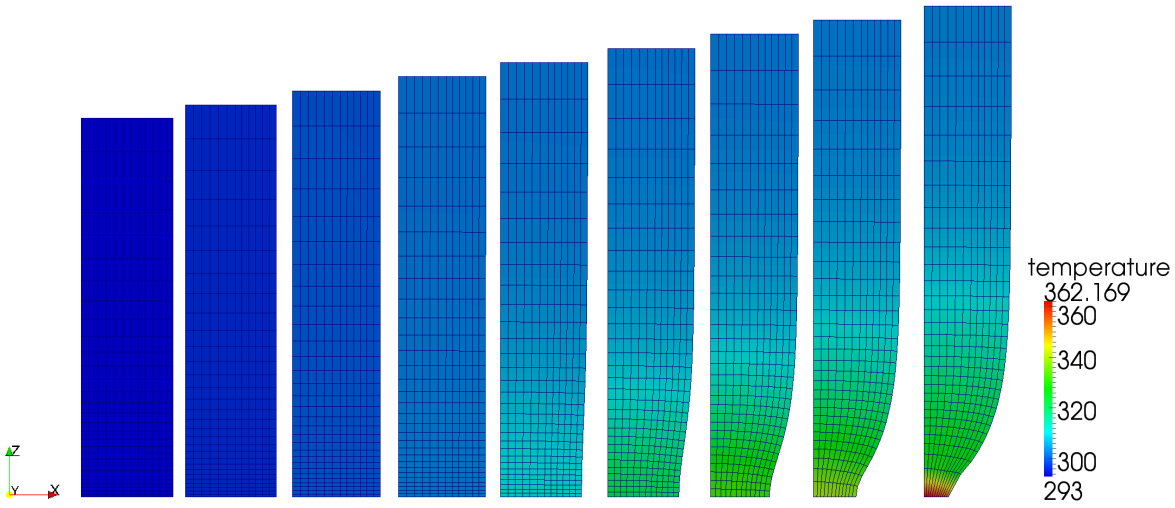

Figure 7.16: Thermally induced necking: temperature distribution of deformed bar over time, starting from $t = 0$ s (left) to $t_{\mathsf{max}} = 8$ s (right) using the mesh of $3,240$ elements.

To validate the present approach, results are compared to results given in Simo and Miehe [122]. In Figure 7.17 and Figure 7.18 (right), a quantitative comparison is realised by presenting a load-displacement diagram and the evolution of the temperature in the necking zone, respectively. Figure 7.17 shows that the reaction force is well approximated by the present model. As expected, the finer the mesh the better the quality of the results and the better the agreement with the results in literature. In contrast, in Figure 7.18 (right) a larger discrepancy is observed in the temperature evolution between the current results and the results of Simo and Miehe [122]. This is caused by the different formulation of the yield function and especially of the mechanical dissipation term $\mathcal{D}_{\mathsf{mech}}$. While Simo and Miehe [122] redefine $\mathcal{D}_{\mathsf{mech}}$ in their numerical example section by introducing a non-physical dissipation factor χ and by using the total yield stress $\sigma_{\mathsf{y}}(\bar{\varepsilon}^p, T)$, i.e.

$$\mathcal{D}_{\mathsf{mech;SIMO}} := \dot{\gamma} \sqrt{\frac{2}{3}} \sigma_{\mathsf{y}}(\bar{\varepsilon}^p, T) \, \chi \,, \tag{7.3}$$

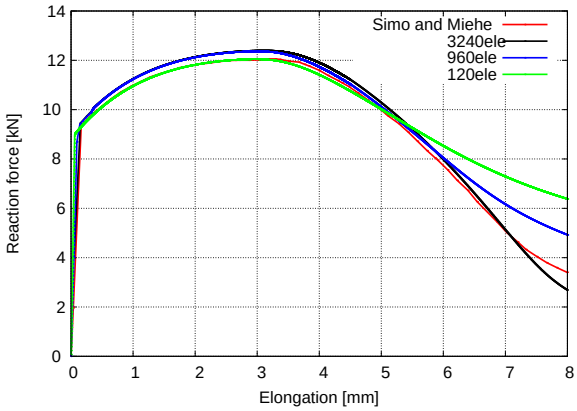

Figure 7.17: Thermally induced necking: reaction force over elongation at point B using the three meshes. Comparison with results from Simo and Miehe [122].

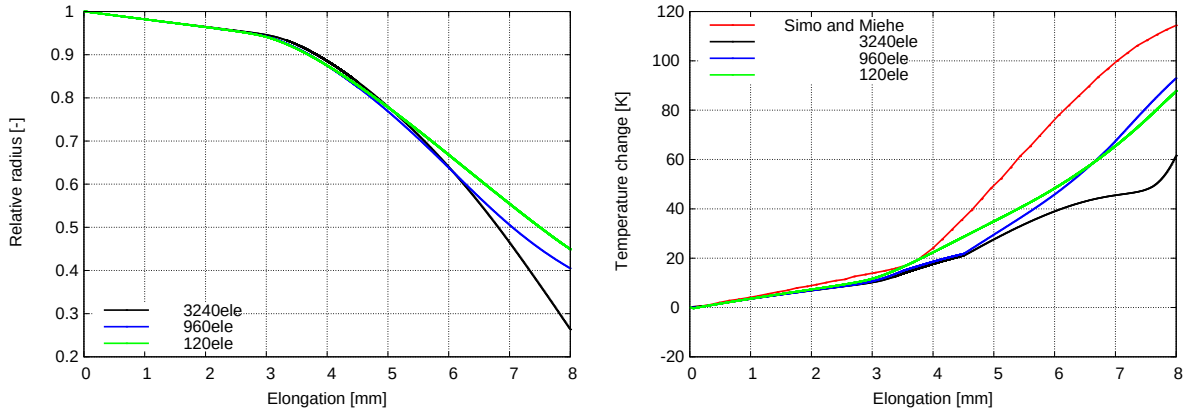

Figure 7.18: Thermally induced necking: evolution of the necking radius r_{neck}/r (left) and temperature change ΔT (right) over elongation at point A. Comparison with results from Simo and Miehe [122].

the present approach utilises the term (5.75) derived within the theory. Consequently, different values are expected for the temperature change. However, the physical behaviour is still captured satisfactorily as well as the mechanical behaviour.

Furthermore, Figure 7.18 (left) depicts the evolution of the radius in the necking zone using a relative quantity, namely the quotient between current necking radius r_{neck} $[\text{mm}]$ and the initial radius r $[\text{mm}]$. Since Simo and Miehe [122] do not provide data about the radius, Figure 7.18 (left) is restricted to the results obtained by the present approach. As expected, the necking increases with increasing numbers of elements.

Finally, it is worth noting that the present results are obtained exclusively using the proposed monolithic TSI algorithm. Unlike the monolithic algorithms, no solution could be found for the partitioned algorithms even if strongly coupled schemes with the Aitken Δ^2 method was utilised. The structural field solver diverged after 50 nonlinear iteration steps although the pseudo-transient continuation (ψTC) strategy has been chosen, which in general enables larger

convergence radius compared to the exact Newton method integrated in the monolithic TSI strategy.

7.1.5 Second Danilovskaya problem

The second Danilovskaya problem as originally proposed in Danilovskaya [28], which has often been used in literature for validation of a fully coupled thermomechanical model (e.g. in Farhat et al. [39], Tamma and Namburu [129], Tanaka et al. [130], and Tosaka and Suh [133]), is considered. The problem is essentially one-dimensional. A linear elastic solid is subjected to a uniform sudden temperature change due to a heat flux $\hat{Q}_{\mathsf{C}} \equiv \hat{q}_{\mathsf{C}}$ on the surface $x = 0$ mm according to (4.15) or (5.16) for small deformations (i.e. a geometrically linear analysis is performed assuming the deformation gradient $\boldsymbol{F} \equiv \boldsymbol{I}$). The geometry in the form of a cuboid of height and width of 4 mm, respectively, and a length of 6 mm is shown in Figure 7.19.

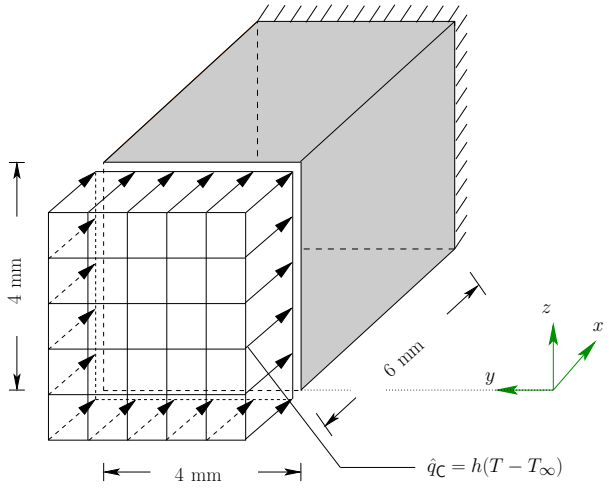

Figure 7.19: Second Danilovskaya problem: initial geometry and prescribed heat convection boundary condition $\hat{q}_{\mathsf{C}}$.

The simulation is carried out in three spatial dimensions, fixing all displacement DOFs in y- and z-direction, such that a quasi-one-dimensional motion is achieved. The body is assumed to be mechanically constrained and thermally insulated. The initial and boundary conditions are given as

$$u_{x;0} = u_x(x, t = 0) = 0 = \dot{u}_{x;0}\,, \quad T_0 = T(x, t = 0)\,, \quad \hat{t}(x = 0, t) = 0\,. \tag{7.4}$$

The mechanical and thermal field properties are given in Table 7.4, where $\bar{h}$ denotes the kinematic heat transfer coefficient, defined as $\bar{h} = \frac{h}{\rho C_{\mathsf{V}}}$ with the linear heat transfer coefficient h. Furthermore, the values for the thermal conductivity k, the coefficient of thermal expansion α_{T} (also known as linear heat expansion coefficient), the constant initial temperature T_0, as well as an ambient temperature T_∞ are given. According to Table 7.4, a Young's modulus E and a Poisson's rate ν are chosen for the structural field.

The discretisation for both structural and thermal field contains each $n_x \times n_y \times n_z = 12 \times 4 \times 4$ Hex8 elements. The simulation time is $t = 4$ s, with a time-step size of $\Delta t = 0.001$ s.

$E = 210\,\mathrm{GPa}$	$\nu = 0.3$	$\alpha_\mathsf{T} = 1.1 \cdot 10^{-5}\,\frac{1}{\mathrm{K}}$	
$k = 1,030\,\frac{\mathrm{mm\,kg}}{\mathrm{s^3\,K}}$	$\bar{h} = 0.1\,\frac{\mathrm{mm}}{\mathrm{s}}$	$T_0 = 273.15\,\mathrm{K}$	$T_\infty = 373.15\,\mathrm{K}$

Table 7.4: Second Danilovskaya problem: material parameters.

Moreover, one-step-θ time integration is chosen with the value $\theta = 0.5$, resulting in a Crank-Nicolson scheme. Heat convection boundary conditions are used at the surface $x = 0$. A linear thermoelastic material is chosen according to (5.30). Hence, for small deformations the linear stress is given by

$$\boldsymbol{\sigma}_{\mathsf{lin}} = \boldsymbol{\sigma}(\boldsymbol{\varepsilon}, T) = 2\,\mu\,\boldsymbol{\varepsilon} + \lambda\,\mathrm{tr}\,\boldsymbol{\varepsilon}\,\boldsymbol{I} + m_0\,\Delta T\,\boldsymbol{I}\,, \tag{7.5}$$

where linearised strains $\boldsymbol{\varepsilon}$ are utilised according to (2.107). Displacements and temperatures are evaluated at the centre point of the plane at $x = 1$ mm.

To enable a comparison with Danilovskaya [28], Farhat et al. [39], or Tanaka et al. [130], the thermomechanical coupling term in the energy balance equation (5.14) is assumed to depend on the initial temperature T_0 instead of the current temperature T for the results presented in Figure 7.20. This simplifies the thermal subproblem, since the linearisation of this term with respect to T can be neglected. Equation (5.14) then reads

$$\rho_0\,C_\mathsf{V}\,\dot{T} + \mathrm{div}\,\boldsymbol{q} - \rho\,r - \underbrace{T_0\,m_0\,\mathrm{tr}\,\dot{\boldsymbol{\varepsilon}}}_{\mathcal{H}^e} = 0\,. \tag{7.6}$$

Hence, the coupling term $\mathcal{H}^e$ is independent of the current temperature solution and can therefore be interpreted as an external load.

The present results are compared to the ones given in Tanaka et al. [130]. Unfortunately, not

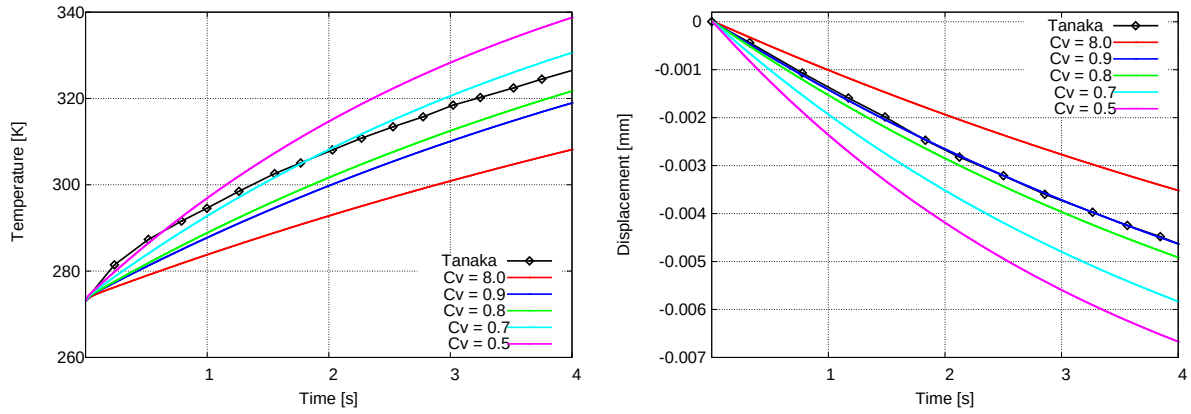

Figure 7.20: Second Danilovskaya problem: temperature (left) and displacement (right) results based on simplifying assumption T_0. Approximation and validation of present TSI algorithm with results from Tanaka et al. [130] can be realised by varying C_V.

all material parameters for the second Danilovskaya problem are specified in the literature, as e.g. Farhat et al. [39], Tamma and Namburu [129], Tanaka et al. [130], or Tosaka and Suh [133]: depending on the dimensionless thermomechanical coupling parameter δ introduced in Armero

and Simo [6], Farhat et al. [39], and Tanaka et al. [130], the density ρ and the heat capacity C_V can be chosen arbitrarily. Figure 7.20 depicts the spread of results for temperatures and displacements in x-direction depending on a variation of the values for C_V. Identical results are obtained for monolithic and partitioned TSI, so that, for the sake of clearness, the TSI algorithm is not specified in Figure 7.20. Choosing a density $\rho = 7,850\,\frac{\mathrm{kg}}{\mathrm{m}^3}$, the heat capacity is computed to be $C_\mathsf{V} = 0.821\,\frac{\mathrm{J}}{\mathrm{kg\,K}}$ (corresponding to the green line which is named $C_\mathsf{V} = 0.8$ in Figure 7.20), resulting in the best approximation of temperatures and displacements to the results of Tanaka et al. [130]. Hence, in the following, these values for density and heat capacity are assumed.

The proposed monolithic TSI algorithm is now compared to the partitioned algorithm. In contrast to the simplifying assumption in Farhat et al. [39], Tamma and Namburu [129], Tanaka et al. [130], and Tosaka and Suh [133] also considered in Figure 7.20, the current temperature T as given in (5.14) is now taken into account. Without this simplifying assumption, i.e. considering the full coupling in the thermal equation, severe problems are observed to occur for the partitioned algorithms in the form of bad convergence. Within a time step t the iteration between the single fields diverges, i.e. the norms of the displacement and the temperature increments, respectively, cannot be dropped down to the prescribed tolerances $\epsilon_{\mathsf{out}} = 1.0 \cdot 10^{-6}$. These problems can be reduced, e.g. by varying the material parameters, but this means changing the problem. In contrast to the partitioned algorithms, even with the inclusion of T in the full coupling term, the monolithic TSI algorithm converges for all choices of material parameters.

Figure 7.21 shows the results obtained with the monolithic algorithm, using (5.14) or (7.6) as thermal equation according to Table 7.5. These results are compared to the results obtained

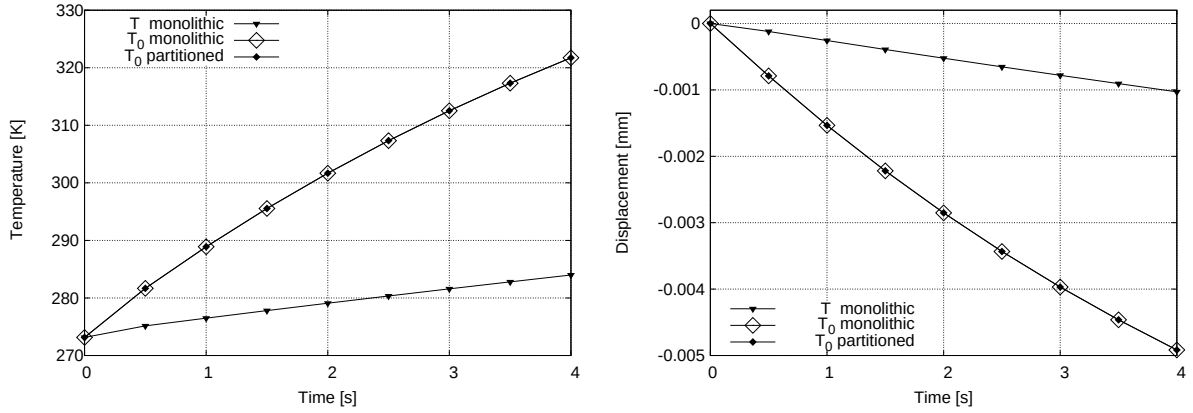

Figure 7.21: Second Danilovskaya problem: temperature (left) and displacement (right) results using $E = 210$ GPa. The naming of the solution strategies is given in Table 7.5.

with the partitioned algorithm using (7.6) and perfect agreement is achieved. Results of the partitioned algorithm utilising (5.14) are not presented, because no solution can be obtained due to divergence. It can be clearly seen that the simplifying assumption has quite some influence on the solution (in contrast to (7.6) decisively smaller temperature and displacement changes are developed regarding (5.14)) and should not just be introduced in order to get partitioned schemes working.

The Young's modulus is identified as an important parameter influencing the observed behaviour of bad convergence. In Figure 7.22, exemplary results for temperatures and displace-

Name	Solution strategy	Temperature considered in coupling term	Thermal balance equation considered in TSI
"monolithic"	monolithic	T	(5.14)
"T_0 monolithic"	monolithic	T_0	(7.6)
"partitioned"	partitioned	T	(5.14)
"T_0 partitioned"	partitioned	T_0	(7.6)

Table 7.5: Second Danilovskaya problem: naming of solution strategies

ments are provided for the reduction of the modulus by a factor of 100. In this case, the simulation using the partitioned algorithm with (5.14) converges and results can again be obtained. Figure 7.22 also shows results obtained with the monolithic TSI algorithm for both values $E = 2.1$ GPa and $E = 210$ GPa. For the reduced modulus, i.e. $E = 2.1$ GPa, the results of the partitioned and the monolithic TSI algorithms are in good agreement. Again, it is emphasized that the monolithic TSI algorithm, as opposed to the partitioned one, is able to handle the complete range of the parameter spectrum without problems.

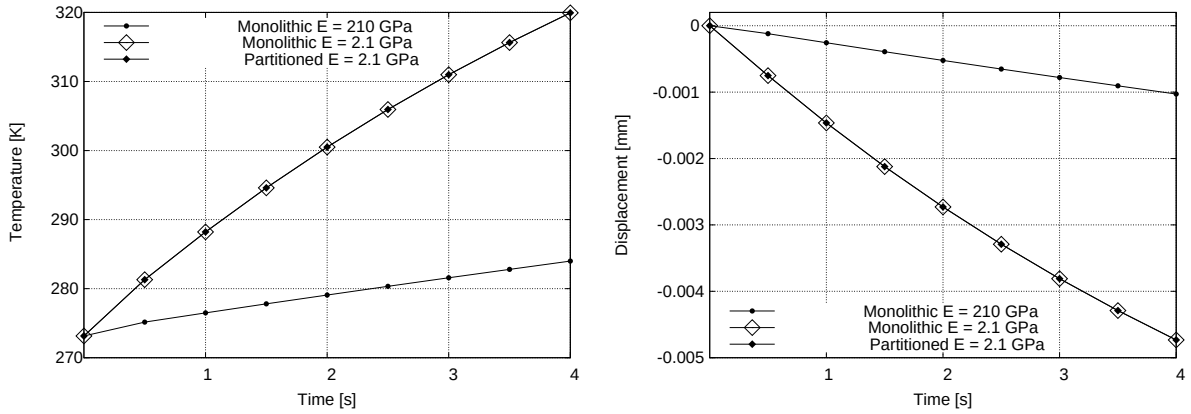

Figure 7.22: Second Danilovskaya problem: temperature (left) and displacement (right) results with varying Young's modulus. The naming of the solution strategies is given in Table 7.5.

As proposed in Armero and Simo [6], Erbts and Düster [38], the coefficient of thermal expansion (CTE) α_T can be used to describe the strength of coupling between the two fields. While a value $\alpha_\mathsf{T} = 1.5 \cdot 10^{-5}\ \frac{1}{\mathrm{K}}$ correlates with a weak coupling, strong coupling arises by $\alpha_\mathsf{T} = 1.5 \cdot 10^{-4}\ \frac{1}{\mathrm{K}}$, see Armero and Simo [6] and Erbts and Düster [38]. As previously mentioned, no convergence could be achieved for the partitioned algorithms using the material parameters presented at the beginning of this section and solving (5.14). Following the suggestions of Armero and Simo [6] or Erbts and Düster [38], the present CTE is reduced by a factor of 10, i.e. using a value $\alpha_\mathsf{T} = 1.1 \cdot 10^{-6}\ \frac{1}{\mathrm{K}}$. Using the reduced CTE, the partitioned algorithm converges and results can be obtained. As before, the monolithic TSI algorithm is able to handle both parameters, as illustrated in Figure 7.23. Consequently, the Young's modulus and the CTE

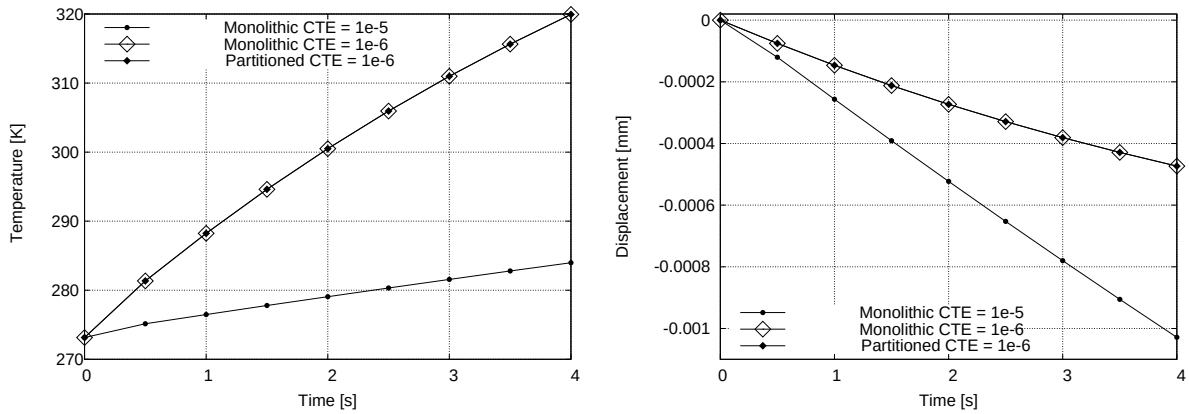

Figure 7.23: Second Danilovskaya problem: temperature (left) and displacement (right) results with varying linear heat expansion coefficient. The naming of the solution strategies is given in Table 7.5.

are important parameters for the behaviour of the partitioned TSI algorithm and can influence the observed behaviour of bad convergence.

Finally, the influence of the discretisation is investigated, i.e. the approximation of the continuous solution via FEs. In the present second Danilovskaya problem, high heat fluxes $\hat{q}_c$ are applied at the left, i.e. at $x = 0$, and zero heat fluxes at the right boundary, i.e. at $x = 6\,\mathrm{mm}$, respectively. If a too coarse mesh is chosen, the temperatures and their gradients cannot be approximated sufficiently. Figure 7.24 depicts the temperature solution at time $t = 0.001\,\mathrm{s}$ choosing an extremely coarse mesh for the discrete solution (consisting of e.g. two elements only). Due to the

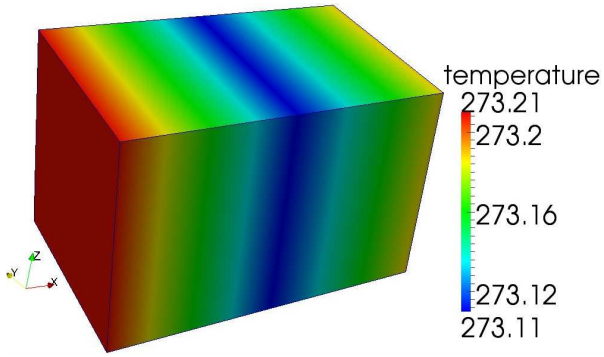

Figure 7.24: Second Danilovskaya problem: overshooting of the temperature solutions at time $t = 0.01\,\mathrm{s}$ using a coarse mesh.

insufficient approximation of the temperatures and their gradients in the middle of the body, i.e. at $x = 3\,\mathrm{mm}$, the temperatures overshoot to fulfil the Neumann boundary conditions the best possible at $x = 0$ and $x = 6\,\mathrm{mm}$, respectively, resulting in an unphysical discrete solution of the numerical example. In order to achieve a good numerical solution the spatial discretisation has to be carefully chosen to avoid this overshooting. In contrast to the coarse mesh, the discretisation utilised for the aforementioned investigations of the present numerical example, using $12 \times 4 \times 4$ elements, resolves the given gradients sufficiently.

7.2 Rocket nozzle

Finally, in order to demonstrate the applicability of the presented TSI approach to real three-dimensional problems, the behaviour of a cylindrical rocket nozzle of a subscale thrust chamber is simulated. In contrast to a real rocket nozzle, the geometry of the computational model of the nozzle is modified slightly: in addition to the real nozzle extension, prior to it, a part of the combustion chamber up to the throat is added. While the result evaluation of the present numerical example is not weakened by the modified geometry, geometry and mesh generation have been facilitated extremely.

The cross section of the given rocket nozzle (see Figure 7.25 (left)) changes continuously in z-direction: at $z = 0$ the radius is $r_{\mathsf{combust}} = 25.3\ \mathrm{mm}$ and reaches $r_{\mathsf{outlet}} = 169.8\ \mathrm{mm}$ at the outlet of the nozzle at $z = 398.5\ \mathrm{mm}$. The front surface ($z = 0$) describes the transition from the combustion chamber to the nozzle extension. The constant height of the cross section is $6.7\ \mathrm{mm}$.

Figure 7.25: Rocket nozzle: initial geometry and prescribed boundary conditions. Three-dimensional view of the considered geometry containing one cooling channel (left) and cross section with the definition of dimensions and loads (right).

The cooling channels are considered in the present example, as shown in Figure 7.25. While the cooling within the nozzle extension in "Vulcain 2" is realised by helicoidal cooling channels, i.e. they are coiled in a spiral around the nozzle wall, in the present numerical example they are assumed to span along the flow direction as illustrated in Figure 7.25 (left), i.e. along the z-direction. As depicted in Figure 7.26, this arrangement is in accordance to Mäding [82] and to the combustion chamber of the "Vulcain 2" thrust chamber (see Figure 1.1). The cooling of the present nozzle is realised by 80 cooling channels distributed equally over the circumference of the body. The cooling channels are described by a constant fin thickness $t_{\mathsf{fin}} = 1\ \mathrm{mm}$. Due to the constant fin thickness, the width $b(y, z)$ changes continuously in y- and along the z-direction. The rocket nozzle is a rotationally symmetric body, so that the computational model can be restricted to one cooling channel only, i.e. the simulation is performed by modelling only $1/80^{\mathrm{th}}$ of the whole nozzle, which is described by an angle of $\vartheta = 4.5°$ (see Figure 7.25 (right)).

The material parameters are adopted from Kuhl et al. [69], meaning that the liner material is a copper alloy and the closure of the channels is realised by a nickel jacket as shown in Figure 7.25. The material parameters according to Kuhl et al. [69] are provided in Table 7.6.

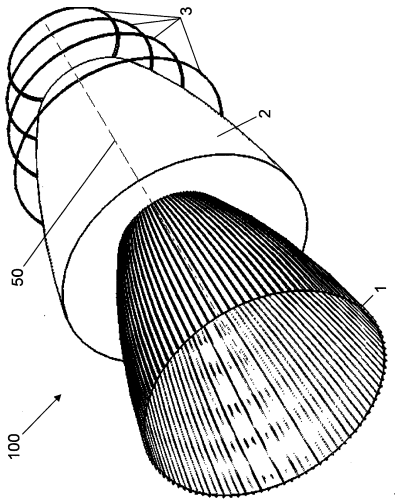

Figure 7.26: Rocket nozzle: schematic drawing of a rocket nozzle illustrating the inner liner material with axial cooling channels marked with number 1 and the jacket material marked with number 2, see Mäding [82].

Copper alloy			
$k_0 = 310\ \frac{\mathrm{W}}{\mathrm{m\,K}}$	$C_{\mathsf{V}} = 373\ \frac{\mathrm{J}}{\mathrm{kg\,K}}$	$\alpha_{\mathsf{T}} = 1.72 \cdot 10^{-5}\ \frac{1}{\mathrm{K}}$	$T_0 = 40\ \mathrm{K}$
$E = 148\ \mathrm{GPa}$		$\nu = 0.3$	$\rho_0 = 9,130\ \frac{\mathrm{kg}}{\mathrm{m}^3}$
Nickel jacket			
$k_0 = 75\ \frac{\mathrm{W}}{\mathrm{m\,K}}$	$C_{\mathsf{V}} = 444\ \frac{\mathrm{J}}{\mathrm{kg\,K}}$	$\alpha_{\mathsf{T}} = 1.22 \cdot 10^{-5}\ \frac{1}{\mathrm{K}}$	$T_0 = 40\ \mathrm{K}$
$E = 193\ \mathrm{GPa}$		$\nu = 0.3$	$\rho_0 = 8,910\ \frac{\mathrm{kg}}{\mathrm{m}^3}$

Table 7.6: Rocket nozzle: material parameters.

The nickel jacket and the copper alloy have a height $l_{\mathsf{ni}} = 4\ \mathrm{mm}$ and $l_{\mathsf{co}} = 2.7\ \mathrm{mm}$, respectively. In addition, the height of the copper alloy l_{co} is divided into the hot gas wall height l_{hg} and the cooling channel height l_{cc}. According to Kuhl et al. [69] for the so-called optimized model, the heat transfer coefficient at the hot gas side is chosen to be $h_{\mathsf{hg}} = 32\ \frac{\mathrm{kW}}{\mathrm{m^2\,K}}$ and at the cooling channel walls to be $h_{\mathsf{cc}} = 100\ \frac{\mathrm{kW}}{\mathrm{m^2\,K}}$. Furthermore, at the beginning of the simulation ($t = 0$) the stress-free chamber has a constant initial temperature $T_0 = 40\ \mathrm{K}$.

The corresponding boundary conditions for heat transfer $\hat{Q}_{\mathsf{C}}$ and pressure $\hat{p}$ at the hot gas side and in the cooling channel are given in Table 7.7. The temporal phases of the loading cycle are taken from Arya and Arnold [10] (see Figure 7.27) proposing a typical reduced loading cycle, which can be split in a cold (I and V) and a hot phase (II to IV), respectively. The pressure $\hat{p}$ is applied normal to the respective surfaces and points inwards. Thus, $\hat{p}$ represents a deformation-dependent external load, which contributes to the stiffness matrix $\mathbf{K}_{\mathsf{SS}}$. After $t = 3.5\ \mathrm{s}$ the load is held constant until $t = 6\ \mathrm{s}$. Apart from the applied loading, structural symmetry boundary conditions are applied at the left and right side of the body. At the front surface ($z = 0$) the

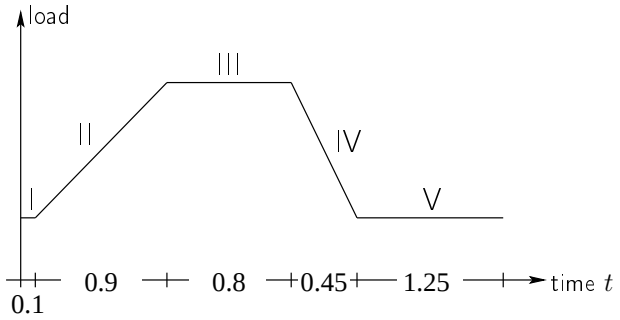

Figure 7.27: Rocket nozzle: cyclic temperature and pressure loading histories. The values for pressure $\hat{p}$ and temperature T_∞ are summarized in Table 7.7.

Phase	Time [s]	Pressure [MPa]		Temperature [K]	
		$\hat{p}_{\mathsf{hg}}$	$\hat{p}_{\mathsf{cc}}$	$T_{\infty,\mathsf{hg}}$	$T_{\infty;\mathsf{cc}}$
I	$0.0 - 0.1$	0.0	0.0	40.0	40.0
II	$0.1 - 1.0$	$0.0 - 10.0$	$0.0 - 2.0$	$40.0 - 950.0$	40.0
III	$1.0 - 1.8$	10.0	2.0	950.0	40.0
IV	$1.8 - 2.25$	$10.0 - 0.0$	$2.0 - 0.0$	$950.0 - 293.15$	40.0
V	$2.25 - 3.5$	0.0	0.0	293.15	40.0

Table 7.7: Rocket nozzle: pressure cycle $\hat{p}$ and internal thermal cycle, given in terms of the ambient temperature T_∞ on the hot gas side (index "$_{\mathsf{hg}}$") and in the cooling channels (index "$_{\mathsf{cc}}$"), respectively.

body is fixed in z-direction, thereby taking into account that the real nozzle is connected to the combustion chamber to build the whole thrust chamber. Furthermore, at the symmetric surfaces and at the outer surfaces, zero flux conditions are prescribed for the thermal field.

The total simulation time is $t = 6$ s, with a time step $\Delta t = 0.05$ s. Three meshes A to C are differentiated as given in Figure 7.28 and Table 7.8. The default element type is a Hex8 element. The number of elements and corresponding DOFs are summarized in Table 7.8 for the three meshes A to C. Exemplarily, the coarsest mesh A, see Figure 7.28 at the top, contains for the structural and the thermal field each $3,685$ nodes and $2,376$ elements, whereby 8 elements are distributed in circumferential direction, 9 elements in radial direction, and 58 elements in z-direction, respectively. Alternatively to the default Hex8 elements, for mesh A Hex27 elements can be chosen. The total number of DOFs are specified in Table 7.8 for all applied meshes. For time integration of both fields either an one-step-θ time integration scheme or a generalised-α scheme are chosen. In case of an one-step-θ scheme, the value θ is chosen to $\theta = \theta_{\mathsf{S}} = \theta_{\mathsf{T}} = 0.66$, which has proven to be a stable choice. In case of a generalised-α scheme the maximal spectral radius ρ_∞ is set to $\rho_\infty = \rho_{\infty;\mathsf{S}} = \rho_{\infty;\mathsf{T}} = 0.5$, which corresponds to a stable, second-order accurate scheme. Thus, based on sections 3.2.2 and 4.2.2, the algorithmic parameter for the structural field follow as $\alpha_{\mathsf{m};\mathsf{S}} = 0$, $\alpha_{\mathsf{f};\mathsf{S}} = 1/3$, $\gamma_{\mathsf{S}} = 5/6$, and $\beta_{\mathsf{S}} = 4/9$, and for the thermo field as $\alpha_{\mathsf{m};\mathsf{S}} = 5/6$, $\alpha_{\mathsf{f};\mathsf{T}} = 2/3$ and $\gamma_{\mathsf{T}} = 2/3$, respectively. The computed results are evaluated at four different points A to D in the middle of the body as shown in Figure 7.29.

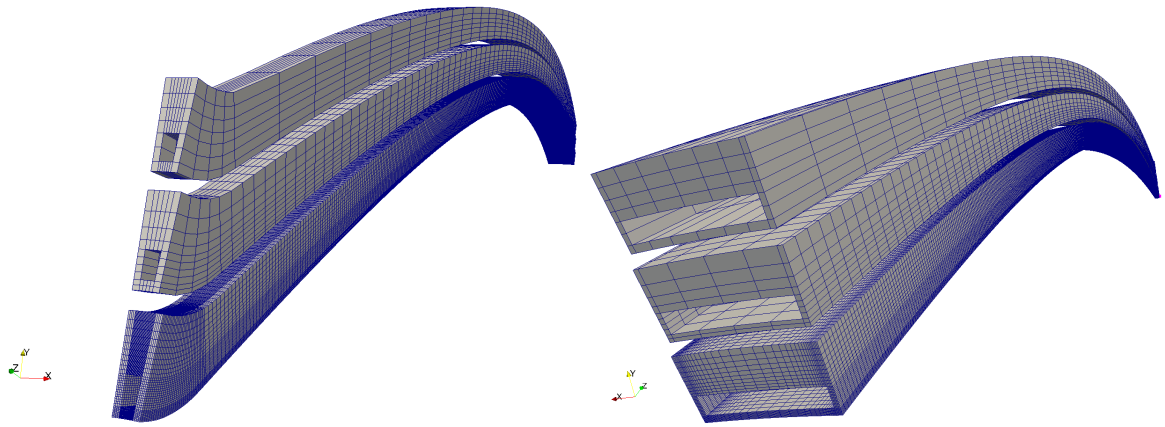

Figure 7.28: Rocket nozzle: mesh A ($2,376$ elements) to C ($551,104$ elements) from top to bottom. Front view (left) and back view (right).

Mesh	Number of elements per field				Total number of DOFs	
	total	circumferential	radial	z	Hex8	Hex27
A	$2,376$	8	9	58	$14,740$	$115,128$
B	$4,576$	10	10	104	$28,560$	-
C	$551,104$	68	34	632	$2,501,616$	-

Table 7.8: Rocket nozzle: overview of the spatial distribution of elements for the three meshes A to C as well as the total number of TSI degrees of freedom.

As illustrated for instance in Figure 7.25 (right), symmetry boundary conditions need to be imposed at the left surface and the inclined right surface of the computational model to simulate a correct physical deformation behaviour, as e.g. expansion along the tangential directions of these surfaces by fixing the normal directions. Unlike the standard structural Dirichlet boundary conditions at the left surface, which constrain the movements in x-directions, so-called inclined structural Dirichlet boundary conditions are required at the inclined right surface. For partitioned TSI algorithms the inclusion of inclined boundary conditions is straightforward and influences only the structural equation with the corresponding tangential stiffness matrix $\mathbf{K}_{\mathsf{SS}}$. However, for the monolithic TSI algorithm these boundary conditions require additional effort. As explained in section 6.3, inclined structural Dirichlet boundary conditions are realised in the monolithic algorithm by transforming the TSI system according to (6.35), where both blocks $\mathbf{K}_{\mathsf{SS}}$ and $\mathbf{K}_{\mathsf{ST}}$ are modified. For further details on inclined structural Dirichlet boundary condition within the monolithic TSI algorithm, the interested reader is referred to the end of section 6.3. Furthermore, in contrast to the previous examples, within the BGS preconditioner of the monolithic TSI algorithm, the potential parameter ω_{BGS} is chosen to be equal to 0.5.

In the following, a variety of results will be presented. Via modification of different parameters, concerning e.g. material (thermoelastic or thermo-elasto-plastic material), time integration, mesh, or solution strategy, a wide range of simulations realised with the present TSI approach

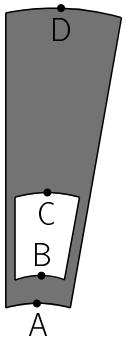

Figure 7.29: Rocket nozzle: definition of evaluation points A to D in the cross section in the middle of the body.

will be illustrated. Hereby, monolithic and partitioned solution algorithms will be used to compute the nozzle example. For the case of strongly coupled partitioned algorithms, static and dynamic relaxation will be integrated to accelerate the convergence. It is noted, that the results which will be presented always correspond to the best partitioned setup with respect to, e.g. the total solution time.

One-step-θ time integration with the thermoelastic Saint Venant-Kirchhoff material

The first setup is based on Danowski et al. [29] and considers a geometrically linear analysis using the monolithic and the strongly coupled partitioned TSI algorithms, as well as the thermoelastic Saint Venant Kirchhoff (TSVK) material. For time integration an one-step-θ method is utilised. Firstly, for spatial discretisation mesh B is chosen.

As anticipated, identical results for both monolithic and strongly coupled partitioned TSI algorithms are achieved. In Figure 7.30, the results for temperatures (left) and displacements in x-direction (right) over time t are exemplary shown for both approaches at points A and B for $z = 0$. After 0.1 s the load is increased. Due to the high temperature $T_{\infty;\mathsf{hg}}$ at the hot gas side the temperature is increasing faster at point A compared to point B. At $t = 1.8$ s, the body experiences the largest mechanical and thermal loading. For instance, at point A a maximal displacement $u_x = 1.5467 \cdot 10^{-02}$ mm and a maximal temperature $T = 350.82$ K are reached. At point B, which is located at the bottom of the cooling channel, the surrounding temperature $T_{\infty;\mathsf{cc}}$ remains constantly at 40 K. Thus, due to the difference of the surrounding temperatures $T_{\infty;\mathsf{hg}}$ and $T_{\infty;\mathsf{cc}}$, the temperature changes at point B are smaller compared to point A. Therefore, the thermal gradients between points A and B are very large at this time.

For the sake of lucidity, subsequent results are restricted to the ones where a monolithic approach is utilised. According to the previously presented results (see for instance Figure 7.30), the partitioned approach yields identical results compared to the monolithic approach. Thus, in Figure 7.31 the results for temperatures and displacements at the back surface of the nozzle for the evaluation points A to D are depicted over time t. Due to the increasing temperature $T_{\infty;\mathsf{hg}}$ up to 950 K, the temperature increases more at point A and B compared to point C and D. The constant temperature $T_{\infty;\mathsf{cc}}$ leads to small thermal changes for the points C and D. As a consequence of the thermal expansion of the whole body, the deformation reaches its maximum for

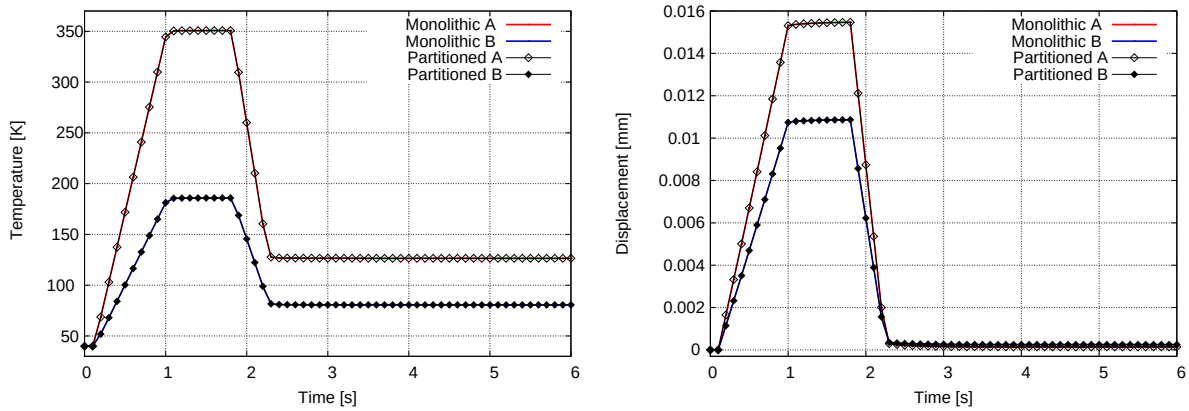

Figure 7.30: Rocket nozzle: temperature (left) and displacement in x-direction (right) at the evaluation points A and B (see Figure 7.29) at the front surface ($z = 0$) using a geometrically linear analysis, mesh B and the TSVK material. For the solution monolithic and partitioned TSI algorithms are utilised.

all points at the front surface at the end of the hot run ($t = 1.8$ s) and at the back surface earlier at the ($t = 1.0$ s).

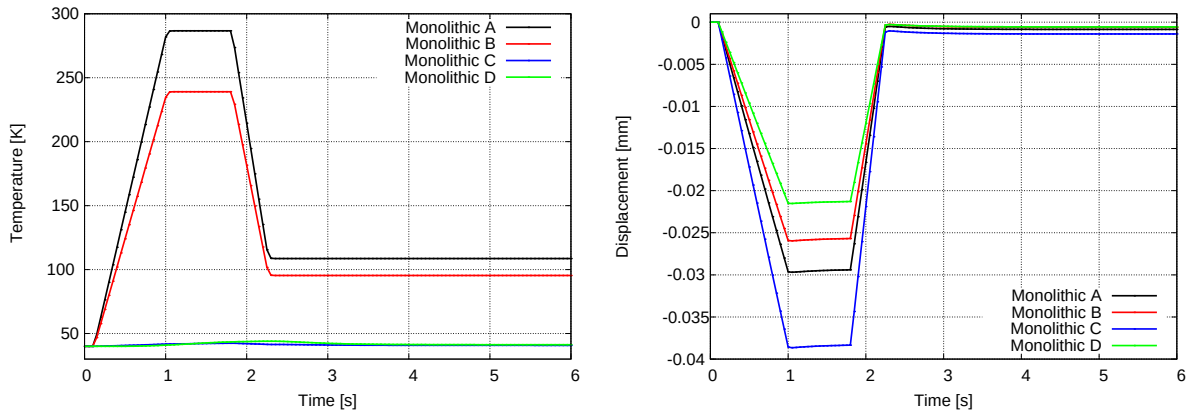

Figure 7.31: Rocket nozzle: temperature (left) and displacement in x-direction (right) for evaluation points A to D according to Figure 7.29 at the back ($z = 398.5$ mm) using a geometrically linear analysis, mesh B, the TSVK material, and the monolithic TSI algorithms.

After having investigated the local development of the temperatures and the displacements over time, Figure 7.32 shows the current deformation state of the nozzle at time $t = 1.8$ s, namely the z-displacements at the end of the hot run. No deformation occurs at the front surface, where the body is fixed in z-direction, whereas the nozzle expands up to $z = 1.251$ mm at the back surface. Furthermore, the inward pointing arrows indicate the direction of the heat flux $\boldsymbol{Q}$ $[\frac{\text{kg}}{\text{ms}^3}]$, i.e. heat is introduced into the body leading to an increase of temperature as well as to thermal expansion of the body. For the given numerical example, the partitioned algorithm can be used as an alternative to the monolithic algorithm. However, the computing time for the solution of the TSI problem is 141.25 % of the solution time of the monolithic algorithm.

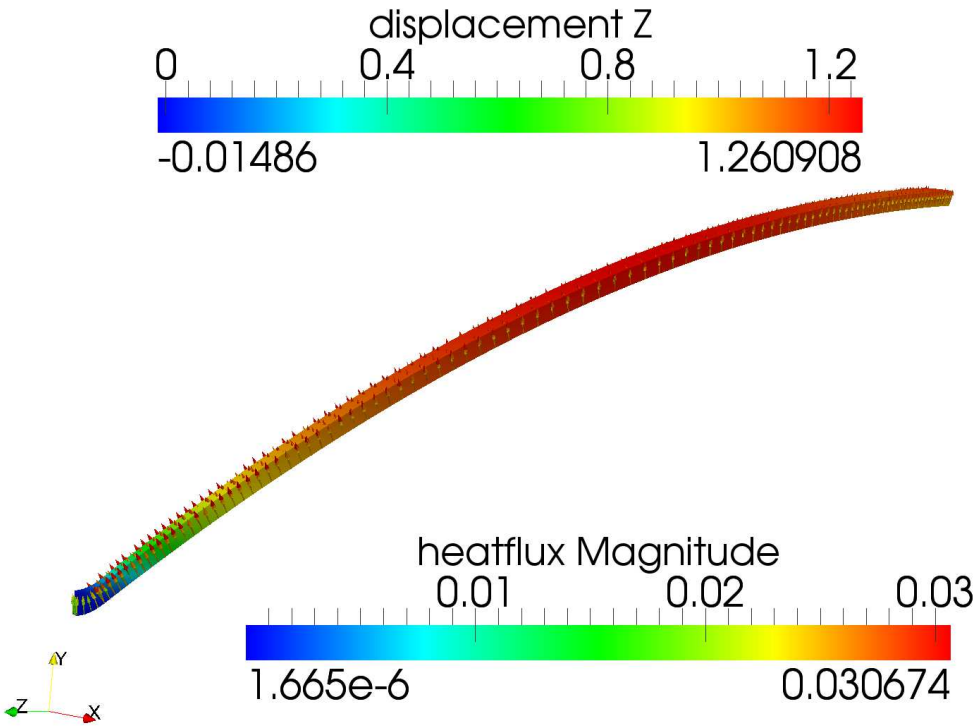

Figure 7.32: Rocket nozzle: displacement in z-direction at time $t = 1.8$ s using a geometrically linear analysis, mesh B, and the TSVK material. The arrows mark the direction of the heat flux.

Secondly, the previous setup is rerun using in addition a geometrically nonlinear analysis. To investigate the influence of a chosen mesh, all three meshes A to C are utilised in the following. Based on the first setup and Figure 7.32, in the subsequent Figures 7.33-7.35 the z-displacements $[\mathrm{mm}]$ and the heat fluxes $\boldsymbol{Q}$ $\left[\frac{\mathrm{kg}}{\mathrm{ms}^3}\right]$ are visualised at time $t = 1.8$ s employing a geometrically nonlinear analysis, i.e. including large deformations. While Figure 7.33 depicts the results for mesh A, Figure 7.34 and Figure 7.35 show the corresponding results for mesh B and C, respectively. The maximal z-displacements and heat fluxes increase with increasing mesh size. Comparing Figure 7.32 and Figure 7.34, i.e. comparing the results using a geometrically linear with the results using a geometrically nonlinear analysis, the heat fluxes range in the same order of magnitude for both analyses. In contrast, the deformation of the linear analysis is smaller. In Figure 7.36, the evolution of temperatures and x-displacements over time are shown for point A using the three meshes as well as small and large deformation TSI. Herein, the abbreviations “GeoLin” and “GeoNln” correspond to the geometrically linear and nonlinear analysis, respectively. While larger discrepancies between the results of mesh B and mesh C are observed, the results of mesh A are in good agreement with the solution of the finest mesh C, although it is coarser compared to mesh B. The discrepancies observed in mesh B are caused by an overshoot of the temperature solution which is explained in more detail in the following. As mentioned in the second Danilovskaya problem, see section 7.1.5, the influence of the spatial discretisation can have a high influence. If a too coarse mesh is chosen, the thermal solution cannot be approximated sufficiently, thus the temperatures overshoot, see Figure 7.24. The effect of overshooting is clearly illustrated in the second Danilovskaya problem due to the simple

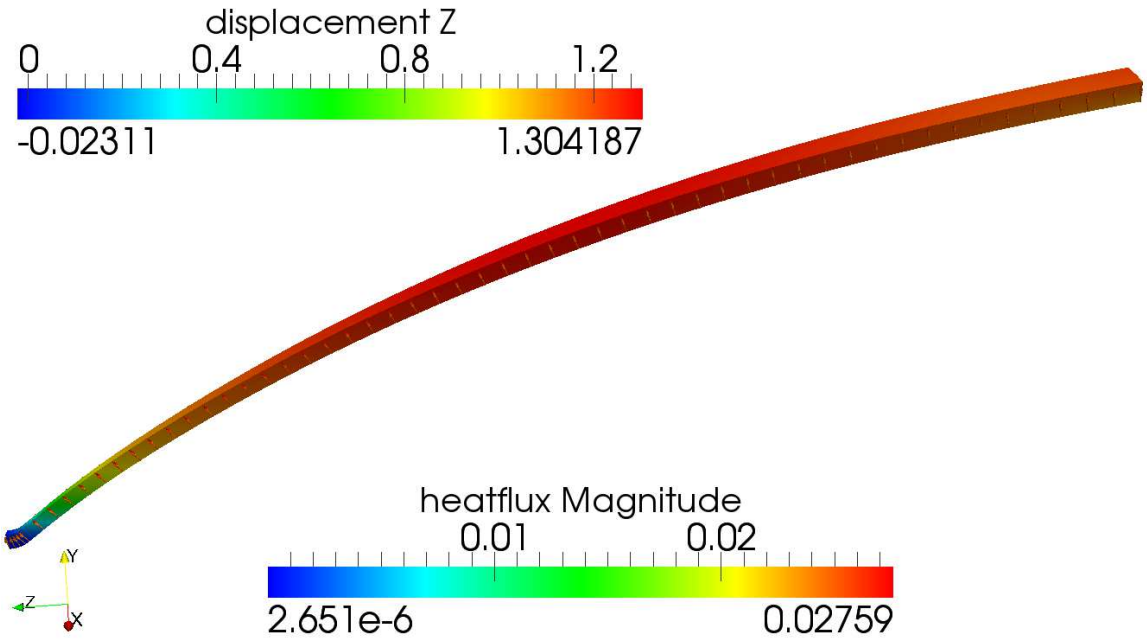

Figure 7.33: Rocket nozzle: displacement in z-direction at time $t = 1.8$ s using a geometrically nonlinear analysis, coarse mesh A, and the TSVK material. The arrows mark the direction of the heat flux.

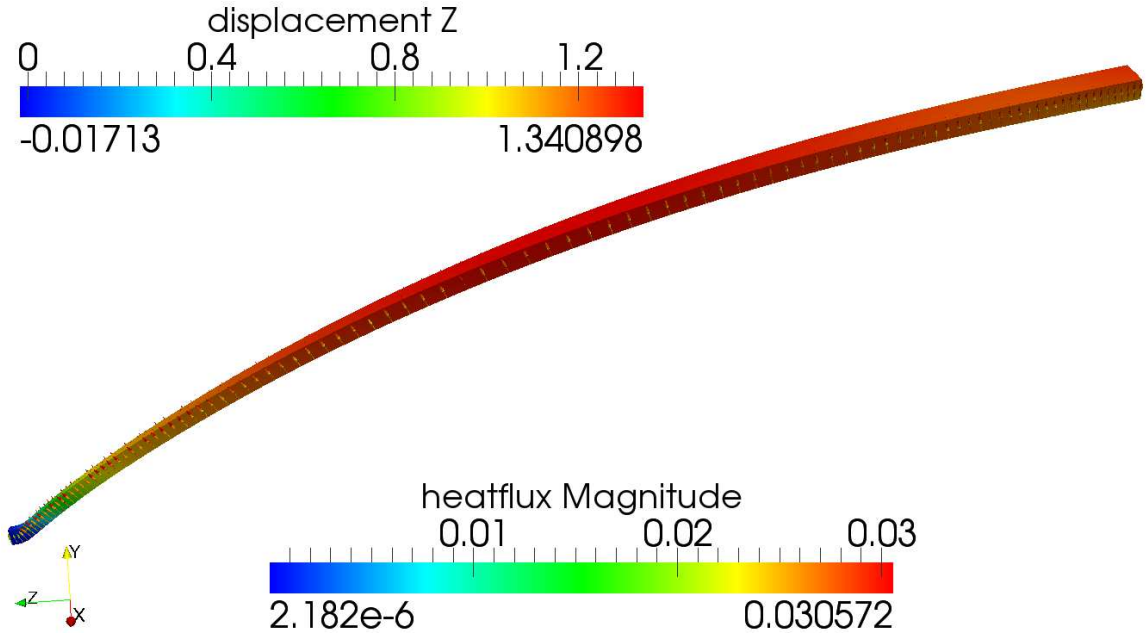

Figure 7.34: Rocket nozzle: displacement in z-direction at time $t = 1.8$ s using a geometrically nonlinear analysis, mesh B, and the TSVK material. The arrows mark the direction of the heat flux.

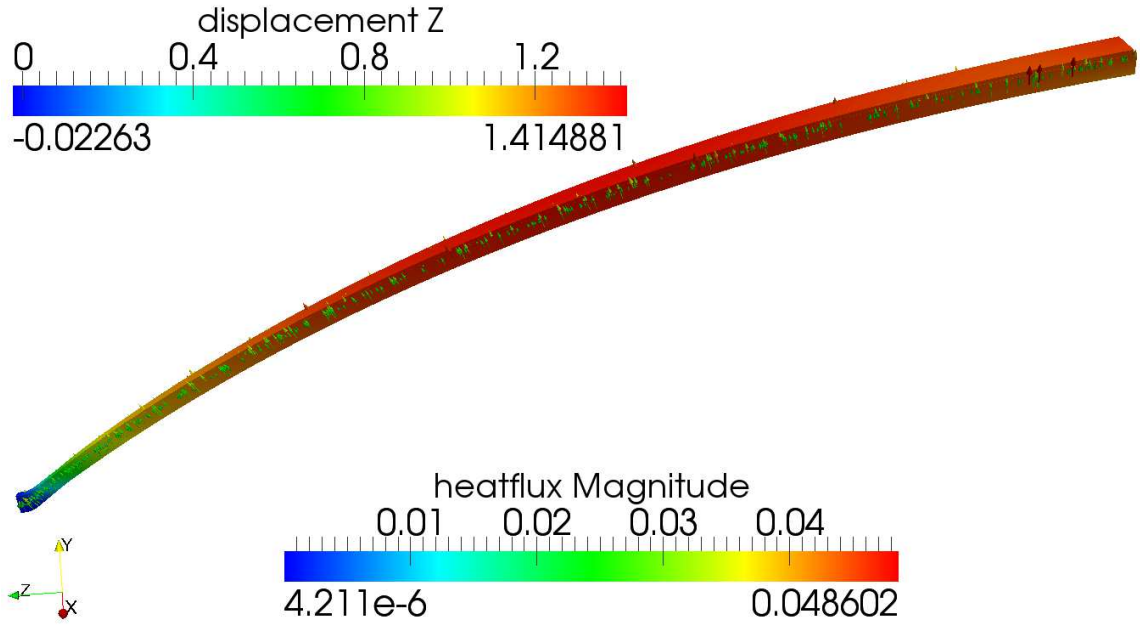

Figure 7.35: Rocket nozzle: displacement in z-direction at time $t = 1.8$ s using a geometrically nonlinear analysis, fine mesh C, and the TSVK material. The arrows mark the direction of the heat flux.

geometry and the one-dimensional loading. Such a clear representation of the overshooting is not possible in the present example due to the more complex geometry and loading. However, as depicted in Figure 7.36, the resulting temperatures using mesh B are much higher compared to the other meshes. Maximal temperature solutions are computed at $t = 1.8$ s, yielding for mesh B $T_{\mathsf{max}}^{\mathsf{meshB}} = 353.80$ K compared to $T_{\mathsf{max}}^{\mathsf{meshA}} = 239.31$ K and $T_{\mathsf{max}}^{\mathsf{meshC}} = 236.53$ K for mesh A and C, respectively. In Figure 7.37, the temperature solution near the front surface is shown for all three meshes at $t = 1.8$ s for the TSVK material and the geometrically nonlinear analysis. Again, the temperature solution of mesh B at the hot gas side is much higher compared to the remaining meshes which is caused by an insufficient approximation of the temperature gradients in y-direction. For instance considering point A at the front surface, the temperature gradients of mesh A and C are $(\mathrm{Grad}\, T)_y^{\mathsf{meshA}} = -64.66\ \frac{\mathrm{K}}{\mathrm{mm}}$ and $(\mathrm{Grad}\, T)_y^{\mathsf{meshC}} = -72.26\ \frac{\mathrm{K}}{\mathrm{mm}}$, respectively. In contrast, the thermal gradients for mesh B are $(\mathrm{Grad}\, T)_y^{\mathsf{meshB}} = -246.19\ \frac{\mathrm{K}}{\mathrm{mm}}$, i.e. more than three times higher compared to the two other meshes. Thus, spatial discretisation of the height l_{hg} with two elements is not sufficient. For the present loading it is noted, that the discretisation with one single element (see mesh A) leads to better results compared to two elements. However, in general it is recommended to choose more elements for spatial discretisation of l_{hg} to guarantee good quality of the computed results. Hence, for the following investigations good quality of the results is pursued by exclusively utilising mesh A and C, while mesh B is not further applied.

Generalised-α time integration with various thermoelastic materials

In the following, the generalised-α scheme is chosen for time integration with spectral radius $\rho_\infty = 0.5$ for both fields. Hence, the resulting algorithmic parameters enable a second-order

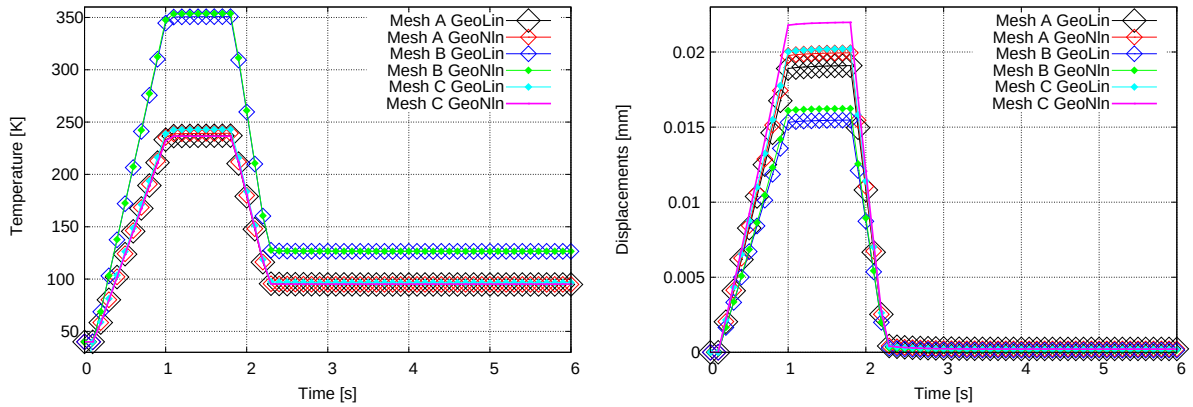

Figure 7.36: Rocket nozzle: temperature (left) and displacement in x-direction (right) over time at evaluation point A at the front ($z = 0$), using geometrically linear and nonlinear analyses, the TSVK material, and the three meshes.

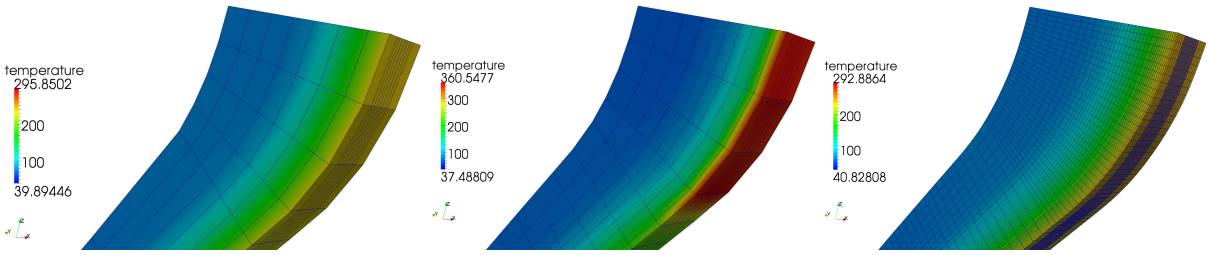

Figure 7.37: Rocket nozzle: temperature solution at $t = 1.8$ s for a geometrically nonlinear analysis and the TSVK material thermal applying mesh A (left), mesh B (middle), and mesh C (right).

accurate and robust scheme for the coupled TSI problem. The subsequent simulation set-ups include large deformations, finite strains and plasticity. Consequently, the accurate and robust generalised-α time integration scheme is in particular appropriate for the following challenging computations.

For the results above, the TSVK material with constant material parameters is used. Subsequently, the nozzle example including the TSVK material is extended to account for a temperature-dependent Young's modulus as proposed in Kuhl et al. [69]. The temperature-dependent Young's modulus is approximated by a linear relationship according to $E = E(T) = 148\ \text{GPa} - 0.073\,T\,\frac{1}{\text{K}}\ \text{GPa}$. While "TSVK" denotes the thermoelastic Saint Venant-Kirchhoff material with constant material parameters, "TSVK E(T)" corresponds to the TSVK material including the temperature-dependent Young's modulus $E(T)$, and finally "TESIMO" to the thermo-hyperelastic material, respectively. The fine mesh C is chosen for the thermoelastic simulations. Figure 7.38 depicts the results for these thermoelastic materials at the back side: all thermoelastic materials predict nearly the same temperature and displacement values over time. However, slight differences can be identified by zooming into a subinterval. This is realised in Figure 7.39, where the corresponding results for temperatures and x-displacements are presented exemplarily for the time interval $t \in [1.1\ \text{s}, 1.8\ \text{s}]$: the largest thermomechanical changes are computed for the TESIMO material, while the lowest changes are obtained for the TSVK material with the

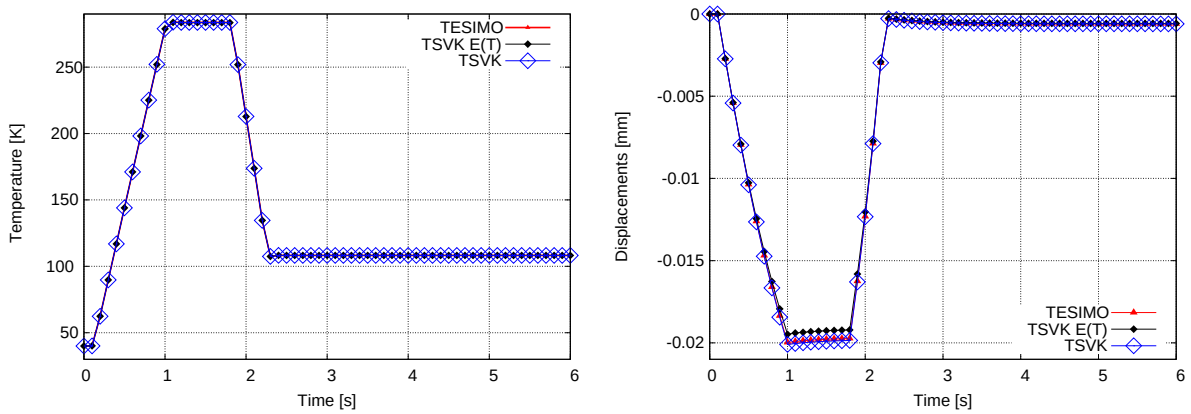

Figure 7.38: Rocket nozzle: temperature (left) and displacement in x-direction (right) over time at point A at the front ($z = 0$), using a geometrically nonlinear analysis, fine mesh C, and different thermoelastic materials.

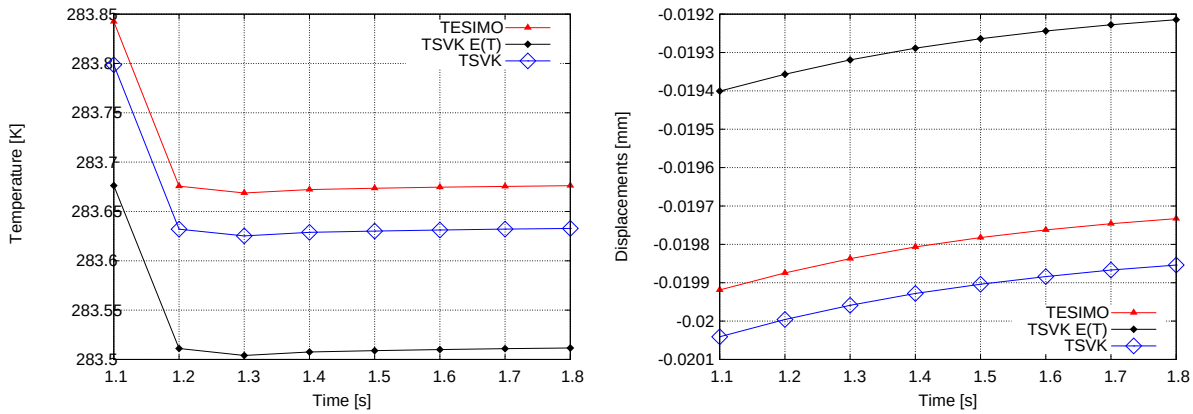

Figure 7.39: Rocket nozzle: temperature (left) and displacement in x-direction (right) over time interval $[1.1\ \mathrm{s}, 1.8\ \mathrm{s}]$ at point A at the front ($z = 0$), using a geometrically nonlinear analysis, fine mesh C, and different thermoelastic materials.

temperature-dependent Young's modulus. In Figure 7.40, the corresponding stress distribution for separate mechanical and thermal stresses, respectively, are shown for $t = 1.8$ s. At this time the stresses reach their maximal values. From left to right, the stress results are depicted for the TESIMO, the TSVK with $E(T)$, and the TSVK material, respectively. As explained previously, the thermal stresses, i.e. $\boldsymbol{S}_{\mathsf{T}}$ [GPa] in (5.30) and $\boldsymbol{S}_{\mathsf{dT}}$ [GPa] in (5.31), respectively, are determined by the temperature difference ΔT defined as difference between current temperature T and initial temperature T_0. For the sake of clarification, the maximal and minimal value of the current temperatures are also visualised in Figure 7.40. Thus, it is shown that the larger the temperatures T, the larger the thermal stresses. For the present simulations, this implies that the largest thermal stresses are computed for all materials at the hot gas side and, in particular, are computed for the TESIMO material. In contrast, the lowest values are obtained for the TSVK including $E(T)$. Consequently, inclusion of the temperature-dependent Young's modulus $E(T)$

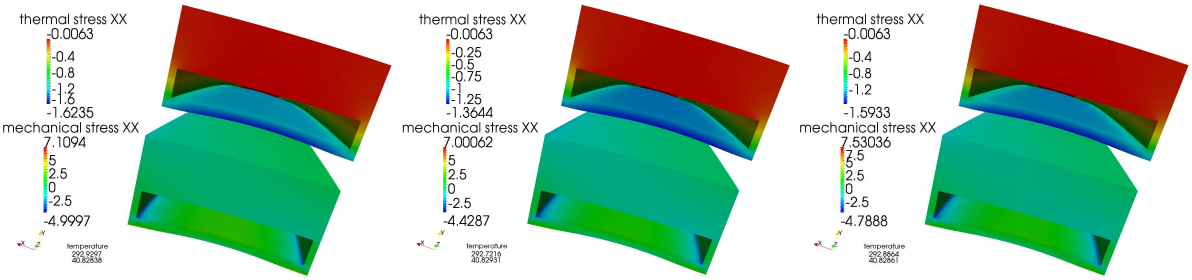

Figure 7.40: Rocket nozzle: thermal (top) and mechanical (bottom) stress distribution at $t = 1.8$ s using a geometrically nonlinear analysis, fine mesh C, and the three thermoelastic materials, i.e. the results for TESIMO (left), TSVK with $E(T)$ (middle), and TSVK (right). Back view of the body.

into the material model leads to smaller deformations and temperature changes, i.e. to a stiffer deformation response.

Thermo-hyperelastic material using different solution strategies

Based on the results in Figures 7.38-7.40, where a geometrically nonlinear analysis with the TESIMO material and the fine mesh C are utilised, in the following the influence of the different fully coupled partitioned strategies is investigated. In this context, loosely and strongly coupled partitioned algorithms are distinguished and moreover for the strongly coupled algorithms static and dynamic relaxation of the temperature and the displacements, respectively, are considered.

The fastest solution is achieved with the strongly coupled partitioned TSI algorithm considering the Aitken Δ^2 method and relaxation of the displacements with a maximal relaxation parameter $\omega_{\max} = 2.0$. Hence, this solution scheme is defined as the reference for the other solution schemes. Firstly, the loosely coupled approaches are analysed. Unlike the reference setup utilising the Aitken method, the solution time requires $108.33\ \%$ and $125.66\ \%$ for a loosely coupled partitioned approach with mechanical and thermal predictor, respectively. Secondly, the strongly coupled partitioned algorithm without relaxation is considered. Neglecting relaxation at all, this slows down the simulation time to $187.04\ \%$ compared to the reference simulation. Subsequently, inclusion of static or fix relaxation with a fix relaxation parameter $\omega = 0.5 = const.$ of the displacements and the temperatures requires $100.76\ \%$ and $167.13\ \%$, respectively. Dynamic relaxation of the temperatures leaded to divergence of the simulation, so that for this setup no solution time is presented.

Comparing the two relaxation methods, i.e. relaxation of the displacements with the relaxation of the temperatures, the solution approach including relaxation of the displacements performs more robust and more efficient. This is in accordance to Erbts and Düster [38], who investigated strongly coupled partitioned TSI algorithms including dynamic relaxation of the displacements. They also showed that this partitioned algorithm enabled the best and most efficient solution approach for their numerical examples. For the sake of completeness, the computation of the present setup with the monolithic TSI algorithm is slower and needs $116.25\ \%$ of the dynamically relaxed partitioned algorithm.

Generalised-α time integration and combined thermoelastic / thermo-elasto-plastic material

As explained in the introduction in chapter 1 and illustrated in Figure 1.1 (right), a rocket nozzle has to withstand high thermal and mechanical loads which may lead to irreversible deformations. To describe irreversible deformations, the elasticity is not sufficient to capture the whole deformation behaviour. Consequently, plasticity needs to be integrated into the computational model. As proposed in Kuhl et al. [69], the copper liner located at the inner hot gas side is assumed to experience irreversible deformations so that plasticity needs to be taken into account. In contrast, the nickel closure is assumed to be deformed only elastically. Hence, simulations are performed which are based on the TSVK material for the nickel and the thermo-elasto-plastic materials presented in section 5.3.2 for the copper. Table 7.6 summarizes the elastic material parameters. In addition, the plastic parameters for small or finite strain thermo-elasto-plastic material will be provided at the suitable place in the following.

For the solution of the plastic setup with the monolithic algorithm, the preconditioner strategy changes. The default preconditioner strategy within the monolithic algorithm is the backward BGS preconditioner, see (6.19)-(6.23). However, for the case of including plasticity into the TSI model, a forward BGS preconditioner is applied instead, see (6.24), i.e. within the preconditioner the structural field is solved first followed by the thermal field. This sequence is physically motivated and assumes that the solution of the structural field, in particular caused by the mechanical dissipation, has a higher influence on the temperature solution compared to the opposite effect of thermal expansion.

Linear thermo-elasto-plastic material

The first plastic setup considers the linear thermo-elasto-plastic material model according to section 5.3.2.1 for the copper and the TSVK material for the nickel within a geometrically linear analysis. In addition to the elastic material parameters in Table 7.6, based on Kuhl et al. [69], the plastic parameters are chosen to $\sigma_{\mathrm{y};0} = 0.232$ GPa, $H^{\mathsf{iso}} = 0.2$ GPa and $H^{\mathsf{kin}} = 0.6045$ GPa. Herein, the kinematic hardening modulus H^{kin} is determined by

$$H^{\mathsf{kin}} = \frac{E\,T}{E - T}\,, \tag{7.7}$$

where the Young's modulus E and the tangent modulus T are used and the latter is computed to $T = 0.602$ GPa. Hence, mixed hardening is included for this simulation. To enable a good resolution of the results, the fine mesh C is utilised.

Figures 7.41-7.43 depict the results of the given rocket nozzle configuration. The maximal plasticity is computed at the back surface ($z = 398.5$ mm) at the bottom corners inside the cooling channel, see Figure 7.41 (right). It is important to note, that these maximal values are caused by singularities at the corners of the computational model introduced by the spatial discretisation: the finer the mesh, the more pronounced these singularities. The singularities lead to unphysical peaks in the stress solution. Since plasticity is determined by the stress state, these stress peaks lead to unphysical high plastic solutions. It is important to keep in mind, that in reality the maximal plasticity does not occur at this corners but in the middle of the cooling channels at the hot gas wall, i.e. at points A and B. However, for the sake of completeness, results are also

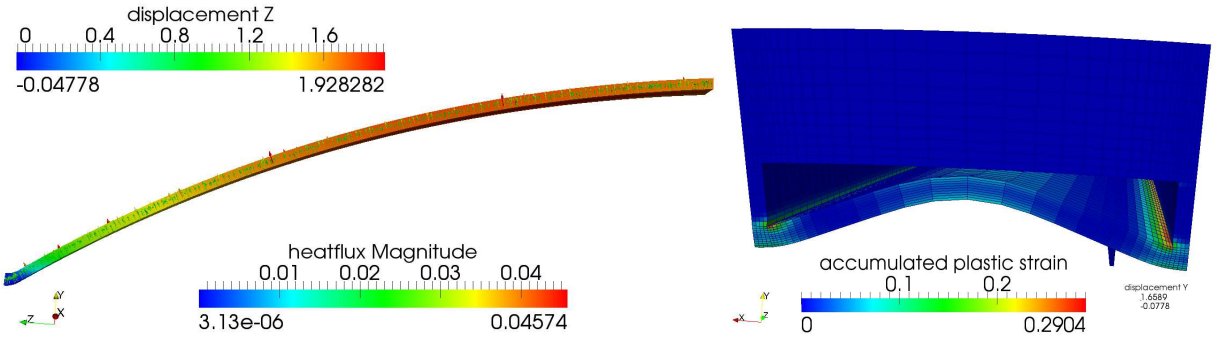

Figure 7.41: Rocket nozzle: displacement in z-direction at time $t = 1.8$ s using a geometrically linear analysis, fine mesh C, the small strain thermo-elasto-plastic material for the liner, and the TSVK material for the nickel jacket. The arrows mark the direction of the heat flux (left). Deformed contour of the back with colour distribution of the accumulated plastic strain at time $t = 6.0$ s (right).

shown for this corner point which is named evaluation point E. In Figures 7.41 (left), the distribution of the z-displacements is drawn at time $t = 1.8$ s. As anticipated, at this point in time, maximal z-displacements are reached at the back of the nozzle yielding $u_{z;\mathsf{max}} = 1.928$ mm. Subsequently, Figure 7.42 shows for the z-direction the evolution of the total normal stresses,

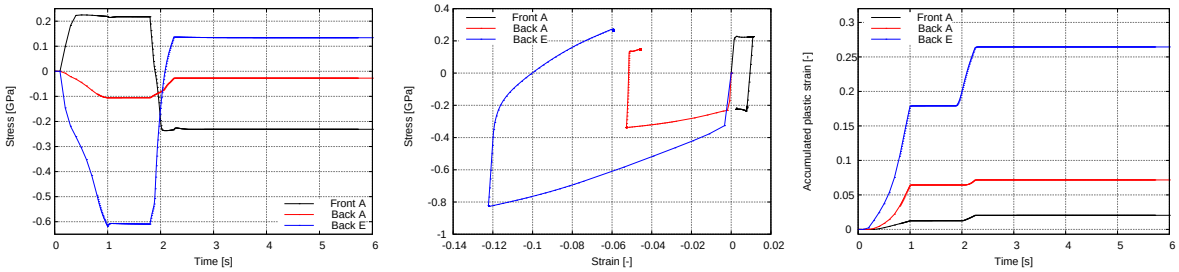

Figure 7.42: Rocket nozzle: total stresses S_{zz} vs. time (left), stress-strain curve for second Piola-Kirchhoff stresses S_{xx} versus Green-Lagrange strains E_{xx} (middle), and accumulated plastic strain $\bar{\varepsilon}^p$ versus time (right) for the evaluation points A at the front and back, as well as for point E at the back using a geometrically linear analysis, the fine mesh C, the small strain thermo-elastoplastic material for the liner, and the TSVK material for the nickel jacket.

i.e. S_{zz} over time for the three evaluation points A at the front and the back (denoted "Front A" and "Back A"), as well as for point E at the back (abbreviated to "Back E"). Since thermal stresses are assumed to be isotropic and volumetric, firstly, identical values are computed for the thermal normal stresses, i.e. $S_{\mathsf{T};xx} = S_{\mathsf{T};yy} = S_{\mathsf{T};zz}$ and secondly, the shear stresses are identical to zero. The largest thermal stresses are obtained at point Back A with $S_{\mathsf{T}}^{\mathsf{Back\,A}} = -1.5546$ GPa. The largest mechanical stresses are computed at point Front A with $S_{\mathsf{d}}^{\mathsf{Front\,A}} = 1.5010$ GPa. The total stresses are obtained as sum of mechanical and thermal stresses, thus the point of maximal total stresses can differ from the point of maximal mechanical or thermal stresses. Exemplarily, in the middle of Figure 7.42, the stress-strain curves for the total second Piola Kirchhoff stresses S_{xx} versus Green-Lagrange strains E_{xx} are depicted. Here, the deformation of point Back E

is the largest compared to the other two evaluation points with respect to largest stresses and strains. Furthermore, the maximal stresses in z-direction are computed at point Back E with $S_{zz}^{\text{Back E}} = -0.5305$ GPa compared to $S_{zz}^{\text{Front A}} = 0.2268$ GPa and $S_{zz}^{\text{Back A}} = -0.1054$ GPa for the evaluation points Front A and Back A, respectively. While the stresses at the back are compression stresses, the stresses at the front are tensile stresses. Hence, considering the absolute stress values, the point of maximal load is evaluation point Back E followed by point Back A and the least results are obtained at point Front A. This is further confirmed by the other two plots of Figure 7.42 where the results are the most pronounced for point Back E and the less for point Front A. Hence, maximal plastic values are expected for point Back E which is confirmed by the right plot of Figure 7.42, where the accumulated plastic strains $\bar{\varepsilon}^p$ $[-]$ versus time are drawn.

Figure 7.41 (right) captures the final deformed shape of the body at the back and $t = 6$ s. Although the applied loading is removed completely, the body still experiences significant deformations. For instance maximal and minimal y-displacements are in the range of $u_{y;\text{max}} = 1.6589$ mm and $u_{y;\text{min}} = -0.0778$ mm, respectively, and $u_{y;\text{max}}$ is computed at the thin wall between hot gas and cooling channel. Thus, the shown deformation u_y is nearly identical to the plastic deformation. Slight changes are still observed due to the coupling to the temperatures, which so far have not reached the steady state.

The level of stresses influences the plastic behaviour, i.e. the higher the stresses, the higher the plastic values. The present example describes a fully three-dimensional problem, hence the stress-strain curve of single stress and strain components, respectively, as illustrated in Figure 7.42, in general not allows for a statement of the overall deformation behaviour. To enable a meaningful statement, especially about the location of maximal plasticity, in Figure 7.43 (left) the von Mises stresses S_{vM}, defined e.g. in Appendix B.3, are evaluated for the three previous evaluation points. In addition, the results are visualised for point B for which the plastic values

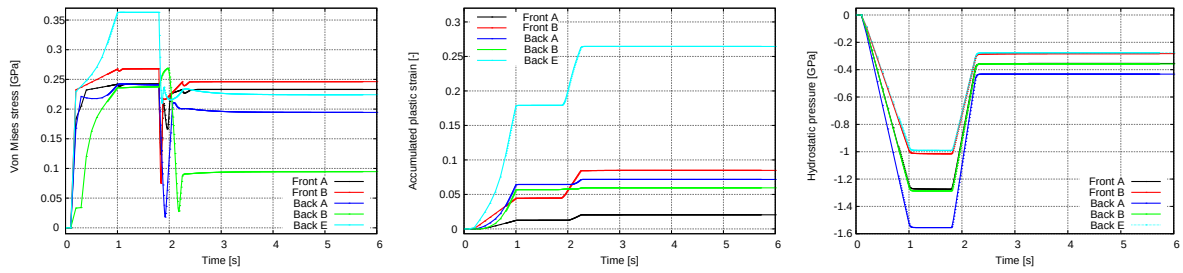

Figure 7.43: Rocket nozzle: von Mises second Piola-Kirchhoff stresses S_{vM} (left), accumulated plastic strain $\bar{\varepsilon}^p$ (middle), and thermal hydrostatic pressure p_{T} (right) over time for points A and B at the front and back surface, and point E at the back using a geometrically linear analysis, fine mesh C, the small strain thermo-elasto-plastic material for the liner, and the TSVK material for the nickel jacket.

are maximal at the front surface. The value of the von Mises stresses S_{vM} is maximal during the hot run phase and reaches the largest values for point Back E followed by Front B. The largest overall stress state is computed for point Back E which experiences the largest plasticity. This is also confirmed by Figure 7.42 (right). However, the results at Back E are achieved as a result of singularities caused by the fine spatial discretisation, thus the actual maximal physical

plasticity is computed at point Front B, see the accumulated plastic strains shown in the middle of Figure 7.43. The von Mises stresses S_{vM} are pressure invariant, i.e. the volumetric thermal stresses do not influence the values of the von Mises stresses. Consequently, for the sake of completeness, the thermal stresses are illustrated in Figure 7.43 (right) by evaluating the hydrostatic pressure p_{T} of the thermal stresses $\boldsymbol{S}_{\mathsf{T}}$ defined as

$$p_{\mathsf{T}} = \frac{1}{3} \operatorname{tr} \boldsymbol{S}_{\mathsf{T}} \,. \tag{7.8}$$

Again, the maximal thermal loadings are observed for point A which reach higher values at the back compared to the front.

Robinson's viscoplastic material

This setup integrates the linear Robinson's viscoplastic material into the present nozzle example. The parameters of the Robinson's material model are not available for copper, however, in Arya and Arnold [10], Robinson's viscoplastic material is applied to a rocket thrust chamber, where a so-called NARloy-Z copper alloy, i.e. silver-zirconium-copper alloy, is chosen. Furthermore, in Bornemann and Wall [18], the NARloy-Z copper alloy is applied to a two-dimensional rocket configuration and in Tini et al. [132] for a lifetime prediction. Hence, the NARloy-Z copper alloy, as proposed in Bornemann and Wall [18], is applied for the liner material in the present simulation and the corresponding material parameters are summarized in Table 7.9. Herein,

$\rho = 8,890\ \frac{\mathrm{kg}}{\mathrm{m}^3}$	$\nu = 0.34$	$\alpha_{\mathsf{T}} = 0.0$
$E = E(T) = 147.0\ \mathrm{GPa} - 7.05 \cdot 10^{-2}\, T\, \frac{1}{\mathrm{K}}\ \mathrm{GPa}$		
$G_0 = 0.04$	$A = 1.385 \cdot 10^{-8}\ \frac{1}{\mathrm{s}}$	$a = 4$
$H_0 = 1.67 \cdot 10^4\ \mathrm{MPa}^3$		$m = 4.365$
$\check{R}_0 = 6.083 \cdot 10^{-4}\ \frac{\mathrm{N}}{\mathrm{m}^2\,\mathrm{ms}^2}$	$Q_0 = 40,000\ \frac{\mathrm{J}}{\mathrm{mol}}$	$\Theta_0 = 811.0\ \mathrm{K}$
$\beta = \beta(T) = 0.8 + 0.553 \cdot 10^{-6}\, T^2\, \frac{1}{\mathrm{K}^2}$		
$K_0^2 = K_0^2(T) = K^2(T) = 6.988 \cdot 10^7\ \mathrm{GPa}^2 - 6.7 \cdot 10^{-8}\, T \frac{1}{\mathrm{K}}\ \mathrm{GPa}^2$		

Table 7.9: Rocket nozzle: material parameters for the Robinson's viscoplastic material.

the temperature-dependent material parameters $H(T)$ and $R(T)$ included in (5.54), (5.55) and $(5.53)_2$, respectively, are approximated according to

$$H(T) = H_0\, 6.895^{\beta+1}\, \frac{1}{3\, K_0^2}\,, \tag{7.9}$$

$$R(T) = \check{R}_0\, (6.895)^{1+\beta-m}\, (3\, K_0^2)^{m-\beta} \exp\Big[Q_0 \Big(\frac{1}{\Theta_0} - \frac{1}{T}\Big)\Big]\,, \tag{7.10}$$

respectively. In accordance with the previous set-ups, this configuration assumes the application of the Robinson's material assuming a NARloy-Z alloy for the copper and the TSVK for the

nickel. Furthermore, the coarse mesh A is chosen with Hex27 elements to circumvent volumetric locking.

In Figure 7.44 from top to bottom, the final distribution of the plastic strains ε_{yy}^{p}, the total strains ε_{yy}, the y-displacements, and the temperatures are shown for the whole computational model at time $t = 6$ s. While the nickel jacket does not experience plastic deformations,

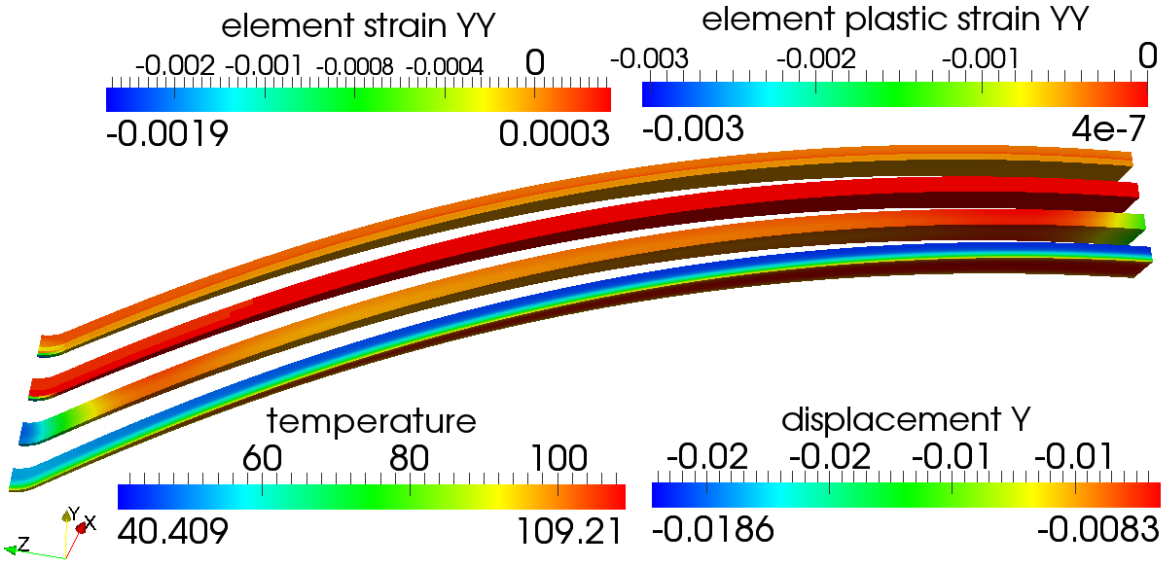

Figure 7.44: Rocket nozzle: from top to bottom: plastic strains ε_{yy}^{p}, total strains ε_{yy}, y-displacements, and temperatures at time $t = 6.0$ s using mesh A, Robinson's material for the liner, and the TSVK material for the nickel jacket.

maximal plastic values are obtained at $z = 0$ at the hot gas wall. At $t = 6$ s, the loading is removed completely, thus the remaining deformations are again nearly identical to the plastic deformations. Accordingly, maximal y-displacements are observed at this front surface with $u_{y;\mathrm{max}} = -0.0185$ mm. In Figure 7.45, the deformed contour, scaled with a factor of 100, is

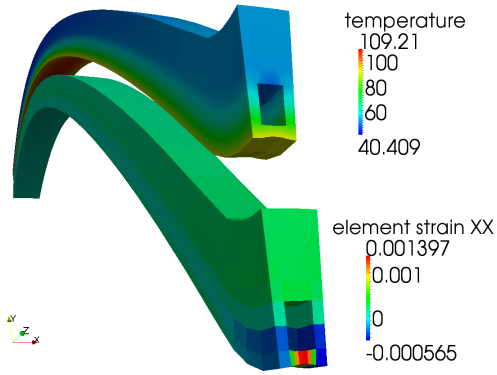

Figure 7.45: Rocket nozzle: deformed contour of the nozzle using a scaling factor of 100 to enhance the irreversible plastic deformations. The colour distribution shows the temperature (top) and the total strains ε_{xx} (bottom) at $t = 6$ s using mesh A, Robinson's material for the liner, and the TSVK material for the nickel jacket.

depicted and focus is set on the front view of the model. The colour distributions show for end time $t = 6$ s the temperatures T and the total strains $\boldsymbol{\varepsilon}_{xx}$. Again, for this final deformation state, the strains have its maximum at the hot gas side and due to the applied loadings the wall thickness l_{hg} is reduced. The present load cycle is not sufficient to represent irreversible effects due to cyclic loading. However, the originally rectangular cooling channel deforms in direction of a dog-house. As introduced in section 1.1 and visualised in Figure 1.1 (right), consequently the tendency of the deformation seems to reproduce the correct physical behaviour, namely a thinning of the hot gas wall in the form of a dog-house.

The present results are obtained using the monolithic approach. Furthermore, the corresponding simulation using a strongly coupled partitioned approach including dynamic relaxation of the displacements is additionally performed. As expected identical results are obtained, thus the representation is exemplarily chosen to the monolithic results only. However, the computing time for the solution of the partitioned TSI approach necessitates $124.65\ \%$ of the solution time of the monolithic approach.

Finite strain thermo-hyperelasto-plastic material

Finally, a geometrically nonlinear analysis is performed using the meshes A and C. For material modelling of the nozzle, the TSVK material is utilised for the nickel and the finite strain thermo-hyperelasto-plastic material according to Simo and Miehe [122] (abbreviated to "SIMO") for the copper. To avoid volumetric locking, Hex8 elements including the F-bar method are used. In addition to the elastic material parameters in Table 7.6, the plastic parameters are chosen as follows: $\sigma_{\mathsf{y};0} = 0.232$ GPa, $\sigma_{\mathsf{y};\infty} = 0.715$ GPa, $\omega_{\mathsf{h}} = \omega_0 = 0.002$, and $\delta = 16.93$.

In Figures 7.46 and 7.47, results are shown for the coarse mesh using monolithic and partitioned solution algorithms. Equivalently to the previous set-ups, the strongly coupled iterative

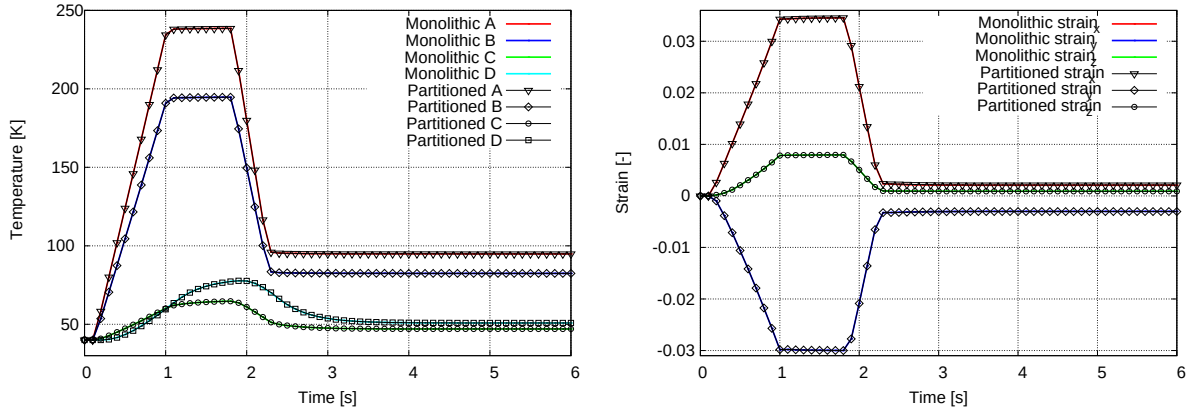

Figure 7.46: Rocket nozzle: temperature at points A-D (left) and normal strains at point A (right) over time at the front surface ($z = 0$), using the coarse mesh A, the SIMO material for the copper liner, and the TSVK material for the nickel jacket. Monolithic and partitioned schemes are applied.

staggered scheme with Aitken relaxation of the displacements is applied with a maximal relaxation parameter $\omega_{\mathsf{max}} = 2.0$. As expected identical results are obtained for both schemes.

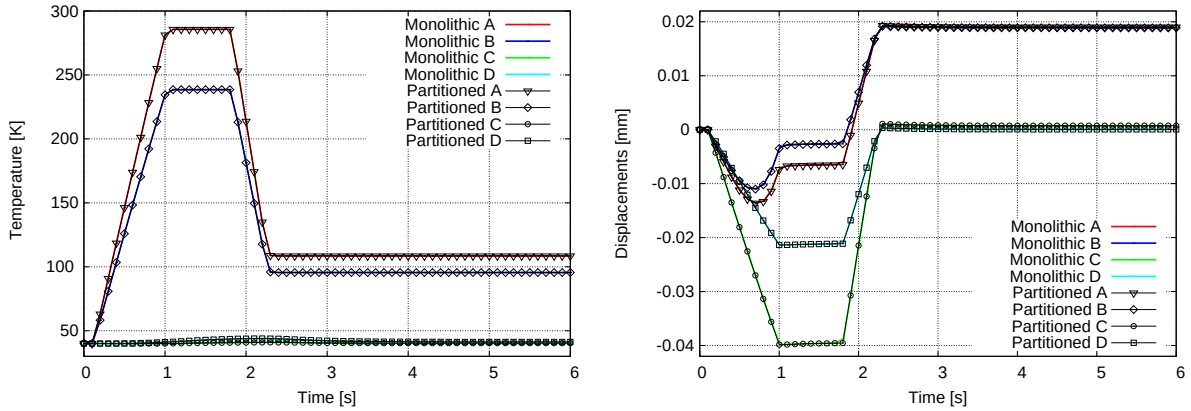

Figure 7.47: Rocket nozzle: temperature (left) and x-displacement (right) over time at points A-D at the back surface (at $z = 398.5$ mm) using the coarse mesh A, the SIMO material for copper, and the TSVK material for nickel. Monolithic and partitioned schemes are applied.

Moreover, solver times are compared showing that the monolithic one is 10% faster compared to the partitioned one.

In the following, focus is set on the plastic behaviour. Hence, the illustration in Figure 7.48 is restricted to the mechanical stresses S_{d} only. On the left of Figure 7.48, the stress-strain curve for the mechanical second Piola-Kirchhoff stresses $S_{\mathsf{d};zz}$ [GPa] versus corresponding Green-Lagrange strains E_{zz} [−] is depicted for point A and $z = 0$. The nonlinear isotropic hardening included in the SIMO material is illustrated by the nonlinear stress-strain relation, where the stresses increase with respect to the strains in a nonlinear relation. For the illustration of the effect of isothermal pure isotropic hardening, the reader is referred to section 7.1.1 and in particular to Figure 7.2 (middle). Moreover, Figure 7.48 (right) shows the mechanical second Piola-Kirchhoff

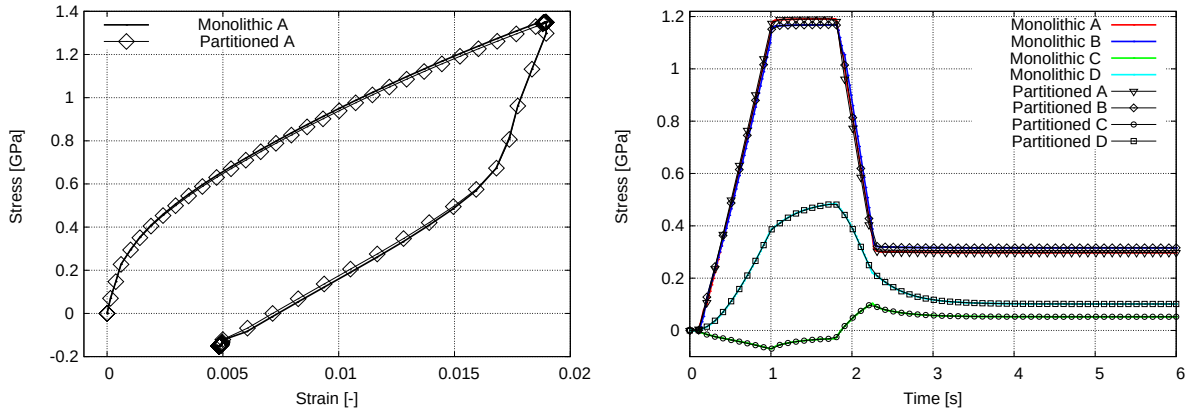

Figure 7.48: Rocket nozzle: stress-strain curve (mechanical stress $\boldsymbol{S}_{\mathsf{d};zz}$ over $\boldsymbol{E}_{zz}$) at point A (left) and normal stress $\boldsymbol{S}_{\mathsf{d};yy}$ over time (right) at points A-D at front surface ($z = 0$), using the coarse mesh A, the SIMO material for the copper, and the TSVK material for the nickel. Monolithic and partitioned schemes are applied.

stresses $S_{\mathsf{d};yy}$ [GPa] versus time for the monolithic and the partitioned algorithm, respectively,

for all four evaluation points. According to the previous results, where only elastic materials are employed, the highest stress values are reached at point A located at the hot gas side. Beyond, Figure 7.49 and Figure 7.50 show for $t = 6.0\ \mathrm{s}$ at the top and in the middle the thermal and the mechanical stress distribution in y-direction, respectively, of the three-dimensional body. Due to the temperature increase (see (5.74)), the thermal stresses are compression stresses which reach the highest values at the hot gas side. In contrast, very small temperature changes ΔT are computed (i.e. $\Delta T \approx 0$), thus leading to the smallest thermal stresses at the outer surface. Furthermore, the mechanical stresses are mainly tension stresses whose largest values are at the hot gas side. At the bottom of Figure 7.49 and Figure 7.50, the accumulated plastic strains

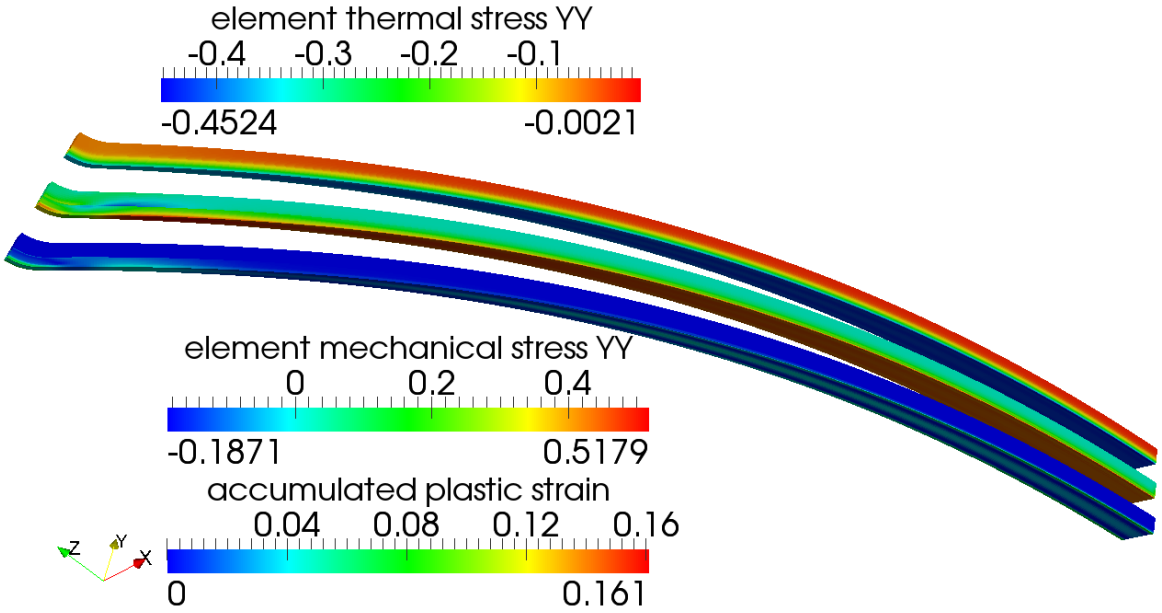

Figure 7.49: Rocket nozzle: normal thermal (top) and mechanical (middle) stresses, $\boldsymbol{S}_{\mathrm{dT};yy}$ and $\boldsymbol{S}_{\mathrm{d};yy}$ respectively, and accumulated plastic strain $\bar{\varepsilon}^p$ at $t = 6.0\ \mathrm{s}$ using the fine mesh C, the SIMO material for copper, and the TSVK material for nickel.

$\bar{\varepsilon}^p\ [-]$ are visualised as elementwise quantities for time $t = 6\ \mathrm{s}$. While the maximal plastic values are computed for the coarse mesh at the smallest cross section at the inner hot side at $z = 0$, the largest values for the fine mesh are computed at the bottom corners of the cooling channel at $z = 398.5\ \mathrm{mm}$. This is in accordance with the small strain thermo-elasto-plastic material, see e.g. Figure 7.41 (right) or Figure 7.42, and is caused by the fine spatial discretisation of mesh C which leads to singularities at these corners. The singularities are not physical and are not observable for the coarser mesh A, see the Figure 7.50 downright. This aspect is further illustrated in Figure 7.51 on the right, where the accumulated plastic strains are depicted for the fine mesh at the top and the coarse mesh at the bottom, respectively. While the corner elements at the bottom of the cooling channels, denoted as point Back E in Figure 7.42, experience the largest plastic deformations with $\bar{\varepsilon}^{p;\text{Back E;mesh C}} = 0.1610$, the corresponding values for the coarse mesh are $\bar{\varepsilon}^{p;\text{Back E;mesh A}} = 0.0273$ compared to the maximal values of $\bar{\varepsilon}^{p;\text{Front A;mesh A}} = 0.0569$ computed at point A at the front. Furthermore, Figure 7.51 shows on the left the final results of the accumulated plastic strains $\bar{\varepsilon}^p\ [-]$ at the end of the simulation for mesh A and C with focus on the distribution at the front. It is noted that the scale in Figure 7.51 corresponds to the one

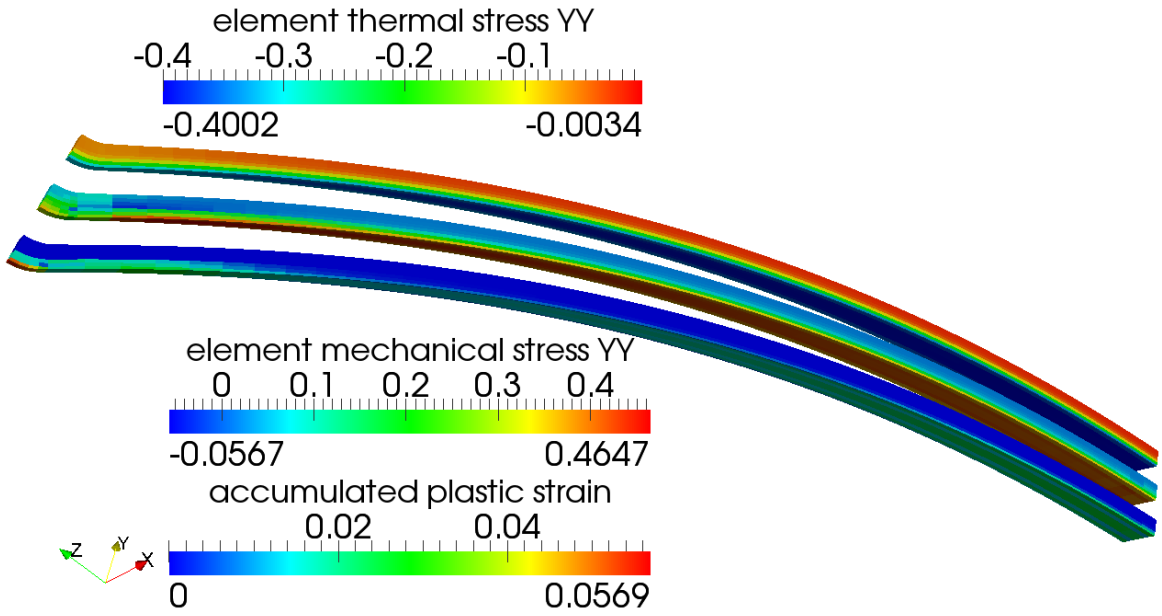

Figure 7.50: Rocket nozzle: thermal (top) and mechanical (middle) stresses, $\boldsymbol{S}_{\mathsf{dT};yy}$ and $\boldsymbol{S}_{\mathsf{d};yy}$, respectively, and accumulated plastic strain $\bar{\varepsilon}^p$ at $t = 6.0$ s using the coarse mesh A, the SIMO material for the copper, and the TSVK material for the nickel.

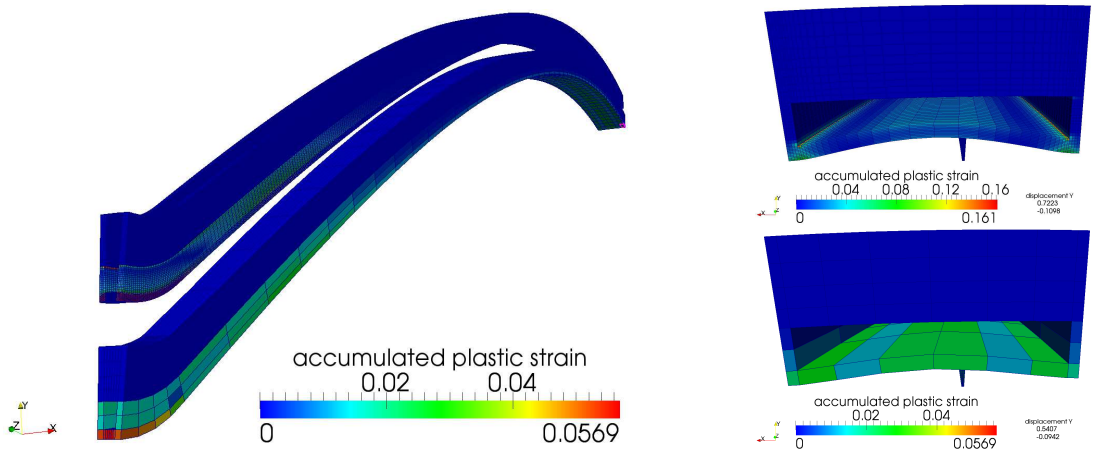

Figure 7.51: Rocket nozzle: accumulated plastic strains $\bar{\varepsilon}^p$ using the fine mesh C (top) and the coarse mesh A (bottom), front view (left) and back view (right), using SIMO material for copper and the TSVK material for the nickel at end time $t = 6$ s.

of the coarse mesh. While the maximum of the accumulated plastic strains is predicted in the middle of the hot gas side using the coarse mesh A, the distribution of the fine mesh is not so pronounced at this location.

It is worth noting, that the present geometrically nonlinear including large deformations is advisable. This can be emphasized by comparing the deformed final shape at time $t = 6$ s illustrated in Figure 7.41 (right) and Figure 7.51 (right) applying a geometrically linear and a nonlinear analysis, respectively. At the end of the simulation, for the linear, small deformation analysis, e.g. the maximal displacement in y-direction results to be $u_{y;\mathsf{max}}^{\mathsf{GeoLin}} = 1.6589$ mm compared to the corresponding values of the nonlinear analysis with $u_{y;\mathsf{max}}^{\mathsf{GeoNln;mesh\ C}} = 0.7223$ mm and $u_{y;\mathsf{max}}^{\mathsf{GeoNln;mesh\ A}} = 0.5407$ mm for the fine and coarse mesh, respectively. Since the remaining displacements are not negligible, the use of a geometrically nonlinear analysis including large deformations is more appropriate.

Finally, in accordance with Figure 7.43, the same measures are evaluated in Figure 7.52 for the finite strain SIMO Material to highlight the point of maximal plasticity. In particular, on the left side of Figure 7.52, the von Mises stresses over time, in the middle the accumulated plastic strains over time, and finally at the right side, the thermal hydrostatic pressure over time are depicted. As expected, the values of $\bar{\varepsilon}^p$ are the highest at point Back E and are more pronounced for

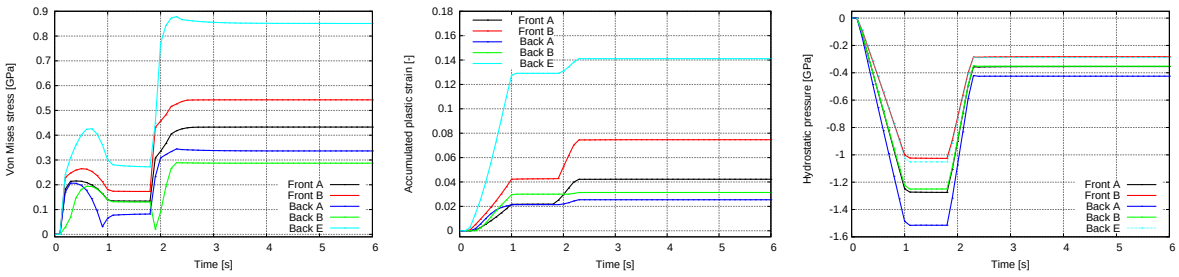

Figure 7.52: Rocket nozzle: von Mises second Piola-Kirchhoff stresses S_{vM} (left), accumulated plastic strains $\bar{\varepsilon}^p$ (middle), and thermal hydrostatic pressure p_{T} (right) over time for points A and B at the front and back surface, and point E at the back using a geometrically nonlinear analysis, the fine mesh C, the SIMO material for the liner, and the TSVK material for the nickel jacket.

the small strain material using a geometrically linear analysis compared to the present nonlinear setup. Furthermore, the influence of the simulation setup for the thermal hydrostatic pressures seems to be only marginal: the maximal values are computed for both at point Back E with $p_{\mathsf{T}}^{\mathsf{GeoLin}} = -1.5546$ GPa for the linear analysis compared to $p_{\mathsf{T}}^{\mathsf{GeoNln}} = -1.5155$ GPa of the nonlinear analysis.

In summary, a successful numerical simulation of a realistic fully three-dimensional rocket nozzle with combined mechanical and thermal loadings is presented. In particular, large deformation TSI with complex finite strain thermo-hyperelasto-plasticity is simulated within a challenging three-dimensional geometry which is discretised with more than two million degrees of freedom. In this context it is worth noting, that the creation of the geometry and subsequently of the mesh needs to be realised carefully, for instance to circumvent an overshooting of the thermal solution. Furthermore, the present geometry includes a rectangular cooling channel with angular corners. Thus, the angular corners in combination with the fine spatial discretisation and a

plastic material enhanced singularities in the solution. Exemplarily, as previously shown for the fine mesh and the plastic materials, e.g. in Figure 7.51, at the angular corners stress singularities arise, which in turn lead to unphysical peaks in the plastic solutions. Hence, instead of angular corners more smoother corners should be pursued to resolve the issues of the singularities.

For the sake of completeness, also simpler configurations for computing elastic and small strain thermo-elasto-plastic distributions with and without temperature-dependent material parameters are considered. Furthermore, two additional coarser meshes are utilised. Although even these simpler approaches perform well, the proposed finite strain thermo-hyperelasto-plastic material model with the fine mesh represents the most general approach. In particular, when a given realistic configuration is investigated for the first time, the more comprehensive model can be used to either justify the use of simpler models in subsequent numerical studies or to show that such simpler approaches are not applicable due to the importance of integrating irreversible processes into the model or due to the necessity of a fine spatial discretisation with large numbers of elements yielding realistic results and preventing overshooting of the solution. Finally, the present nozzle example is computed with the monolithic Newton-Krylov method with problem-dependent preconditioner as well as with different partitioned algorithms. It is emphasized that the partitioned algorithms can be used as an alternative to the monolithic algorithm. However, for a general TSI problem, the monolithic approach is the method of choice and its superiority is demonstrated in numerous configurations.

8 Summary and outlook

In this thesis, a comprehensive numerical model for the volume-coupled problem of thermo-structure interaction (TSI) has been developed. It is aimed at improving the understanding of the complex interactions and strong coupling effects in rocket nozzles in flight conditions. For this purpose, a general computational modelling approach to TSI has been realised, which includes all coupling terms and features the main aspects of a nonlinear thermomechanical solid simulation.

The present approach for coupled TSI problems has been exclusively based on the finite element method for both structural and thermal field, yielding two independent discretisations. While the structural field was already available in the in-house finite element solver BACI, the first step of the present work has introduced the thermal field into BACI, including various element formulations and time integration schemes. Subsequently, the coupled TSI problem has been established by a conforming equal-order finite element approach for both fields. Furthermore, with different time integration schemes available for structural and thermal field, respectively, a broad spectrum of stable, usually implicit schemes has been realised for the target TSI problem.

For modelling rocket nozzle structures, various isotropic, temperature-dependent, elastic as well as elastoplastic materials for small and finite strains, respectively, have been applied. With regard to irreversible deformations, for instance von Mises plasticity has been chosen. Furthermore, first steps towards including damage into the present computational model have been accomplished using Lemaitre's isothermal, small strain material model.

For solving a TSI problem, various partitioned and monolithic solution strategies have been proposed. On the one hand, different loosely and strongly coupled partitioned algorithms, some of them including acceleration techniques in form of, e.g. the Aitken Δ^2 method, have been implemented. On the other hand, a novel monolithic Newton-Krylov approach with a block Gauss-Seidel (BGS) preconditioner and an algebraic multigrid (AMG) method for approximating the tangent matrices $\mathbf{K}_{SS}$ and $\mathbf{K}_{TT}$ has been developed. This preconditioning strategy has been called BGS(AMG). It has been shown that both partitioned and monolithic algorithms enable solutions of TSI problems. However, for several problem configurations, monolithic schemes have exhibited improved robustness compared to partitioned schemes, enabling the computation of a broader spectrum of physical parameters. Furthermore, in contrast to partitioned schemes, monolithic schemes have turned out to be considerably faster. Hence, it has been demonstrated that the monolithic TSI algorithms are superior to strongly coupled partitioned schemes, even if acceleration techniques are utilised for the latter ones. This is in agreement to the preceding work of Gee et al. [47], where the coupled problem of fluid-structure interaction (FSI) was investigated using similar approaches. Moreover, the significant problems usually observed for partitioned algorithms, such as conditional stability of loosely coupled schemes and slow convergence of strongly coupled schemes, respectively, have been circumvented by utilising the proposed monolithic algorithm. Consequently, as a result of thorough comparison, the mono-

lithic Newton-Krylov approach with problem-specific preconditioner is the method of choice and has been shown to be superior for solving challenging TSI problems.

The model has been tested for six meaningful numerical examples, where the first examples have been considered for validating the different (temperature-dependent) elastoplastic material models for small and finite strains, respectively, possibly including ductile damage. Subsequently, for validation of the TSI algorithms, the proposed method has been applied to the second Danilovskaya problem. Finally, a fully three-dimensional rocket nozzle of a subscale thrust chamber has been computed. In this example, various aspects such as solution strategy, material modelling, time integration, high performance computing with large numbers of degrees of freedom have been combined in one complex simulation. It has been shown for all numerical examples that the numerical solutions for displacements and temperatures are in good agreement with results in the literature. Differences to other numerical studies have been discussed and attributed to, e.g. deviating modelling assumptions such as the computation of a two-dimensional problem in contrast to a fully three-dimensional analysis or alternative expressions for the coupling terms, such as the mechanical dissipation and the yield criterion.

Consequently, a broad spectrum of exemplary TSI applications have been investigated in this work, ranging from geometrically linear analysis with small strain thermoelastic materials to geometrically nonlinear analysis with finite strain thermo-hyperelasto-plastic materials. After all, it has been demonstrated that the proposed computational model is robust and provides accurate results. Among others, realistic three-dimensional problem configurations have been considered, illustrating that the method can be applied to complex geometries, which is essential for simulating real-world rocket configurations.

In summary, a comprehensive and validated computational model for truly general thermomechanical solid problems has been successfully established. Nevertheless, there is still room for improvements with regard to several aspects, which were only marginally covered in this thesis or not addressed at all. Hence, selected concepts for improving the individual building blocks, such as the overall TSI solution strategy or the material formulation and its efficient local solution will be briefly addressed in the following.

With regard to the monolithic TSI algorithm, the overall monolithic Newton-Krylov method can be notably accelerated by improving the preconditioners. For instance in Gee et al. [47], an alternative preconditioning approach, named AMG(BGS), was proposed for FSI problems. In this approach, within one single algebraic multigrid V-cycle, independent Gauss-Seidel iterations on each grid level were used. For FSI, this preconditioner was shown to further improve the field coupling compared to the alternative BGS(AMG) approach in many cases. Thus, in addition to the utilised BGS(AMG) approach, a similar AMG(BGS) approach may also be developed for the TSI problem discussed in this work and investigated in the future. Apart from improving the preconditioners of the monolithic TSI algorithm, in Gee et al. [46], the pseudo-transient continuation (ψTC) strategy has been developed for structural dynamics and has shown to enable a more robust solution compared to standard exact Newton methods. Consequently, the exact Newton method of the monolithic TSI approach may be replaced by a ψTC strategy such that, e.g. larger time steps may be applied.

Further potential improvements concern, in particular, TSI problems including irreversible, plastic deformations. Irreversible deformations imply the solution of the plasticity at each Gauss point. In the present work, plasticity is solved using an elastic predictor/plastic corrector scheme. However, as proposed in Seitz et al. [116] for isothermal finite strain plasticity, an alternative,

more efficient strategy using a semi-smooth Newton method combined with global nonlinear complementary (NCP) functions enables superior, more robust behaviour over classical return-mapping algorithms. Hence, the overall TSI simulation may be accelerated by replacing the classical return-mapping at each Gauss point with such a semi-smooth Newton method with NCP functions. Furthermore, in the context of thermoplasticity, additional improvements can be realised with respect to the finite element technology utilised to circumvent volumetric locking. For instance according to Simo and Miehe [122], element technology may be considered in both fields. Hence, for example the F-bar method may be extended to the (mechanical) coupling terms in the thermal equation. Since locking is caused by parasitic stresses, which are derived from the constitutive law, the coupling terms, which also follow from the constitutive law, may be treated in a more consistent way.

Besides improvements of the solution of plasticity, future work may be concerned with other extensions of the material formulations. For instance Lemaitre's material model for isothermal, ductile damage may be enhanced. Exemplarily, following the material model of Schwarz et al. [114], which is aimed at predicting the dog-house failure in rocket nozzles, Lemaitre's material model may be extended to temperature-dependent, anisotropic damage, including mixed isotropic and kinematic hardening as well as the so-called crack-closure effect. The crack-closure effect takes into account the closure of microcracks under compression loadings by separating the effective stresses in tensile and compression parts. Furthermore, anisotropic damage is described by a second-order damage tensor $\boldsymbol{D}$ instead of the scalar-valued damage variable D utilised in this work. In addition, for the sake of universal validity, the damage material model may be extended to finite strains, see e.g. Tini et al. [132] and Vladimirov et al. [139].

So far, a so-called matching grid approach has been utilised for the present TSI model. However, since the TSI model has been based on separate discretisations for both fields, the extension to non-matching grids represents another potential future step. Due to a manifold of reasons, e.g. different resolution requirements in the different physical fields, non-conforming or non-matching grids would be advantageous. In Klöppel et al. [67], non-matching interface grids were realised for the surface-coupled problem of FSI by applying a dual mortar method. Non-matching grids for the volume-coupled TSI problem might also be based on mortar methods, which is already part of current research at the Institute of Computational Mechanics. It is expected that non-conforming grids will substantially increase the flexibility and the efficiency of the coupled TSI solution.

Furthermore, first steps towards integrating thermomechanical aspects into the problem of nonlinear contact dynamics, such as wear, were already realised in Gitterle [49] by combining the present model with a mortar method for contact dynamics. Further work in this context will broaden the applicability of the present TSI model towards additional multiphysics problems. Finally, for a comprehensive study of the target system of a rocket nozzle in real flight conditions, the influence of the fluid field is of course not negligible. Hence, the present TSI approach is currently combined with a fluid solver to enable the simulation of thermo-fluid-structure interaction (TFSI) problems. First steps towards TFSI were already presented in Hammerl et al. [53] and Grilli et al. [52], where the present TSI model was combined with a compressible flow solver within a loosely coupled scheme.

A Material parameters and units

SI units

Length	metre	$[\,\mathrm{m}]$
Mass	kilogram	$[\,\mathrm{kg}]$
Time	second	$[\,\mathrm{s}]$
Temperature	kelvin	$[\,\mathrm{K}]$

Derived units

Bar	$[\,\mathrm{bar}]$	$[100\ \mathrm{kPa} = 10^5\ \frac{\mathrm{kg}}{\mathrm{m\,s^2}}]$
Joule	$[\,\mathrm{J}]$	$[\,\mathrm{N\,m} = \frac{\mathrm{m^2\,kg}}{\mathrm{s^2}}]$
Newton	$[\,\mathrm{N}]$	$[\frac{\mathrm{m\,kg}}{\mathrm{s^2}}]$
Pascal	$[\,\mathrm{Pa}]$	$[\frac{\mathrm{N}}{\mathrm{m^2}} = \frac{\mathrm{kg}}{\mathrm{m\,s^2}}]$
Watt	$[\,\mathrm{W}]$	$[\frac{\mathrm{J}}{\mathrm{K}}]$

Material parameters and their units

Density	ρ	$[\frac{\mathrm{kg}}{\mathrm{m^3}}]$
Force	$\boldsymbol{f}$	$[\,\mathrm{N} = \frac{\mathrm{m\,kg}}{\mathrm{s^2}}]$
Power	$\mathcal{P}$	$[\,\mathrm{W} = \frac{\mathrm{J}}{\mathrm{s}} = \frac{\mathrm{m^2\,kg}}{\mathrm{s^3}}]$
Energy	ψ, e, ζ, ξ	$[\,\mathrm{J} = \mathrm{Nm} = \frac{\mathrm{m^2\,kg}}{\mathrm{s^2}}]$
Entropy	η	$[\frac{\mathrm{J}}{\mathrm{K}} = \frac{\mathrm{m^2\,kg}}{\mathrm{s^2\,K}}]$
Stress	$\boldsymbol{\sigma}$	$[\,\mathrm{Pa} = \frac{\mathrm{N}}{\mathrm{m^2}} = \frac{\mathrm{kg}}{\mathrm{m\,s^2}}]$
Work	$\mathcal{W}$	$[\,\mathrm{J} = \mathrm{Nm} = \frac{\mathrm{m^2\,kg}}{\mathrm{s^2}}]$
Coefficient of thermal expansion	α_{T}	$[\frac{1}{\mathrm{K}}]$
Heat capacity	C_{V}	$[\frac{\mathrm{J}}{\mathrm{kg\,K}} = \frac{\mathrm{m^2}}{\mathrm{s^2\,K}}]$
Heat flux	$\boldsymbol{q}$	$[\frac{\mathrm{W}}{\mathrm{m^2}} = \frac{\mathrm{kg}}{\mathrm{s^3}}]$
Heat transfer coefficient	h	$[\frac{\mathrm{W}}{\mathrm{m^2\,K}} = \frac{\mathrm{kg}}{\mathrm{s^3\,K}}]$
Kinematic heat transfer coefficient	$\bar{h} = \frac{h}{\rho\, C_{\mathsf{V}}}$	$[\frac{\mathrm{m}}{\mathrm{s}}]$
Stress-temperature modulus	m_0	$[\frac{\mathrm{N}}{\mathrm{m^2\,K}} = \frac{\mathrm{kg}}{\mathrm{m^2\,K\,s^2}}]$
Thermal conductivity	k	$[\frac{\mathrm{W}}{\mathrm{m\,K}} = \frac{\mathrm{m\,kg}}{\mathrm{s^3\,K}}]$
Thermal diffusivity	$\bar{\kappa} = \frac{k}{\rho \mathrm{C_V}}$	$[\frac{\mathrm{m^2}}{\mathrm{s}}]$

B Tensor calculus

B.1 Basic laws

Scalar products of tensors

$$\begin{aligned} \boldsymbol{A} : \boldsymbol{B} &= \boldsymbol{B} : \boldsymbol{A} && \text{commutative law} \\ \boldsymbol{A} : (\boldsymbol{B} + \boldsymbol{C}) &= \boldsymbol{A} : \boldsymbol{B} + \boldsymbol{A} : \boldsymbol{C} && \text{distributive law} \\ (\alpha\, \boldsymbol{A}) : \boldsymbol{B} &= \boldsymbol{A} : (\alpha\, \boldsymbol{B}) = \alpha\, (\boldsymbol{A} : \boldsymbol{B}) && \text{associative law} \\ \boldsymbol{A} : (\boldsymbol{B} \cdot \boldsymbol{C}) &= (\boldsymbol{B}^{\mathsf{T}} \cdot \boldsymbol{A}) : \boldsymbol{C} = (\boldsymbol{A} \cdot \boldsymbol{C}^{\mathsf{T}}) : \boldsymbol{B} \end{aligned} \tag{B.1}$$

Symmetric tensors

$$\begin{aligned} \boldsymbol{A} &= \boldsymbol{A}^{\mathsf{T}} \\ \boldsymbol{A} &= \frac{1}{2}(\boldsymbol{A} + \boldsymbol{A}^{\mathsf{T}}) \end{aligned} \tag{B.2}$$

Transposed tensors

$$\begin{aligned} (\boldsymbol{A}^{\mathsf{T}})^{\mathsf{T}} &= \boldsymbol{A} \\ (\boldsymbol{A} + \boldsymbol{B})^{\mathsf{T}} &= \boldsymbol{A}^{\mathsf{T}} + \boldsymbol{B}^{\mathsf{T}} \\ (\boldsymbol{A} \cdot \boldsymbol{B})^{\mathsf{T}} &= \boldsymbol{B}^{\mathsf{T}} \cdot \boldsymbol{A}^{\mathsf{T}} \\ (\boldsymbol{A} \cdot \boldsymbol{B}) : \boldsymbol{I} &= \boldsymbol{B} : \boldsymbol{A}^{\mathsf{T}} = \boldsymbol{B}^{\mathsf{T}} : \boldsymbol{A} \end{aligned} \tag{B.3}$$

Inverse tensor

$$\begin{aligned} \boldsymbol{A} \cdot \boldsymbol{A}^{-1} &= \boldsymbol{A}^{-1} \cdot \boldsymbol{A} = \boldsymbol{I} \\ (\boldsymbol{A}^{-1})^{\mathsf{T}} &= (\boldsymbol{A}^{\mathsf{T}})^{-1} =: \boldsymbol{A}^{-\mathsf{T}} \\ (\boldsymbol{A} \cdot \boldsymbol{B})^{-1} &= \boldsymbol{B}^{-1} \cdot \boldsymbol{A}^{-1} \end{aligned} \tag{B.4}$$

B.2 Voigt or matrix notation

Physical quantities are often described by higher-order symmetric tensors. In this context, the Voigt or matrix notation enables an alternative and simplified way to write these tensors. Given

is a symmetric second-order matrix $\boldsymbol{A}$ (B.2). Using the matrix notation, the tensor $\boldsymbol{A}$ can be converted to a one-dimensional vector according to

$$\boldsymbol{A} = \begin{bmatrix} A_{11} & A_{12} & A_{13} \\ A_{21} & A_{22} & A_{23} \\ A_{31} & A_{32} & A_{33} \end{bmatrix} = \begin{bmatrix} A_1 & A_4 & A_6 \\ \cdot & A_2 & A_5 \\ \cdot & \cdot & A_3 \end{bmatrix} = \begin{bmatrix} A_1 \\ A_2 \\ A_3 \\ A_4 \\ A_5 \\ A_6 \end{bmatrix}, \tag{B.5}$$

where the order in the vector is a matter of convention. Consequently, the Voigt or matrix notation enables to represent a symmetric second-order tensor as a six-component vector.

In case the Voigt notation is utilised for the symmetric second-order tensors stress or strain, as e.g. the Cauchy stress tensor $\boldsymbol{\sigma}$ and the corresponding Euler-Almansi strain tensor $\boldsymbol{E}_{\mathsf{EA}}$, some special conventions need to be taken into account. First, the Cauchy stress tensor reads

$$\boldsymbol{\sigma} = \begin{bmatrix} \sigma_{11} & \sigma_{12} & \sigma_{13} \\ \sigma_{21} & \sigma_{22} & \sigma_{23} \\ \sigma_{31} & \sigma_{32} & \sigma_{33} \end{bmatrix} = \begin{bmatrix} \sigma_1 & \sigma_4 & \sigma_6 \\ \cdot & \sigma_2 & \sigma_5 \\ \cdot & \cdot & \sigma_3 \end{bmatrix} = \begin{bmatrix} \sigma_1 \\ \sigma_2 \\ \sigma_3 \\ \sigma_4 \\ \sigma_5 \\ \sigma_6 \end{bmatrix}. \tag{B.6}$$

Subsequently, a scaling factor has to be introduced when converting the strain tensor $\boldsymbol{E}_{\mathsf{EA}}$ into Voigt notation. The shear components of the strain tensor, i.e. the off-diagonal components of the tensor, are converted such that they correspond to the engineering shear strains. Hence,

$$\begin{aligned} \boldsymbol{E}_{\mathsf{EA}} &= \begin{bmatrix} E_{\mathsf{EA};11} & E_{\mathsf{EA};12} & E_{\mathsf{EA};13} \\ E_{\mathsf{EA};21} & E_{\mathsf{EA};22} & E_{\mathsf{EA};23} \\ E_{\mathsf{EA};31} & E_{\mathsf{EA};32} & E_{\mathsf{EA};33} \end{bmatrix} = \begin{bmatrix} E_{\mathsf{EA};11} & \frac{1}{2}\gamma_{12} & \frac{1}{2}\gamma_{13} \\ \frac{1}{2}\gamma_{21} & E_{\mathsf{EA};22} & \frac{1}{2}\gamma_{23} \\ \frac{1}{2}\gamma_{31} & \frac{1}{2}\gamma_{32} & E_{\mathsf{EA};33} \end{bmatrix} \\ &= \begin{bmatrix} E_{\mathsf{EA};1} & 2\,E_{\mathsf{EA};4} & 2\,E_{\mathsf{EA};6} \\ \cdot & E_{\mathsf{EA};2} & 2\,E_{\mathsf{EA};5} \\ \cdot & \cdot & E_{\mathsf{EA};3} \end{bmatrix}, \end{aligned} \tag{B.7}$$

where $\frac{1}{2}\gamma_{12} = E_{\mathsf{EA};12}$, $\frac{1}{2}\gamma_{23} = E_{\mathsf{EA};23}$, $\frac{1}{2}\gamma_{13} = E_{\mathsf{EA};13}$ are the engineering shear strains. Subsequent conversion to the vector notation yields

$$\boldsymbol{E}_{\mathsf{EA}} = \begin{bmatrix} E_{\mathsf{EA};11} \\ E_{\mathsf{EA};22} \\ E_{\mathsf{EA};33} \\ E_{\mathsf{EA};12} + E_{\mathsf{EA};21} \\ E_{\mathsf{EA};23} + E_{\mathsf{EA};32} \\ E_{\mathsf{EA};13} + E_{\mathsf{EA};31} \end{bmatrix} = \begin{bmatrix} E_{\mathsf{EA};11} \\ E_{\mathsf{EA};22} \\ E_{\mathsf{EA};33} \\ 2\,E_{\mathsf{EA};12} \\ 2\,E_{\mathsf{EA};23} \\ 2\,E_{\mathsf{EA};13} \end{bmatrix} = \begin{bmatrix} E_{\mathsf{EA};1} \\ E_{\mathsf{EA};2} \\ E_{\mathsf{EA};3} \\ 2\,E_{\mathsf{EA};4} \\ 2\,E_{\mathsf{EA};5} \\ 2\,E_{\mathsf{EA};6} \end{bmatrix}. \tag{B.8}$$

The benefit of using different representations for stress and strain in matrix notation is the scalar invariance

$$\boldsymbol{\sigma} \cdot \boldsymbol{E}_{\mathsf{EA}} = \sigma_{ij}\, E_{\mathsf{EA};\mathsf{ij}} = \sigma_i E_{\mathsf{EA};i}\,. \tag{B.9}$$

The additional factor 2 of the last three components of the strain matrix enables that the scalar product of stress and strain is identical to the inner tensor product of the stress and strain tensor. This relation is only valid for the scalar product of stress and strain, but not for scalar products in general.

The elasticity law $\sigma_{ij} = \mathscr{C}_{ijkl} : E_{\mathsf{EA};kl}$ is written in tensor notation by

$$\boldsymbol{\sigma} = \boldsymbol{\mathscr{C}} : \boldsymbol{E}_{\mathsf{EA}} \tag{B.10}$$

and equivalently follows using the matrix notation by

$$\boldsymbol{\sigma} = \boldsymbol{\mathscr{C}}\, \boldsymbol{E}_{\mathsf{EA}} \tag{B.11}$$

which requires conversion of the fourth-order tensor $\boldsymbol{\mathscr{C}}$ into a (6×6)-matrix, so that

$$\boldsymbol{\mathscr{C}} = \begin{bmatrix} \mathscr{C}_{11} & \mathscr{C}_{12} & \mathscr{C}_{13} & \mathscr{C}_{14} & \mathscr{C}_{15} & \mathscr{C}_{16} \\ & \mathscr{C}_{22} & \mathscr{C}_{23} & \mathscr{C}_{24} & \mathscr{C}_{25} & \mathscr{C}_{26} \\ & & \mathscr{C}_{33} & \mathscr{C}_{34} & \mathscr{C}_{35} & \mathscr{C}_{36} \\ & & & \mathscr{C}_{44} & \mathscr{C}_{45} & \mathscr{C}_{46} \\ & \text{sym.} & & & \mathscr{C}_{55} & \mathscr{C}_{56} \\ & & & & & \mathscr{C}_{66} \end{bmatrix} \tag{B.12}$$

leading to the elasticity constitutive equation in matrix notation

$$\begin{bmatrix} \sigma_{11} \\ \sigma_{22} \\ \sigma_{33} \\ \sigma_{23} \\ \sigma_{13} \\ \sigma_{12} \end{bmatrix} = \begin{bmatrix} \mathscr{C}_{11} & \mathscr{C}_{12} & \mathscr{C}_{13} & \mathscr{C}_{14} & \mathscr{C}_{15} & \mathscr{C}_{16} \\ \mathscr{C}_{21} & \mathscr{C}_{22} & \mathscr{C}_{23} & \mathscr{C}_{24} & \mathscr{C}_{25} & \mathscr{C}_{26} \\ \mathscr{C}_{31} & \mathscr{C}_{32} & \mathscr{C}_{33} & \mathscr{C}_{34} & \mathscr{C}_{35} & \mathscr{C}_{36} \\ \mathscr{C}_{41} & \mathscr{C}_{42} & \mathscr{C}_{43} & \mathscr{C}_{44} & \mathscr{C}_{45} & \mathscr{C}_{46} \\ \mathscr{C}_{51} & \mathscr{C}_{52} & \mathscr{C}_{53} & \mathscr{C}_{54} & \mathscr{C}_{55} & \mathscr{C}_{56} \\ \mathscr{C}_{61} & \mathscr{C}_{62} & \mathscr{C}_{63} & \mathscr{C}_{64} & \mathscr{C}_{65} & \mathscr{C}_{66} \end{bmatrix} \begin{bmatrix} E_{\mathsf{EA};11} \\ E_{\mathsf{EA};22} \\ E_{\mathsf{EA};33} \\ 2\,E_{\mathsf{EA};12} \\ 2\,E_{\mathsf{EA};23} \\ 2\,E_{\mathsf{EA};13} \end{bmatrix} . \tag{B.13}$$

In order to preserve the product relation of tensors, the components $\mathscr{C}_{pg}$ of the matrix are related to the components of the tensor $\boldsymbol{\mathscr{C}}$ (i.e. $\mathscr{C}_{ijkl}$) through an appropriate mapping. For instance the two components $\mathscr{C}_{11}$ or $\mathscr{C}_{14}$ of the matrix are related to the corresponding tensor entries by

$$\mathscr{C}_{11} = \mathscr{C}_{1111}\,, \quad \text{or } 2\,\mathscr{C}_{14} = \mathscr{C}_{1112} + \mathscr{C}_{1121}\,. \tag{B.14}$$

Including these relations, exemplarily the stress component σ_{11} yields

$$\begin{aligned} \sigma_{11} &= \underbrace{\mathscr{C}_{1111}}_{\mathscr{C}_{11}} E_{\mathsf{EA};11} + \underbrace{\mathscr{C}_{1122}}_{\mathscr{C}_{12}} E_{\mathsf{EA};22} + \underbrace{\mathscr{C}_{1133}}_{\mathscr{C}_{13}} E_{\mathsf{EA};33} + \\ &\quad + \underbrace{\mathscr{C}_{1112}\, E_{\mathsf{EA};12} + \mathscr{C}_{1121}\, E_{\mathsf{EA};21}}_{\mathscr{C}_{14}\, 2\, E_{\mathsf{EA};12}} + \\ &\quad + \underbrace{\mathscr{C}_{1123}\, E_{\mathsf{EA};23} + \mathscr{C}_{1132}\, E_{\mathsf{EA};32}}_{\mathscr{C}_{15}\, 2\, E_{\mathsf{EA};23}} + \underbrace{\mathscr{C}_{1113}\, E_{\mathsf{EA};13} + \mathscr{C}_{1131}\, E_{\mathsf{EA};31}}_{\mathscr{C}_{16}\, 2\, E_{\mathsf{EA};13}} \\ &= \mathscr{C}_{11}\, E_{\mathsf{EA};11} + \mathscr{C}_{12}\, E_{\mathsf{EA};22} + \mathscr{C}_{13}\, E_{\mathsf{EA};33} + \\ &\quad + \mathscr{C}_{14}\, 2\, E_{\mathsf{EA};12} + \mathscr{C}_{15}\, 2\, E_{\mathsf{EA};23} + \mathscr{C}_{16}\, 2\, E_{\mathsf{EA};13} \end{aligned} \tag{B.15}$$

The above relations are utilised in the implementation in BACI in the context of constitutive material modelling for stress, strain, and the material tangent $\boldsymbol{\mathscr{C}} = \boldsymbol{\mathscr{C}}_{\mathsf{mat}}$.

B.3 Transformations

In the following, transformations of stress- and strain-like tensors, as e.g. the symmetric, second-order stress tensors Cauchy stress $\boldsymbol{\sigma}$ and Euler-Almansi strain tensor $\boldsymbol{E}_{\mathsf{EA}}$, as well as special identity tensors are summarized. Furthermore, some special tensor products applied within the calculation of the material tangent $\mathscr{C}_{\mathsf{mat}}$ are given.

Split of a tensor in deviatoric and volumetric parts

A second-order tensor $\boldsymbol{\sigma}$ can be split in its deviatoric part $\operatorname{dev}\boldsymbol{\sigma}$ and volumetric part $\boldsymbol{\sigma}_v$ by

$$\boldsymbol{\sigma} = \operatorname{dev}\boldsymbol{\sigma} + \boldsymbol{\sigma}_v = \operatorname{dev}\boldsymbol{\sigma} + \frac{1}{3}(\operatorname{tr}\boldsymbol{\sigma})\,\boldsymbol{I}\,, \tag{B.16}$$

$$\operatorname{tr}(\operatorname{dev}\boldsymbol{\sigma}) = 0\,, \tag{B.17}$$

where the latter represents the characteristic condition of deviatoric tensors $\operatorname{dev}\boldsymbol{\sigma}$.

Equivalent von Mises stress

The equivalent von Mises stress of a stress tensor $\boldsymbol{\sigma}$ is a common scalar-valued measure in engineering applications which is defined, e.g. in (3.97). Additionally, various alternative forms of the equivalent von Mises stress are available, as for instance

$$\begin{aligned}\sigma_{\mathsf{vM}} &= q \\ &= \sqrt{\sigma_{xx}^2 + \sigma_{yy}^2 + \sigma_{zz}^2 - \sigma_{xx}\,\sigma_{yy} - \sigma_{xx}\,\sigma_{zz} - \sigma_{xx}\,\sigma_{zz} - \sigma_{yy}\,\sigma_{zz} + 3\,(\tau_{xy}^2 + \tau_{xz}^2 + \tau_{yz})}\,.\end{aligned} \tag{B.18}$$

Invariants of a second-order tensor

In the following, the invariants of a second-order tensor, as e.g. the stresses $\boldsymbol{\sigma}$ are calculated by

$$I_1 = \operatorname{tr}\boldsymbol{\sigma} = \boldsymbol{\sigma}_{11} + \boldsymbol{\sigma}_{22} + \boldsymbol{\sigma}_{33} = \sigma_{kk}\,, \tag{B.19}$$

$$I_2 = \frac{1}{2}\left[(\operatorname{tr}\boldsymbol{\sigma})^2 - \operatorname{tr}(\boldsymbol{\sigma}\cdot\boldsymbol{\sigma})\right] = \frac{1}{2}\left[I_1^2 - (\boldsymbol{\sigma}\cdot\boldsymbol{\sigma}) : \boldsymbol{I}\right] = \frac{1}{2}\left(\sigma_{ii}\,\sigma_{jj} - \sigma_{ij}\,\sigma_{ji}\right), \tag{B.20}$$

$$I_3 = \det\boldsymbol{\sigma} = \frac{1}{3}\,\sigma_{ij}\,\sigma_{jk}\,\sigma_{ki}\,. \tag{B.21}$$

Based on (B.16), the invariants of the stress deviator $\boldsymbol{s} = \operatorname{dev}\boldsymbol{\sigma}$ are summarized

$$J_1 = \operatorname{tr}\boldsymbol{s} = \boldsymbol{s}_{11} + \boldsymbol{s}_{22} + \boldsymbol{s}_{33} = s_{kk} = 0\,, \tag{B.22}$$

$$J_2 = \frac{1}{2}\left[(\operatorname{tr}\boldsymbol{s})^2 - \operatorname{tr}(\boldsymbol{s}\cdot\boldsymbol{s})\right] = \frac{1}{2}\,\boldsymbol{s} : \boldsymbol{s} = \frac{1}{2}\,s_{ij}\,s_{ji}\,, \tag{B.23}$$

$$J_3 = \det s_{ij} = \frac{1}{3}\,s_{ij}\,s_{jk}\,s_{ki}\,. \tag{B.24}$$

The stress deviator (2.49) is utilised in particular within the plastic material modelling, see e.g. section 3.4.2.

Mappings using an isotropic fourth-order tensors

In continuum mechanics, a symmetric isotropic fourth-order tensor $\boldsymbol{\mathcal{I}}_\sigma$ is frequently used, which is defined as

$$\boldsymbol{\mathcal{I}}_\sigma = \frac{1}{2}\left(\boldsymbol{\mathcal{I}} + \boldsymbol{\mathcal{I}}^{\mathsf{T}}\right) \quad \rightarrow (\boldsymbol{\mathcal{I}}_\sigma)_{ijkl} = \frac{1}{2}\left(\delta_{ik}\,\delta_{jl} + \delta_{il}\,\delta_{jk}\right). \tag{B.25}$$

This tensor maps any second-order tensor (here $\boldsymbol{\sigma}$) into its symmetric part, according to

$$\boldsymbol{\mathcal{I}}_\sigma : \boldsymbol{\sigma} = \boldsymbol{\sigma} : \boldsymbol{\mathcal{I}}_\sigma = \operatorname{sym}(\boldsymbol{\sigma}). \tag{B.26}$$

i.e. the tensor remains unchanged due to the mapping. Furthermore, the deviatoric projection tensor $\boldsymbol{\mathcal{I}}_d$ follows as

$$\boldsymbol{\mathcal{I}}_d \equiv \boldsymbol{\mathcal{I}}_\sigma - \frac{1}{3}\boldsymbol{I}\otimes\boldsymbol{I}, \tag{B.27}$$

which projects a second-order symmetric tensor (like the stress tensor $\boldsymbol{\sigma}$) into the deviatoric subspace, i.e. into the space of traceless tensors:

$$\boldsymbol{\mathcal{I}}_d : \boldsymbol{\sigma} = \operatorname{dev}\boldsymbol{\sigma}. \tag{B.28}$$

In the following, the fourth-order identity-tensors are summarized in matrix notation (cf. section B.2) by

$$\boldsymbol{\mathcal{I}}_\sigma = \left[\begin{array}{ccc:ccc} 1 & 0 & 0 & 0 & 0 & 0 \\ & 1 & 0 & 0 & 0 & 0 \\ & & 1 & 0 & 0 & 0 \\ \hdashline & & & 1 & 0 & 0 \\ & & & & 1 & 0 \\ & & & & & 1 \end{array}\right], \tag{B.29}$$

$$\boldsymbol{\mathcal{I}}_\sigma^{\sharp} = \left[\begin{array}{ccc:ccc} 1 & 0 & 0 & 0 & 0 & 0 \\ & 1 & 0 & 0 & 0 & 0 \\ & & 1 & 0 & 0 & 0 \\ \hdashline & & & 0.5 & 0 & 0 \\ & & & & 0.5 & 0 \\ & & & & & 0.5 \end{array}\right], \tag{B.30}$$

$$\boldsymbol{I}\otimes\boldsymbol{I} = \left[\begin{array}{ccc:ccc} 1 & 1 & 1 & 0 & 0 & 0 \\ & 1 & 1 & 0 & 0 & 0 \\ & & 1 & 0 & 0 & 0 \\ \hdashline & & & 0 & 0 & 0 \\ & & & & 0 & 0 \\ & & & & & 0 \end{array}\right], \tag{B.31}$$

$$\boldsymbol{\mathcal{I}}_d = \boldsymbol{\mathcal{I}}_\sigma - \frac{1}{3}(\boldsymbol{I}\otimes\boldsymbol{I}) = \left[\begin{array}{ccc:ccc} \frac{2}{3} & -\frac{1}{3} & -\frac{1}{3} & 0 & 0 & 0 \\ & \frac{2}{3} & -\frac{1}{3} & 0 & 0 & 0 \\ & & \frac{2}{3} & 0 & 0 & 0 \\ \hdashline & & & 1 & 0 & 0 \\ & & & & 1 & 0 \\ & & & & & 1 \end{array}\right]. \tag{B.32}$$

Hereby, the fourth-order tensor $\mathscr{I}_{\sigma}^{\sharp}$ (B.30) is utilised, e.g. within the material call to compute the material tangent in connection with the Voigt notation. As previously mentioned in section B.2, the material tangent $\mathscr{C}_{\mathsf{mat}}$ is applied to a strain tensor, as e.g. the Euler-Almansi strain tensor $\boldsymbol{E}_{\mathsf{EA}}$. Utilising the Voigt notation, the tensors are transformed to matrices, i.e. the fourth-order material tangent tensor is transformed to a matrix of dimension 6×6 and the strain tensor to a vector of dimension 6×1. Furthermore, to correctly describe the strain state, the shear strains are scaled with a factor 2, see (B.8). Accordingly, to compute the stresses correctly, the identity matrix $\mathscr{I}_{\sigma}^{\sharp}$ (B.30) is employed instead of identity matrix $\mathscr{I}_{\sigma}$ (B.29). Otherwise, the shear stresses would be the double of the actual result.

Special tensor products

According to Holzapfel [58], two special tensor products can be distinguished. By assuming a tensor, for instance the symmetric second-order right Cauchy-Green deformation tensor $\boldsymbol{C}$, to be invertible and smooth, the tensor products follow as

$$-(\boldsymbol{C}^{-1} \odot \boldsymbol{C}^{-1})_{ijkl} = -\frac{1}{2}\left(C_{ik}^{-1}\, C_{lj}^{-1} + C_{il}^{-1}\, C_{kl}^{-1}\right) = \frac{\partial C_{ij}^{-1}}{\partial C_{kl}}\,, \tag{B.33}$$

$$(\boldsymbol{C} \otimes \boldsymbol{C})_{ijkl} = (\boldsymbol{C}_{ij}\, \boldsymbol{C}_{kl})\,. \tag{B.34}$$

C Differentiation

C.1 Basics

Based on section 2.1, useful relations in the context of linearisations will be summarized in this appendix. Herein, the initial position $\boldsymbol{X}$ (2.1), the displacements $\boldsymbol{u}$ (2.2), and the deformation gradient $\boldsymbol{F}$ (2.3) will be utilised. Moreover, in the context of line elements (2.5) of reference and current configuration, $\mathrm{d}\boldsymbol{X}$ and $\mathrm{d}\boldsymbol{x}$, respectively, will be used.

Kinematic relations of the deformation gradient

$$\begin{aligned} \boldsymbol{F} &= \frac{\mathrm{d}\boldsymbol{x}}{\mathrm{d}\boldsymbol{X}} = \operatorname{Grad}\boldsymbol{X} + \boldsymbol{u} = \boldsymbol{I} + \operatorname{Grad}\boldsymbol{u} \\ \boldsymbol{F}^{-1} &= \frac{\mathrm{d}\boldsymbol{X}}{\mathrm{d}\boldsymbol{x}} = \operatorname{grad}\boldsymbol{x} - \boldsymbol{u} = \boldsymbol{I} - \operatorname{grad}\boldsymbol{u} \\ \boldsymbol{F}^{-1} &= \frac{\partial \boldsymbol{X}}{\partial \boldsymbol{x}} = \frac{\partial \boldsymbol{X}}{\partial \boldsymbol{x}} \left(\frac{\partial \boldsymbol{x}}{\partial \boldsymbol{X}} \frac{\partial \boldsymbol{X}}{\partial \boldsymbol{x}} \right) = \boldsymbol{F}^{-1} \cdot \boldsymbol{F} \cdot \boldsymbol{F}^{-1} \end{aligned} \tag{C.1}$$

Mappings

$$\begin{aligned} \operatorname{Grad}\boldsymbol{u} &= \operatorname{grad}\boldsymbol{u} \cdot \boldsymbol{F} \\ \operatorname{Grad}^{\mathsf{T}}\boldsymbol{u} &= \boldsymbol{F}^{\mathsf{T}} \cdot \operatorname{grad}^{\mathsf{T}}\boldsymbol{u} \\ \operatorname{grad}\boldsymbol{u} &= \operatorname{Grad}\boldsymbol{u} \cdot \boldsymbol{F}^{-1} \\ \operatorname{grad}^{\mathsf{T}}\boldsymbol{u} &= (\operatorname{Grad}\boldsymbol{u} \cdot \boldsymbol{F}^{-1})^{\mathsf{T}} = \boldsymbol{F}^{-\mathsf{T}} \cdot \operatorname{Grad}^{\mathsf{T}}\boldsymbol{u} \end{aligned} \tag{C.2}$$

C.2 Derivatives of functions

In the present section useful derivations for functions of different order are summarized.

Scalar function $y(x)$ of a scalar argument $x(u)$

$$y(x) = x^2 \longrightarrow \frac{\partial y(x)}{\partial u} \cdot \Delta u = 2\, x_0 \cdot \Delta u \tag{C.3}$$

Scalar function $y(\boldsymbol{x})$ of a vector argument $\boldsymbol{x}(\boldsymbol{u})$

$$\begin{aligned} y(\boldsymbol{x}) &= \boldsymbol{x}\cdot\boldsymbol{x} \quad\longrightarrow\quad \frac{\partial y(\boldsymbol{x})}{\partial \boldsymbol{u}}\cdot\Delta\boldsymbol{u} = 2\,\boldsymbol{x}\cdot\Delta\boldsymbol{u} \\ y(\boldsymbol{x}) &= ||\boldsymbol{x}|| \quad\longrightarrow\quad \frac{\partial y(\boldsymbol{x})}{\partial \boldsymbol{u}}\Delta\boldsymbol{u} = \frac{\boldsymbol{x}}{||\boldsymbol{x}||}\cdot\Delta\boldsymbol{u} \end{aligned} \tag{C.4}$$

Scalar function $y(\boldsymbol{X})$ of a tensor argument $\boldsymbol{X}(\boldsymbol{U})$

$$\begin{aligned} y(\boldsymbol{X}) &\equiv \boldsymbol{X}:\boldsymbol{X} \quad\longrightarrow\quad \frac{\partial y(\boldsymbol{X})}{\partial \boldsymbol{U}}\cdot\Delta\boldsymbol{U} = 2\,\boldsymbol{X}:\Delta\boldsymbol{U} \\ y(\boldsymbol{X}) &\equiv ||\boldsymbol{X}|| \quad\longrightarrow\quad \frac{\partial y(\boldsymbol{X})}{\partial \Delta\boldsymbol{U}}\cdot\Delta\boldsymbol{U} = \frac{\boldsymbol{X}}{||\boldsymbol{X}||}:\Delta\boldsymbol{U} \end{aligned} \tag{C.5}$$

C.3 Collection of linearisations

This section will give an overview of useful linearisations. The section will be split into a part where derivations with respect to the continuous displacements $\boldsymbol{u}$ and with respect to the discrete displacements $\mathbf{d}$, respectively, will be presented.

Basic linearisations with respect to continuous displacements

Prerequisite for all following linearisations is the following relation:

$$\frac{\partial \mathrm{Grad}\,\boldsymbol{u}}{\partial \boldsymbol{u}} = \frac{\partial^2 \boldsymbol{u}}{\partial \boldsymbol{x}\otimes\partial \boldsymbol{u}} = 0\,, \quad \text{using the relation } \frac{\partial \boldsymbol{u}}{\partial \boldsymbol{u}} = \mathbf{0}\,. \tag{C.6}$$

For a consistent linearisation of the present problem of thermo-structure interaction the following linearisations are used:

Linearisations of the deformation gradient

$$\begin{aligned} \frac{\partial \boldsymbol{F}}{\partial \boldsymbol{u}} &= \frac{\mathrm{d}}{\mathrm{d}\epsilon}\,\mathrm{Grad}\,(\boldsymbol{x}+\epsilon\,\boldsymbol{u})\big|_{\epsilon=0} = \mathrm{Grad}\,\boldsymbol{u} \\ \frac{\partial \boldsymbol{F}^{\mathsf{T}}}{\partial \boldsymbol{u}} &= \frac{\mathrm{d}}{\mathrm{d}\epsilon}\,\mathrm{Grad}^{\mathsf{T}}\,(\boldsymbol{x}+\epsilon\,\boldsymbol{u})\big|_{\epsilon=0} = \mathrm{Grad}^{\mathsf{T}}\,\boldsymbol{u} \\ \frac{\partial \boldsymbol{F}^{-1}}{\partial \boldsymbol{u}} &= -\boldsymbol{F}^{-1}\cdot\Big(\frac{\partial \boldsymbol{F}}{\partial \boldsymbol{u}}\Big)\cdot\boldsymbol{F}^{-1} = -\boldsymbol{F}^{-1}\cdot\mathrm{Grad}\,\boldsymbol{u}\cdot\boldsymbol{F}^{-1} = -\boldsymbol{F}^{-1}\cdot\mathrm{grad}\,\boldsymbol{u} \\ \frac{\partial \boldsymbol{F}^{-\mathsf{T}}}{\partial \boldsymbol{u}} &= \Big(\frac{\partial \boldsymbol{F}^{-1}}{\partial \boldsymbol{u}}\Big)^{\mathsf{T}} = (-\boldsymbol{F}^{-1}\cdot\mathrm{grad}\,\boldsymbol{u})^{\mathsf{T}} = -\mathrm{grad}^{\mathsf{T}}\,\boldsymbol{u}\cdot\boldsymbol{F}^{-\mathsf{T}} \end{aligned} \tag{C.7}$$

$$\frac{\partial J}{\partial \boldsymbol{u}} = \frac{\partial J}{\partial \boldsymbol{F}}:\frac{\partial \boldsymbol{F}}{\partial \boldsymbol{u}} = J\,\boldsymbol{F}^{-\mathsf{T}}:\mathrm{Grad}\,\boldsymbol{u} = J\,\boldsymbol{I}:\mathrm{Grad}\,\boldsymbol{u}\cdot\boldsymbol{F}^{-1} = J\,\mathrm{div}\,\boldsymbol{u} \tag{C.8}$$

The virtual displacements $\delta\boldsymbol{u}$ are arbitrary so that they do not contribute to the linearisation. Thus, derivatives of the virtual displacements $\delta\boldsymbol{u}$ and the general scalar-valued and vector-valued

mechanical quantities, χ and $\boldsymbol{\chi}$, respectively, introduced in section 2.3.1, follow as

$$\begin{aligned}
\frac{\partial(\operatorname{grad}\delta\boldsymbol{u})}{\partial\boldsymbol{u}} &= (\operatorname{Grad}\delta\boldsymbol{u})\cdot\boldsymbol{F}^{-1} = -(\operatorname{grad}\delta\boldsymbol{u})\cdot\operatorname{grad}\boldsymbol{u} \\
\frac{\partial(\operatorname{grad}\boldsymbol{\chi})}{\partial\boldsymbol{u}} &= \operatorname{Grad}\boldsymbol{\chi}\cdot\left[\frac{\partial\boldsymbol{F}^{-1}}{\partial\boldsymbol{u}}\right] = -(\operatorname{grad}^{\mathsf{T}}\boldsymbol{u})\cdot\operatorname{grad}\boldsymbol{\chi} \\
\frac{\partial(\operatorname{grad}\chi)}{\partial\boldsymbol{u}} &= \left[\frac{\partial\boldsymbol{F}^{-\mathsf{T}}}{\partial\boldsymbol{u}}\right]\cdot\operatorname{Grad}\chi = -(\operatorname{grad}^{\mathsf{T}}\boldsymbol{u})\cdot\operatorname{grad}\chi
\end{aligned} \tag{C.9}$$

Linearisations of the right Cauchy-Green deformation tensor

$$\begin{aligned}
\frac{\partial\boldsymbol{C}}{\partial\boldsymbol{u}} &= \frac{\partial}{\partial\boldsymbol{u}}(\boldsymbol{F}^{\mathsf{T}}\cdot\boldsymbol{F}) = \boldsymbol{F}^{\mathsf{T}}\cdot\operatorname{Grad}\boldsymbol{u} + \operatorname{Grad}^{\mathsf{T}}\boldsymbol{u}\cdot\boldsymbol{F} = 2\operatorname{sym}(\boldsymbol{F}^{\mathsf{T}}\cdot\operatorname{Grad}\boldsymbol{u}) \\
\frac{\partial\boldsymbol{C}^{-1}}{\partial\boldsymbol{u}} &= \frac{\partial}{\partial\boldsymbol{u}}(\boldsymbol{F}^{-1}\cdot\boldsymbol{F}^{-\mathsf{T}}) = -\boldsymbol{F}^{-1}\cdot(\operatorname{grad}\boldsymbol{u} + \operatorname{grad}^{\mathsf{T}}\boldsymbol{u})\cdot\boldsymbol{F}^{-\mathsf{T}}
\end{aligned} \tag{C.10}$$

For $(\text{C.10})_2$, the following relations are included

$$\begin{aligned}
\boldsymbol{C}^{-1} &= \boldsymbol{F}^{-1}\cdot\boldsymbol{F}^{-\mathsf{T}} = \boldsymbol{F}^{-1}\cdot\boldsymbol{I}\cdot\boldsymbol{F}^{-\mathsf{T}} \\
&= (\boldsymbol{F}^{-1}\cdot\boldsymbol{F})\cdot\boldsymbol{F}^{-1}\cdot\boldsymbol{F}^{-\mathsf{T}}\cdot(\boldsymbol{F}^{\mathsf{T}}\cdot\boldsymbol{F}^{-\mathsf{T}}) \\
&= \boldsymbol{F}^{-1}\cdot(\boldsymbol{F}^{-\mathsf{T}}\cdot\boldsymbol{F}^{\mathsf{T}})\cdot(\boldsymbol{F}\cdot\boldsymbol{F}^{-1})\cdot\boldsymbol{F}^{-\mathsf{T}} \\
&= \boldsymbol{C}^{-1}\cdot\boldsymbol{C}\cdot\boldsymbol{C}^{-1}.
\end{aligned} \tag{C.11}$$

Linearisations of the Green-Lagrange strain tensor

$$\begin{aligned}
\frac{\partial\boldsymbol{E}_{\mathsf{GL}}}{\partial\boldsymbol{u}} &= \frac{\partial}{\partial\boldsymbol{u}}\left[\frac{1}{2}\boldsymbol{C}\right] = \frac{\partial}{\partial\boldsymbol{u}}\left[\frac{1}{2}(\boldsymbol{F}^{\mathsf{T}}\cdot\boldsymbol{F})\right] = \operatorname{sym}(\boldsymbol{F}^{\mathsf{T}}\cdot\operatorname{Grad}\boldsymbol{u}) \\
\frac{\partial\delta\boldsymbol{E}_{\mathsf{GL}}}{\partial\boldsymbol{u}} &= \frac{1}{2}[\operatorname{Grad}^{\mathsf{T}}\delta\boldsymbol{u}\cdot\operatorname{Grad}^{\mathsf{T}}\boldsymbol{u}) + \operatorname{Grad}^{\mathsf{T}}\delta\boldsymbol{u}\cdot\operatorname{Grad}\boldsymbol{u}]
\end{aligned} \tag{C.12}$$

Collection of further linearisations

Using (2.7), derivatives of the Jacobi determinant J with respect to deformation measures result in

$$\begin{aligned}
\frac{\partial J}{\partial\boldsymbol{F}} &= \frac{\partial(\det\boldsymbol{F})}{\partial\boldsymbol{F}} = J\,\boldsymbol{F}^{-\mathsf{T}} \\
\frac{\partial J}{\partial\boldsymbol{C}} &= \frac{1}{2}J\,\boldsymbol{C}^{-1} \\
\frac{\partial J^2}{\partial\boldsymbol{C}} &= J^2\,\boldsymbol{C}^{-1} \\
\dot{J} &= \frac{\partial J}{\partial t} = J\operatorname{div}\dot{\boldsymbol{u}}\,\boldsymbol{F}^{-1} = J\operatorname{tr}d = \frac{\partial J}{\partial\boldsymbol{C}}:\dot{\boldsymbol{C}} = J\,\boldsymbol{C}^{-1}:\frac{1}{2}\dot{\boldsymbol{C}}
\end{aligned} \tag{C.13}$$

Basic linearisations with respect to discrete displacements

Linearisations of the deformation gradient

The discrete elementwise deformation gradient $\mathbf{F}$ is defined as

$$\mathbf{F} \;=\; \mathbf{B}_{\mathsf{L}}\,\mathbf{d}\,, \tag{C.14}$$

including the linear gradient operator $\mathbf{B}_{\mathsf{L}}$, often denoted the so-called linear B-operator. Furthermore, within the nonlinear finite-element method the nonlinear B-operator $\mathbf{B}$ is utilised which is given as

$$\mathbf{B} \;=\; \mathbf{F}^{\mathsf{T}}\,\mathbf{B}_{\mathsf{L}}\,. \tag{C.15}$$

Thus, the following linearisations are based on (C.14) and (C.15). Linearisation of the deformation gradient $\mathbf{F}$ with respect to the discrete displacements $\mathbf{d}$ yields

$$\frac{\partial \mathbf{F}}{\partial \mathbf{d}} \;=\; \mathbf{B}_{\mathsf{L}}\,. \tag{C.16}$$

Subsequently, linearisations required for the present TSI model are summarized:

$$\begin{aligned}
\frac{\partial \dot{\mathbf{F}}}{\partial \mathbf{d}} \;&=\; \frac{\partial \dot{\mathbf{F}}}{\partial \mathbf{d}} \;=\; \mathbf{B}_{\mathsf{L}}\,\frac{\partial \dot{\mathbf{d}}}{\partial \mathbf{d}} \\
\frac{\partial J}{\partial \mathbf{d}} \;&=\; J\,\mathbf{F}^{-\mathsf{T}} : \mathbf{B}_{\mathsf{L}} \\
\frac{\partial (\operatorname{div} \dot{\mathbf{d}})}{\partial \mathbf{d}} \;&=\; \operatorname{Grad} \dot{\mathbf{d}}\,(-\mathbf{F}^{-1}\,\frac{\partial \mathbf{F}}{\partial \mathbf{d}}\,\mathbf{F}^{-1}) \;=\; -\mathbf{B}_{\mathsf{L}}\,\frac{\partial \dot{\mathbf{d}}}{\partial \mathbf{d}}\,\mathbf{F}^{-1}\,\mathbf{B}_{\mathsf{L}}\,\mathbf{F}^{-1}
\end{aligned} \tag{C.17}$$

Linearisations of the right Cauchy-Green deformation tensor

$$\begin{aligned}
\frac{\partial \mathbf{C}}{\partial \mathbf{d}} \;&=\; \mathbf{F}^{\mathsf{T}}\,\mathbf{B}_{\mathsf{L}} \;+\; \mathbf{B}_{\mathsf{L}}^{\mathsf{T}}\,\mathbf{F} \;=\; \mathbf{B} \;+\; \mathbf{B}^{\mathsf{T}} \;=\; 2\,\operatorname{sym}(\mathbf{B}) \\
\frac{\partial \dot{\mathbf{C}}}{\partial \mathbf{d}} \;&=\; \frac{\partial \dot{\mathbf{F}}^{\mathsf{T}}}{\partial \mathbf{d}}\,\mathbf{F} \;+\; \mathbf{F}^{\mathsf{T}}\,\frac{\partial \dot{\mathbf{F}}}{\partial \mathbf{d}} \;=\; 2\,\operatorname{sym}\Big[\mathbf{F}^{\mathsf{T}}\,\Big(\mathbf{B}_{\mathsf{L}}\,\frac{\partial \dot{\mathbf{d}}}{\partial \mathbf{d}}\Big)\Big]
\end{aligned} \tag{C.18}$$

Linearisations of the Green-Lagrange strain tensor

$$\begin{aligned}
\frac{\partial \mathbf{E}_{\mathsf{GL}}}{\partial \mathbf{d}} \;&=\; \frac{1}{2}\,\frac{\partial \mathbf{C}}{\partial \mathbf{d}} \;=\; \frac{1}{2}\,(\mathbf{B} \;+\; \mathbf{B}^{\mathsf{T}}) \;=\; \operatorname{sym}(\mathbf{B}) \\
\frac{\partial \delta \mathbf{E}_{\mathsf{GL}}}{\partial \mathbf{d}} \;&=\; \frac{\partial \mathbf{E}_{\mathsf{GL}}}{\partial \mathbf{F}} : \delta \mathbf{F} \;=\; \frac{1}{2}\,(\delta \mathbf{F}^{\mathsf{T}}\,\boldsymbol{F} \;+\; \mathbf{F}^{\mathsf{T}}\,\delta \mathbf{F})
\end{aligned} \tag{C.19}$$

D Details on material formulations

D.1 Small strain elastoplastic material including ductile damage

Based on the Lemaitre material model presented in section 3.4.2.4, the so-called full Lemaitre material is formulated in the following. The model of section 3.4.2.4 considers pure isotropic hardening, hence it is often called simplified Lemaitre material model. In contrast, the full Lemaitre model includes mixed hardening, i.e. in addition to the isotropic hardening, this model is extended to account for kinematic hardening. Hence, it is defined in the following internal variables $\boldsymbol{\alpha}_{\mathsf{k}}$ and their corresponding thermodynamical forces $\boldsymbol{A}_{\mathsf{k}}$ specified each to

$$\boldsymbol{\alpha}_{\mathsf{k}} \,=\, \{\boldsymbol{\varepsilon}^p, R, \boldsymbol{Z}, D\}\,, \quad \boldsymbol{A}_{\mathsf{k}} \,=\, \{-\boldsymbol{\sigma}, \kappa, \boldsymbol{\beta}, -Y\}\,, \tag{D.1}$$

respectively. Herein, in addition to (3.147), the tensor-valued variable $\boldsymbol{Z}$ and its conjugated thermodynamical force, the back stress tensor $\boldsymbol{\beta}$ appear to enable kinematic hardening. Exemplarily, the thermodynamic potential in form of the Helmholtz free energy reads

$$\rho_0\,\psi(\boldsymbol{\varepsilon}^e, R, \boldsymbol{Z}) \,=\, \rho_0\,\psi^{ed}(\boldsymbol{\varepsilon}^e, D) \,+\, \rho_0\,\psi^{p}(R, \boldsymbol{Z})\,, \tag{D.2}$$

with the elastic damaged and the plastic potential,

$$\rho_0\,\psi^{ed}(\boldsymbol{\varepsilon}^e, D) = \frac{1}{2}\,\boldsymbol{\varepsilon}^e : [(1 \,-\, D)\,\boldsymbol{\mathscr{C}}^e_{\mathsf{mat}}] : \boldsymbol{\varepsilon}^e\,, \tag{D.3}$$

$$\rho_0\,\psi^{p}(R, \boldsymbol{Z}) = \sigma_{\mathsf{y};\infty}\left[R \,-\, [1 \,-\, \exp(-\delta\, R)]\right]\frac{1}{\delta} \,+\, \frac{1}{2}\,a\,\boldsymbol{Z} : \boldsymbol{Z}\,, \tag{D.4}$$

respectively. In (D.4), the saturation hardening yield stress $\sigma_{\mathsf{y};\infty}$ with $\sigma_{\mathsf{y};\infty} \geq \sigma_{\mathsf{y};0}$, the hardening exponent $\delta \,>\, 0$, and an additional material parameter a are utilised. The saturation hardening yield stress $\sigma_{\mathsf{y};\infty}$ can be identified with the maximal stress σ_{m} in Figure 3.2. Based on (D.4), the full Lemaitre material model enables exponential isotropic hardening behaviour including saturation and softening. The relation (3.151) is still valid with $R = \dot{\gamma} = \bar{\varepsilon}^p$ for an undamaged load step, i.e. $D \equiv 0$. Subsequently, the von Mises yield function is assumed to

$$\Phi \,=\, \sqrt{3\,J_2(\boldsymbol{s}_{\mathsf{eff}} \,-\, \boldsymbol{\beta})} \,-\, \sigma_{\mathsf{y}}(R) \,=\, \sqrt{3\,J_2(\boldsymbol{\eta}_{\mathsf{eff}})} \,-\, \sigma_{\mathsf{y}}(R) \,\leq\, 0\,, \tag{D.5}$$

where based on (3.144) and $(3.153)_1$, the effective relative stresses $\boldsymbol{\eta}_{\mathsf{eff}}$ and the effective relative von Mises equivalent stresses read

$$\boldsymbol{\eta}_{\mathsf{eff}} \,=\, \boldsymbol{s}_{\mathsf{eff}} \,-\, \boldsymbol{\beta}\,, \quad \tilde{q}_{\mathsf{eff}} \,=\, \sqrt{\frac{3}{2}}\,||\boldsymbol{\eta}_{\mathsf{eff}}||\,, \tag{D.6}$$

respectively. The yield stress σ_{y} is given according to (3.154). The flow vector considers (3.93) and (D.5) and follows as

$$\boldsymbol{N} = \frac{\partial \Phi}{\partial \boldsymbol{\sigma}_{\mathsf{eff}}} = \sqrt{\frac{3}{2}} \frac{\boldsymbol{s}_{\mathsf{eff}} - \boldsymbol{\beta}}{||\boldsymbol{s}_{\mathsf{eff}} - \boldsymbol{\beta}||} = \sqrt{\frac{3}{2}} \frac{\boldsymbol{\eta}_{\mathsf{eff}}}{||\boldsymbol{\eta}_{\mathsf{eff}}||} , \tag{D.7}$$

where the evolution of the back stress is determined by the nonlinear Armstrong-Frederik law

$$\dot{\boldsymbol{\beta}} = (1 - D) (a \, \dot{\boldsymbol{\varepsilon}}^p - b \, \bar{\varepsilon}^p \, \boldsymbol{\beta}) , \tag{D.8}$$

where b is an additional material parameter.

In section 3.4.2.4, a solution of the ductile damage model could be achieved using a very efficient strategy which enabled the reduction of the solution of the given system of equations to the solution of one single equation (3.158). Unlike the Lemaitre material of section 3.4.2.4, the full Lemaitre material model considers the back stresses in the system of equations which is described by equation (D.5), (D.8), (3.146), and (3.156). As shown in (D.8), the back stress tensor $\boldsymbol{\beta}$ depends on the plastic multiplier via the accumulated plastic strains and on the damage. Consequently, further nonlinearities are introduced into the given system of equations, so that an equivalent efficient approach such as the one presented in section 3.4.2.4 is not realisable for the full Lemaitre material model. In contrast, a system of equations has to be solved. Furthermore, in Doghri [34], an alternative strategy for the solution of the full Lemaitre model is proposed, which utilises explicit updating schemes. Hence, it enables a solution without solving a system of equations.

D.2 Finite strain thermo-hyperelasto-plastic material

In section 3.4.2.5, the isothermal and in section 5.3.2.3, the corresponding non-isothermal material model, respectively, for finite strain elastoplasticity are presented. Since in these sections only the final results are summarized, details about selected terms and derivations are explained in more detail in this section.

Determination of the thermo-hyperelasto-plastic heating term

First, the derivations of the thermo-elasto-plastic heating term $\mathcal{H}^{ep}$, see (5.76), are considered. Based on (5.13), the spatial version reads

$$\int_{\Omega} \mathcal{H}^{ep}_{\mathsf{cur}} \, \mathrm{d}V := \int_{\Omega} \rho \, T \Big[\frac{1}{2 \, \rho_0} \, m_0 \Big(\frac{J^{e\,2} + 1}{J^e} \Big) \operatorname{tr} \boldsymbol{D} - \frac{1}{\rho_0} \frac{\partial \kappa(\bar{\varepsilon}^p, T)}{\partial T} \, \dot{\bar{\varepsilon}}^p \Big] \, \mathrm{d}V , \tag{D.9}$$

where the index $(\cdot)_{\mathsf{cur}}$ emphasizes the reference to the current configuration. Via pull-back of $\mathcal{H}^{ep}_{\mathsf{cur}}$ the material version $\mathcal{H}^{ep}$ is achieved. For the pull-back of (D.9), the relations (2.8), (2.54), (2.27), and

$$\boldsymbol{I} = \boldsymbol{F} \cdot \boldsymbol{C}^{-1} \cdot \boldsymbol{F}^{\mathsf{T}} \tag{D.10}$$

are considered. Subsequently, including these equations and rearranging the equation yields

$$\begin{aligned}
&\int_{\Omega} \mathcal{H}^{ep}_{\mathsf{cur}} \,\mathrm{d}V \\
&= \int_{\Omega_0} T \,\frac{\rho}{J\,\rho} \Big[\frac{1}{2}\, m_0 \left(\frac{J^{e\,2} + 1}{J^e} \right) (\boldsymbol{F} \cdot \boldsymbol{C}^{-1} \cdot \boldsymbol{F}^{\mathsf{T}}) : (\boldsymbol{F}^{-\mathsf{T}} \cdot \dot{\boldsymbol{E}}_{\mathsf{GL}} \cdot \boldsymbol{F}^{-1}) \,-\, \frac{\partial \kappa(\bar{\varepsilon}^p, T)}{\partial T}\, \dot{\bar{\varepsilon}}^p \Big] \, J \,\mathrm{d}V_0 \\
&= \int_{\Omega_0} T \left[\frac{m_0}{2} \left(\frac{J^{e\,2} + 1}{J^e} \right) \boldsymbol{C}^{-1} : \dot{\boldsymbol{E}}_{\mathsf{GL}} \,-\, \frac{\partial \kappa(\bar{\varepsilon}^p, T)}{\partial T}\, \dot{\bar{\varepsilon}}^p \right] \mathrm{d}V_0 \equiv \int_{\Omega_0} \mathcal{H}^{ep} \,\mathrm{d}V_0 \,,
\end{aligned} \tag{D.11}$$

i.e. the material version of the thermo-elasto-plastic heating term $\mathcal{H}^{ep}$ (5.76) is received.

Linearisations of the thermo-hyperelasto-plastic material

In the following, details about the resulting linearisation terms are provided. All presented quantities refer to the current time t_{n+1} if no explicit index is specified.

For the application of Newton's method and in the context of consistent linearisation, the linearisation is performed with respect to discrete quantities, i.e. with respect to the discrete displacements $\mathbf{d}$ and temperatures $\mathbf{T}$.

However, to derive the theory of a material model it is common and in particular easier to express all relations in their continuous forms, see exemplarily section 5.3.2.3, where the stress and the corresponding material tangents are specified as continuous measures, i.e. continuous stresses and material tangents $\mathscr{C}_{\mathsf{mat}}$ and $\boldsymbol{C}_{\mathsf{T}}$ according to (3.200) and (5.86), respectively. The actual solution using the finite element method is computed based on discrete quantities, hence the terms are fully discretised, which then leads, for instance to the consistent tangent operators required for quadratic convergence.

Mechanical linearisations

In particular, subsequent explanations concern the derivation of the material tangent $\mathscr{C}_{\mathsf{mat}}$. First, the derivations with respect to the plastic multiplier $\Delta\gamma$, i.e. (3.209), are considered. For this derivation, it is exploited that an admissible plastic step is computed in the return-mapping, assuming $\Delta\gamma \neq 0$, and that the resulting admissible state is the projection of the trial stress state onto the yield surface with $\check{\Phi} = 0$. Hence, at the end of the time step t_{n+1} and based on the fulfilled yield criterion (3.185) including (3.203), it follows

$$\check{\Phi} \stackrel{!}{=} 0 = ||\boldsymbol{s}^{\mathsf{trial}}|| \,-\, 2\,\tilde{\mu}\,\Delta\gamma \,-\, \sqrt{\frac{2}{3}}\,\sigma_{\mathsf{y}} \tag{D.12}$$

using

$$\sigma_{\mathsf{y}} = \sigma_{\mathsf{y};0}(T) \,+\, \kappa(\bar{\varepsilon}^p, T)\,. \tag{D.13}$$

Thus, based on (D.12), consistent linearisation with respect to the Euler-Almansi strains is performed, yielding

$$0 = \frac{\partial ||\boldsymbol{s}^{\mathsf{trial}}||}{\partial \boldsymbol{E}_{\mathsf{EA}}} \,-\, 2\,\frac{\partial \tilde{\mu}}{\partial \boldsymbol{E}_{\mathsf{EA}}}\,\Delta\gamma \,-\, 2\,\tilde{\mu}\,\frac{\partial \Delta\gamma}{\partial \boldsymbol{E}_{\mathsf{EA}}} \,-\, \sqrt{\frac{2}{3}}\,\frac{\partial \sigma_{\mathsf{y}}}{\partial \boldsymbol{E}_{\mathsf{EA}}}\,, \tag{D.14}$$

where the last term is determined by

$$\frac{\partial \sigma_{\mathsf{y}}}{\partial \boldsymbol{E}_{\mathsf{EA}}} = \underbrace{\frac{\partial \sigma_{\mathsf{y};0}(T)}{\partial \boldsymbol{E}_{\mathsf{EA}}}}_{\equiv 0} + \frac{\partial \kappa(\bar{\varepsilon}^p, T)}{\partial \boldsymbol{E}_{\mathsf{EA}}} = \frac{\partial \kappa(\bar{\varepsilon}^p, T)}{\partial \bar{\varepsilon}^p} \frac{\partial \bar{\varepsilon}^p}{\partial \Delta\gamma} \frac{\partial \Delta\gamma}{\partial \boldsymbol{E}_{\mathsf{EA}}}, \tag{D.15}$$

and the last term in (D.15) can be simplified according to (3.187) leading to

$$\frac{\partial \bar{\varepsilon}^p}{\partial \Delta\gamma} = \sqrt{\frac{2}{3}}. \tag{D.16}$$

Inserting the previous relations into (D.14), and rearranging with respect to $\frac{\partial \Delta\gamma}{\partial \boldsymbol{E}_{\mathsf{EA}}}$, results in

$$\frac{\partial \Delta\gamma}{\partial \boldsymbol{E}_{\mathsf{EA}}} = \frac{\left[\dfrac{\partial ||\boldsymbol{s}^{\mathsf{trial}}||}{\partial \boldsymbol{E}_{\mathsf{EA}}} - 2 \dfrac{\partial \tilde{\mu}}{\partial \boldsymbol{E}_{\mathsf{EA}}} \Delta\gamma\right]}{2\,\tilde{\mu} + \sqrt{\frac{2}{3}} \dfrac{\partial \kappa(\bar{\varepsilon}^p, T)}{\partial \bar{\varepsilon}^p} \sqrt{\frac{2}{3}}} = \frac{\left[\dfrac{\partial ||\boldsymbol{s}^{\mathsf{trial}}||}{\partial \boldsymbol{E}_{\mathsf{EA}}} - 2 \dfrac{\partial \tilde{\mu}}{\partial \boldsymbol{E}_{\mathsf{EA}}} \Delta\gamma\right]}{2\,\tilde{\mu} + \frac{2}{3} \dfrac{\partial \kappa(\bar{\varepsilon}^p, T)}{\partial \bar{\varepsilon}^p}}. \tag{D.17}$$

The coefficient β_0, defined in (3.213) for the isothermal mechanical analysis, follows for the non-isothermal case as

$$\beta_0 = 1 + \frac{1}{3\,\bar{\mu}} \frac{\partial \kappa(\bar{\varepsilon}^p, T)}{\partial \bar{\varepsilon}^p}. \tag{D.18}$$

This relation is used, e.g. in (5.79) and implicitly in the material tangents (3.201) and (5.88). The coefficient β_0 can be inserted into (D.17), so that the equation reduces to

$$\frac{\partial \Delta\gamma}{\partial \boldsymbol{E}_{\mathsf{EA}}} = \frac{\left[\dfrac{\partial ||\boldsymbol{s}^{\mathsf{trial}}||}{\partial \boldsymbol{E}_{\mathsf{EA}}} - 2 \dfrac{\partial \tilde{\mu}}{\partial \boldsymbol{E}_{\mathsf{EA}}} \Delta\gamma\right]}{2\,\tilde{\mu}\,\beta_0}, \tag{D.19}$$

which represents the basic equations for (3.209). The linearisation in (D.19) is performed with respect to the strains $\boldsymbol{E}_{\mathsf{EA}}$. However, the actual linearisation is performed with respect to the primary variables, i.e. the displacements. Hence, for instance the linearisation of the plastic multiplier $\Delta\gamma$ with respect to the displacements $\boldsymbol{u}$ follows as pull-back of (D.19) and applying the chain rule. Furthermore, instead of the spatial deformation measure, the material Green-Lagrange strain tensor $\boldsymbol{E}_{\mathsf{GL}}$ is used, so that the linearisation results in

$$\frac{\partial \Delta\gamma}{\partial u_k} = \frac{\partial \Delta\gamma}{\partial E_{\mathsf{GL};IJ}} : \frac{\partial E_{\mathsf{GL};IJ}}{\partial u_k}, \tag{D.20}$$

where the first term of the right side is identified as part of the material tangent $\mathscr{C}_{\mathsf{mat}}$ and the second term is obtained as a result of the chosen deformation measure with respect to the primary variable displacements according to $(\mathrm{C}.12)_1$. Using the pull-back of (3.209) and $(\mathrm{C}.10)_1$, the linearisation finally reads

$$\frac{\partial \Delta\gamma}{\partial u_k} = \frac{1}{\beta_0} \left[\left(1 - \frac{2\,q^{\mathsf{trial}}\,\Delta\gamma}{3\,\bar{\mu}}\right) \boldsymbol{N} + \frac{q^{\mathsf{trial}}}{\bar{\mu}} \boldsymbol{F}^{-1} \cdot \mathrm{dev}\left[\boldsymbol{N}^2_{\mathsf{cur}}\right] \cdot \boldsymbol{F}^{-\mathsf{T}} \right] \cdot \mathrm{sym}\left(\boldsymbol{F}^{\mathsf{T}} \cdot \mathrm{Grad}\,\boldsymbol{u}\right), \tag{D.21}$$

Accordingly, the linearisation of the accumulated plastic strain is achieved by scaling (D.21) with the factor $\sqrt{\frac{2}{3}}$.

Thermal linearisations

Based on (5.86), the thermal material tangent $\boldsymbol{C}_{\mathsf{T}}$ evolves as a result of linearising the stresses with respect to the temperatures. Equivalently to the derivation of the material tangent tensor $\mathscr{C}_{\mathsf{mat}}$, the thermal material tangent $\boldsymbol{C}_{\mathsf{T}}$ is derived considering (5.26). As previously shown for the plastic multiplier, the complete linearisation term is computed with respect to discrete quantities. Correspondingly, based on (4.19) the full linearisation comprises

$$\frac{\partial(\cdot)}{\partial \mathbf{T}} = \frac{\partial(\cdot)}{\partial T}\frac{\partial T}{\partial \mathbf{T}} = \frac{\partial(\cdot)}{\partial T}\,\mathbf{N}_{\mathsf{T}}\,, \tag{D.22}$$

where the matrix of the thermal shape functions $\mathbf{N}_{\mathsf{T}}$ is used.

In accordance with the previously presented contribution of the plastic multiplier for the mechanical matrix block $\mathbf{K}_{\mathsf{SS}}$, included e.g. in (6.5), the corresponding thermal linearisation terms for matrix $\mathbf{K}_{\mathsf{ST}}$ are determined. Starting point is again (D.12) which is fulfilled for an admissible plastic solution step. Subsequent linearisation with respect to the temperatures T results in

$$0 = \frac{\partial ||\boldsymbol{s}^{\mathsf{trial}}||}{\partial T} - 2\,\frac{\partial \tilde{\mu}}{\partial T}\,\Delta\gamma - 2\,\tilde{\mu}\,\frac{\partial \Delta\gamma}{\partial T} - \sqrt{\frac{2}{3}}\,\frac{\partial \sigma_{\mathsf{y}}}{\partial T}\,, \tag{D.23}$$

where the last term is specified by

$$\frac{\partial \sigma_{\mathsf{y}}}{\partial T} = \frac{\partial \sigma_{\mathsf{y};0}(T)}{\partial T} + \frac{\partial \kappa(\bar{\varepsilon}^p, T)}{\partial T} + \frac{\partial \kappa(\bar{\varepsilon}^p, T)}{\partial \bar{\varepsilon}^p}\,\frac{\partial \bar{\varepsilon}^p}{\partial \Delta\gamma}\,\frac{\partial \Delta\gamma}{\partial T}\,, \tag{D.24}$$

where (5.77) is included. The trial deviatoric stresses $\boldsymbol{s}^{\mathsf{trial}}$ and the deformation-dependent Lamé constant $\tilde{\mu}$ are temperature-independent, thus these terms vanish. Subsequently, including the relations (5.80), (5.81), (5.82), and rearranging the resulting equation with respect to $\frac{\partial \Delta\gamma}{\partial T}$, yields

$$\frac{\partial \Delta\gamma}{\partial T} = \frac{\sqrt{\frac{2}{3}}\left(\frac{\partial \sigma_{\mathsf{y};0}(T)}{\partial T} + \frac{\partial \kappa(\bar{\varepsilon}^p, T)}{\partial T}\right)}{-2\,\tilde{\mu} - \frac{2}{3}\,\frac{\partial \kappa(\bar{\varepsilon}^p, T)}{\partial \bar{\varepsilon}^p}} = \sqrt{\frac{2}{3}}\,\frac{\frac{\partial \sigma_{\mathsf{y};0}(T)}{\partial T} + \frac{\partial \kappa(\bar{\varepsilon}^p, T)}{\partial T}}{2\,\tilde{\mu}\,\beta_0}\,, \tag{D.25}$$

which recovers the equation presented in (5.79).

Application of the F-bar method

The computation of a TSI problem including finite strain thermo-hyperelasto-plastic material behaviour requires the use of element technology. In the present work, to prevent volumetric locking issues, the F-bar method in conjunction with three-dimensional (tri-)linearly interpolated hexahedral elements is applied. For more details on the F-bar method, the interested reader is referred to section 3.2.1.2.

As a result of the F-bar method, a modified internal force vector (3.25) is obtained. For realisation of the consistent linearisation this modified internal force vector is considered, hence leading to a modified, different tangential system $\bar{\mathbf{K}}$. As explained in section 3.2.1.1, the consistent tangential matrix $\mathbf{K}$ is composed of elementwise contributions $\mathbf{K}^{(e)}$ by the assembly of these

elementwise terms into the global matrix $\mathbf{K}$. Accordingly, the global modified tangential matrix $\bar{\mathbf{K}}$ is determined by elementwise contributions $\bar{\mathbf{K}}^{(e)}$, which are based on (3.25). Moreover, the temperature-dependent finite strain material is considered, thus the purely mechanical vector in (3.25) is extended to

$$\mathbf{f}_{\mathsf{int;S}}^{(e)} = \int\limits_{\Omega_0^{(e)}} \Big(\frac{\det \mathbf{F}_0}{\det \mathbf{F}}\Big)^{-\frac{1}{3}} \delta\mathbf{E}^{\mathsf{T}} : \bar{\mathbf{S}}(\mathbf{d}, \mathbf{T})\, \mathrm{d}V_0 \tag{D.26}$$

with the second Piola-Kirchhoff stress (5.74) which depends on the deformations $\mathbf{d}$ and the temperatures $\mathbf{T}$. In the following, the stresses are split into

$$\begin{aligned} \bar{\mathbf{S}}(\mathbf{d}, \mathbf{T}) \;=\; & \underbrace{\frac{K}{2}\,(\bar{J}^{e\,2} - 1)\,\bar{\mathbf{C}}^{-1} + \bar{\mathbf{F}}^{-1} \cdot (\mu \operatorname{dev} \tilde{\mathbf{B}}^{e}) \cdot \bar{\mathbf{F}}^{-\mathsf{T}}}_{\bar{\mathbf{S}}_{\mathsf{d}}} + \\ & + \underbrace{\frac{m_0}{2}\,\Delta T \Big(\frac{\bar{J}^{e\,2} + 1}{\bar{J}^{e}}\Big)\,\bar{\mathbf{C}}^{-1}}_{\bar{\mathbf{S}}_{\mathsf{dT}}}, \end{aligned} \tag{D.27}$$

which differs from the split in (5.74), but which summarizes the isothermal purely mechanical model of section 3.4.2.5 in the mechanical stresses $\bar{\mathbf{S}}_{\mathsf{d}}$. Furthermore, in (D.27), the modified deformation gradient $\bar{\mathbf{F}}$ is utilised.

The stresses (D.27) depend on the displacements $\mathbf{d}$ and the temperatures $\mathbf{T}$, hence consistent linearisation leads to contributions for the purely mechanical block $\bar{\mathbf{K}}_{\mathsf{SS}}$ as well to the mechanical coupling block $\bar{\mathbf{K}}_{\mathsf{ST}}$. The derivations of $\bar{\mathbf{S}}_{\mathsf{d}}$ for $\bar{\mathbf{K}}_{\mathsf{SS}}$ for the current element, i.e.

$$\bar{\mathbf{K}}_{\mathsf{SS;d}}^{(e)} = \frac{\partial}{\partial \mathbf{d}} \Big[\int\limits_{\Omega_0^{(e)}} \Big(\frac{\det \mathbf{F}_0}{\det \mathbf{F}}\Big)^{-\frac{1}{3}} \delta\mathbf{E}^{\mathsf{T}}\, \bar{\mathbf{S}}_{\mathsf{d}}\, \mathrm{d}V_0 \Big] \tag{D.28}$$

are straightforward and are explained in detail, e.g. in Tsoukalas [137] assuming an isothermal finite strain elastoplastic material model. Hence, the representation is restricted here to the final expression, leading to

$$\begin{aligned} \bar{\mathbf{K}}_{\mathsf{SS;d}}^{(e)} \;=\; & \int\limits_{\Omega_0^{(e)}} \Big(\frac{\det \mathbf{F}_0}{\det \mathbf{F}}\Big)^{-\frac{1}{3}} \mathbf{B}_{\mathsf{L}}^{\mathsf{T}}\, \bar{\mathbf{S}}_{\mathsf{d}}\, \mathbf{B}_{\mathsf{L}}\, \mathrm{d}V_0 - \\ & - \int\limits_{\Omega_0^{(e)}} \frac{1}{3} \Big(\frac{\det \mathbf{F}_0}{\det \mathbf{F}}\Big)^{-\frac{1}{3}} \mathbf{B}^{\mathsf{T}}\, \bar{\mathbf{S}}_{\mathsf{d}}\, \mathbf{H}^{\mathsf{T}}\, \mathrm{d}V_0 + \\ & + \int\limits_{\Omega_0^{(e)}} \Big(\frac{\det \mathbf{F}_0}{\det \mathbf{F}}\Big)^{\frac{1}{3}} \mathbf{B}^{\mathsf{T}}\, \mathscr{C}_{\mathsf{mat}}\, \mathbf{C}\, \mathbf{H}^{\mathsf{T}}\, \mathrm{d}V_0 + \\ & + \int\limits_{\Omega_0^{(e)}} \frac{1}{3} \Big(\frac{\det \mathbf{F}_0}{\det \mathbf{F}}\Big)^{\frac{1}{3}} \mathbf{B}^{\mathsf{T}}\, \mathscr{C}_{\mathsf{mat}}\, \mathbf{B}\, \mathrm{d}V_0\,, \end{aligned} \tag{D.29}$$

with the linear and nonlinear B-operators, $\mathbf{B}_{\mathsf{L}}$ and $\mathbf{B}$, introduced in (C.14) and (C.15), respectively, and the discrete form of the mechanical material tangent $\mathscr{C}_{\mathsf{mat}}$. Furthermore, the matrix

$\mathbf{H}$ is given in index notation by

$$(\mathbf{H})_j \;=\; \Big(\frac{\det \mathbf{F}_0}{\det \mathbf{F}}\Big)^{-1} \frac{\partial}{\partial \mathsf{d}_j}\Big(\frac{\det \mathbf{F}_0}{\det \mathbf{F}}\Big) \;=\; (\mathsf{F}_0^{-1})_{Ii}\,(\mathsf{B}_{\mathsf{L};0})_{iIj} \;-\; (\mathsf{F}^{-1})_{Ii}\,(\mathsf{B}_{\mathsf{L}})_{iIj}\,. \tag{D.30}$$

For the present thermo-hyperelasto-plastic material, additional terms arise for $\bar{\mathbf{K}}$ in contrast to Tsoukalas [137]. For instance contributions arise for the structural or mechanical block $\bar{\mathbf{K}}_{\mathsf{SS}}$ due to the thermal stresses $\bar{\mathbf{S}}_{\mathsf{dT}}$ and for the coupling matrix $\bar{\mathbf{K}}_{\mathsf{ST}}$ due to the the temperature-dependence of the yield stresses, see (5.71)-(5.73) included in the isochoric stresses $\bar{\tilde{\mathbf{S}}}_{\mathsf{d}}$. First, the additional terms for $\bar{\mathbf{K}}^{(e)}_{\mathsf{SS}}$ are considered, i.e.

$$\bar{\mathbf{K}}^{(e)}_{\mathsf{SS};\mathsf{T}} \;=\; \frac{\partial}{\partial \mathbf{d}}\Big[\int\limits_{\Omega_0^{(e)}} \Big(\frac{\det \mathbf{F}_0}{\det \mathbf{F}}\Big)^{-\frac{1}{3}} \delta\mathbf{E}^{\mathsf{T}}\,\bar{\mathbf{S}}_{\mathsf{dT}}(\mathbf{d},\mathbf{T})\,\mathrm{d}V_0\Big]\,, \tag{D.31}$$

which result in

$$\begin{aligned}
\bar{\mathbf{K}}^{(e)}_{\mathsf{SS};\mathsf{T}} \;=\; & \int\limits_{\Omega_0^{(e)}} \Big(\frac{\det \mathbf{F}_0}{\det \mathbf{F}}\Big)^{-\frac{1}{3}} \mathbf{B}_{\mathsf{L}}^{\mathsf{T}}\,\bar{\mathbf{S}}_{\mathsf{dT}}\,\mathbf{B}_{\mathsf{L}}\,\mathrm{d}V_0 - \\
& - \int\limits_{\Omega_0^{(e)}} \frac{1}{3}\Big(\frac{\det \mathbf{F}_0}{\det \mathbf{F}}\Big)^{-\frac{1}{3}} \mathbf{B}^{\mathsf{T}}\,\bar{\mathbf{S}}_{\mathsf{dT}}\,\mathbf{H}^{\mathsf{T}}\,\mathrm{d}V_0 + \\
& + \int\limits_{\Omega_0^{(e)}} \Big(\frac{\det \mathbf{F}_0}{\det \mathbf{F}}\Big)^{\frac{1}{3}} \mathbf{B}^{\mathsf{T}}\,\mathscr{C}_{\mathsf{mat};v;\mathsf{T}}\,\mathbf{C}\,\mathbf{H}^{\mathsf{T}}\,\mathrm{d}V_0 + \\
& + \int\limits_{\Omega_0^{(e)}} \frac{1}{3}\Big(\frac{\det \mathbf{F}_0}{\det \mathbf{F}}\Big)^{\frac{1}{3}} \mathbf{B}^{\mathsf{T}}\,\mathscr{C}_{\mathsf{mat};v;\mathsf{T}}\,\mathbf{B}\,\mathrm{d}V_0\,,
\end{aligned} \tag{D.32}$$

where the discrete temperature-dependent mechanical tangent $\mathscr{C}_{\mathsf{mat};v;\mathsf{T}}$ based on the continuous form (5.85) is utilised. Finally, the total matrix is composed as sum of (D.29) and (D.32), i.e.

$$\bar{\mathbf{K}}^{(e)}_{\mathsf{SS}} \;=\; \bar{\mathbf{K}}^{(e)}_{\mathsf{SS};\mathsf{d}} \;+\; \bar{\mathbf{K}}^{(e)}_{\mathsf{SS};\mathsf{T}}\,. \tag{D.33}$$

Subsequently, the linearisation with respect to the temperatures $\mathbf{T}$ are investigated resulting in contributions for the matrix block $\bar{\mathbf{K}}_{\mathsf{ST}}$. In this context it is worth mentioning, that this coupling matrix block $\bar{\mathbf{K}}_{\mathsf{ST}}$ only evolves for the case of the monolithic TSI algorithms introduced in section 6.3. The linearisation of the terms for $\bar{\mathbf{K}}^{(e)}_{\mathsf{ST}}$ is computed according to (D.28) by

$$\bar{\mathbf{K}}^{(e)}_{\mathsf{ST}} \;=\; \frac{\partial}{\partial \mathbf{T}}\Big[\int\limits_{\Omega_0^{(e)}} \Big(\frac{\det \mathbf{F}_0}{\det \mathbf{F}}\Big)^{-\frac{1}{3}} \delta\mathbf{E}^{\mathsf{T}}\,\bar{\mathbf{S}}(\mathbf{d},\mathbf{T})\,\mathrm{d}V_0\Big] = \int\limits_{\Omega_0^{(e)}} \Big(\frac{\det \mathbf{F}_0}{\det \mathbf{F}}\Big)^{-\frac{1}{3}} \delta\mathbf{E}^{\mathsf{T}}\,\frac{\partial \bar{\mathbf{S}}(\mathbf{d},\mathbf{T})}{\partial \mathbf{T}}\,\mathrm{d}V_0\,, \tag{D.34}$$

i.e. the stresses are the only temperature-dependent component of the internal force vector (3.25). Based on (5.86), (5.87), (5.88), and (D.27), the linearisation of the stresses is expressed as

$$\frac{\partial \bar{\mathbf{S}}(\mathbf{d},\mathbf{T})}{\partial \mathbf{T}} \;=\; \frac{\partial \bar{\mathbf{S}}_{\mathsf{d}}(\mathbf{d},\mathbf{T})}{\partial \mathbf{T}} \;+\; \frac{\partial \bar{\mathbf{S}}_{\mathsf{dT}}(\mathbf{d},\mathbf{T})}{\partial \mathbf{T}} \;=\; \bar{\tilde{\boldsymbol{C}}}_{\mathsf{T}}\,\mathbf{N}_{\mathsf{T}} \;+\; \bar{\boldsymbol{C}}_{\mathsf{T}}\,\mathbf{N}_{\mathsf{T}}\,. \tag{D.35}$$

Herein, $\bar{\boldsymbol{C}}_{\mathsf{T}}$ and $\bar{\bar{\boldsymbol{C}}}_{\mathsf{T}}$ are the discrete versions of (5.87) and (5.88), respectively. Furthermore, $\mathbf{N}_{\mathsf{T}}$ denotes the matrix containing the shape functions of the temperature field included in (D.22). Thus, the coupling matrix for the current element is determined by

$$\bar{\mathbf{K}}_{\mathsf{ST}}^{(e)} = \int_{\Omega_0^{(e)}} \left(\frac{\det \mathbf{F}_0}{\det \mathbf{F}}\right)^{-\frac{1}{3}} \mathbf{B}^{\mathsf{T}}\, \bar{\bar{\boldsymbol{C}}}_{\mathsf{T}}\, \mathbf{N}_{\mathsf{T}}\, \mathrm{d}V_0 + \int_{\Omega_0^{(e)}} \left(\frac{\det \mathbf{F}_0}{\det \mathbf{F}}\right)^{-\frac{1}{3}} \mathbf{B}^{\mathsf{T}}\, \bar{\boldsymbol{C}}_{\mathsf{T}}\, \mathbf{N}_{\mathsf{T}}\, \mathrm{d}V_0 \,. \tag{D.36}$$

Finally, the global matrices are composed by assembly of the elementwise contributions, i.e.

$$\bar{\mathbf{K}}_{\mathsf{SS}} = \sum_{e=1}^{\mathsf{nele}} \bar{\mathbf{K}}_{\mathsf{SS}}^{(e)}\,, \quad \bar{\mathbf{K}}_{\mathsf{ST}} = \sum_{e=1}^{\mathsf{nele}} \bar{\mathbf{K}}_{\mathsf{ST}}^{(e)}\,. \tag{D.37}$$

Curriculum Vitae

Personal Data:

Name	Caroline Danowski
Parents	Dr. med. Siegfried Danowski and Christine Danowski
Sibling	Dr. rer. nat. Katrin Danowski, M.Sc.
Date of birth	9 October, 1983
Place of birth	Oberndorf a. N., Germany
Nationality	German
Marital status	Unmarried

Education:

04/2009	Degree: “Diplom-Ingenieur (Dipl.-Ing.) Bauingenieurwesen”
10/2003 – 04/2009	Studies in Civil Engineering at the University of Stuttgart
09/2006 – 02/2007	University of Seville, Spain
07/2003	Degree: “Allgemeine Hochschulreife” (high school diploma)
09/1994 – 07/2003	Secondary/high school “Gymnasium am Rosenberg”, Oberndorf a. N.
09/1990 – 08/1994	Elementary school “Grundschule Aistaig”

Work Experience / Internships:

since 04/2010	Degree: “Grundstufe, Breitensporttrainer C” for ski alpine
09/2008 – 04/2009	Student teaching assistent at the Institute of Applied Mechanics at the University of Stuttgart
10/2007 – 06/2008	Werner Sobek Stuttgart GmbH & Co. KG, Degerloch
09/2004 – 08/2007	Student teaching assistent at the Institute of Applied Mechanics at the University of Stuttgart
08/2003 – 09/2003	DaimlerChrysler AG, Untertürkheim
09/2005	KitzlingerHaus GmbH & Co. KG, Sulz a. N.
03 – 04/2004 and 09/2004	Gebr. Stumpp Bauunternehmung GmbH & Co. KG, Rottweil
since 1999	Trainer for ski alpine at the “Skiclub Oberndorf”, Oberndorf a. N.

Professional Occupation:

since 05/2009	Research associate at the Institute for Computational Mechanics at the Technische Universität München

Reports of the Institute for Computational Mechanics at Technische Universität München

21 (2014) **Caroline Danowski:**
Computational modelling of thermo-structure interaction with application to rocket nozzles.

20 (2014) **Kei Müller:**
Simulation of self-assembly and mechanics of transiently crosslinked, semiflexible biopolymer networks.

19 (2014) **Mahmoud Ismail:**
Reduced dimensional modeling of the entire human lung.

18 (2013) **Florian Henke:**
An extended finite element method for turbulent premixed combustion.

17 (2012) **Markus Gitterle:**
A dual mortar formulation for finite deformation frictional contact problems including wear and thermal coupling.

16 (2012) **Andreas Maier:**
Computational modeling of rupture risk in abdominal aortic aneurysms.

15 (2012) **Georg Bauer:**
A coupled finite element approach for electrochemical systems.

14 (2012) **Alexander Popp:**
Mortar methods for computational contact mechanics and general interface problems.

13 (2012) **Thomas Klöppel:**
A finite element model for the human red blood cell.

12 (2012) **Sophie Rausch:**
Computational and experimental modeling of lung parenchyma.

11 (2011) **Christian Cyron:**
Micromechanical continuum approach for the analysis of biopolymer networks.

10 (2011) **Lena Wiechert:**
Computational modeling of multi-field and multi-scale phenomena in respiratory mechanics.

9 (2010) **Peter Gamnitzer:**
Residual-based variational multiscale methods for turbulent flows and fluid-structure interaction.

8 (2010) **Axel Gerstenberger:**
An XFEM based fixed grid approach to fluid-structure interaction.

7 (2009) **Ulrich Küttler:**
Effiziente Lösungsverfahren für Fluid-Struktur-Interaktions-Probleme.

6 (2009) **Moritz Frenzel:**
Advanced structural finite element modeling of arterial walls for patient-specific geometries.

5 (2007)* **Christiane Förster:**
Robust methods for fluid-structure interaction with stabilised finite elements.

4 (2004)* **Tobias Erhart:**
Strategien zur Numerischen Modellierung transienter Impaktvorgänge bei nichtlinearem Materialverhalten.

3 (2004)* **Michael Gee:**
Effiziente Lösungsstrategien in der nichtlinearen Schalenmechanik.

2 (2003)* **Volker Gravemeier:**
The variational multiscale method for laminar and turbulent incompressible flow.

1 (2001)* **Daniel Mok:**
Partitionierte Lösungsverfahren in der Strukturdynamik und der Fluid-Struktur-Interaktion.

* This dissertation was supervised by Prof. Dr.-Ing. Wolfgang A. Wall at the Institute for Structural Mechanics at the University of Stuttgart and is published in the respective report series.

Bibliography

[1] L. Adam and J.-P. Ponthot, Thermomechanical modeling of metals at finite strains: First and mixed order finite elements, *International Journal of Solids and Structures* **42**, 5615–5655, 2005.

[2] C. Agelet de Saracibar, M. Cervera, and M. Chiumenti, On the formulation of coupled thermoplastic problems with phase-change, *International Journal of Plasticity* **15**, 1–34, 1999.

[3] F. M. Andrade Pires, J. M. A. César de Sá, L. Costa Sousa, and R. M. Natal Jorge, Numerical modelling of ductile plastic damage in bulk metal forming, *International Journal of Mechanical Sciences* **45**, 273–294, 2003.

[4] F. M. Andrade Pires, E. A. de Souza Neto, and J. L. de la Cuesta Padilla, An assessment of the average nodal volume formulation for the analysis of nearly incompressible solids under finite strains, *Communications in Numerical Methods in Engineering* **20**, 569–583, 2004.

[5] M. André, *Thermomechanisches Verhalten von Gummimaterialien während der Vulkanisation, Theorie und Numerik*, PhD thesis, Institute of Mechanics and Computational Mechanics, Leibniz Universität Hannover, 2001.

[6] F. Armero and J. C. Simo, A new unconditionally stable fractional step method for nonlinear coupled thermomechanical problems, *International Journal for Numerical Methods in Engineering* **35**, 737–766, 1992.

[7] F. Armero and J. C. Simo, A priori stability estimates and unconditionally stable product formula algorithms for nonlinear coupled thermoplasticity, *International Journal of Plasticity* **9**, 749–782, 1993.

[8] V. K. Arya, Analytical and finite element solutions of some problems using a viscoplastic model, *Computers and Structures* **33**, 957–967, 1989.

[9] V. K. Arya, Nonlinear structural-analysis of cylindrical thrust chambers using viscoplastic models, *Journal of Propulsion and Power* **8**, 598–604, 1992.

[10] V. K. Arya and S. M. Arnold, Viscoplastic analysis of an experimental cylindrical thrust chamber liner, *AIAA Journal* **30**, 781–789, 1992.

[11] V. K. Arya and A. Kaufmann, Finite element implementation of Robinson's unified viscoplastic model and its application to some uniaxial and multiaxial problems, *NASA Technical Memorandum* **89891**, 1–19, 1987.

[12] W. J. Baars, C. E. Tinney, J. H. Ruf, A. M. Brown, and D. M. McDaniels, On the unsteadiness associated with shock-induced separation in overexpanded rocket nozzles, *AIAA Paper 2010-6728*, 2010.

[13] S. Bargmann and P. Steinmann, Finite element approaches to non-classical heat conduction in solids, *Computer Modeling in Engineering and Sciences* **9**, 133–150, 2005.

[14] S. Bargmann, R. Denzer, and P. Steinmann, On configurational forces within Green Naghdi thermo-hyperelasticity, In P. Steinmann (ed.), *Proceedings of the IUTAM Symposium on Progress in the Theory and Numerics of Configurational Mechanics*, Volume 17 of *IUTAM Bookseries*, pages 205–214, Springer Netherlands, 2009.

[15] K.-J. Bathe, *Finite element procedures*, Prentice Hall, 1996.

[16] T. Belytschko, W. K. Liu, and B. Moran, *Nonlinear finite elements for continua and structures*, Wiley, 2000.

[17] J. Bonet and R. D. Wood, *Nonlinear continuum mechanics for finite element analysis*, Cambridge University Press, 2008.

[18] P. B. Bornemann and W. A. Wall, A computational approach for thermo-structure-coupled dynamics of thin-walled structures at elevated temperatures, In *Proceedings of the ECCOMAS Thematic Conference on Computational Methods in Structural Dynamics and Earthquake Engineering*, 2007.

[19] P. B. Bornemann and W. A. Wall, Thermo-structure-coupled dynamics of thin-walled structures at elevated temperatures, In *Proceedings of the ECCOMAS - Computational Methods for Coupled Problems in Science and Engineering Conference*, Santa Eulalia, Ibiza, Spain, 2007.

[20] A. M. Brown, J. Ruf, D. Reed, M. D'Agostino, and R. Keanini, Characterization of side load phenomena using measurement of fluid-structure interaction, *AIAA Paper 2002-3999*, 2002.

[21] M. A. Caminero, F. J. Montáns, and K.-J. Bathe, Modeling large strain anisotropic elasto-plasticity with logarithmic strain and stress measures, *Computers and Structure* **89**, 826–843, 2011.

[22] M. Canadija and J. Brnic, Associative coupled thermoplasticity at finite strain with temperature-dependent material parameters, *International Journal of Plasticity* **20**, 1851–1874, 2004.

[23] M. Canadija and J. Mosler, On the thermomechanical coupling in finite strain plasticity theory with non-linear kinematic hardening by means of incremental energy minimization, *International Journal of Solids and Structures* **48**, 1120–1129, 2011.

[24] J. P. Carter and J. R. Booker, Finite-element analysis of coupled thermoelasticity, *Computers and Structures* **31**, 73–80, 1989.

[25] J. Chung and G. M. Hulbert, A time integration algorithm for structural dynamics with improved numerical dissipation: the generalized–α method, *Journal of Applied Mechanics* **60**, 371–375, 1993.

[26] B. D. Coleman and W. Noll, The thermodynamics of elastic materials with heat conduction and viscosity, *Archive for Rational Mechanics and Analysis* **13**, 167–178, 1963.

[27] M. A. Crisfield, Plasticity computations using the Mohr-Coulomb yield criterion, *Engineering Computations* **4**, 300–308, 1987.

[28] V. I. Danilovskaya, On a dynamical problem of thermoelasticity, *Prikladnaya Matematika i Mekhanika* **16**, 341–344, 1952.

[29] C. Danowski, V. Gravemeier, L. Yoshihara, and W. A. Wall, A monolithic computational approach to thermo-structure interaction, *International Journal for Numerical Methods in Engineering* **95**, 1053–1078, 2013.

[30] E. A. de Souza Neto, A fast, one-equation integration algorithm for the Lemaitre ductile damage model, *Communications in Numerical Methods in Engineering* **18**, 541–554, 2002.

[31] E. A. de Souza Neto, D. Peric, M. Dutko, and D. R. J. Owen, Design of simple low order finite elements for large strain analysis of nearly incompressible solids, *International Journal of Solids and Structures* **33**, 3277–3296, 1996.

[32] E. A. de Souza Neto, F. M. Andrade Pires, and D. R. J. Owen, F-bar-based linear triangles and tetrahedra for finite strain analysis of nearly incompressible solids. Part I: formulation and benchmarking, *International Journal for Numerical Methods in Engineering* **62**, 353–383, 2005.

[33] E. A. de Souza Neto, D. Peric, and D. R. J. Owen, *Computational methods for plasticity - theory and applications*, John Wiley & Sons, 2008.

[34] I. Doghri, Numerical implementation and analysis of a class of metal plasticity models coupled with ductile damage, *International Journal for Numerical Methods in Engineering* **38**, 3403–3431, 1995.

[35] S. Doll and K. Schweizerhof, On the development of volumetric strain energy functions, *Journal of Applied Mechanics-Transactions of the ASME* **67**, 17–21, 2000.

[36] S. Doll, K. Schweizerhof, R. Hauptmann, and C. Freischläger, On volumetric locking of low-order solid and solid-shell elements for finite elastoviscoplastic deformations and selective reduced integration, *Engineering Computations* **17**, 874–902, 2000.

[37] D. C. Drucker and W. Prager, Soil mechanics and plastic analysis for limit design, *Quarterly of Applied Mathematics* **10**, 157–165, 1952.

[38] P. Erbts and A. Düster, Accelerated staggered coupling schemes for problems of thermoelasticity at finite strains, *Computers & Mathematics with Applications* **64**, 2408–2430, 2012.

[39] C. Farhat, K. C. Park, and Y. Dubois-Pelerin, An unconditionally stable staggered algorithm for transient finite element analysis of coupled thermoelastic problems, *Computer Methods in Applied Mechanics and Engineering* **85**, 349–365, 1991.

[40] C. A. Felippa, K. C. Park, and C. Farhat, Partitioned analysis of coupled mechanical systems, *Computer Methods in Applied Mechanics and Engineering* **190**, 3247–3270, 2001.

[41] J. Fourier, *Théorie analytique de la chaleur (in French)*, Paris: Firmin Didot Père et Fils., 1822.

[42] A. D. Freed, J.-L. Chaboche, and K. P. Walker, A viscoplastic theory with thermodynamic considerations, *Acta Mechanica* **90**, 155–174, 1991.

[43] M. Frey and G. Hagemann, Restricted shock separation in rocket nozzles, *Journal of Propulsion and Power* **16**, 478–484, 2000.

[44] A. Fritsch, *Finite Thermoplastizität: Materialmodellierung und Numerik thermoplastischer Werkstoffe bei finiten Deformationen*, Fortschrittberichte VDI / 18, VDI-Verlag, 2004.

[45] M. W. Gee, C. M. Siefert, J. J. Hu, R. S. Tuminaro, and M. G. Sala, ML 5.0 smoothed aggregation user's guide, Technical Report SAND2006-2649, Sandia National Laboratories, 2007.

[46] M. W. Gee, C. T. Kelley, and R. B. Lehoucq, Pseudo-transient continuation for nonlinear transient elasticity, *International Journal for Numerical Methods in Engineering* **78**, 1209–1219, 2009.

[47] M. W. Gee, U. Küttler, and W. A. Wall, Truly monolithic algebraic multigrid for fluid-structure interaction, *International Journal for Numerical Methods in Engineering* **85**, 987–1016, 2011.

[48] S. Ghadiani, *A mutliphasic continuum mechanical model for design investigations of an effusion-cooled rocket thrust chamber*, PhD thesis, Institute of Applied Mechanics, University of Stuttgart, 2005.

[49] M. Gitterle, *A dual mortar formulation for finite deformation frictional contact problems including wear and thermal coupling*, PhD thesis, Institute for Computational Mechanics, Technische Universität München, 2012.

[50] S. Glaser, *Berechnung gekoppelter thermomechanischer Prozess*, PhD thesis, Institut für Statik und Dynamik der Luft- und Raumfahrtkonstruktion, University of Stuttgart, 1992.

[51] S. Glaser, *Gekoppelte thermomechanische Berechnung dünnwandiger Strukturen mit der Methode der Finiten Elemente*, Habilitation thesis, Institut für Statik und Dynamik der Luft- und Raumfahrtkonstruktion, University of Stuttgart, 1998.

[52] M. Grilli, N. A. Adams, G. Hammerl, C. Danowski, and W. A. Wall, An innovative approach to thermo-fluid-structure interaction based on an immersed interface method and a monolithic thermo-structure interaction algorithm, In *Proceedings of the 42nd AIAA Fluid Dynamics Conference and Exhibit*, number AIAA 2012-3267, New Orleans, LA, USA, 2012.

[53] G. Hammerl, C. Danowski, M. Grilli, N. A. Adams, and W. A. Wall, A coupled thermo-fluid-structure interaction approach based on an immersed interface method and a monolithic thermo-structure interaction algorithms, In *Proceedings of the 1st ECCOMAS – Young Investigators Conference*, number 127, Aveiro, Portugal, 2012.

[54] S. Hartmann, Comparison of the multiplicative decompositions $\boldsymbol{F} = \boldsymbol{F}_\Theta \boldsymbol{F}_m$ and $\boldsymbol{F} = \boldsymbol{F}_m \boldsymbol{F}_\Theta$ in finite strain thermo-elasticity, Technical report, Faculty of mathematics/computer science and mechanical engineering, Clausthal University of Technology, 2012.

[55] M. Heil, An efficient solver for the fully coupled solution of large-displacement fluid-structure interaction problems, *Computer Methods in Applied Mechanics and Engineering* **193**, 1–23, 2004.

[56] M. A. Heroux, R. A. Bartlett, V. E. Howle, R. J. Hoekstra, J. J. Hu, T. G. Kolda, R. B. Lehoucq, K. R. Long, R. P. Pawlowski, E. T. Phipps, A. G. Salinger, H. K. Thornquist, R. S. Tuminaro, J. M. Willenbring, A. Williams, and K. S. Stanley, An overview of the Trilinos project, *ACM Transactions on Mathematical Software* **31**, 397–423, 2005.

[57] R. Hill, *The mathematical theory of plasticity*, Oxford University Press, 1998.

[58] G. A. Holzapfel, *Nonlinear solid mechanics*, Wiley, 2007.

[59] G. A. Holzapfel and J. C. Simo, Entropy elasticity of isotropic rubber-like solids at finite strains, *Computer Methods in Applied Mechanics and Engineering* **132**, 17–44, 1996.

[60] T. J. R. Hughes, *The finite element method - linear static and dynamic finite element analysis*, Dover Publications, 2000.

[61] A. Ibrahimbegovic and L. Chorfi, Covariant principal axis formulation of associated coupled thermoplasticity at finite strains and its numerical implementation, *International Journal of Solids and Structures* **39**, 499–528, 2002.

[62] B. M. Irons and R. C. Tuck, A version of the Aitken accelerator for computer iteration, *International Journal for Numerical Methods in Engineering* **1**, 275–277, 1969.

[63] K. E. Jansen, C. H. Whiting, and G. M. Hulbert, A generalized–α method for integrating the filtered Navier-Stokes equations with a stabilized finite element method, *Computer Methods in Applied Mechanics and Engineering* **190**, 305–319, 2000.

[64] L. M. Kachanov, *Introduction to continuum damage mechanics*, Springer, 1986.

[65] N. Karajan, *An extended biphasic description of the inhomogeneous and anisotropic intervertebral disc*, PhD thesis, Institute of Applied Mechanics, University of Stuttgart, 2009.

[66] T. Klöppel, *A finite element model for the human red blood cell*, PhD thesis, Institute for Computational Mechanics, Technische Universität München, 2012.

[67] T. Klöppel, A. Popp, U. Küttler, and W. A. Wall, Fluid-structure interaction for non-conforming interfaces based on a dual mortar formulation, *Computer Methods in Applied Mechanics and Engineering* **200**, 3111–3126, 2011.

[68] D. Kuhl, Thermomechanical analysis of rocket combustion chambers, In S. R. Idelsohn, E. Oñate, and E. N. Dvorkin (eds.), *Proceedings of the 4$^{\text{th}}$ World Congress on Computational Mechanics in Applied Sciences and Engineering: Computational Mechanics - New Trends and Applications*, Buenos Aires, Argentina, 1998.

[69] D. Kuhl, J. Riccius, and O. J. Haidn, Thermomechanical analysis and optimization of cryogenic liquid rocket engines, *Journal of Propulsion and Power* **18**, 835–846, 2002.

[70] U. Küttler, *Effiziente Lösungsverfahren für Fluid-Struktur-Interaktions-Probleme*, PhD thesis, Institute for Computational Mechanics, Technische Universität München, 2009.

[71] U. Küttler and W. A. Wall, Fixed-point fluid-structure interaction solvers with dynamic relaxation, *Computational Mechanics* **43**, 61–72, 2008.

[72] U. Küttler and W. A. Wall, Vector extrapolation for strong coupling fluid-structure interaction solvers, *Journal of Applied Mechanics* **76**, 1–7, 2009.

[73] E. H. Lee, Elastic-plastic deformation at finite strains, *Journal of Applied Mechanics* **36**, 1–6, 1969.

[74] T. Lehmann and U. Blix, On the influence of the coupling of thermal and mechanical processes in the necking problem in uniaxial tension, *Journal of Thermal Stresses* **8**, 153–165, 1985.

[75] J. Lemaitre, A continous damage mechanics model for ductile fracture, *Journal of Engineering Materials and Technology* **107**, 83–89, 1985.

[76] J. Lemaitre, Coupled elasto-plasticity and damage constitutive-equations, *Computer Methods in Applied Mechanics and Engineering* **51**, 31–49, 1985.

[77] J. Lemaitre, *A course on damage mechanics*, Springer, 1996.

[78] J. Lemaitre and J.-L. Chaboche, *Mechanics of solid materials*, Cambridge University Press, 2000.

[79] J. Lemaitre and R. Desmorat, *Engineering damage mechanics*, Springer, 2005.

[80] R. Löhner, C. Yang, J. Cebral, J. D. Baum, H. Luo, D. Pelessone, and C. Charman, Fluid-structure-thermal interaction using a loose coupling algorithm and adaptive unstructured grids, *AIAA Paper 98-2419*, 1998.

[81] S. C. H. Lu and K. S. Pister, Decomposition of deformation and representation of the free energy function for isotropic thermoelastic solids, *International Journal of Solids and Structures* **11**, 927–934, 1975.

[82] C. U. D. Mäding. A method for producing a regeneratively cooled rocket nozzle expansion of the combustion chamber and nozzle expansion, 2011. URL `http://www.google.com/patents/DE102010007272A1?cl=en`. DE Patent App. DE201,010,007,272.

[83] A. Maier, M. Essler, M. W. Gee, H.-H. Eckstein, W. A. Wall, and C. Reeps, Correlation of biomechanics to tissue reaction in aortic aneurysms assessed by finite elements and [18f]-fluorodeoxyglucose-PET/CT, *International Journal of Numerical Methods in Biomedical Engineering* **28**, 456–471, 2012.

[84] G. A. Maugin, *The thermomechanics of nonlinear irreversible behavior*, World Scientific Publishing Co. Pte. Ltd., 1999.

[85] G. A. Maugin, R. Drouot, and F. Sidoroff, *Continuum thermomechanics*, Kluwer Academic Publisher, 2002.

[86] M. Mayr, T. Klöppel, W. A. Wall, and M. W. Gee, A temporal consistent monolithic approach to fluid-structure interaction enabling single field predictors, *Preprint, submitted to SIAM Journal of Scientific Computing*, 2014.

[87] C. Miehe, *Zur Numerischen Behandlung Thermomechanischer Prozesse*, PhD thesis, Institute of Mechanics and Computational Mechanics, Leibniz Universität Hannover, 1988.

[88] C. Miehe, *Kanonische Modelle multiplikativer Elasto-Plastizität. Thermodynamische Formulierung und Numerische Implementation*, Habilitation thesis, Institute of Mechanics and Computational Mechanics, Leibniz Universität Hannover, 1993.

[89] C. Miehe, Entropic thermoelasticity at finite strains. Aspects of the formulation and numerical implementation, *Computer Methods in Applied Mechanics and Engineering* **120**, 243–269, 1995.

[90] C. Miehe, A theory of large-strain isotropic thermoplasticity based on metric transformation tensors, *Archive of Applied Mechanics* **66**, 45–64, 1995.

[91] C. Miehe and J. Schröder, Computational micro-macro-transitions in thermoplastic analysis at finite strains, In O. Bruhns and E. Stein (eds.), *IUTAM Symposium on Micro- and Macrostructural Aspects of Thermoplasticity*, Volume 62 of *Solid Mechanics and its Applications*, pages 137–146, Springer Netherlands, 2002.

[92] C. Miehe, J. Méndez Diez, S. Göktepe, and L.-M. Schänzel, Coupled thermoviscoplasticity of glassy polymers in the logarithmic strain space based on the free volume theory, *International Journal of Solids and Structures* **48**, 1799–1817, 2011.

[93] D. P. Mok, *Partitionierte Lösungsansätze in der Strukturdynamik und der Fluid-Struktur-Interaktion*, PhD thesis, Institute for Structural Mechanics, University of Stuttgart, 2001.

[94] D. P. Mok and W. A. Wall, Partitioned analysis schemes for the transient interaction of incompressible flows and nonlinear flexible structures, In W. A. Wall, K. U. Bletzinger, and K. Schweizerhof (eds.), *Proceedings of Trends in Computational Structural Mechanics*, pages 689–698, Schloss Hofen, Austria, 2001, CIMNE: Barcelona, Spain.

[95] F. J. R. Montáns and K. J. Bathe, Computational issues in large strain elasto-plasticity: an algorithm for mixed hardening and plastic spin, *International Journal for Numerical Methods in Engineering* **63**, 159–196, 2005.

[96] T. Netz, *High-oder space and time discretization schemes applied to problems of finite thermo-viscoelasticity*, PhD thesis, Institute of Applied Mechanics, Clausthal University of Technology, 2013.

[97] N. M. Newmark, A method of computation for structural dynamics, *Journal of the Engineering Mechanics Division ASCE* **85**, 67–94, 1959.

[98] W. Noll, On the continuity of the solid and fluid states, *Journal of Rational Mechanics and Analysis* **4**, 3–81, 1955.

[99] W. Noll, A mathematical theory of the mechanical behavior of continuous media, *Archive for Rational Mechanics and Analysis* **2**, 197–226, 1958.

[100] R. W. Ogden, *Non-linear elastic deformations*, Dover Publications, 1997.

[101] M. Ortiz and J. C. Simo, An analysis of a new class of integration algorithms for elasto-plastic constitutive relations, *International Journal for Numerical Methods in Engineering* **23**, 353–366, 1986.

[102] J. Östlund, T. Damgaard, and M. Frey, Side-load phenomena in highly overexpanded rocket nozzles, *Journal of Propulsion and Power* **20**, 695–704, 2004.

[103] H. Parkus, *Thermoelasticity*, Springer, 1976.

[104] D. Peric and E. A. de Souza Neto, A new computational model for Tresca plasticity at finite strains with an optimal parametrization in the principal space, *Computer Methods in Applied Mechanics and Engineering* **171**, 463–489, 1999.

[105] W. Polifke and J. Kopitz, *Wärmeübertragung: Grundlagen, analytische und numerische Methoden*, Pearson Studium, 2009.

[106] C. P. Providakis, D/BEM implementation of Robinson's viscoplastic model in creep analysis of metals using a complex variable numerical technique, *Advances in Engineering Software* **33**, 805–816, 2002.

[107] A. Quarteroni, R. Sacco, and F. Saleri, *Numerical mathematics*, Springer, 2007.

[108] S. Reese and S. Govindjee, A theory of finite viscoelasticity and numerical aspects, *International Journal of Solids and Structures* **35**, 3455–3482, 1998.

[109] J. R. Riccius and E. B. Zametaev, Stationary and dynamic thermal analyses of cryogenic liquid rocket combustion chamber walls, In *Proceedings of the 38th AIAA/ASME/SAE/ASEE Joint Propulsion Conference and Exhibit*, number AIAA 2002-3694, Indianapolis, IN, USA, 2002.

[110] D. N. Robinson and R. W. Swindeman, Unified creep-plasticity constitutive equations for $2 - 1/4$ Cr – 1 Mo steel at elevated temperature, *ORNL / TM–8444*, 1982.

[111] I. Romero, Algorithms for coupled problems that preserve symmetries and the laws of thermodynamics: Part II: fractional step methods, *Computer Methods in Applied Mechanics and Engineering* **199**, 2235–2248, 2010.

[112] I. Romero, Algorithms for coupled problems that preserve symmetries and the laws of thermodynamics: Part I: monolithic integrators and their application to finite strain thermoelasticity, *Computer Methods in Applied Mechanics and Engineering* **199**, 1841–1858, 2010.

[113] Y. Saad and M. H. Schultz, GMRES: A generalized minimal residual algorithm for solving nonsymmetric linear systems, *SIAM Journal on Scientific and Statistical Computing* **7**, 856–869, 1986.

[114] W. Schwarz, S. Schwub, K. Quering, D. Wiedmann, H. Höppel, and M. Göken, Life prediction of thermally highly loaded components: modelling the damage process of a rocket combustion chamber hot wall, *CEAS Space Journal* **1**, 83–97, 2011.

[115] R. Sedlácek, *Finite Elemente in der Werkstoffmechanik*, Verlag Dr. Hut, 2009.

[116] A. Seitz, A. Popp, and W. A. Wall, A semi-smooth Newton method for orthotropic plasticity and frictional contact at finite strains, *in preparation*, 2014.

[117] H. Sherief and A. M. Abd El-Latief, Effect of variable thermal conductivity on a half-space under the fractional order theory of thermoelasticity, *International Journal of Mechanical Sciences* **74**, 185–189, 2013.

[118] J. C. Simo, Algorithms for static and dynamic multiplicative plasticity that preserve the classical return mapping schemes of the infinitesimal theory, *Computer Methods in Applied Mechanics and Engineering* **99**, 61–112, 1992.

[119] J. C. Simo and F. Armero, Geometrically non-linear enhanced strain mixed methods and the method of incompatible modes, *International Journal for Numerical Methods in Engineering* **33**, 1413–1449, 1992.

[120] J. C. Simo and T. J. R. Hughes, *Computational inelasticity*, Springer, 1998.

[121] J. C. Simo and J. W. Ju, On continuum damage-elastoplasticity at finite strains, *Computational Mechanics* **5**, 375–400, 1989.

[122] J. C. Simo and C. Miehe, Associative coupled thermoplasticity at finite strains - formulation, numerical-analysis and implementation, *Computer Methods in Applied Mechanics and Engineering* **98**, 41–104, 1992.

[123] J. C. Simo and R. L. Taylor, A return mapping algorithm for plane-stress elastoplasticity, *International Journal for Numerical Methods in Engineering* **22**, 649–670, 1986.

[124] J. C. Simo, R. L. Taylor, and K. S. Pister, Variational and projection methods for the volume constraint in finite deformation elasto-plasticity, *Computer Methods in Applied Mechanics and Engineering* **51**, 177–208, 1985.

[125] J. Simo, A framework for finite strain elastoplasticity based on maximum plastic dissipation and the multiplicative decomposition: Part I. continuum formulation, *Computer Methods in Applied Mechanics and Engineering* **66**, 199–219, 1988.

[126] J. Simo, A framework for finite strain elastoplasticity based on maximum plastic dissipation and the multiplicative decomposition: Part II. computational aspects, *Computer Methods in Applied Mechanics and Engineering* **68**, 1–31, 1988.

[127] A. Srikanth and N. Zabaras, A computational model for the finite element analysis of thermoplasticity coupled with ductile damage at finite strains, *International Journal for Numerical Methods in Engineering* **45**, 1569–1605, 1999.

[128] L. Stainier and M. Ortiz, Study and validation of a variational theory of thermo-mechanical coupling in finite visco-plasticity, *International Journal of Solids and Structures* **47**, 705–715, 2010.

[129] K. K. Tamma and R. R. Namburu, An effective finite element modeling/analysis approach for dynamic thermoelasticity due to second sound effects, *Computational Mechanics* **9**, 73–84, 1992.

[130] M. Tanaka, T. Matsumoto, and M. Moradi, Application of boundary element method to 3-D problems of coupled thermoelasticity, *Engineering Analysis with Boundary Elements* **16**, 297–303, 1995.

[131] R. L. Taylor. *FEAP - a finite element analysis program*. Department of Civil and Environmental Engineering, University of Berkeley, CA, USA, 2013.

[132] V. Tini, I. N. Vladimirov, Y. Kiliclar, and S. Reese, Finite deformation damage modeling in challenging applications - forming limit diagrams and life time analysis for a rocket thrust chamber, In *Proceedings of the ECCOMAS - XI International Conference on Computational Plasticity. Fundamentals and Applications*, Barcelona, Spain, 2011.

[133] N. Tosaka and I. G. Suh, Boundary element analysis of dynamic coupled thermoelasticity problems, *Computational Mechanics* **8**, 331–342, 1991.

[134] H. Tresca, Mémoire sur l'écoulement des corps solides, *Mémoires présentés par divers savants á l'institut impérial de France* **18**, 733–799, 1868.

[135] C. Truesdell, A new definition of a fluid, II. the Maxwellian fluid, Technical Report P-3553, § 19, US Naval Research Laboratory, 1949.

[136] C. Truesdell and W. Noll, *The non-linear field theories of mechanics*, Springer, 2004.

[137] S. Tsoukalas. Eine verschiebungsbasierte Elementformulierung zur Simulation von inkompressiblem Materialverhalten. Semesterarbeit, Institute for Computational Mechanics, Technische Universität München, 2010.

[138] R. S. Tuminaro, M. Heroux, S. A. Hutchinson, and J. N. Shadid, Official Aztec user's guide, Version 2.1 SAND99-8801J, Sandia National Laboratories, 1999.

[139] I. N. Vladimirov, M. P. Pietryga, Y. Kiliclar, V. Tini, and S. Reese, Failure modelling in metal forming by means of an anisotropic hyperelastic-plasticity model with damage, *International Journal of Damage Mechanics*, 2014.

[140] R. von Mises, Mechanik der festen Körper im plastisch-deformablen Zustand, *Nachrichten von der Gesellschaft der Wissenschaften zu Göttingen, Mathematisch-physikalische Klasse* **1913**, 582–592, 1913.

[141] W. A. Wall, *Fluid-Struktur-Interaktion mit stabilisierten Finiten Elementen*, PhD thesis, Institute for Structural Mechanics, University of Stuttgart, 1999.

[142] W. A. Wall and M. W. Gee, BACI: A parallel multiphysics finite element environment, Technical report, Institute for Computational Mechanics, Technische Universität München, 2014.

[143] L. Wiechert, *Computational modeling of multi-field and multi-scale phenomena in respiratory mechanics*, PhD thesis, Institute for Computational Mechanics, Technische Universität München, 2011.

[144] M. L. Wilkins, Calculation of elastic-plastic flow, In *Methods in Computational Physics*, pages 211–263, Academic Press, New York, NY, USA, 1964.

[145] K. Willner, *Kontinuums- und Kontaktmechanik*, Springer, 2003.

[146] P. Wriggers, C. Miehe, M. Kleiber, and J. C. Simo, On the coupled thermomechanical treatment of necking problems via finite element methods, *International Journal for Numerical Methods in Engineering* **33**, 869–883, 1992.

[147] Q. Yang, L. Stainier, and M. Ortiz, A variational formulation of the coupled thermo-mechanical boundary-value problem for general dissipative solids, *Journal of the Mechanics and Physics of Solids* **54**, 401–424, 2006.

[148] L. Yoshihara, M. Ismail, and W. A. Wall, Bridging scales in respiratory mechanics, *Computer Models in Biomechanics - From Nano to Macro, Springer*, 395–407, 2013.

[149] O. Zienkiewicz and R. L. Taylor, *The Finite Element Method for Solid and Structural Mechanics*, Butterworth Heinemann, 2000.

[150] O. Zienkiewicz, R. L. Taylor, and J. Z. Zhu, *The Finite Element Method: Its Basis & Fundamentals*, Butterworth Heinemann, 2005.